2016

Seismic Collapse Assessment of Self-Centering Steel Moment Resisting Frame Systems with Web Friction Devices

Omid Ahmadi
Lehigh University

Seismic Collapse Assessment of Self-Centering Steel Moment Resisting Frame Systems with Web Friction Devices

by

Omid Ahmadi

Presented to the Graduate and Research Committee
of Lehigh University
in Candidacy for the Degree of
Doctor of Philosophy

in

Structural Engineering

Lehigh University

September 2016

Approved and recommended for acceptance as a dissertation in partial fulfillment of the requirements for the degree of Doctor of Philosophy.

_____
Date

_____
Dr. James M. Ricles
Dissertation Co-Supervisor

_____
Dr. Richard Sause
Dissertation Co-Supervisor

_____
Accepted Date

Committee members:

_____
Dr. John L. Wilson
Committee Chairperson

_____
Dr. Shamim N. Pakzad
Committee Member

_____
Dr. Maria Garlock
External Member

Dedicated to my parents for their endless love and support

Acknowledgements

The research presented in this dissertation was conducted at the Engineering Research Center for Advanced Technology for Large Structural System (ATLSS), Department of Civil and Engineering, Lehigh University, Bethlehem, Pennsylvania. The financial support from the Civil and Environmental Engineering Department of Lehigh University is greatly appreciated.

I would like to thank my research advisors, Dr. James M. Ricles and Dr. Richard Sause for their guidance, advice, and patience. I would like to thank Dr. John L. Wilson, the chair of my research committee for his advice and support. I would also like to thank my other research committee members, Dr. Shamim N. Pakzad and Dr. Maria Garlock for their time and contribution.

I would like to thank my friends at Lehigh University and specifically my fellow graduate students at ATLSS Engineering Research Center, particularly my friend Karim Kazemi Bidokhti for helping me get through difficult times during my doctoral studies. I greatly appreciate the support of ATLSS personnel, specifically Peter Bryan, Darrick J. Fritchman and Carl Bowman.

Finally, and most importantly, I am thankful to my loving parents, Mr. Majid Ahmadi and Mrs. Mehri Atarod, for their constant support and their faith in me throughout my entire life. I would have not been able to complete this dissertation without the support from my parents.

Contents

List of Tables

List of Figures

ABSTRACT

The design method used for conventional steel special moment resisting frame (SMRF) with welded beam-to-column connections leads to significant inelastic deformations and formation of plastic hinges in the beams under the design earthquake for seismic resistant steel frame buildings. This may cause significant damage. A self-centering (SC) moment resisting frame (SC-MRF) is a viable alternative to a conventional SMRF. The beams in an SC-MRF are post-tensioned to the columns by high strength post-tensioning (PT) strands oriented horizontally to provide SC forces when gap opening occurs. An SC-MRF is characterized by gap opening and closing at the beam-column interface under earthquake loading. The SC-MRF is typically designed to meet several seismic performance objectives, including no structural damage under the DBE in order to perform in a resilient manner. Recent analytical and experimental research has shown that an SC-MRF can achieve this performance objective. Since an SC-MRF system is a new concept little is known about its collapse resistance under extreme seismic ground motions. For an SC-MRF to be accepted in practice, the collapse resistance of this type of structural system under extreme ground motions must be established to assess whether it is adequate. Incremental Dynamic Analysis (IDA) are performed using an ensemble of 44 far-field ground motions to determine the probability of collapse of a 4-story low-rise building with perimeter SC-MRFs. A model of the SC-MRF was developed that included both stress-resultant and continuum finite elements to enable the important limit states, including local buckling in the beams, to be accounted for in the IDA. In order to compare the collapse performance of an SC-MRF with an

SMRF a 4-story SMRF was designed and IDA performed to determine the collapse resistance of the SMRF. The results show that the collapse resistance of an SC-MRF system can exceed that of a conventional steel SMRF. In addition, the design of the SC-MRF is modified to investigate the collapse resistance sensitivity to the PT strand detailing, by varying the number of PT strands and level of PT force. The results show that collapse resistance is affected by the level of PT force, where an increased number of strands lead to a higher post-gap opening stiffness resulting in larger axial forces and local buckling developing in the beams. This leads to a higher probability of collapse than the original design and comparable with the collapse resistance of SMRF.

Structures are built where active faults may be in close proximity. The probability of collapse of a 4-story low-rise building with perimeter SC-MRFs subjected to near-field ground motions was studied and compared to the results for far-field ground motions. IDA are performed using an ensemble of 56 near-field ground motions. The results show that the SC-MRF built close to active faults has less collapse resistance in contrast to the one built in seismic zones away from active faults. The structure has larger spectral acceleration for near-field ground motions than far-field ground motions at the fundamental period, leading to excessive inelastic deformations that cause structure collapse earlier. The results obtained, however, show that an acceptable margin against collapse is still achieved and therefore indicate a potential for an SC-MRF to be used in seismic zones with active near-field faults.

Chapter 1

Introduction

1.1. Overview

Conventional steel welded special moment resisting frames (SMRFs) use fully restrained welded connections between the beams and columns (Figure 1.1). The design method used for SMRFs leads to significant inelastic deformations and the formation of plastic hinges in the beams under the design basis earthquake (DBE). Plastic hinges may cause significant damage which may result in residual drift. Miranda (2009) found that the amplitude of residual story drift is the most important contributor to economic losses of buildings following an earthquake and leads to the demolition of the structure after an earthquake. Repair or replacement of damaged members and removing residual drift is usually prohibitively expensive and difficult. Thus, it is often more economical to demolish rather than to repair a building with residual drift.

To minimize structural damage during the DBE and avoid permanent residual drift, post-tensioned beam-to-column connections for self-centering moment resisting frames (SC-MRF) were developed by Ricles et al. (2001). The behavior of an SC-MRF is characterized by connection gap opening and closing at the beam column interface (see Figure 1.2(a) and (b)). Figure 1.2(c) shows the conceptual moment-relative rotation behavior of an SC connection. The gap opening allows the beam to rotate relative to the column, enabling an SC-MRF to soften without damaging the beams or columns. An SC-MRF uses horizontally-oriented high strength post-tensioning (PT) strands to pre-compress the beams to the columns. The PT force closes the gaps that develop under

earthquake loading, returning (i.e., self-centering) the frame to its initial pre-earthquake position. Energy is dissipated by using energy dissipation devices to reduce the seismic response of an SC-MRF rather than by forming inelastic regions in the structural members. Several research studies (Garlock et al. 1998; Ricles et al. 2001; Rojas et al. 2005; Tsai et al. 2008; Kim and Christopoulos 2008; Wolski et al. 2009; Iyama et al. 2009; Lin 2012) have experimentally demonstrated that a properly designed connection in an SC-MRF is capable of developing softening behavior and self-centering without causing structural damage, with negligible residual drift under the design earthquake. Prior research has focused on experimental studies of connection subassemblies and numerical studies of SC-MRF systems. The behavior, performance, and design concepts of an SC-MRF system at various earthquake input levels were investigated.

A comprehensive knowledge of the collapse resistance of an SC-MRF system under strong ground motions is still lacking. This knowledge gap forms the basis for this research. Four different case studies are investigated in this research, namely, seismic collapse resistance assessment of an SC-MRF under far-field and near-field ground motions. In addition to these effects, the effects of PT strand yielding on seismic collapse resistance is investigated.

1.2. Research Objectives

The overall research objectives are: (1) to investigate the collapse performance of a low-rise SC-MRF system; and (2) to compare the seismic collapse performance of an SC-MRF with a comparable conventional SMRF system.

1.3. Research Scope

To achieve the research objectives, the following tasks are conducted:

1. Design of a low-rise prototype building with SC-MRFs as the lateral force resisting system:

   A low-rise 4-story prototype building designed by Lin (2012) is selected for the analytical studies in this research. This building is located in a high seismic zone (e.g., Southern California). The SC-MRFs are designed using a performance-based design (PBD) procedure developed by Lin.

2. Modeling of SC-MRF for response prediction to an extreme earthquake:

   The beams in an SC-MRF are expected to yield and develop potential local buckling from appreciable member axial force and bending moment formed under extreme ground motions. This is an important collapse limit state that needs to be taken into account. To evaluate the seismic collapse performance of an SC-MRF there is a need for a finite element model of the complete structural system that can capture the important limit states that can occur under extreme ground motions, including gap opening at the beam-column interface, yielding of the PT strands, yielding and inelastic deformations in the members (beams, columns, panel zones), second order (P-delta) effects due to gravity loads imposed on the gravity load frames, and beam local flange and web buckling in the plastic hinge region. It is required to be computationally efficient in order to efficiently perform many incremental dynamic analyses (IDAs), therefore the analysis model includes stress resultant and continuum shell elements. The continuum elements are started

from the end of the reinforcing plates and continued for one beam depth where local buckling is expected to develop in the plastic hinge region of the beam.

3. Calibration of SC-MRF model:

   In order to develop a computational efficient model capable of capturing the beam local buckling limit state, the experimental test data (Garlock (2002)) for an interior connection subassembly is used to calibrate the model. Initial imperfections are imposed on the shell elements used in the model to initiate any local buckling in the beams. The first buckling mode shape is scaled to impose web and flange out-of-flatness imperfections in the beams of the model. A sensitivity analysis is performed using representative values of web and flange out-of-flatness.

4. Seismic collapse assessment of an SC-MRF:

   The IDA method is used to assess the seismic collapse capacity of the SC-MRF under a pair of 22 far-field records which included 44 ground motion components from FEMA P695 (2009). IDA is a parametric analysis method (Vamvatsikos and Cornell (2006)) in which individual ground motions are scaled to increasing intensities until the structure reaches a collapse point. The collapse point can be defined in many ways, including when the structure reaches a relatively large story drift value (for instance, 10 percent as the maximum story drift) under dynamic loading or when the structure undergoes dynamic instability which means the structure experiences a large story drift under a small incremental increase in ground motion intensity. Both of the above definitions for collapse are adopted in this research. A collapse fragility curve is obtained by fitting a

cumulative distribution function, assuming a lognormal distribution, to the collapse data (Ibarra et al. (2002)). Different sources of uncertainty are considered in order to adjust the fragility curves based on FEMA P695 to determine the probability of collapse under the Maximum Considered Earthquake (MCE) level. The collapse margin ratio (CMR) is obtained which is the ratio of the spectral acceleration intensity at which half of the ground motions cause the structure to collapse, to the MCE code specified spectral acceleration intensity at the fundamental period of the structure. This case study is named as SC-MRF Design 1: far-field.

5. Parameter study on design limit for the maximum PT strand force:

   Designers have the option to lower the design limit for the maximum PT strand force in order to avoid PT strand yielding and fracture scenarios. In order to investigate the implication of this design parameter on the seismic collapse resistance of an SC-MRF, the SC-MRF design is modified to limit the total PT force under MCE to 75 percent of the total PT yield force instead of 90 percent of the total PT yield force, as used in the original design, while maintaining the same initial total PT force. To maintain the same initial total PT force, the number of PT strands is increased. In the design with more PT strands the total axial stiffness of the PT strands increases, which leads to larger PT strand forces and therefore larger beam axial forces after gap opening occurs in the connection. The beam axial forces and bending moments that develop require a design change of the reinforcing plate length in accordance with the PBD procedure. The IDA method is used to assess the seismic collapse resistance of the SC-MRF with the revised

design criterion for PT strands for far-field ground motions. This case study is named SC-MRF Design 2: far-field. For this case the total PT force under MCE is limited to 75 percent of the total PT yield force in design.

6. Seismic collapse resistance of an SC-MRF for near-field ground motions:

   Structures are built where active faults may be in close proximity. The seismic collapse resistance of SC-MRF Design 1 is studied for near-field ground motions. The IDA method is used to assess the seismic collapse capacity using a pair of 28 near-field records, which included 56 ground motion components from FEMA P695 (2009). CMR is obtained when half of the ground motions cause the structure to collapse for near-field ground motions This case study is named SC-MRF Design 1: near-field.

7. Compare seismic collapse resistance of SC-MRFs with a comparable conventional SMRF:

   A 4-story prototype office building with SMRFs is designed with the same floor plan and elevation as the prototype building with SC-MRFs. The building is assumed to be located at the same site as the prototype building with SC-MRFs. The SMRF is modeled similar to the SC-MRF using continuum and stress-resultant elements. In the model the continuum elements were started from the face of column and continued for one beam depth where local buckling is expected to develop in the beam. In order to validate the modeling procedure for an SMRF the connection behavior is studied by comparing the analytical model results with the experimental test data (Ricles et al. (2000)) for an interior subassembly connection. IDA are performed to obtain the CMR and a collapse

fragility curve is obtained for the SMRF for far-field ground motions and compared to an SC-MRF. This case study is named SMRF: far-field.

1.4. Organization of Dissertation

This dissertation is divided into twelve chapters, including the present chapter. The remaining chapters are organized as follows:

- Chapter 2 reviews prior relevant research on post-tensioned steel SC connections.
- Chapter 3 describes the PBD procedure and design criteria for SC-MRFs.
- Chapter 4 describes the prototype building adapted for this research including SC-MRF Design 1, SC-MRF Design 2 and conventional SMRF.
- Chapter 5 presents connection finite element (FE) modeling and the calibration process.
- Chapter 6 presents the frame finite element development utilized to assess the seismic collapse resistance of SC-MRF and SMRF systems under dynamic loading.
- Chapter 7 describes collapse assessment background and methodology.
- Chapter 8 presents collapse assessment of the SC-MRF Design 1: far-field and SC-MRF Design 2: far-field.
- Chapter 9 presents collapse assessment of the SMRF: far-field.
- Chapter 10 presents collapse assessment of SC-MRF Design 1: near-field.
- Chapter 11 compares the seismic collapse resistance of SC-MRFs with the SMRF.
- Chapter 12 summarizes the research program, conclusions, and recommendations for future research.

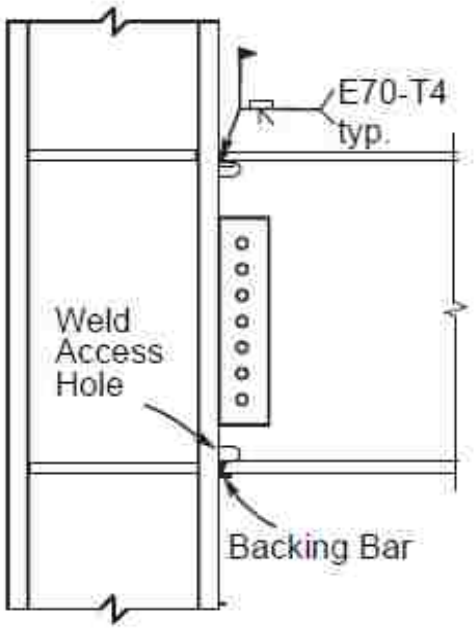

Figure 1. 1. Typical welded SMRF connection (Garlock (2002)).

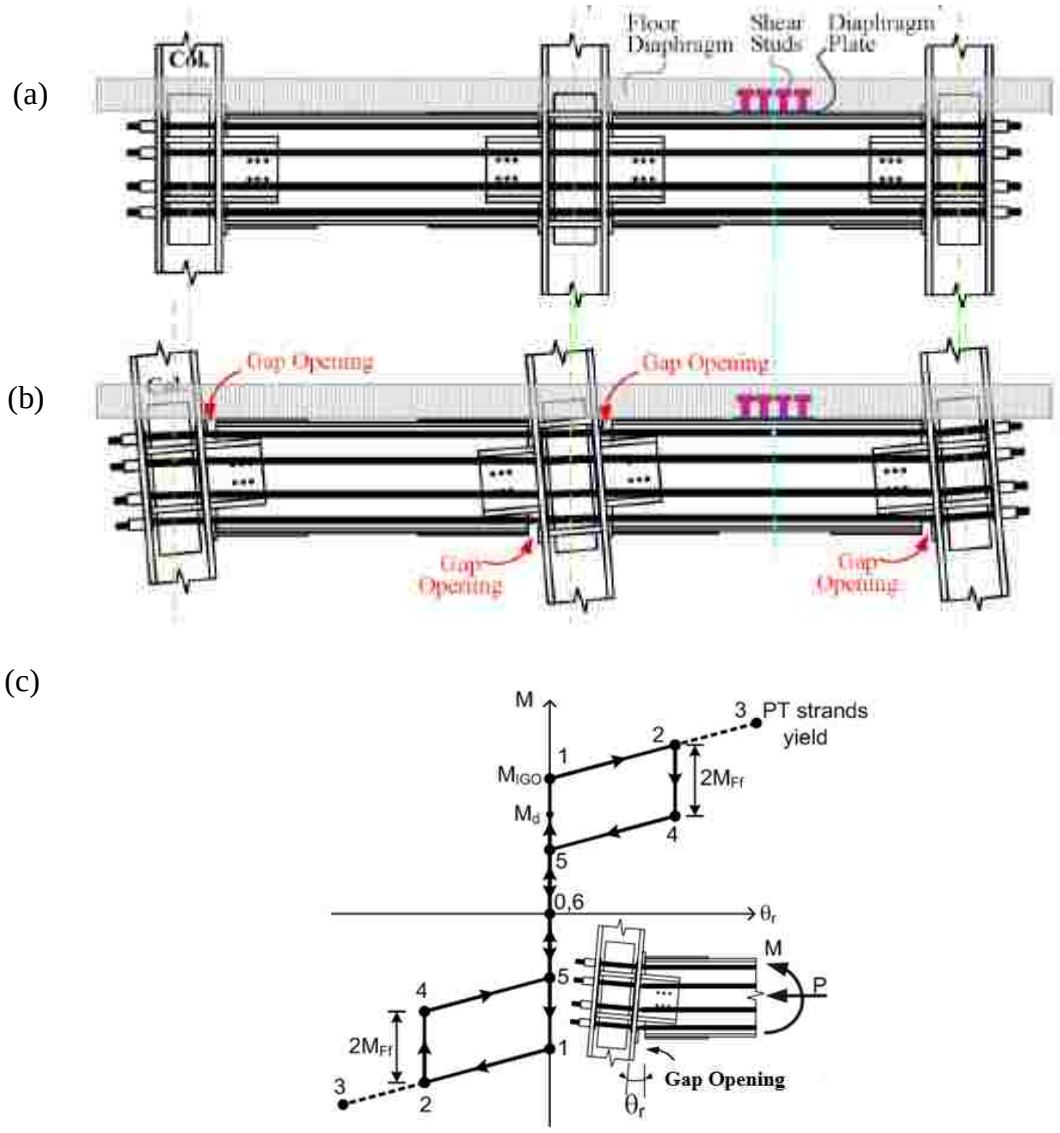

Figure 1. 2. Schematic of SC-MRF elevation (a) without gap opening, and (b) with gap opening at beam-to-column connections; (c) conceptual moment-relative rotation behavior of SC connections (Lin (2012)).

Chapter 2

Prior Relevant Research on Post-Tensioned Steel SC Connections

2.1. General

This chapter presents a brief overview of steel self-centering (SC) systems. During a severe earthquake, the SC capability is provided by unbonded post-tensioning (PT) steel elements, and damage to structural members (beams and columns) is prevented. First, the motivation for the post-tensioned steel SC connection is discussed. Then, the prior relevant research on post-tensioned steel SC systems is presented. The behavior of steel SC connection with web friction devices (WFDs), denoted by SC-WFD, is discussed in detail. The performance-based design (PBD) procedure used to design an SC-MRF is summarized. Finally, the inertial force floor diaphragm collector system is presented.

2.2. Motivation for the SC Connections

Following the 1994 Northridge earthquake, beam-to-column connection failures were found in over 130 steel MRF buildings with field-welded connections (Youssef et al. (1995)). In many cases brittle fractures initiated within the connections at a low level of plastic demand, and in some cases, while the structures remained elastic (Interim (1995)). Thus, new moment connection details, including the use of reinforcing plates, bolted haunch brackets, welded haunch brackets, and the removal of part of the beam flanges to ensure that plastic hinges form in the beams (Engelhardt and Sobol (1998); Kasai (1998) and Chen et al. (1996)), had been developed that are intended to avoid weld failure and force inelastic deformations to develop in the beams. These connections will undergo

significant yielding under the DBE that result in permanent structural damage as well as residual drift following the earthquake. Recent research has been conducted to develop new seismic resisting structural systems which can withstand earthquakes with less damage and residual drift compared to conventional systems. This system utilizes post-tensioned beam-to-column connections and ED devices in steel MRFs that avoids the use of field welding, reduces the potential for damage in the beams, and results in SC capability for MRFs that leads to relatively little residual drift after an earthquake. Energy is dissipated in ED devices by inelastic deformations or friction mechanisms. The ED devices might become damaged and need to be replaced after the earthquake. This connection is referred to as a post-tensioned steel SC connection.

2.3. Steel SC Systems

As stated previously, numerous new moment connection details have been developed after the 1994 Northridge earthquake. These connections have potential for significant residual drift under the design level ground motions. Repairing this damage or eliminating this residual drift may require considerable expense. Although the structural damage might be repairable, it is often more economical to demolish rather than to repair a building with large residual drift. Miranda (2009) found despite the fact that ductile structures are highly resistant to collapse when subjected to intense ground motions, residual drift leads the likelihood of the structure being demolished after an earthquake.

To minimize structural damage and residual drift under earthquake loading, a new type of steel moment resisting connection, referred as a post-tensioned steel SC connection, was initially developed by Garlock et al. (1998) and Ricles et al. (2001). Currently, several types of beam-to-column connections have been proposed for the

actual implementation of the PT concept in steel moment resisting frames. In particular, the proposed PT systems are based on the use of high resistant steel strands or bars, whereas the proposed ED systems are based on yielding or friction mechanisms.

Prior research focused on experimental studies of connection subassemblies and numerical studies of SC-MRF systems. The behavior, performance, and design concepts of an SC-MRF system at various earthquake input levels were investigated. A comprehensive knowledge of the collapse resistance of an SC-MRF system under strong ground motions is still lacking. This knowledge gap forms the basis for this research presented herein.

2.3.1. Prior Research on Steel SC Connections

Ricles et al. (2001) and Garlock (2002) developed a post-tensioned connection for steel MRFs (see Figures 2.1 and 2.2). The connection is based on a series of high resistance steel strands, whereas the ED system is composed of bolted steel top-and-seat angles. PT strands clamp the beam to the column at their interface. The force in the PT strands provides a restoring moment to the connection to prevent residual connection rotation and residual story drift. When the gap at the beam column interface opens, the steel strands elastically elongate and the angles deform. The dissipative mechanism is based on the formation of plastic hinges in the legs of each angle. The connection resists shear forces through the friction at the beam flange-to-column interface, while the ED angles resist directly the gravity loads. Results showed that when the connection is properly designed, the inelastic deformation is limited to the angles.

Rojas (2003) and Rojas et al. (2005) developed a post-tensioned friction damped connection (PFDC) for use in SC-MRFs (see Figure 2.3). A PFDC uses a slotted shear tab to connect the column to the beam web. Friction devices are located at the top and bottom of the beam flanges, which dissipate the energy during the cyclic gap openings at the beam column interface. Each of the friction devices consists of a friction plate sandwiched by two brass shim plates (Figure 2.3(b)). An analytical model of a MRF with PFDCs was developed by means of using fiber elements. The seismic response of the SC-MRF was studied using nonlinear dynamic time history analyses under earthquake ground motion. The SC-MRF was also compared with the seismic response of a conventional SMRF with fully-restrained (FR) (i.e., welded) moment connections. The comparison showed that the maximum story drifts of the two MRFs are similar. However, the MRF with PFDCs had no significant residual drift compared to the conventional FR-MRF (see Figure 2.4(a) and (b)). In Figure 2.4(c), M is the connection moment, $M_{p,n}$ is the nominal plastic moment capacity of the beam, θ_p is the beam plastic rotation and θ_r is the connection relative rotation in PFDC connection that occurs between the beam and the column.

Wolski (2006) and Wolski et al. (2009) developed a post-tensioned connection with a beam bottom flange friction device (BFFD) for added energy dissipation (Figure 2.5(a)). The BFFD is located only below the beam bottom flange to avoid interference with the floor slab at the beam top flange. Friction bolts are used to provide a normal force on the friction surfaces in the BFFD. Experiments were conducted on a series of BFFD connection subassembly specimens (Figure 2.5(b)). Experimental results showed the BFFD provides reliable energy dissipation. The connection moment-rotation was,

however, asymmetric (Figure 2.5(c)). A further study of the seismic response of a MRF with BFFD connections (denoted as BFFD-MRF) was conducted by Iyama et al. (2009). They designed a prototype BFFD-MRF for seismic response analysis and found that the inflection point in a beam was far away from the mid-span of the beam due to the asymmetric moment-rotation behavior of the BFFD (Figure 2.6). The consequence of this result is that the beam design was uneconomical.

In a connection conceived by Tsai et al. (2008), beam web friction devices (BWFDs) work as ED system (Figure 2.7(a)). It was found that the friction coefficient ranged from 0.34 to 0.37 through uniaxial tests on individual friction device specimens. The test setup for the connection specimens with BWFD is shown in Figure 2.7(b). Loading was applied at the top of the column. Typical test results shown in Figure 2.7(c) which demonstrate the SC behavior of the connection.

Kim and Christopoulos (2008) developed a SC friction damped (SCFR) connection. Instead of using PT strands, PT bars were used to self-center the connection. Subassembly tests were performed with a displacement-based cyclic loading protocol. Typical test results (Figure 2.8) showed good energy dissipation capacity of the SCFR. One of the specimens had two 40 mm holes drilled in the beam flanges at the ends of the beam reinforcing plates, to reduce the nominal plastic moment and expedite yielding and hinge formation (Kim and Christopoulos (2008)), and longitudinal stiffeners welded to the beam web at the end of beam reinforcing plates. The longitudinal web stiffeners prevented beam web buckling and the beam formed a plastic hinge in this region at a drift of 2.8% rad (see Figure 2.9).

To experimentally investigate the performance of an SC-MRF, a 0.6-scale 4-story 2-bay frame designed in accordance with a PBD procedure was tested by Lin (2012). The beams are post-tensioned to the columns by high strength PT strands oriented horizontally to provide SC forces when gap opening occurs. Energy dissipation is provided by beam web friction devices (WFDs) attached to the columns at the beam column interface (Figure 2.10(a)). Brass plates fabricated from ASTM B-19 UNS half-hard cartridge brass material are placed on the friction surface between the beam and friction channels to provide a controlled level of friction. The brass plates were designed to slide against the beam webs. The coefficient of friction for the steel plate-brass plate friction surface is assumed to be 0.4, which is the lower bound value from test results by Petty (1999). Lin (2012) concluded that SC-MRFs can be designed to enable immediate occupancy (IO) performance of an SC-MRF building with minimal yielding in the main structural members under the DBE, and to achieve collapse prevention (CP) performance with minor damage while maintaining SC behavior under the MCE. The results showed that the seismic design procedure and criteria for SC-MRF systems are effective, enabling IO and CP performance to be reached under the DBE and MCE, respectively.

Since a steel MRF with SC-WFD connections is utilized in this research, the behavior of an SC-WFD connection is discussed in detail.

2.3.2. Conceptual Behavior of an SC-WFD Connection

Figure 2.10(b) shows the conceptual moment-relative rotation (M-θ_r) behavior of a post-tensioned steel SC connection with a WFD where θ_r is the relative rotation between the beam and column when gap opening occurs and M is the moment at the connection. The total moment resistance of the connection is provided by the contribution of the PT

force in the strands, an axial force from the diaphragm and friction force produced by the WFD. From event 0 to 1 in Figure 2.10(b), the connection behaves as a fully restrained connection where it has an initial stiffness that is similar to a conventional welded moment connection when θ_r is equal to zero. Once the applied moment reaches the moment resistance due to the initial PT force in the strands, decompression of the beam from the column face occurs. This moment is called the decompression moment, M_d, and computed using Equation (2.1):

$$M_d = T_0 d \tag{2.1}$$

where T_0 is the initial PT force and d is the distance from the PT force centroid to the center of rotation (COR) of the connection. The strands are arranged symmetrically about the centroid of the beam so the resultant PT force passes through the beam section centroid. The moment is called the imminent gap opening moment, M_{IGO}, and occurs at event 1 in Figure 2.10(b), which is the point of imminent rotation and is the sum of the decompression moment M_d due to the initial PT force and the friction moment, M_{Ff}, associated with the friction force in the WFD:

$$M_{IGO} = T_0 d + F_f r \tag{2.2}$$

The product F_f r is denoted as the friction moment, M_{Ff}, where r is the distance from the WFD friction force resultant to the COR as shown in Figure 2.10(c). The COR is at the point of the beam compression flange in contact with the column, and assumed to be located at the mid- thickness of the beam reinforcing plate. The WFD friction force resultant is located at the centroid of the friction bolts that provide the normal frictional

force. This friction force is a function of normal force produced by friction bolts, N, and the friction coefficient, μ, where

$$F_f = \mu N \tag{2.3}$$

μ is assumed to be 0.4 for design purposes which is the lower bound value using from test results by Petty (1999).

At this point, the beam tension flange loses contact with the shim plate at the column face and the gap opening and the corresponding relative rotation θ_r begins. The shim plates are used to provide good contact surfaces for the beam flanges. The stiffness of the connection after gap opening is associated with the elastic axial stiffness of the PT strands. The connection moment, M, continues to increase as the PT strand force increases with strand elongation due to the gap opening (event 1 to event 2) in Figure 2.10(a). Thus, M is controlled by the axial force in the beam, P, and the friction force resultant in the WFD, F_f, after gap opening occurs:

$$M = Pd + F_f r \tag{2.4}$$

In Equation (2.4) P is due to the PT force, T, and an additional axial force, F_{fd}, produced by the interaction of the SC-MRF with the floor diaphragm (Garlock et al. 2005):

$$P = T + F_{fd} \tag{2.5}$$

where

$$T = T_0 + 2d\theta_r^{ave}\left(\frac{k_b k_s}{k_b + k_s}\right) \quad (2.6)$$

In Equation (2.6), k_b and k_s are the axial stiffness of the beam and the PT strands within one bay, respectively, and θ_r^{ave} is the average connection relative rotation for all connections at one floor level. Yielding of the strands eventually may occur at event 3 in Figure 2.10(a). Upon unloading, θ_r remains constant but the moment decreases by $2M_{Ff}$ due to the reversal in friction force in the WFD. Continued unloading between events 4 and 5 reduces θ_r to zero as the beam tension flange comes in contact with the shim plate at the column face. Between events 5 and 6 the value of the moment decreases with the beam being compressed against the shim plates and the moment eventually reaches zero at event point 6. A similar behavior occurs when the applied moment is reversed. As long as the strands remain elastic and there is no significant beam yielding, the PT force is preserved and the connection will self-center upon unloading. After the first half cycle, the forces in the connection are indeterminate due to a residual friction force that exists at event 6 until imminent gap opening is again reached. Thus, there is no clear point of decompression on the curve following the first half cycle. The beam vertical shear force is resisted by friction forces developed at the beam flange-to-column interface due to the presence of the beam compression force, which produces the normal force required to develop the friction force at the beam column interface.

2.3.3. Performance Based Design of MRFs with SC-WFDs

Lin (2012) developed a PBD approach and associated design objectives for post-tensioned steel MRFs with SC-WFDs. The PBD considers two levels of seismic input, the DBE and the MCE. Under the DBE level ground motions, an SC-MRF system is

designed to sustain minimal structural damage and no significant residual drift. This level of performance would enable immediate occupancy after the DBE, depending on the amount of non-structural damage. In the present research, an SC-MRF system is designed to also achieve the collapse prevention (CP) performance level under MCE level ground motions. Different limit states for an SC-MRF are shown in the conceptual base shear-roof drift (V-θ_{rf}) response in Figure 2.11.

Figure 2.12 shows the relationship between different limit states and the M-θ_r relationship. IO and CP performance levels are noted in association with the limit states. As indicated in Figure 2.12, before the IO performance limit is reached the moment in the beam-to-column connection may exceed M_{IGO} and gap opening is permitted. Beam flange yielding is also permitted, but the strain should be less than twice the yield strain ε_y at the end of reinforcing plates under the DBE level to prevent beam flange local bucking under the MCE level. Before the CP performance limit, panel zone yielding, beam web yielding in shear, and a beam flange strain at the end of reinforcing plates greater than $2\varepsilon_y$ are permitted. Before the CP performance limit is reached, PT strand yielding and beam local web buckling are not permitted. PT strand yielding and beam local web buckling lead to PT strand force and connections capacity loss.

The design procedure for an SC-MRF developed by Lin (2012) is summarized in Figure 2.13. More details about the design criteria are given in Chapter 3. In Step 1, the design demands are established from the equivalent lateral force (ELF) procedure of ASCE 7-10 (2010). By the amplifying linear elastic response (from Step 3) with appropriate factors, SC-MRF deformation demands are estimated (Step 4). Force demands are established from the ELF procedure directly, or from analysis of the

connection response under the design deformation demands. In Step 5, the connection is designed. An SC connection must have sufficient moment capacity at the design level. Thus, the M_{IGO} (in Step 5) should be greater or equal to M_{des}, where M_{des} is the connection moment when the building is subjected to the ELF corresponding to the design base shear, V_{des}. The effective energy dissipation ratio (β_E) quantifies the energy dissipation characteristics of an SC connection, where:

$$\beta_E = \frac{M_{Ff}}{M_{IGO}} \tag{2.7}$$

Seo and Sause (2005) showed that as β_E increases, the lateral drift demand for an SC system decreases. For design purposes, $0.25 \leq \beta_E \leq 0.4$ was established as the target range (in Step 5). The beam flange reinforcing plates enlarge the contact surface and therefore decrease the contact stresses that develop on the beam flanges. In addition, reinforcing plates strengthen the beam where large moments develop, in combination with the axial force resulting from the post-tensioning. In Step 6, the beam flange reinforcing plates are designed based on limiting the beam flange strain to be limited to $2\varepsilon_y$ at the end of the cover plates and preventing beam horizontal shear yielding under the DBE. There are numerous checks in the design procedure, including story drift (Check 1 and Check 4), PT strand force (Check 2), and weak bream-strong column and section compactness (Check 3). In Check 1 and Check 4, based on ASCE 7-10 the maximum story drift of the building should be less than or equal to 2%. In Check 2, the PT force at the MCE level is limited to 81% of the ultimate tensile capacity of PT strands. In Check 3, conventional AISC compactness criterion is checked. More details are given in

Chapter 3 since this PBD procedure is used for the prototype building investigated in this research.

2.3.4. Inertial Force Transfer Systems

The inertial force is transferred from the floor diaphragm to the lateral load resisting frame. Thus, floor diaphragm is attached to the beam at selected points in the lateral load resisting frame. Garlock (2002) and Garlock at al. (2007) showed that a conventional floor diaphragm system will restrain gap opening at the beam-to-column connections of an SC-MRF. The concept of using flexible collector beams (Figure 2.14) in the floor diaphragm was therefore proposed. The flexible collector beams were designed to deform in the plane of the floor diaphragm while gap opening develops at the beam-to-column connections.

King (2007) suggested another floor diaphragm connection concept for an SC-MRF system. As shown in Figure 2.15, the floor diaphragm is attached to only one bay of each SC-MRF (denoted as the fixed bay). The floor diaphragm slides on the beams in the other bays of each SC-MRF (denoted as sliding bays). This concept was proposed to allow SC-MRF connections to develop gap opening without restraint from the floor diaphragm. This floor diaphragm connection also avoids the inelastic deformation of the flexible collector beams recommended by Garlock (2002).

Lin (2012) utilized the previously mentioned system where the floor diaphragm is attached to only one bay of each SC-MRF. By attaching the floor diaphragm to only one bay, the beam-to-column connections are free to develop gap opening. This type of floor diaphragm system was used in this dissertation research.

(a)

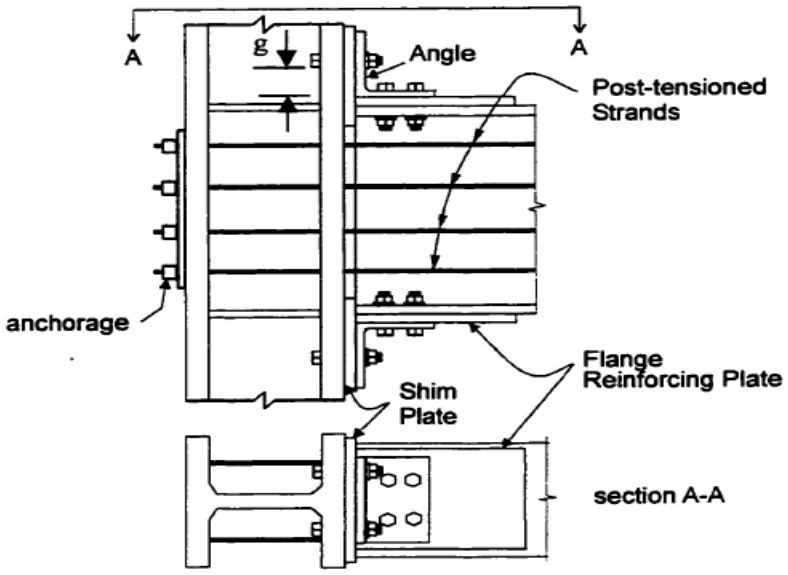

(b)

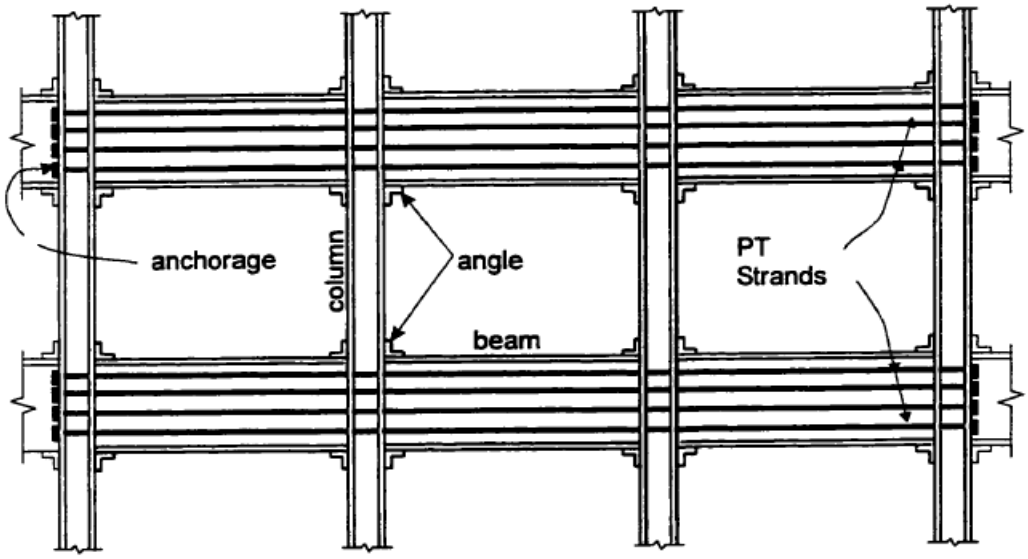

Figure 2. 1. Schematic of (a) SC connection and (b) SC-MRF with SC connections (Ricles et al. (2001)).

(a)

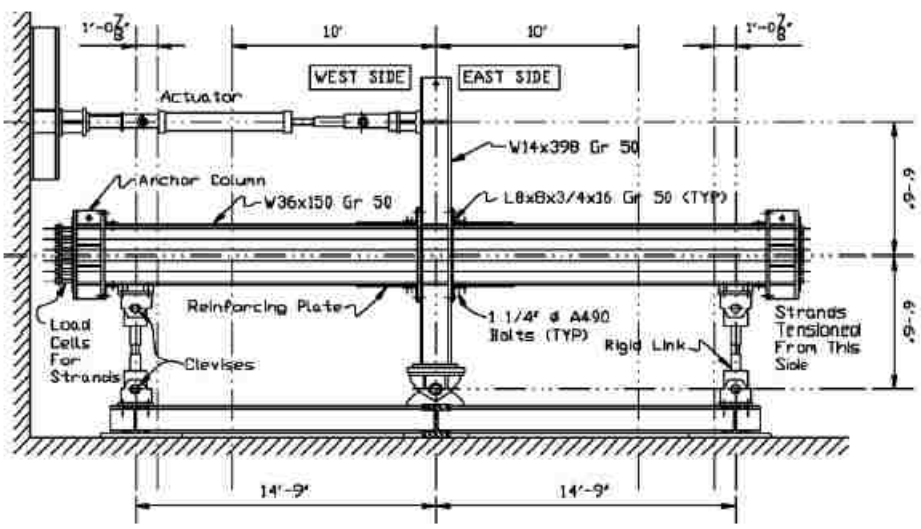

(b)

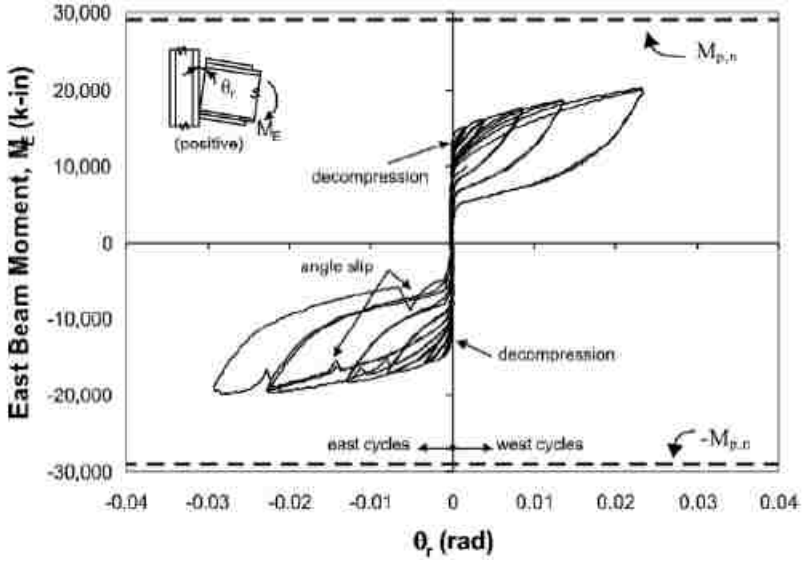

Figure 2. 2. Test by Garlock: (a) SC connection subassembly test setup; (b) typical connection moment-relative rotation results (Garlock (2002)).

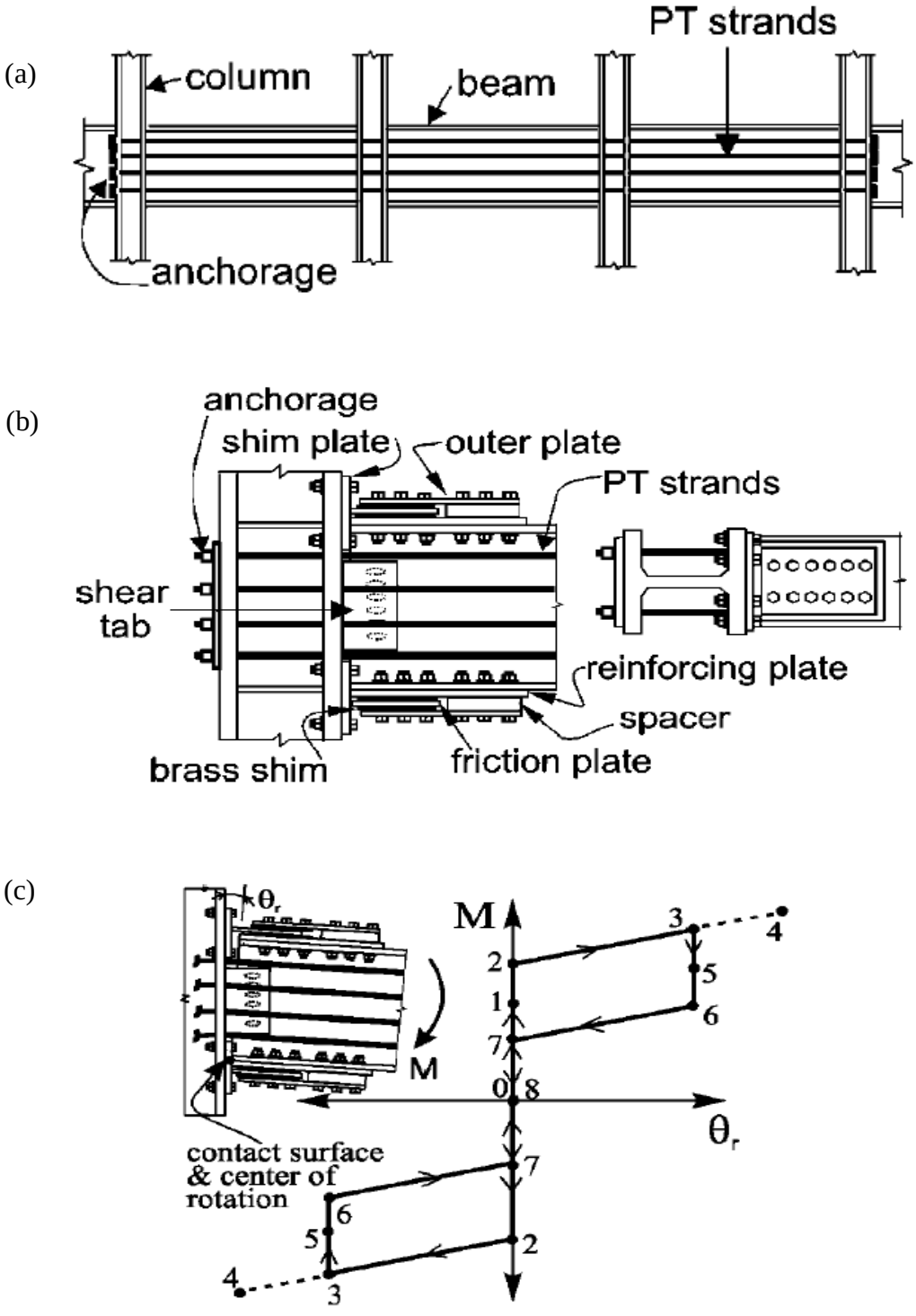

Figure 2. 3. (a) One floor of MRF with PFDCs; (b) PFDC details; (c) conceptual moment-relative rotation behavior (Rojas et al. (2005)).

(a)

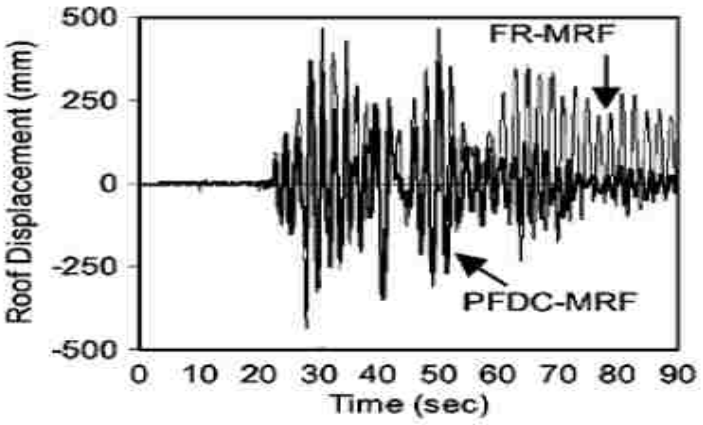

(b)

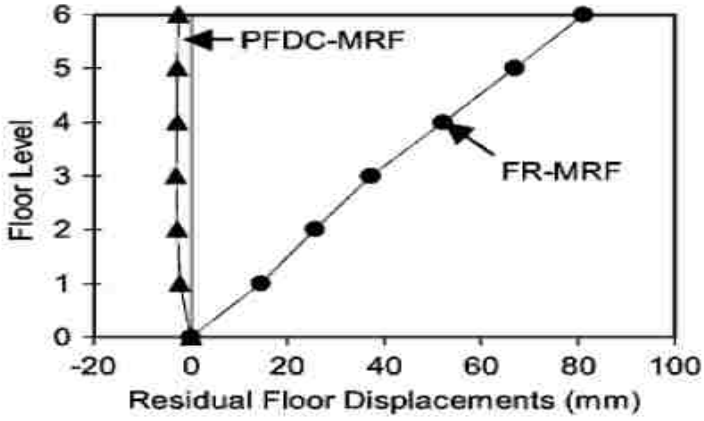

(c)

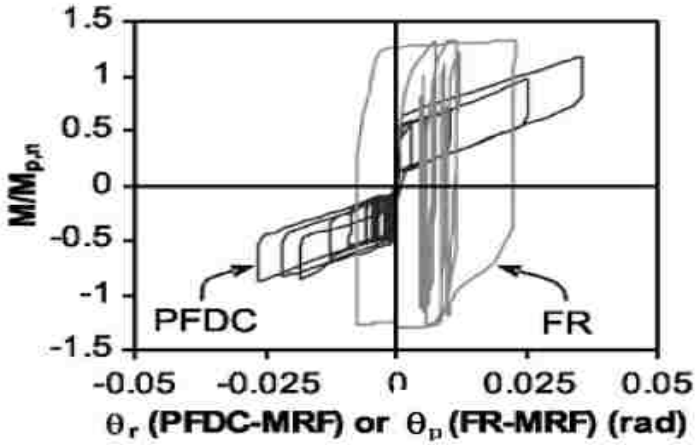

Figure 2. 4. (a) Roof displacement time history; (b) residual floor displacements; (c) connection response (Rojas et al. (2005)).

(a)

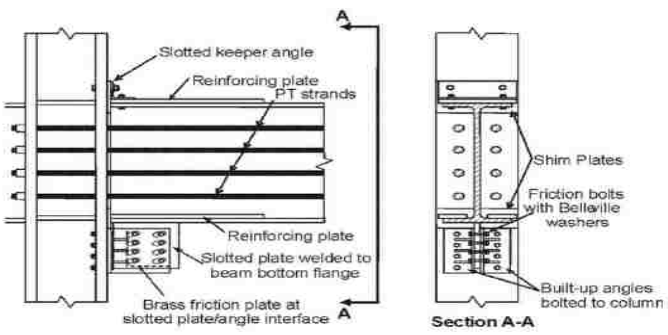

(b)

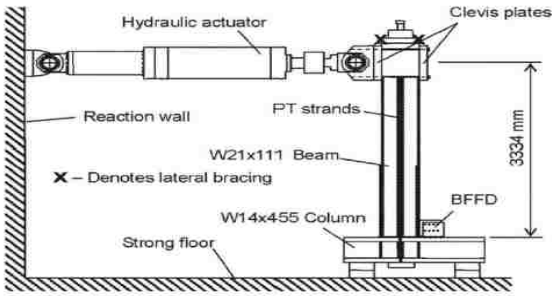

(c)

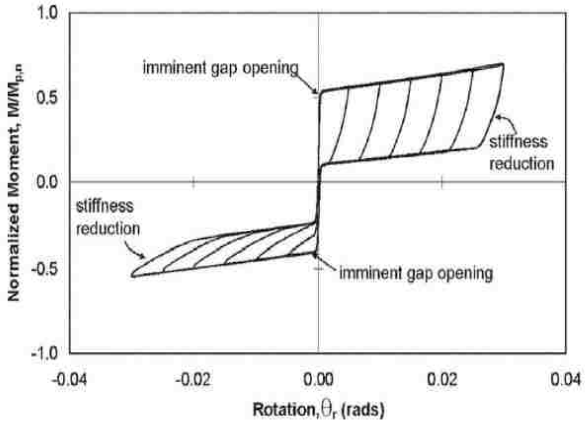

Figure 2. 5. Test by Wolski et al.: (a) BFFD connection details; (b) test setup; (c) typical connection response (Wolski et al. (2009)).

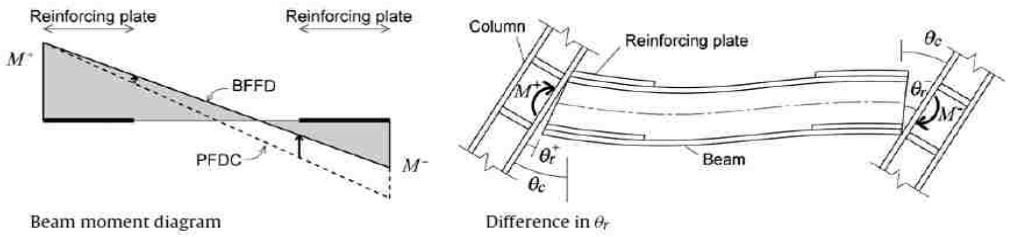

Figure 2. 6. Asymmetric behavior in BFFD frame (Iyama et al. (2009)).

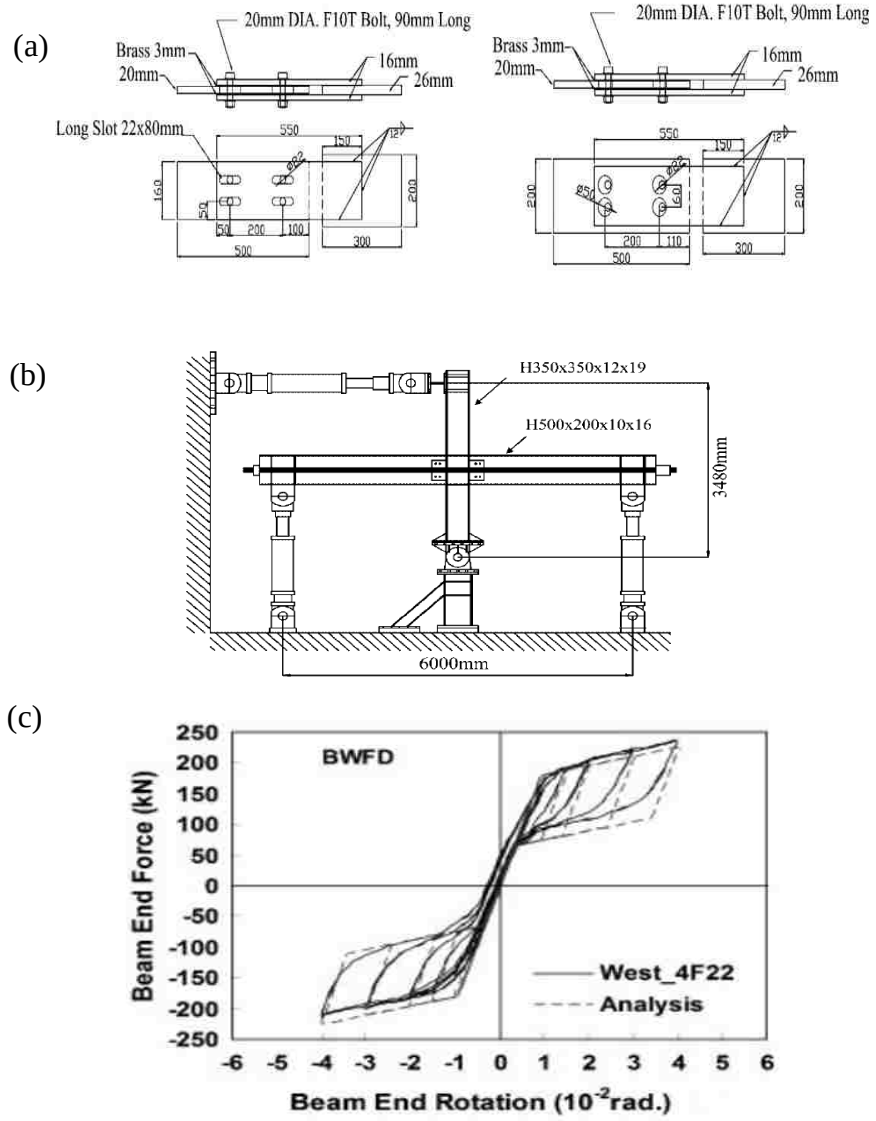

Figure 2. 7. Test by Tsai et al.: (a) Details of bolted friction device specimens; (b) test setup of the BWFD connection specimens; (c) test results of BWFD4F22 specimen, west beam (Tsai et al. (2008)).

(a)

(b)

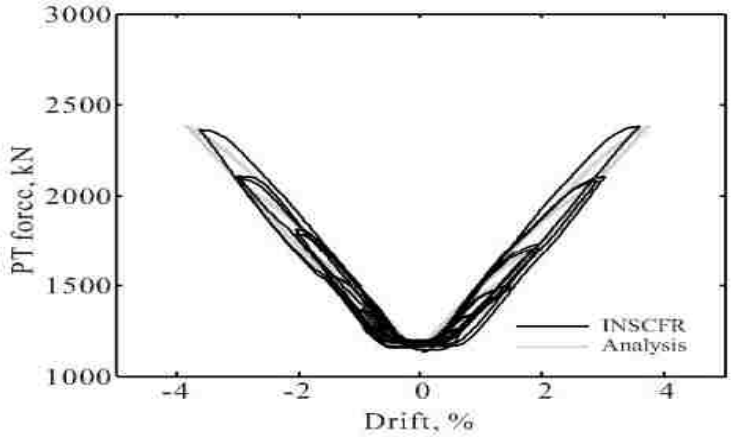

(c)

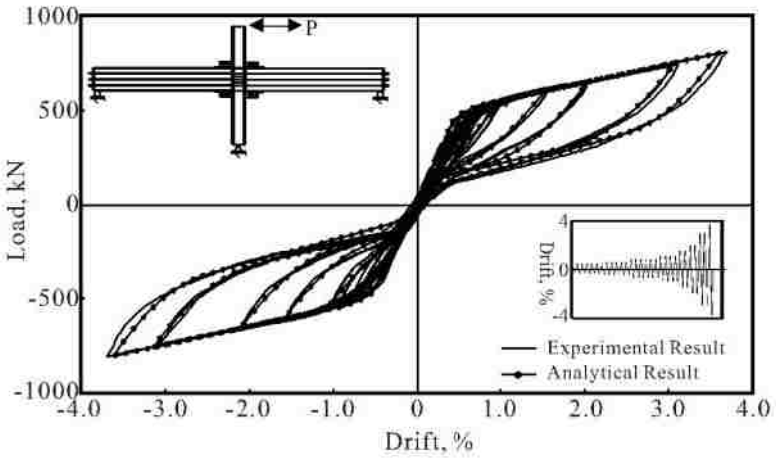

Figure 2. 8. Test by Kim and Christopoulos: (a) Test setup; (b) PT force variation; (c) load-drift relation (Kim and Christopoulos (2008)).

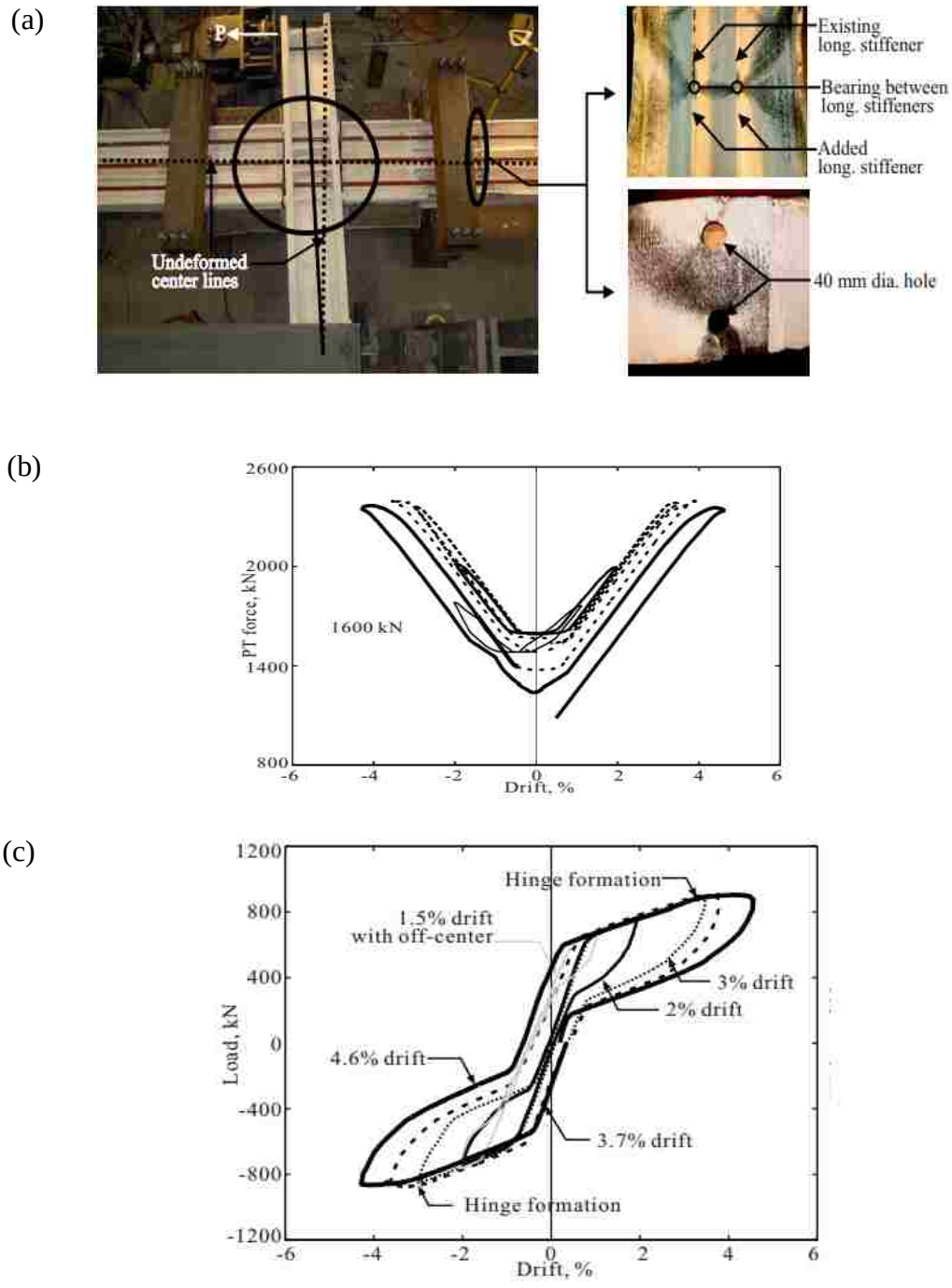

Figure 2. 9. Test by Kim and Christopoulos: (a) Picture of the deformed shape; (b) PT force variation; (c) load-drift relation (Kim and Christopoulos (2008)).

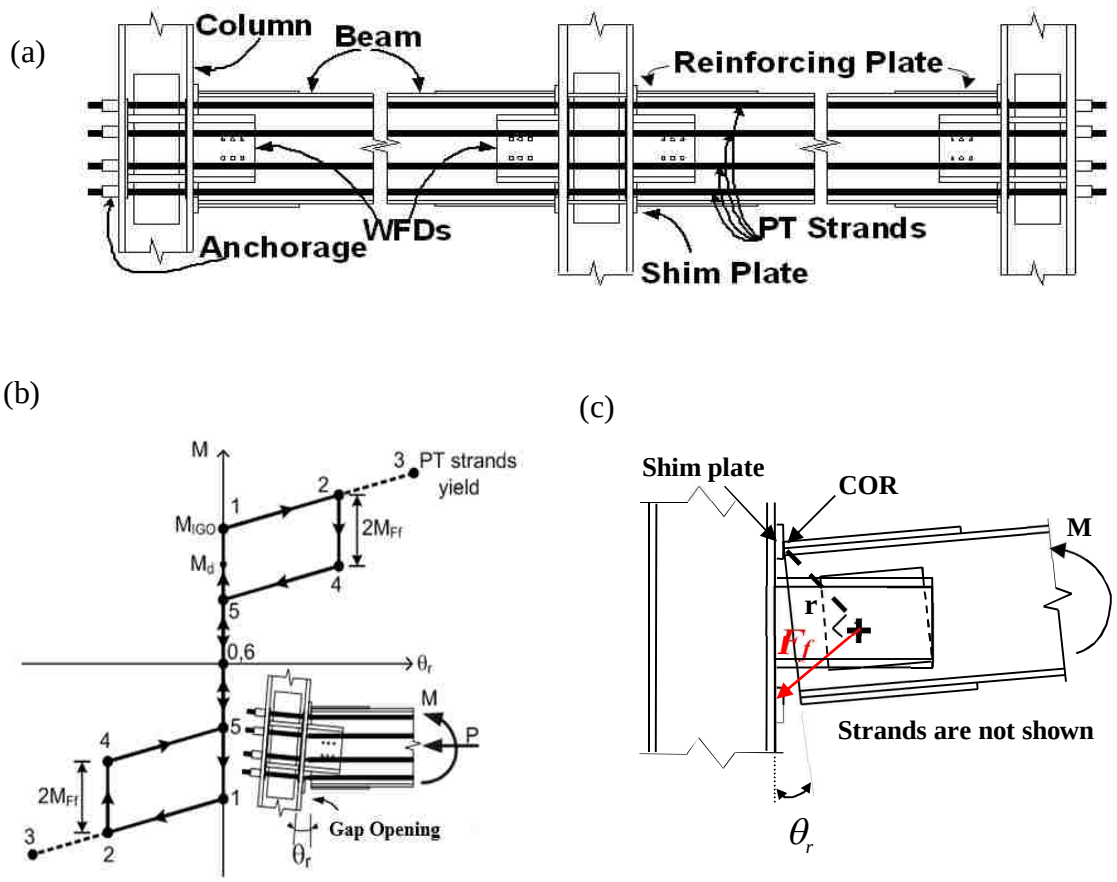

Figure 2. 10. Schematic of (a) elevation of a 2-bay SC-MRF with SC-WFDs; (b) conceptual moment-relative rotation behavior of SC connection; (c) beam-to-column connection relative rotation θ_r(Lin (2012)).

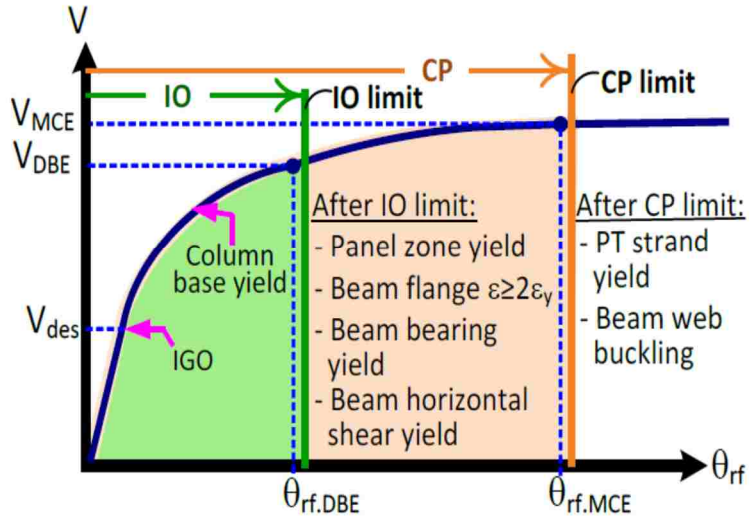

Figure 2. 11. Design objectives related to base shear-roof drift (V-θ_{rf}) global response (Lin (2012)).

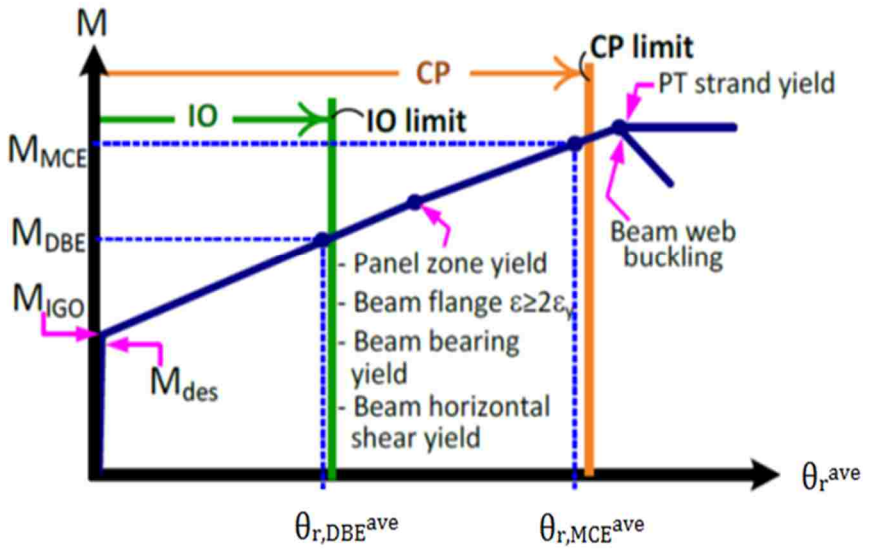

Figure 2. 12. Design objectives related to connection response (Lin (2012)).

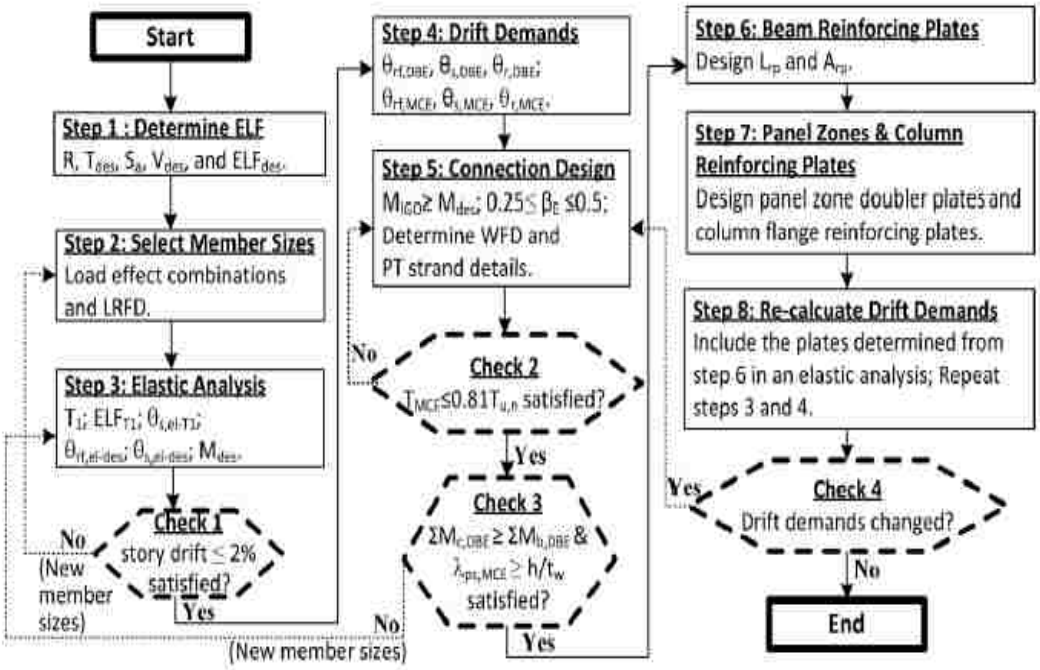

Figure 2. 13. Flow chart for SC-MRF design by Lin (2012).

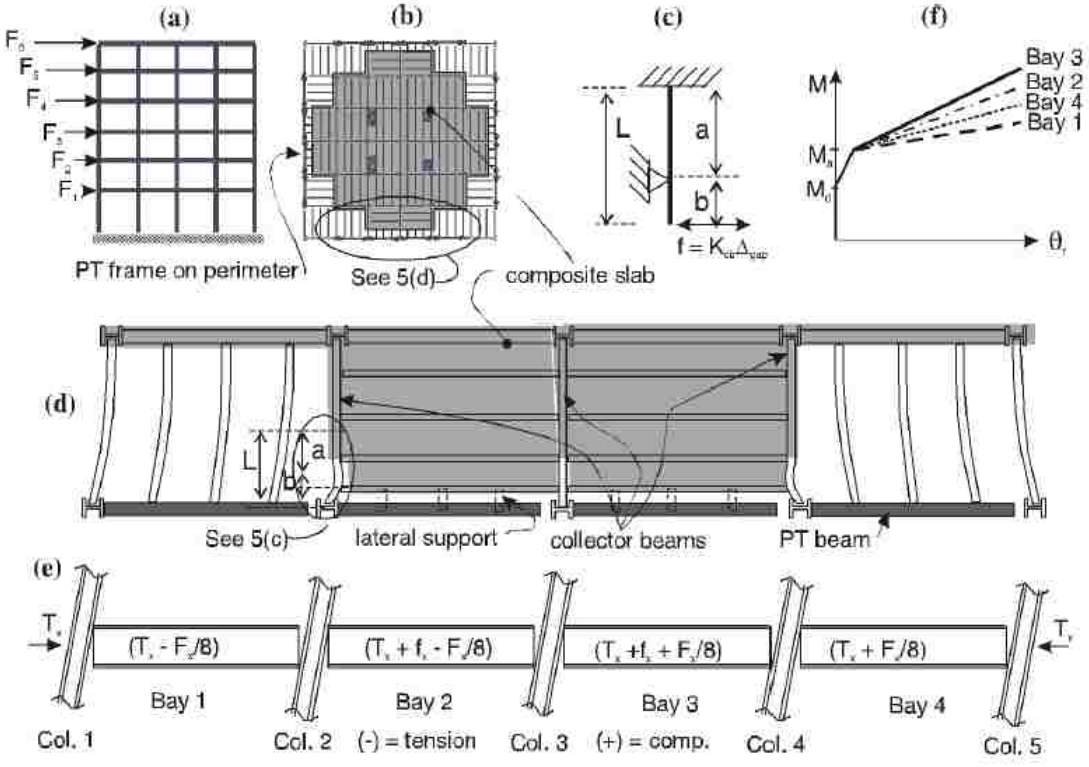

Figure 2. 14. Flexible floor diaphragm system concept (Garlock (2002)).

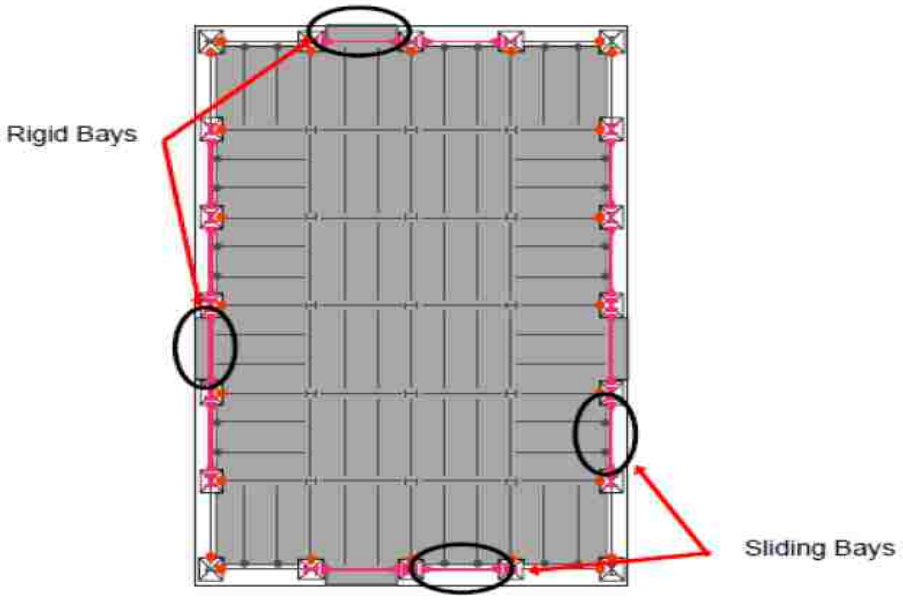

Figure 2. 15. Floor diaphragm system concept (King (2007)).

Chapter 3

Performance Based Design Procedure for SC-MRFs

3.1. General

This chapter describes the details of the performance-based design (PBD) procedure and main design criteria used to design the prototype building with SC-MRFs by Lin (2012). The SC-MRF designed by the PBD procedure by Lin (2012) is used to study the seismic collapse resistance of an SC system in subsequent chapters. Design criteria are listed in this chapter and those that influence the seismic collapse resistance of an SC-MRF are explained in more detail to relate the relevance of these criteria to the limit states that lead to collapse under seismic loading. More details for other design criteria are found in Lin (2012).

3.2. PBD procedure of SC-MRFs

This section presents the PBD procedure for SC-MRF systems developed by Lin (2012). The PBD procedure developed by Lin includes parts of PBD procedure developed by Garlock et al. (2007) and work by Rojas (2005). This PBD procedure is used for the design of a prototype building with SC-MRFs. As stated previously in Chapter 2 (Section 2.3.3), the PBD considers two levels of seismic input, the DBE and the MCE. The design procedure enables immediate occupancy (IO) performance level after the DBE and collapse prevention (CP) performance level under MCE level ground motions. Different limit states for an SC-MRF are presented in the conceptual base shear-roof drift ($V\text{-}\theta_{rf}$) response shown previously in Figure 2.11. IO and CP performance levels are noted in association with the limit states. Limit states and performance levels

were described in Chapter 2. The design demands are obtained to design the members, in order to provide an acceptable design capacity based on the design criteria that enable the desired performance level to be achieved. The design criteria and provided design capacity influence the seismic collapse resistance of the system. The design capacity may expedite or delay the occurrence of limit states that lead to collapse and affect the collapse resistance of the system. More details are given below about the main design demands under the DBE and the MCE to be used in the design procedure.

3.2.1. Design demands

The design demands are established from the equivalent lateral force procedure of ASCE 7-10 (2010). SC-MRF deformation demands are estimated by amplifying linear elastic response with appropriate factors (Section 3.2.1.1). Force demands are established from the equivalent lateral force procedure directly, or from analysis of the connection response under the design deformation demands (Section 3.2.1.2). The design demands are used in Chapter 4 to design the SC-MRFs studied in this research.

3.2.1.1. Story drift and connection relative rotation demands

The drift and connection relative rotation demands under the DBE are the maximum roof drift, $\theta_{r,DBE}$, the maximum story drift, $\theta_{s,DBE}$, and the maximum average connection relative rotation for all connections on one floor level, $\theta_{r,DBE}^{ave}$. These demands are estimated as follows (Garlock et al. 2007):

$$\theta_{rf,DBE} = C_\xi C_T R \theta_{rf,el-des} \tag{3.1}$$

$$C_\xi = \frac{\sqrt{(1 + 25\xi_{5\%})}}{\sqrt{(1 + 25\xi)}} \; and \; \xi_{5\%} = 0.05 \tag{3.2}$$

$$C_T = \frac{T_{des}}{T_{1,eigen}} \tag{3.3}$$

where C_T is the period correction factor, and C_ξ is the damping correction factor to account for the difference between the 5% damping ratio assumed for the ASCE 7-10 design spectra and the damping assumed for design. T_{des} is the design period determined per ASCE 7-10 and $T_{1,eigen}$ is the 1st mode period of the building. R=8 is the response modification factor for an SMRF defined in ASCE 7-10, assuming the SC-MRF is a special moment resisting frame. $\theta_{rf,el\text{-}des}$ is the roof drift from an elastic analysis of the structure under the equivalent lateral force (ELF) corresponding to the design base shear V_{des} (i.e., corresponding to period T_{des}). Note that when the period of the building is not in the velocity controlled (i.e., 1/T) region of design spectrum, $\theta_{rf,DBE}$ should be found by the following equation:

$$\theta_{rf,DBE} = C_\xi R \theta_{rf,el-T1,eigen} \tag{3.4}$$

Where $\theta_{rf,el\text{-}T1,eigen}$ is the roof drift from an elastic analysis of the structure under the equivalent lateral force (ELF) corresponding to $V_{T1,eigen}$ (i.e., corresponding to period $T_{1,eigen}$).

$\theta_{s,DBE}$ is calculated from $\theta_{rf,DBE}$ as follows (Garlock et al. 2007; Rojas et al. 2005):

$$\theta_{s,DBE} = C_\theta \theta_{rf,DBE} \tag{3.5}$$

A value of C_θ=1.5 is suggested by Rojas et al. (2005). $\theta_{r,DBE}{}^{ave}$ is estimated from $\theta_{s,DBE}$ by using the factor C_{rs}=0.81 as follows (Rojas et al. 2003):

$$\theta_{r,DBE}^{ave} = C_{rs}\theta_{s,DBE} \quad (3.6)$$

Based on the intensity ratio of the MCE to the DBE, which is 1.5 as defined by FEMA 450 (BSSC 2003), the corresponding drift and connection relative rotation demands under the MCE can be calculated as follows (Garlock et al. 2007):

$$\theta_{rf,MCE} = 1.5\theta_{rf,DBE} \quad (3.7)$$

$$\theta_{s,MCE} = 1.5\theta_{s,DBE} \quad (3.8)$$

$$\theta_{r,MCE}^{ave} = 1.5\theta_{r,DBE}^{ave} \quad (3.9)$$

3.2.1.2. Connection moment and total PT strand demands

The connection moment demand used to establish the minimum strength of the connection (at the design level) is the beam design moment at the column face (M_{des}) when the building is subjected to the ELF corresponding to V_{des}. M_{des} is determined from linear elastic analysis of the SC-MRF, assuming the connections are rigid, using the load combinations from ASCE 7-10 with the ELF corresponding to V_{des}. The connection moment demands under the DBE and the MCE are the beam moment at the column faces under the DBE and the MCE (denoted as M_{DBE} and M_{MCE}), respectively. They are calculated using Equation (2.4) by setting P equal to P_{DBE} and P_{MCE} respectively, as follows:

$$M_{DBE} = P_{DBE}d + F_f r \quad (3.10)$$

$$M_{MCE} = P_{MCE}d + F_f r \quad (3.11)$$

P_{DBE} and P_{MCE} are the beam axial force at the DBE and the MCE, respectively. They are calculated as follows using Equation (2.5):

$$P_{DBE} = T_{DBE} + F_{fd,DBE} \tag{3.12}$$

$$P_{MCE} = T_{MCE} + F_{fd,MCE} \tag{3.13}$$

T_{DBE} and T_{MCE} are the PT stand force under the DBE and the MCE, respectively. T_{DBE} and T_{MCE} are calculated using Equation (2.6):

$$T_{DBE} = T_0 + 2d\theta_{r,DBE}^{ave}\left(\frac{k_b k_s}{k_b + k_s}\right) \tag{3.14}$$

$$T_{MCE} = T_0 + 2d\theta_{r,MCE}^{ave}\left(\frac{k_b k_s}{k_b + k_s}\right) \tag{3.15}$$

$\theta_{r,DBE}^{ave}$ and $\theta_{r,MCE}^{ave}$ are the maximum average connection relative rotation for all connections on one floor level under the DBE and MCE, respectively.

$F_{fd,DBE}$ and $F_{fd,MCE}$ are the beam axial force from the inertial force transferred by the floor diaphragm under the DBE and the MCE, respectively, which can be estimated as follows:

$$F_{fd,DBE} = \Omega_{DBE} P_{fd,des} \tag{3.16}$$

$$F_{fd,MCE} = \Omega_{MCE} P_{fd,des} \tag{3.17}$$

In Equations (3.16) and (3.17), $\Omega_{DBE} = 2.3$ and $\Omega_{MCE} = 2.5$ are the overstrength factors suggested by Garlock (2002) and Rojas (2003). $P_{fd,des}$ is the beam axial force from the inertial force transferred by the floor diaphragm when the building is subjected to the ELF corresponding to V_{des}.

3.2.2. Design criteria

The design criteria are divided into two categories under the DBE and MCE to provide enough capacity for the SC connections to reach a specific limit state under the DBE and MCE in order to achieve the desired performance level for the SC-MRF. In this section, design criteria for an SC-MRF are listed that include:

- Connection moment at imminent gap opening criterion
- Story drift limit criterion
- Beam horizontal shear yield criterion under DBE
- Beam flange bearing yield criterion under DBE
- Beam flange strain criterion under DBE
- Panel zone yield criterion under DBE
- Column flange low cycle fatigue criterion under DBE
- Column plastic hinge criterion under DBE (i.e., strong column-weak beam principal)
- Beam web compactness criterion under MCE
- Strand yield criterion under MCE

More details for each design criterion are given in Lin (2012). PT strand yielding and beam flange and web local buckling are the main limit states that lead to collapse. The PBD procedure attempts to prevent the occurrence of these limit states under the MCE level to reach the CP performance for an SC-MRF (see Figure 2.11). In order to evaluate the seismic collapse resistance of an SC-MRF, the system is studied for extreme ground motions that exceed the MCE hazard level that lead to the occurrence of PT strand yielding, beam flange and web local buckling. The occurrence of these limit states results

in a loss of PT force and subsequent moment capacity of a post-tensioned SC connection that can lead to collapse. Beams are subject to large moments combined with appreciable axial force in an SC connection, causing the beams to possibly locally buckle. The PBD procedure limits the strain at the end of reinforcing plates and prevents the beams to yield horizontally in shear that subsequently determines the required reinforcing plate length to prevent beam local buckling at MCE level. In addition, the PBD procedure limits the total PT force at MCE level to prevent the PT strand yielding at MCE level. The relevant criteria are presented herein. Furthermore, the PT strand yield criterion is modified to assess the sensitivity of the seismic collapse resistance to this design criterion. More details are given in subsequent chapters.

3.2.2.1. Beam flange strain criterion under DBE

This criterion is supposed to control excessive plastic deformation and beam flange and web buckling under the MCE level. Seismic collapse resistance of an SC-MRF is influenced by the reinforcing plate lengths that control the occurrence of beam flange and web local bucking limit state that lead to collapse. The reinforcing plate lengths need to be determined to avoid beam local buckling under the MCE level and provide enough capacity to achieve CP performance level under the MCE. Based on the PBD objectives shown in Figure 2.11, yielding of the beam flange at the end of beam reinforcing plate is permitted under the DBE, but the strain should be less than $2\varepsilon_y$ to avoid excessive plastic deformation under the MCE. The beam flange strain at the end of the reinforcing plate under the DBE ($\varepsilon_{rp,DBE}$) can be calculated using the procedure proposed by Garlock (2002) (Figure 3.1). $\varepsilon_{rp,DBE}$ should satisfy the following inequality (Garlock et al. 2007):

$$\frac{\varepsilon_{rp,DBE}}{2\varepsilon_y} \leq 1 \tag{3.18}$$

According to the procedure by Garlock (2002), $\varepsilon_{rp,DBE}$ is determined from section analysis of the beam under the combination of P_{DBE} and the bending moment at the end of the beam reinforcing plate (M_{rp}) under the DBE (denoted $M_{rp,DBE}$). The section analysis assumes that plane sections remain plane. The analysis determines the stress distribution over the cross section from which $\varepsilon_{rp,DBE}$ is calculated. More details are given in Garlock (2002).

3.2.2.2. Beam horizontal shear yield criterion under DBE

Reinforcing plate length at an SC-MRF connection shown in Figure 3.2 must be long enough to prevent horizontal shear yielding in the beam web adjacent to the compression flange. The force demand is the total contact force under the DBE (C_{DBE}), which equals the axial force in the beam P_{DBE} plus the horizontal component of the friction force in the WFD. This force demand must be less than or equal to the sum of the yield strength of the beam flange and the horizontal shear yield strength of the beam web over the length of the reinforcing plate. Considering horizontal equilibrium and to avoid shear yielding, the beam flange reinforcing plate length L_{rp} must be selected to satisfy the following inequality (Garlock et al. 2007):

$$\frac{C_{DBE} - C_{f,y}}{L_{rp}\tau_y t_w} \leq 1 \tag{3.19}$$

where $C_{f,y}$ is the beam flange yield strength, which is assumed to be equal to the specified minimal yield stress (F_y) of the beam multiplied by the flange area; τ_y is the shear yield

stress assumed to be equal to $0.6F_y$, and t_w is the beam web thickness; and C_{DBE} is the beam flange contact force under the DBE, which is estimated as follows:

$$C_{DBE} = P_{DBE} + F_f \tag{3.20}$$

Equation (3.20) uses the resultant friction force F_f from the WFD, ignoring the difference between the horizontal component of the friction force and F_f.

3.2.2.3. Beam web compactness criterion under MCE

As stated previously, seismic collapse resistance of an SC-MRF is influenced by the occurrence of beam flange and web local bucking. Controlling beam web compactness criterion is also important to prevent beam local buckling occurrence under the MCE. SC-MRF beams should satisfy the seismic compact section criterion for the web defined in the AISC Seismic Provisions for Steel Buildings (2010) as follows:

$$\frac{h/t_w}{\lambda_{PS,MCE}} \leq 1 \tag{3.21}$$

where h/t_w is the beam web width-thickness ratio and $\lambda_{PS,MCE}$ is the limiting width thickness ratio under the MCE. $\lambda_{PS,MCE}$ can be calculated as follows:

$$\lambda_{PS,MCE} = \max[1.12(2.33 - C_a)\sqrt{\frac{E}{F_y}}, 1.49\sqrt{\frac{E}{F_y}}] \tag{3.22}$$

where E is Young's modulus and $C_a = P_{MCE}/0.9P_y$ is the ratio of the beam axial force demand under the MCE to the design axial yield strength. P_y is the beam axial yield strength. It should be noted that Equation (3.22) is valid only for $C_a > 0.125$. For $C_a \leq 0.125$, $\lambda_{PS,\,MCE}$ is calculated as follows:

$$\lambda_{PS,MCE} = 3.14\sqrt{\frac{E}{F_y}}(1 - 1.54C_a) \tag{3.23}$$

Since the floor diaphragm of the SC-MRF building is attached to only one bay of each SC-MRF as stated in Chapter 2, the SC-MRF beams carry a large beam axial force under the MCE, leading to Ca >0.125. Therefore, Equation (3.22) is typically used to calculate $\lambda_{PS,\,MCE}$.

3.2.2.4. Strand yield criterion under MCE

This criterion influences the seismic collapse resistance of an SC-MRF. Strand yielding should be prevented under the MCE in order to reach CP performance level for an SC-MRF (see Figure 2.11). The total PT strand force under the MCE (T_{MCE}) should not exceed 90 percent of the nominal total PT strand yield force $T_{y,n}$ (Lin 2012). The following inequality should be satisfied:

$$\frac{T_{MCE}}{0.9T_{y,n}} \leq 1 \tag{3.24}$$

where $T_{y,n}$ is the nominal total PT strand yield force. Based on ASTM A416, $T_{y,n}$ is assumed to be equal to $0.9T_{u,n}$ (ASTM A416), where $T_{u,n}$ is the total nominal PT strand ultimate force capacity, which can be calculated as follows:

$$T_{u,n} = N_s A_{s,n} \sigma_{s,u} \tag{3.25}$$

In Equation (3.25) N_s is the total number of PT strands at one floor level, $A_{s,n}$ is the cross sectional area of a PT strand, and $\sigma_{s,u}$ is the specified minimum ultimate stress of a PT strand (ASTM A416).

The sensitivity of seismic collapse resistance of an SC-MRF to this design criterion is also investigated in this research. In order to avoid PT strand yielding and fracture scenarios, the design criterion is modified to limit the total PT force under MCE to 75 percent of the total PT yield force, while maintaining the same initial total PT force.

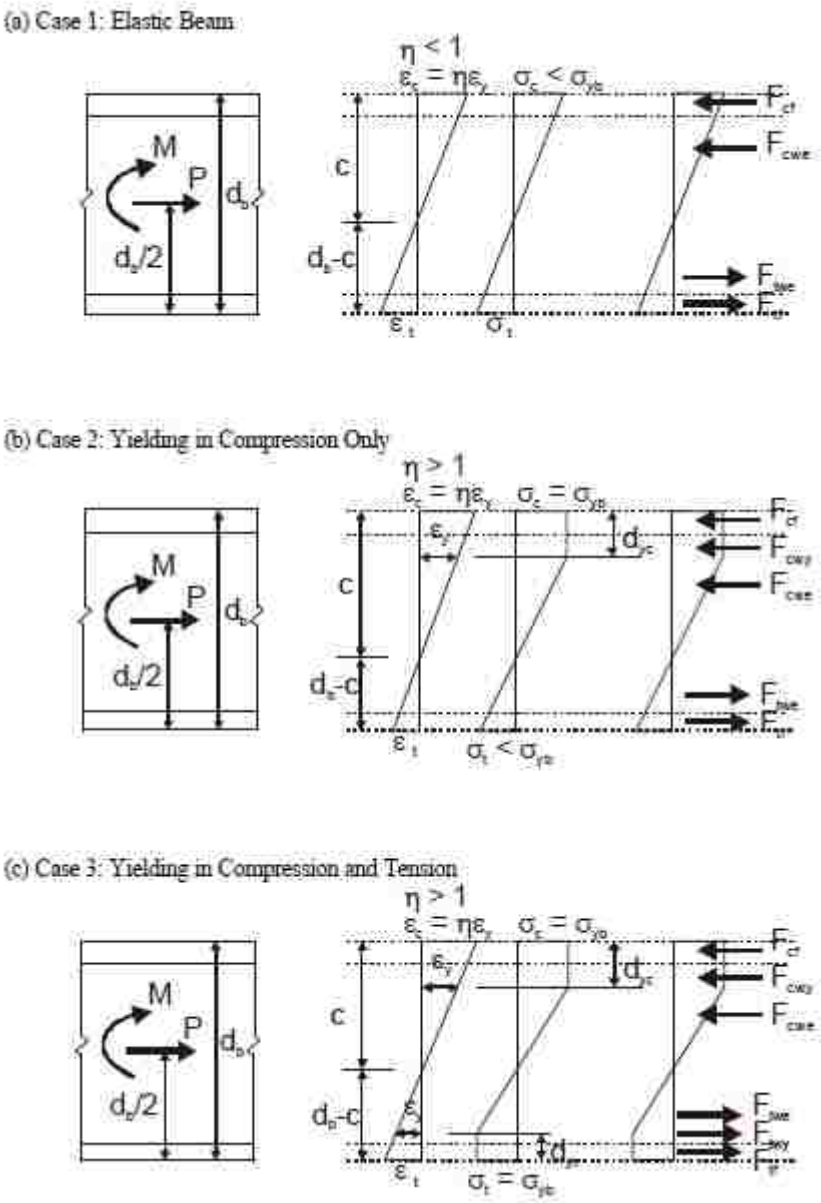

Figure 3. 1. Stress-strain distribution of beam at the section adjacent to the end of beam flange reinforcing plate (Garlock (2002)).

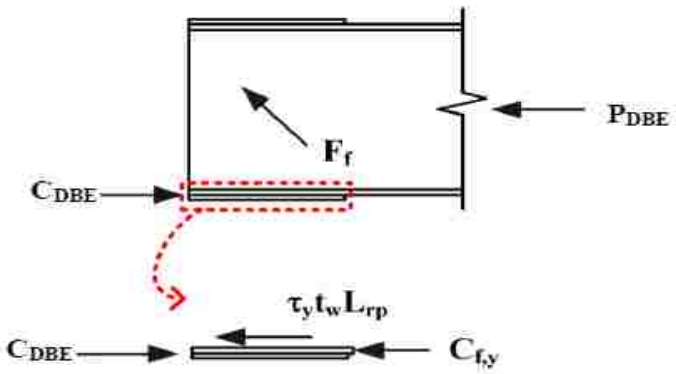

Figure 3. 2. Design of reinforcing plate for beam horizontal shear yield criterion under the DBE (Lin (2012)).

Chapter 4

Design of Prototype Buildings

4.1. General

This chapter presents the prototype buildings utilized in this study to assess the collapse resistance of a 4-story SC-MRF and SMRF in accordance with FEMA P695. The PBD procedure by Lin (2012) (presented in Chapter 3) was used to design a 4-story SC prototype steel frame, referred to herein as SC-MRF Design 1. In addition, a change in the design criterion for the steel PT strands is presented in this chapter which forms the basis for the design of second 4-story SC-MRF, referred to as SC-MRF Design 2. By performing incremental nonlinear analyses on these frames, their seismic collapse resistance will be evaluated in subsequent chapters. In order to compare the collapse resistance of an SC-MRF system with a conventional welded steel MRF, a comparable 4-story SMRF prototype building is also designed. The prototype building geometry and a summary of the values of the design parameters is given herein.

4.2. Prototype SC-MRF Design 1

The prototype building was designed using the PBD procedure by Lin (2012). The design is denoted as Design 1. The prototype building with perimeter SC-MRFs is a 7x7-bay office building shown in Figure 4.1. The building is assumed to be located in Van Nuys, California (Latitude = 34.22° and Longitude = -118.47°) in the Los Angeles region. The building has four stories above ground and a one-story basement below ground. Each side of the building perimeter contains two 2-bay SC-MRFs as shown in

Figure 4.1. The floor diaphragm at each floor level is attached to only one bay (denoted as the fixed bay) of each SC-MRF (see Figure 4.2(a) and (b)), where it is denoted as FD Bay in Figures 4.2(a) and (b). By attaching the floor diaphragm to only one bay, the beam-to-column connections in the SC-MRFs are free to develop gap opening as depicted in Figures 4.2 (b) and (c). A brief description of the design procedure is given herein. More details are given in Lin (2012).

4.2.1. Design Loads

4.2.1.1. Gravity Load and Effective Seismic Weight

The dead and live design loads are listed in Table 4.1 and Table 4.2, respectively. The building live loads are established in accordance with ASCE 7-10 (2010). The seismic weight was determined from the dead loads summarized in Table 4.1 plus the partition live load listed in Table 4.2. The effective seismic weight for the entire building was calculated as W=17,592 kips.

4.2.1.2. Seismic Lateral Loads

The Equivalent Lateral Force (ELF) procedure described by ASCE 7-10 was used to calculate the design seismic lateral forces for the building. In the ELF procedure static design forces equivalent to the actual earthquake forces are calculated. These forces account for site seismicity, soil conditions, redundancy, structural layout, structure's importance and occupancy. The seismic design parameters according to ASCE 7-10 are summarized in Table 4.3. The SC-MRF building was assumed to be an office building, corresponding to Occupancy Category II, with an importance factor I equal to 1.0. The building is located on a stiff soil site, corresponding to site Class D. The specified location of this building gives the mapped MCE spectral acceleration a short-period of S_S

equal to 1.5g, and at a period of 1 second of S_1 equal to 0.6g. The short-period site coefficient F_a is equal to 1.0 and the long-period site coefficient F_v equal to 1.5. For the building site the 5 percent damped MCE spectral response acceleration at short periods adjusted for site class effects equals 1.5g ($S_{MS}=F_aS_S$), and 0.9g ($S_{M1}=F_v S_1$) at a period of 1 second.

According to the ASCE 7-10 definition of the DBE spectrum (2/3 of the MCE spectrum), the design spectral response acceleration at short periods (with 5 percent damping) equals 1.0g ($S_{DS}=2S_{MS}/3$). The design spectral response acceleration at a period of 1 second (with 5 percent damping) equals 0.6g ($S_{D1}=2S_{M1}/3$). The building is assumed to be a SMRF, which has a response modification coefficient of R=8 according to ASCE 7-10. The seismic base shear, V is calculated as:

$$V = C_s W \tag{4.1}$$

where W is the effective seismic weight and C_s is the seismic response coefficient. To calculate C_s the building design period, T_{des}, was calculated per ASCE 7-10 as follows:

$$T_{des} = \min(T_{1,eigen}, C_u T_a) \tag{4.2}$$

where $T_{1,eigen}$ is the 1st mode period from an elastic structural analysis and C_uT_a is the upper limit of the period defined by ASCE 7-10. C_u=1.4 is the coefficient for the upper limit for the calculated period and T_a is the approximate fundamental period determined by the following equation:

$$T_a = C_t h_n^x \tag{4.3}$$

In Equation (4.3), C_t = 0.028 and x = 0.8, as defined per ASCE 7-10 for steel moment resisting frames, and h_n is the height above the base to the highest level of the structure, which is equal to 52.5 ft. Therefore, $C_u T_a$=0.932 sec. $T_{1,eigen}$ is equal to 1.52 sec. as determined from an eigenvalue analysis of the prototype building assuming rigid beam-to-column connections. Therefore, based on Equation (4.2) T_{des}= 0.932 sec. C_s is calculated from the following equations given by ASCE 7-10:

$$C_s = \begin{cases} max\left[0.01, 0.044 S_{DS} I, \min\left(\frac{S_{DS}}{\frac{R}{I}}, \frac{S_{D1}}{T\left(\frac{R}{I}\right)}\right)\right] & \text{for } T \leq T_L \\ max\left[0.01, 0.044 S_{DS} I, \min\left(\frac{S_{DS}}{\frac{R}{I}}, \frac{S_{D1} T_L}{T^2\left(\frac{R}{I}\right)}\right)\right] & \text{for } T \geq T_L \end{cases} \quad (4.4)$$

In addition, for structures located where $S_1 \geq 0.6g$, C_s shall not be less than Equation (4.5):

$$C_s = \frac{0.5 S_1}{\frac{R}{I_e}} \quad (4.5)$$

where T in Equation (4.4) is the fundamental period of the structure, and T_L is the long-period transition period which equals 8.0 sec. for the Los Angeles region. Using $T=T_{des}$ in Equations (4.4) and (4.5), it is found that C_s=0.081, enabling then V_{des} to be calculated from Equation (4.1). The vertical distribution of the ELF is determined by multiplying V_{des} by a vertical distribution factor C_{vx}, where:

$$C_{vx} = \frac{w_x h_x^k}{\sum_{i=1}^{n} w_i h_i^k} \quad (4.6)$$

In Equation (4.6), h_i and h_x are the height of levels i and x, respectively, and w_i and w_x are the effective seismic weight at level i and x, respectively. n is the number of building floor levels and k is a distribution exponent related to the building period, where

$$k = 1 + 0.5(T - 0.5) \quad , \quad 0.5 < T \leq 2.5 \tag{4.7}$$

Thus, the lateral load at level x, F_x is:

$$F_x = C_{vx}V \tag{4.8}$$

Using $T=T_{des}$ in Equation (4.7), the ELF corresponding to T_{des} can be calculated. $F_{x,des}$ is obtained from Equation (4.8) corresponding to $V=V_{des}$.

By using $T=T_{1,eigen}$ in Equations (4.4) and (4.5), C_s corresponding to $T_{1,eigen}$ (C_s=0.049) is calculated. Subsequently, $V_{T1,eigen}$ is obtained from Equation (4.1) and used to ensure that the design complies with the drift criteria in ASCE 7-10. The equivalent lateral forces $F_{x,T1,eigen}$ is calculated by using Equations (4.6), (4.7), and (4.8) corresponding to $T=T_{1,eigen}$. Table 4.4 lists for $F_{x,des}$ and $F_{x,T1,eigen}$. The building is first designed for strength using $F_{x,des}$, and then checked for drift using $F_{x,T1,eigen}$.

4.2.1.3. Load Combinations

The following load combinations are considered for the design of the prototype building according to ASCE 7-10:

$$1.4D \tag{4.9,a}$$

$$1.2D + 1.6L + 0.5L_r \tag{4.9,b}$$

$$1.2D + 0.5L + 1.6L_r \quad (4.9,c)$$

$$(1.2 + 0.2S_{DS})D + \rho Q_E + 0.5L \quad (4.9,d)$$

$$(0.9 - 0.2S_{DS})D + \rho Q_E \quad (4.9,e)$$

where D is the effect of dead loads presented in Table 4.1; L and L_r are the effects of live loads and roof live load listed in Table 4.2; Q_E is the effect of the horizontal seismic loads presented in Table 4.4. ρ is the system redundancy factor equal to 1.0 based on section 12.3.4.2 in ASCE 7-10. To determine the required strength of the members and connections of the SC-MRF, Q_E is estimated using $T=T_{des}$ in the above combinations. For determining compliance with the story drift limitations, Q_E is estimated using $T=T_{1,eigen}$.

4.2.2. SAP2000 Model

Lin (2012) developed an elastic analysis model using SAP2000 to design the prototype SC-MRF building. This 3-dimensional model was used to determine the member design forces, story drifts and the elastic 1st modal period of the structure. The following limitations exist in this model:

- Only the perimeter SC-MRFs are included in the model;
- The connections of the SC-MRFs are assumed to be fully rigid;
- The model is used centerline-to-centerline dimensions;
- The SC-MRF model include a rigid end zone at each beam-to-column joint;
- A lean-on column is included in the SAP2000 model to account for the P-Δ effects from the vertical loads acting on the interior gravity columns of the gravity frames of the prototype building. The cross-section area and flexural

stiffness of the lean-on column is based on the summation of the areas and flexural stiffness of the gravity columns;

- At each floor the ELF are applied at the eccentric node (an eccentricity of 5% from the center of mass) to account for accidental torsion;
- The PT strands and PT forces are not modeled;
- The beam flange reinforcing plates are included in the elastic analysis model;
- At each floor level a rigid diaphragm connects the quarter points of the fixed bay beams of the SC-MRFs with the lean-on column node and the eccentric node.

4.2.2.1. Design Results

Considering T_{des}=0.932 sec. and $T_{1,eigen}$=1.52 sec. (determined from SAP2000 model by Lin), V_{des} and $V_{T1,eigen}$ are equal to 0.081 and 0.049 of the effective seismic weight of building. The story drifts of the building under $ELF_{T1,eigen}$ (denoted $\theta_{s,el\text{-}T1,eigen}$), amplified by C_d=5.5 and divided by I=1, are listed in Table 4.5. The maximum value for $\theta_{s,el\text{-}T1,eigen}C_d/I$ is 1.86%, which is less than the story drift limit of 2% defined in ASCE7-10.

The story drifts and connection relative rotation demands of the prototype SC-MRF building, $\theta_{rf,DBE}$, $\theta_{s,DBE}$, $\theta_{r,DBE}^{ave}$, $\theta_{rf,MCE}$, $\theta_{s,MCE}$, and $\theta_{r,MCE}^{ave}$ (from Equations (3.4) through (3.9)), are listed in Table 4.6. $\theta_{rf,el\text{-}des}$=0.42% was determined from the SAP2000 model. The response modification coefficient R=8, the period correction factor C_T=0.61, the damping correction factor C_ζ=1.22 (assuming the prototype SC-MRF building has a 2% damping ratio) were used to calculate the demand for $\theta_{rf,DBE}$ from Equation (3.1). Note

that the PT strand force was limited to 90% of the PT yield force at the MCE level per Lin (2012).

4.3. Prototype SC-MRF Design 2

Designers may want to consider lowering design limit for the maximum PT strand force in order to avoid PT strand yielding and fracture scenarios. In order to investigate the implication of this design parameter on the seismic collapse resistance of an SC-MRF, the SC-MRF design was modified to limit the PT force to 75 percent of the PT yield force (denoted as Design 2) while keeping the initial PT force T_0 the same as in Design 1 (see Table 4.7):

$$\frac{T_{MCE}}{0.75T_{y,n}} \leq 1 \tag{4.10}$$

where T_{MCE} and $T_{y,n}$ are the total PT stand force under the MCE and the nominal total PT strand yield force, respectively, as stated in Chapter 3. It was desired to keep T_0 the same for both designs since it affects the imminent gap opening, M_{IGO} and the effective energy dissipation ratio, β_E (see Equation (2.2) and (2.7) for definitions). To maintain the same initial total PT force, the number of PT strands was increased in Design 2 (see Table 4.8). As a result, the force per PT strand in Design 2 is reduced compared to that of the Design 1. However, in Design 2 the total axial stiffness k_s of the PT strands increases, which leads to larger PT strand forces developing in accordance with Equation (2.6) and therefore larger beam axial forces after gap opening occurs (Equation (2.5)). The beam axial forces and bending moments that develop in Design 2 requires a design change in the beam flange reinforcing plates. The lengths of the reinforcing plates are obtained

from Equations (3.18) and (3.19) in accordance with the PBD procedure discussed previously in chapter 3.

Prototype building member sizes and characteristics are presented in Table 4.7 and Table 4.8 for one of the SC-MRFs along the building perimeter (Design 1 and Design 2). The beams and columns are wide flange sections fabricated from A992 steel. β_E ranges from 25% at the 1st floor to 34% at the roof (Table 4.7). L_{rp} represents reinforcing plate length in Table 4.8. As seen in Table (4.8), the reinforcing plate lengths of the two-first floors of the Design 2 are increased. The reinforcing plate lengths for the third and fourth floors from Design 1 satisfy Equations (3.18) and (3.19) for Design 2 and need not be changed. In SC-MRF Design 1, the total number of PT strands are 24 for the 1st and 2nd floors, 16 for the 3rd floor, and 8 for the roof while in SC-MRF Design 2 the total number of PT strands are 34 for the 1st floor, 32 for the 2nd floor, 22 for the 3rd floor, and 10 for the roof. Like Design 1, all of the PT strands in Design 2 are 0.6 in. diameter seven-wire low-relaxation ASTM A416 Grade 270 strands (which have a nominal ultimate stress $F_{su,n}$ of 270 ksi and an area of A_s=0.217 in^2).

In Table (4.8) $t_0/t_{u,n}$ defines the ratio of initial PT force to the nominal ultimate PT strand tensile capacity per strand. In order to keep T_0 the same value for both Designs 1 and 2, $t_0/t_{u,n}$ is smaller in Design 2 and the number of PT strands are more than that in Design 1.

4.4. Prototype SMRF

The comparable conventional 4-story, 7x7-bay prototype office building with SMRFs is designed with the same floor plan and elevation as the prototype building with SC-MRFs. The building is assumed to be located at the same site as the prototype building

with SC-MRFs on a stiff soil site. It has two 2-bay perimeter steel SMRFs at each side to resist lateral forces. The moment resisting frame is designed as an SMRF in accordance with International Building Code (IBC 2012) and the AISC Seismic Provisions (2010). All of the steel sections of the SMRF are assumed to be A992 steel. Table 4.9 summarizes the beam and column sections for the SMRF design. A SAP 2000 model similar to that for the SC-MRF building was developed for the SMRF building. The beam-to-column connections of the SMRF are assumed to be fully rigid. T_{des} is found using Equation (4.2). Considering T_{des}=0.932 sec. and $T_{1,eigen}$=1.70 sec. (determined from SAP2000 model), V_{des} and $V_{T1,eigen}$ equal 0.081 and 0.044 of the effective seismic weight of entire building. Table 4.10 lists two sets of ELF used for the SMRF, where $F_{x,des}$ and $F_{x,T1,eigen}$ are based on T_{des} and $T_{1,eigen}$, respectively. Load combinations are considered for the design in accordance with ASCE 7-10, as presented earlier. The story drifts of the building under $ELF_{T1,eigen}$ (denoted $\theta_{s,el\text{-}T1,eigen}$), amplified by C_d=5.5 and divided by I=1, are listed in Table 4.11. The maximum value for $\theta_{s,el\text{-}T1,eigen}C_d/I$ is 2.05%, which is slightly larger than the story drift limit of 2% defined in ASCE 7-10, but deemed to be acceptable.

Table 4. 1. Design dead loads.

Item	Description	Uniform floor load (psf)		
		1st floor	2nd,3rd floors	Roof
Slab	3.5 in. normal weight concrete on 2 in. deep metal deck	43	43	-
Material deck	2VLI18 metal deck (2 in. deep and 0.0598 in. thick)	3	3	3
Roofing		-	-	10
Mechanical/Electrical		7	7	25
Ceiling		3	3	3
Floor finish	Carpet	2	2	-
Fireproofing		2	2	2
Steel structures		14	14	14
Curtain wall	25 psf on vertical projection	23	21	10
Total		97	95	67

Table 4. 2. Design live loads.

Item	Uniform floor load (psf)	
	1st, 2nd, 3rd floors	Roof
Office	50	20
Partition	15	-
Total	65	20
Live Load Included in Seismic Mass	15	0

Table 4. 3. Seismic design parameters according to ASCE 7-10.

Seismic Design Parameter	Value
Occupancy Category	II
Importance Factor, I	1
Response Modification Coefficient, R	8
Deflection Amplification Factor, C_d	5.5
Soil	stiff
Long-period transition period (Los Angeles region), T_L	8
Mapped Acceleration Parameters (Section 11.4.1): Provided at USGS Web site (Latitude=34.22, Longitude=-118.47)	
Site Class (Section 11.4.2)	D
F_a (Table 11.4-1)	1
F_v (Table 11.4-2)	1.5
$S_{MS}=F_aS_s$ (Section 11.4.3)	1.5g
$S_{M1}=F_vS_1$ (Section 11.4.3)	0.9g
$S_{DS}=2/3S_{MS}$ (Section 11.4.4)	1g
$S_{D1}=2/3S_{M1}$ (Section 11.4.4)	0.6g
Seismic Design Category (Tables 11.6-1, 2)	D
C_u (Tables 2.8-1)	1.4
Redundancy Factor, ρ (Section 12.3.4.2)	1

Table 4. 4. Lateral forces for 4-story prototype SC-MRF building based on strength ($F_{x,des}$) and drift control ($F_{x,T1,eigen}$).

	Equivalent lateral forces (kips)	
Floor level	$F_{x,des}$ (Strength)	$F_{x,T1,eigen}$ (Drift)
Roof	432	295
3rd	506	319
2nd	321	181
1st	156	74
Sum	1416	868

Table 4. 5. Drift design demands.

Story	$\theta_{s,el\text{-}T1,eigen}C_d/I$ (%)
4th	1.41
3rd	1.7
2nd	1.86
1st	1.85

Table 4. 6. Design demands.

$\theta_{rf,DBE}$ (% rad)	$\theta_{s,DBE}$ (% rad)	$\theta_{r,DBE}^{ave}$ (% rad)	$\theta_{rf,MCE}$ (% rad)	$\theta_{s,MCE}$ (% rad)	$\theta_{r,MCE}^{ave}$ (% rad)
2.6	3.9	3.1	3.9	5.9	4.7

Table 4. 7. Prototype building design member sizes, T_0 and β_E at each floor level for SC-MRF Designs 1 and 2.

Floor	Beam	Column		T_0 (kips)	β_E
		Interior	Exterior		
Roof	W24x94	W14x193	W14x176	201.6	0.34
3	W30x132	W14x193	W14x176	356.2	0.35
2	W30x148	W14x257	W14x233	534.3	0.26
1	W30x148	W14x257	W14x233	576.5	0.25

Table 4. 8. Number of PT strands, N, initial PT force-to-ultimate PT force per strand, $t_0/t_{u,n}$, and reinforcing plate length, L_{rp}, at each floor level for SC-MRF Designs 1 and 2.

Floor	SC-MRF Design 1			SC-MRF Design 2		
	Number of Strands, N	$t_0/t_{u,n}$	L_{rp} (in.)	Number of Strands, N	$t_0/t_{u,n}$	L_{rp} (in.)
Roof	8	0.43	10	10	0.34	10
3	16	0.38	22	22	0.28	22
2	24	0.38	22	32	0.29	34
1	24	0.41	22	34	0.29	33

Table 4. 9. Prototype building design member sizes for SMRF.

Floor	Beam	Column
Roof	W18x55	W14x257
3	W30x108	W14x257
2	W33x130	W14x342
1	W33x141	W14x342

Table 4. 10. Lateral forces for 4-story prototype building with SMRFs based on strength ($F_{x,des}$) and drift control ($F_{x,T1,eigen}$).

	Equivalent lateral forces (kips)	
Floor	$F_{x,des}$ (Strength)	$F_{x,T1,eigen}$ (Drift)
Roof	432	272
3rd	506	286
2nd	321	157
1st	156	61
Sum	1416	776

Table 4. 11. Drift design demands for SMRF.

Story	$\theta_{s,el\text{-}T1,eigen}C_d/I$ (%)
4th	1.87
3rd	2.05
2nd	2.02
1st	1.83

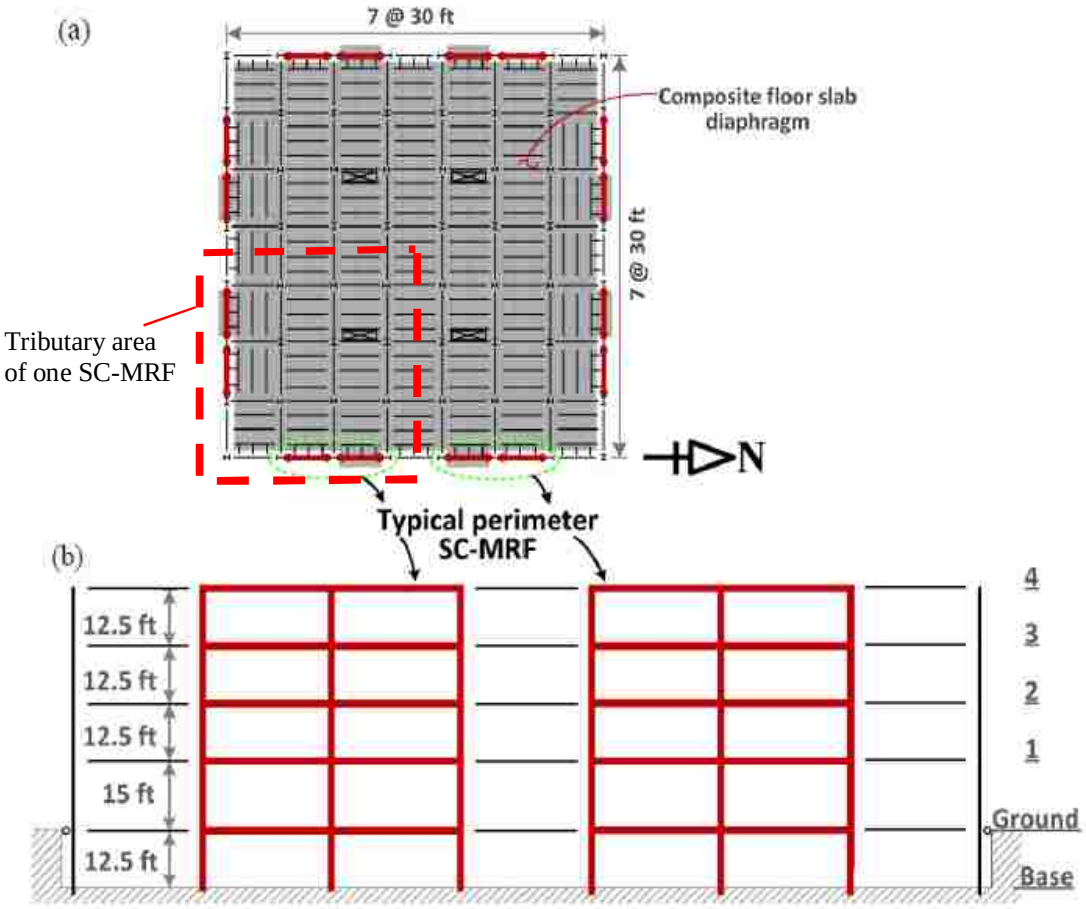

Figure 4. 1. Schematic of prototype SC-MRF: (a) plan and (b) elevation (Lin (2012)).

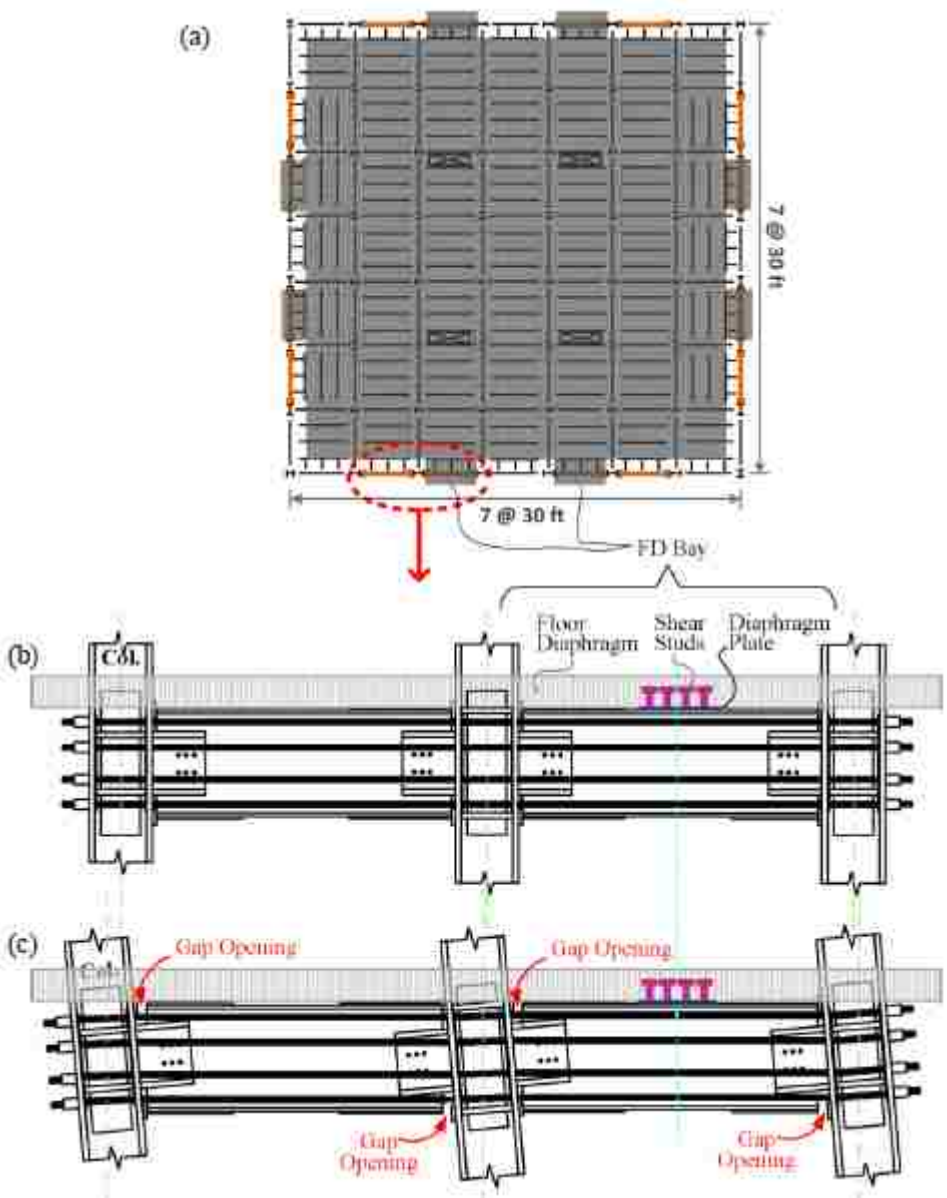

Figure 4. 2. Schematic of the SC-MRF: (a) plan, (b) elevation without gap opening, and (c) elevation with gap opening at beam-column interface (Lin (2012)).

Chapter 5

Self-Centering Beam-to-Column Moment Connection Finite Element Modeling

5.1. General

In order to investigate the collapse resistance of a steel SC-MRF system, there is a need for a complex finite element model capable of capturing the limit states that occur beyond the MCE level, where collapse modes are expected to develop under severe dynamic loading. This chapter describes the self-centering (SC) beam-to-column moment connection behavior under extreme seismic loading conditions and the SC connection finite element model which is used in the SC-MRF to assess its collapse resistance in accordance with FEMA P695 discussed in subsequent chapters. Since the SC-MRF response is compared with that of an SMRF, a finite element model of an SMRF connection is also developed and described. To verify the models, calibration studies are performed, including that of simplified models developed for purposes of computational efficiency. The SC-MRF and SMRF finite element models of the buildings are presented in Chapter 6.

5.2. SC Connection Behavior under Extreme Seismic Loading

As stated previously in Chapter 2, there are different types of ED devices utilized in steel SC connections. A SC-MRF connection with a web friction device (WFD) is utilized in this research, where the conceptual behavior of a steel SC connection with WFD was provided in Chapter 2. Regardless of the type of SC connection being studied,

the beams in an SC-MRF are subject to large moments, M, combined with appreciable axial force, P, caused by the PT and diaphragm forces (see Equations (2.4) and (2.5)), making the beams susceptible to local buckling under extreme seismic loading scenarios. Although the proposed PBD procedure attempts to prevent beam local bucking and PT strand yielding under the MCE level (see Chapter 3), it likely will occur under ground motions that exceed the MCE hazard level. Beam local buckling at the end of the reinforcing plates is an important limit state that must be considered in developing the analytical model of the SC-MRF. The occurrence of local buckling in the beam leads to shortening of the member, which in turn results in a loss of PT force and, since the moment capacity is affected by axial force P, subsequent loss of moment capacity, M, of a post-tensioned SC connection. Similarly, PT strand yielding results in a loss of PT force which leads to a loss of moment capacity of the SC connection. A computational efficient model is needed for the collapse assessment of an SC-MRF, where many simulations are required for the incremental dynamic analyses. To reduce the number of degrees of freedom in the analytical model, the finite element model developed for the study therefore consists of stress-resultant beam-column and continuum shell elements in order to model the complete structural system while capturing the important limit states that can occur and influence the seismic collapse resistance of an SC-MRF under extreme dynamic loading. The limit states include beam flange and web local buckling at the end of the reinforcing plates, PT strand yielding, gap opening at the beam column interface, inelastic deformations in the members (beams, columns, panel zones), and second order (P-delta) effects due to gravity loads imposed on the gravity load frames. The ABAQUS program is used to develop the model. The experimental test results of Garlock (2002)

are compared with model predictions to perform a verification study of the model capable of capturing the beam local buckling limit state at the end of the reinforcing plates.

5.3. SC Connection Verification Study

5.3.1. SC Connection Subassembly

As noted above, the beams are expected to yield and develop potential local buckling under appreciable axial force and bending moment. There is a need to develop a computational efficient model capable of capturing this important limit state to investigate the seismic collapse resistance of an SC-MRF. In order to develop and calibrate a model that captures this limit state, the connection behavior is studied and analytical model predictions are compared with the experimental test data by Garlock (2002) for an interior subassembly connection. Note that as stated before, an SC-MRF with WFDs is studied in this research. However, the experimental test data from Garlock (2002) is used to verify the model can capture the beam local buckling limit state.

Figure 2.2(a) in Chapter 2 shows the SC connection subassembly test setup of Garlock (2002). The subassembly was derived from the prototype building described in Garlock (2002) where it is a full-scale model of an interior joint from the 3rd floor of the prototype frame as shown in Figure 5.1(a). The lengths of the beams and columns in the subassembly were designed so that zero moment locations are located approximately at the column mid-height and beam mid-span in the prototype frame to simulate points of inflection in the prototype frame (see Figure 5.1(a)). In the experimental setup the distance between beam supports, L, was 29.5 feet and the column height, h, was 13 feet. A roller boundary condition was used at the end of each beam where inflection points

were located. The column was pinned at the base and free at the top where the lateral load (H) was applied as seen in Figure 5.1(b).

As stated in Chapter 2, the connection of Garlock (2002) is based on the use of high resistance steel PT strands, whereas the ED system is composed of bolted steel top-and-seat angles. PT strands clamp the beam to the column at their interface. The force in the PT strands provides a restoring moment to the connection to prevent residual connection rotation and residual story drift.

The beams and column are fabricated from W36x150 and W14x398 sections, respectively. Garlock (2002) studied 6 test specimens to investigate the effects of the reinforcing plate length (L_{rp}), the number of post-tensioning strands (N_s), the initial post-tensioning force (T_0), and the initial post-tensioning force per strand (T_0/N_s) on connection behavior. These variables were chosen so that different limit states in the connection would occur. These limit states include angle failure, PT strand yielding, and beam local buckling. In this study, Test Specimens 20s-18 and 36s-30 of Garlock (2002) were used to verify the model ability to predict the SC behavior compared to the test results. Table 5.1 summarizes the important parameters of the test specimens of Garlock (2002) used in this research. In Table 5.1, T_0 is the initial total PT strand force, P_y is the nominal beam axial yield force defined as the beam cross section area multiplied by the steel yield stress F_y=50 ksi, and T_u is the ultimate total PT strand force. Model development and results compared with the experimental data, along with model simplifications are presented below.

5.3.2. SC Connection Model Development

The following models are studied herein:

- The Model-A (see Figure 5.2) is composed of continuum elements for modeling the beams and the panel zone region while the stress-resultant elements are used to model columns. Compression-only gap elements and spring elements are used at the beam column interface to simulate the gap opening-closing behavior and the force-deformation relation of the angles, respectively. A truss element is used for modeling the PT strands. Imperfections are imposed to the model to initiate any beam local buckling in order to predict the experimental results. The first buckling mode is scaled to impose the amplitude of imperfections to the model.
- The Model-B uses the same elements as the Model-A, but with the corresponding test specimen characteristics (see Table 5.1).
- The Model-C (see Figure 5.3(a)) is a simplified model which uses the continuum elements along one beam depth at the end of the reinforcing plates where beam local buckling is expected. The model uses a fine mesh for the continuum elements. A kinematic based panel zone model (discussed later) is utilized to model the panel zone. The remaining of the beams and the columns are modeled using the stress-resultant elements. A truss element is used to model the PT strands. As in Model-A and Model-B, in Model-C compression-only gap elements and spring elements are also used at the beam column interface to simulate the gap opening-closing behavior and the force-deformation relation of the angles, respectively. Initial imperfections are imposed to the model.
- The Model-D (see Figure 5.3(b)) is the same as Model-C, except that for computational efficiency purposes is based on a coarse mesh to reduce the number of degrees of freedom in contrast to the above models.

5.3.2.1. Material Modeling

The measured material properties for the beam flanges and beam web for the test specimens are reported in Garlock (2002), where the beam flange yield stress σ_y is 52.5 ksi and ultimate stress σ_u is 72.3 ksi, and σ_y=62.1 ksi and σ_u=76.5 ksi for the beam web. The cyclic hardening formulation of the material model was calibrated using the steel coupon cyclic test data from Kaufmann (2001), where the material properties for yield and ultimate stress were normalized to the material properties of the test specimens of Garlock (2002). Figure 5.4 shows the test data from Kaufmann (2001) along with the material behavior modeled in ABAQUS for A572 Gr 50 steel material to account for cyclic behavior up to 4% strain. The nonlinear combined kinematic-isotropic hardening model of Lemaitre and Chaboche (1990) available in the ABAQUS material model library was used to account for nonlinear cyclic behavior of the material. The PT strand material is modeled using a bi-linear stress-strain relation with kinematic hardening to account for cyclic behavior, where the tensile yield stress was assumed to be equal to 243 ksi. A strain hardening slope of 0.03E was used, where E=27600 ksi is the Young's Modulus of the strand. The experimental data from Walsh and Kurama (2010) shows that the stress-strain relationship of PT strands similar to those used in this study follows a bi-linear curve (see Figure 5.5). However, the PT strand maximum strains developed in the subassembly connection models studied herein did not exceed their yield strain and PT strands remained elastic. Fracture of the PT strands was not modeled. In the incremental dynamic analyses performed in Chapter 8, it was determined that the PT strands did not surpass their fracture strain and therefore it was appropriate to exclude PT strand fracture in the model.

5.3.2.2. Continuum Elements

In order to develop a model capable of capturing the effects of beam local buckling on member behavior, continuum elements need to be used to be able to simulate the out of plane displacements due to cross section element distortion as the beam locally buckles. An 8-node shell element, S8R, available in the ABAQUS element library with five section integration points through the thickness (Simpson's rule) is utilized in this research. Each node has 6 degrees of freedom. Thus, the number of elements can significantly affect the model computation efficiency. Enough elements need to be used to obtain accurate results which match the experimental data well. The shell element thickness is assigned depending on the flange and web thickness. In addition, to model the beam flange reinforcing plates, the flange thickness in the model is increased over the length of the reinforcing plates. The material properties defined previously are assigned to the shell elements utilized for the beam flanges and beam web. Initial imperfections are imposed on the shell elements to initiate any local buckling in the beam. The buckling mode shapes are scaled to impose web and flange out-of-flatness imperfections in the beams. A sensitivity analysis is performed using a range of web and flange out-of-flatness values, and is presented later.

5.3.2.3. Stress-Resultant Elements

Where beam local buckling is not expected, far away from the SC connection, or where the elements remain elastic like the column, stress-resultant elements can be utilized in order to simplify the model and reduce the number of degrees of freedom to make the analysis more computationally efficient. A stress-resultant Timoshenko beam-column element (element B32OS in the ABAQUS element library) is used. A multi-point

constraint boundary condition is used to model plane sections remaining plane at the interface between the shell elements and a stress-resultant element in the modeling of the beams. The Timoshenko beam-column elements account for transverse shear deformations. The stress-resultant elements do not permit the material properties to be unique in the flanges and web of the beams and columns. Hence, the flange material properties are used for the stress-resultant elements to obtain a more reasonable flexural capacity, which is dominated by the stresses developed in the flanges in actual wide flange sections.

5.3.2.4. Truss and Gap Elements

The PT strands are modeled using an inelastic truss element (element T3D2 in the ABAQUS element library). In the model the strands were lumped together to form one strand at the centroid of the force resultant of the group of strands. The cross-sectional area assigned to the truss element is based on the sum of the areas of all PT strands. The material properties defined previously are assigned to the elements. The amount of strain in the PT strands is calculated to produce the target initial PT force, T_0 summarized in Table 5.1. A larger than the calculated strain is imposed to the PT strand elements as an initial condition to accommodate the PT force loss due to beam shortening. A Static analysis is performed and the initial strain is transformed to the internal force in the model by satisfying an internal equilibrium.

At the beam column interface, where gap opening occurs in the SC connection, there is a need for elements which are able to transfer only compressive forces. Compression-only gap elements (element GAPUNI in the ABAQUS element library) are used to

transfer the compressive force between nodes at the beam column interface in SC connections.

5.3.2.5. Panel Zone Model

As stated, the panel zone region was modeled with continuum elements for Model-A and Model-B. The panel zone model is used for Model-C and Model-D. While the state of stress in the panel zone is extremely complex, the source of deformation can be divided into three parts: axial, flexural, and shear. Among these deformation components, shear deformations are dominant. So the focus is on taking into account in the modeling of the panel zone shear deformations using an assemblage of rigid links and rotational springs. For model simplification, a kinematic based panel zone model by Herrera (2005) is used to model the panel zone. Figure 5.6 shows a schematic of the panel zone model used in the simplified SC connection models. In the panel zone model the boundary node displacements and rotations are appropriately slaved to the displacements and rotations of two nodes at the center of panel zone (see Figure 5.6) which are connected with a nonlinear rotational spring. The properties of the rotational spring are based on moment-rotational characteristics derived from the shear force-shear deformation behavior of the panel zone. The two center nodes have the same displacements but independent rotations to simulate the shear deformations in the panel zone. The panel zone used in this model includes a rigid link with hinges on the ends. As a result, the moment developed at the rotational spring is related to the panel zone shear. The following equations describe the model:

$$V_{pz,y} = 0.55\sigma_y d_c(t_{wc} + t_{dp)} \tag{5.1}$$

$$V_{pz,u} = 0.55\,\sigma_y d_c t_w \left\{1 + \frac{3.45 b_{fc} t_{fc}^2}{d_b d_c t_{wc}}\right\} + \frac{\sigma_y}{\sqrt{3}}(d_c - t_{fc}) t_{dp} \tag{5.2}$$

$$\gamma_{pz,y} = \frac{\sigma_y}{\sqrt{3}G} \tag{5.3}$$

where $V_{pz,y}$ is the panel zone shear yield force. The panel zone ultimate shear capacity, $V_{pz,u}$, is assumed to occur at a shear deformation of $4\gamma_{pz,y}$, where $\gamma_{pz,y}$ is the panel zone shear yield distortion. σ_y is the yield stress of the column material (σ_y=55.8 ksi), and G is the shear modulus of steel material. d_b =35.85 inches, d_c=18.29 inches, t_{wc}=1.77 inches, t_{fc}=2.85 inches, t_{dp}=0.5 inches, and b_{fc}=16.59 inches are the beam depth, column depth, column web thickness, column flange thickness, total doubler plate thickness, and column width, respectively (the section dimensions are given in Garlock (2002)). The Krawinkler panel zone model (1978) does not give recommendations for the panel zone stiffness when the shear distortion is greater than four-times the distortion at yield. Therefore, the stiffness of the panel zone beyond $4\gamma_{pz,y}$ is assumed to be 0.04 times the panel zone the initial stiffness in the panel zone model(see Figure 5.7).

The panel zone shear force-deformation behavior relatioship is transformed to a moment-rotation relationship for the rotational springs as follows:

$$M_{pz,s} = V_{pz} h_{pz} \tag{5.4}$$

$$\theta_{pz} = \gamma_{pz} \tag{5.5}$$

where $M_{pz,s}$ is the moment in the rotational spring that is used to model the panel zone flexibility, θ_{pz} is the rotation of the spring, and h_{pz} is the height of panel zone. The rotational spring is modeled with element type CONN3D2 in the ABAQUS element library, and located between two center nodes shown in the panel zone model (see Figure 5.6). $V_{pz,y}$,$V_{pz,u}$ and $\gamma_{pz,y}$ are 1274 kips, 1640 kips and 0.0029, respectively. h_{pz} is found by adding one beam depth (d_b) and one reinforcing plate thickness (t_{rp}= 1 inch).

5.3.2.6. Angle Model

The energy dissipation devices are top and seat angles, which are modeled with nonlinear translational spring elements with kinematic hardening for cyclic behavior to provide force-deformation relationship of the angles when gap opening occurs. Figure 5.8(a) shows a photograph of an angle from Test Specimen 20s-18 of Garlock (2002). Since beam local buckling does not occur in the Test Specimen 20s-18, the analytical model is used primarily to calibrate the force-deformation relationship of the springs used for modeling the angles. Element type CONN3D2 in the ABAQUS element library is used for this purpose. Figure 5.8(b) shows the spring behavior calibrated with the test data from Garlock (2002) for Test Specimen 20s-18. As seen, the angle model predict the experimental data well. This model is utilized for the Test Specimen 36s-30 model.

5.3.3. ABAQUS Model Schematic and Results

5.3.3.1. Model-A

A schematic of ABAQUS Model-A is shown in Figure 5.2. The model is subjected to the cyclic static loading imposed at the top of the column. The cyclic quasi-static loading time history is presented is Figure 5.9. By performing an eigenvalue analysis to find the buckling mode shape (see Figure 5.10), the first buckling mode shape is scaled to impose

0.17 inches (the measured value by Garlock (2002) for W36x150 web out-of-flatness) as the maximum web out-of-flatness for the beam located on the east side of the column, where beam local buckling is expected to occur in the model for validation purposes (see the photograph shown in Figure 5.13(b)), to initiate local buckling in the analytical model in order to predict the experimental response.

Figure 5.11 presents the top column applied force, H, vs. top column displacement, Δ for the Model-A of the Test specimen 20s-18. In addition, Figure 5.12 shows the total PT strand force, T vs. top column displacement, Δ. As seen, the analytical model results match the experimental data well. No beam local buckling occurred in Test Specimen 20s-18. This shows the ABAQUS model is able to capture SC behavior.

5.3.3.2. Model-B

A schematic of the deformed shape of ABAQUS Model-B is shown in Figures 5.13(a) under cyclic static loading imposed at the top of the column. A photograph from the experiment of Test Specimen 36s-30 is shown in Figure 5.13(b), where beam local buckling occurred in the test specimen at the end of the reinforcing plate of the beam located on the east side of the column. The west beam showed no clear evidence of buckling (Garlock (2002)). Hence for validation purposes, the imperfection is imposed to the model where the beam on the east side experiences the maximum web out-of-flatness (0.17 inches) in the model (see Figure 5.13(a)), to initiate the beam local buckling where it occurred in the experiment and predict the experimental response. Therefore, the beam on the west side of the column experiences less out-of-flatness compared to the beam on the east side of the column. When beam local buckling occurs, the beam axial force reduces due to the PT strand force loss. Note that the imperfection amplitude is applied

equally to all of the beams of the frames studied in subsequent chapters to assess the collapse resistance of the systems. Figures 5.14 and 5.15 show the H-Δ and T-Δ for Model-B of Test Specimen 36s-30. The loss of PT force due to local buckling is observed in Figure 5.15 in both the experimental data and analytical model. Due to beam local buckling, the loss of connection moment capacity is seen to occur in Figure 5.14. The results show that not only does the model predictions match well with the experimental results but also the model is capable of capturing beam local buckling under extreme loading conditions.

5.3.4. ABAQUS Model Simplification

As noted previously, a computational efficient model is needed for the collapse assessment of SC-MRFs, where many simulations are required for the incremental dynamic analyses. Simplified models are therefore developed by using continuum shell elements at the end of reinforcing plates where beam local buckling is expected to happen in the beams (see the photograph in Figure 5.13(b)). The continuum elements are utilized for a length of one beam depth where local buckling is expected to occur. Stress-resultant elements and the kinematic-based panel zone model are used to model the rest of the beams, the column, and the panel zone, respectively. Figure 5.6 shows a schematic of the connection details where the panel zone and the angle models are located. Gap elements transfer the nodal compression at the beam column interface. Multi-point constraints are used at the cross sections, where stress-resultant elements are connected with continuum elements in order to keep plane sections to remain plane. Proper mesh refinement of the continuum elements is investigated by considering two models with a fine mesh (Model-C) and a coarse mesh (Model-D) for the continuum elements (see Figure 5.3). 1600

continuum 8-node shell elements were used for the fine mesh model in contrast with the 192 elements for the coarse mesh model. In order to impose the initial imperfections to the model, the first buckling mode shape was scaled. The maximum out of flatness is imposed to be the same as that used for the Model-B. The deflected shapes of the simplified models are shown in Figure 5.16 for the Model-C and Model-D of Test Specimen 36s-30. The H-Δ and T-Δ relations are shown in Figures 5.17 and 5.18, respectively, for the simplified models. It is seen that the analytical model results follow the experimental data well and capture the local buckling behavior and the loss of PT force. The analytical model with the coarse mesh (Model-D) is more computational efficient by having fewer number of degrees of freedom, and is used to develop the SC-MRF model discussed in Chapter 6. Table 5.3 summarizes the total number of elements used in each analytical model for SC connection subassembly along with the total number of degrees of freedom.

5.3.5. Initial Imperfection Sensitivity Analysis

As stated previously, initial imperfections are imposed on the shell elements to initiate any local buckling in the beam. The buckling mode shape is scaled to impose web and flange out-of-flatness imperfections in the beams to compare the subassembly model prediction of the test specimen. However, in order to investigate the collapse resistance of an SC-MFR system in subsequent chapters, there is a need for a sensitivity analysis to choose an appropriate amount of imperfection imposed on the beam elements for the frames. A sensitivity analysis is performed using representative values of web and flange out-of-flatness based on the test data of Garlock (2002). Table 5.2 summarizes different values used for the maximum beam web and flange out-of-flatness. Five different cases

are shown in Table 5.2. A percentage of the web thickness is used for developing different cases for the maximum beam web out-of-flatness while the maximum flange out of flatness is based on a percentage of the AISC standard (AISC 2010) for mill tolerance for the beam flanges (see Figure 5.19). Figure 5.20 and Figure 5.21 represent the H-Δ and T-Δ of the sensitivity analyses using the simplified model with a coarse mesh (Model-D) As seen in Figure 5.19 and Figure 5.20, values of 50% of the web thickness (Case 5 in Table 5.2) for the beam web out-of-flatness and 50% of the mill tolerance for the beam flange imperfections lead to conservative results while the amount of imposed imperfections are still realistic in contrast to measured values for W-sections. Hence, the values of 50% of the web thickness for the beam web out-of-flatness and 50% of the mill tolerance for the beam flanges out-of-flatness are selected for the maximum imposed imperfection amplitude utilized for the continuum elements in the frames studied in the subsequent chapters.

5.4. SMRF Connection Verification Study

5.4.1. Connection Subassembly

The SC-MRF seismic collapse resistance is compared with a conventional comparable SMRF system in this research. Thus, a verification study is done for a conventional SMRF connection model. The test data from Ricles et. al (2000) for a subassembly with a SMRF beam-to-column moment connection is used to investigate the capability of ABAQUS model to capture beam local buckling behavior in these type of connections. The beams and column are fabricated from W36x150 and W14x398 sections, respectively. Figure 5.22 shows a schematic of test-setup. More details are given in Ricles et. al (2000).

5.4.2. Connection Model Development

Elements used for the model development are similar to elements used for the SC connection. There is no need however for gap and truss elements for a conventional SMRF connection. Note that there is no beam flange reinforcing plates in this model, thus the continuum elements need to be started at the face of the column as seen in the model schematics (see Figures 5.23 and 5.24). Material modeling is the same as what was presented earlier for the SC connection, except that the measured material properties of Ricles et. Al. (2000) were used with the yield stress of 56.7 ksi and 62.9 ksi for the beam flanges and web, respectively.

5.4.2.1. ABAQUS Model Schematic and Results

First, the whole beams are modeled with shell elements similar to the SC connection subassembly studies using Model-A presented earlier in this chapter. For simplicity, a kinematic based panel zone model (see Figure 5.23) and stress-resultant elements are used for modeling the column. The amount of imperfection imposed was 0.13 inches (20% of web thickness) for the beam web out-of-flatness (the measured values reported by Ricles et. al (2000)). 20% of the mill tolerance is also used for the beam flange out-of-flatness. Figure 5.23 shows the deflected shape of the model under quasi-static cyclic loading applied at the top of the column along with a photograph from Ricles et. al (2000) where beam local buckling is seen in the beams. The analysis result for the H-Δ relation is shown in Figure 5.25(see Detailed Model) compared with the experimental data. As seen, the model predicts the experimental data well prior to the occurrence of top flange fracture in the experimental specimen.

5.4.2.2. ABAQUS Model Simplifications

For model simplification and computational efficiency, shell elements are used along one beam depth from the column face, and the rest of both beams and the column are modeled with stress-resultant elements. The same amount of imperfection used for the Detailed Model, i.e., 20% of the web thickness for the beam web out-of-flatness and 20% of the mill tolerance for the beam flange out-of-flatness is imposed to the beams in the Simplified Model. Figures 5.24 shows the deflected shape of the Simplified Model. The analysis result for H-Δ relation is shown in Figure 5.25 for the Simplified Model and compared with the experimental data. As seen, the analytical results follow the test data well prior to the occurrence of top flange fracture in the experimental specimen. In order to develop a computational efficient SMRF model, the Simplified Model will be utilized in the subsequent chapters with the same amount of imperfection discussed earlier for the SC-MRF, which is 50% of the web thickness for the beam web out-of-flatness and 50% of the mill tolerance for the beam flange out-of-flatness imposed on the continuum elements in the frames.

Table 5. 1. Test specimen characteristics from Garlock (2002) for SC beam-to-column moment connection model calibration.

Test Specimen	Number of strands, N_s	Initial PT force, T_0 (kips)	T_0/N_s (kips)	T_0/P_y	T_0/T_u	Length of reinforcing plate, L_{rp} (in.)
20s-18	20	343	17.1	0.15	0.29	36
36s-30	36	1063	29.5	0.46	0.49	36

Table 5. 2. Maximum beam web and flange out-of-flatness values for sensitivity studies.

Case	Web out-of-flatness		Flange out-of-flatness	
	Value (in.)	Normalized by t_w	Value (in.)	Normalized by Mill Tolerance
1	0.17 (Measured)	0.27	0.15	1
2	h/150 (=0.23)	0.37	0.15	1
3	0.32	0.5	0.15	1
4	0.63	1	0.08	0.5
5	0.32	0.5	0.08	0.5

Table 5. 3. Total number of elements used in each model for SC connection subassembly along with the total number of degrees of freedom.

Model	Total number of elements	Total number of degrees of freedom
Model-A	11050	209903
Model-B	11050	209903
Model-C	1665	31206
Model-D	262	4682

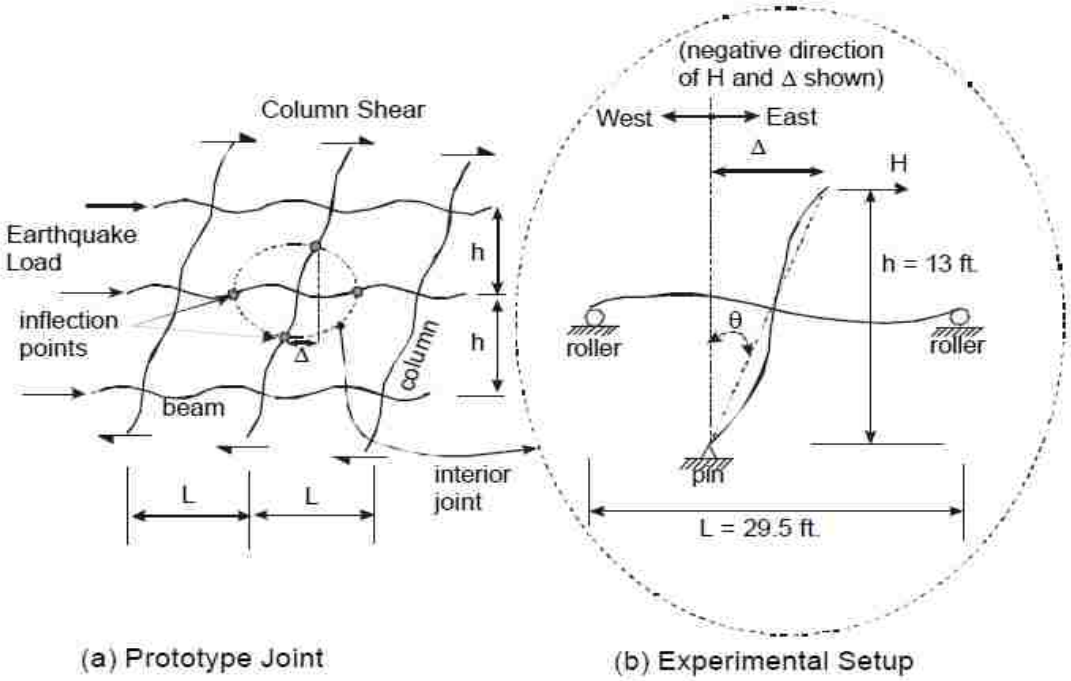

Figure 5. 1. Kinematics of (a) prototype structure in connection region, (b) experimental setup (Garlock (2002)).

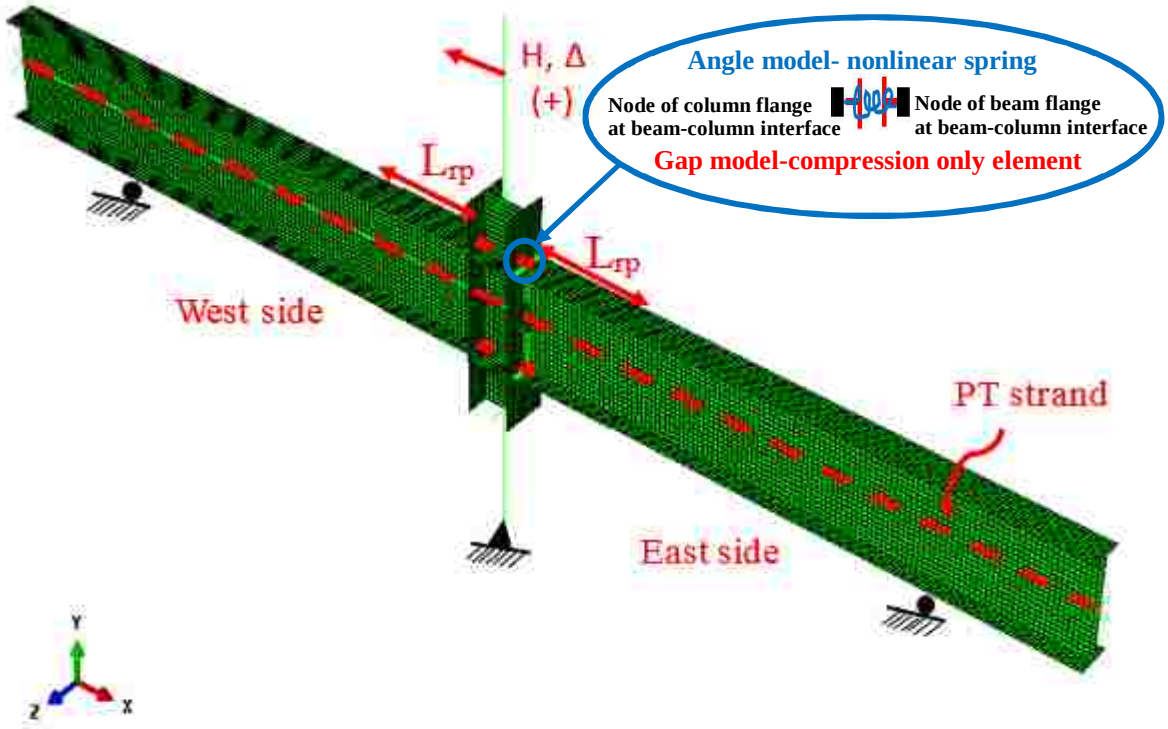

Figure 5. 2. Schematic of ABAQUS model (Model-A and Model-B) for SC beam-to-column moment connection subassembly.

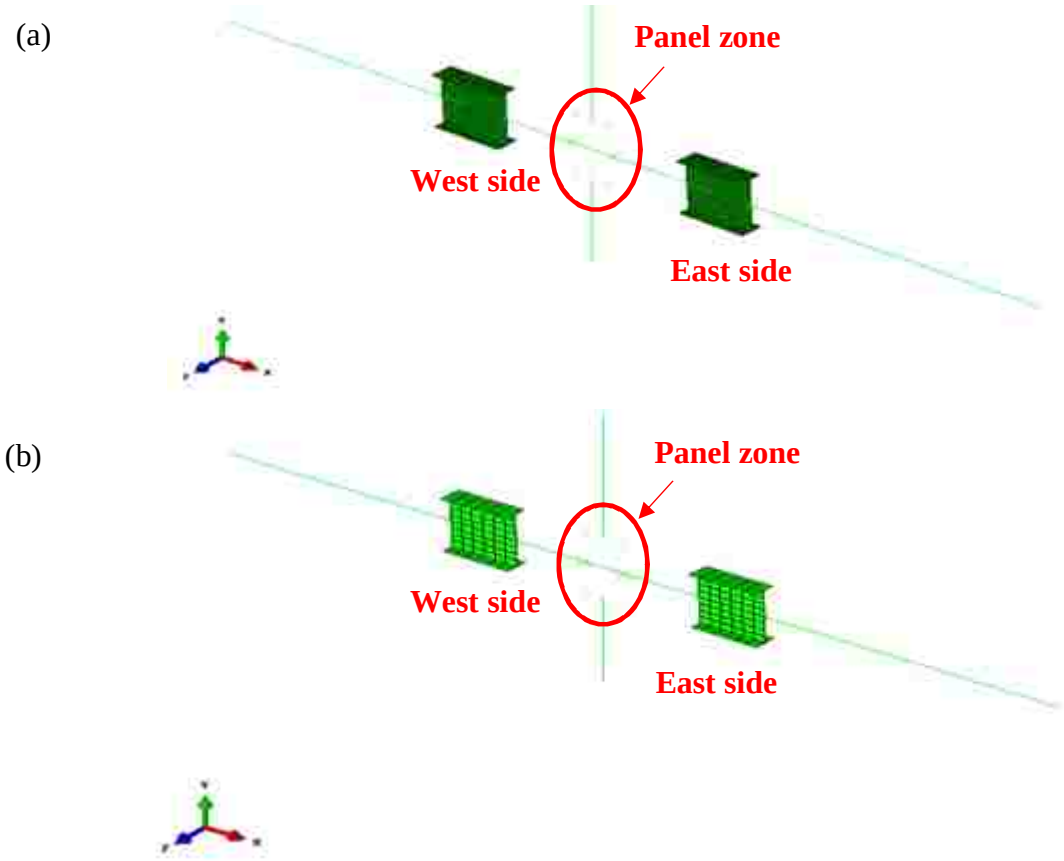

Figure 5. 3. Schematic of: (a) simplified model with fine mesh (Model-C), (b) simplified model with coarse mesh (Model-D).

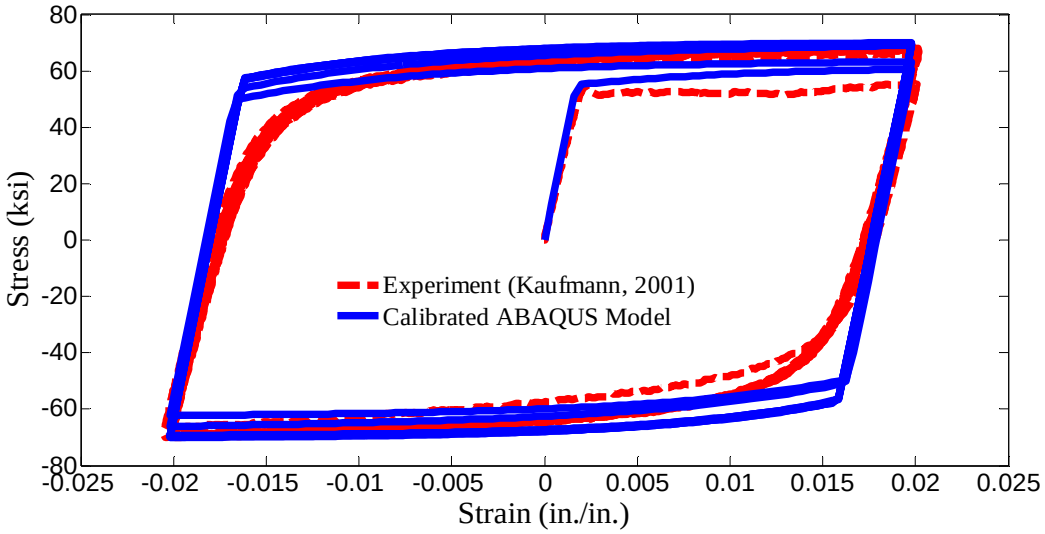

Figure 5. 4. Test data from Kaufmann (2001) and comparison with ABAQUS calibrated material model, A572 Gr. 50 steel.

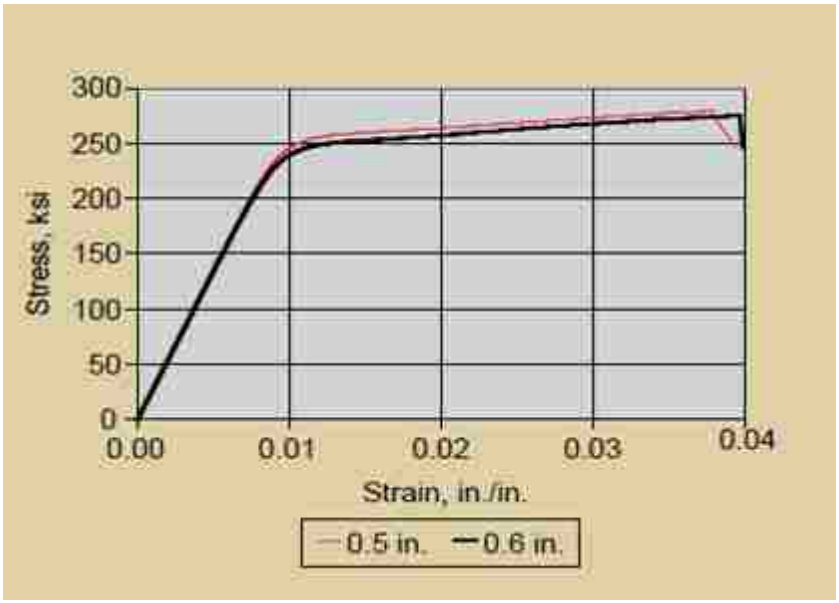

Figure 5. 5. Stress-strain relation for 0.5 and 0.6 inch diameter PT strands (Walsh and Kurama (2010)).

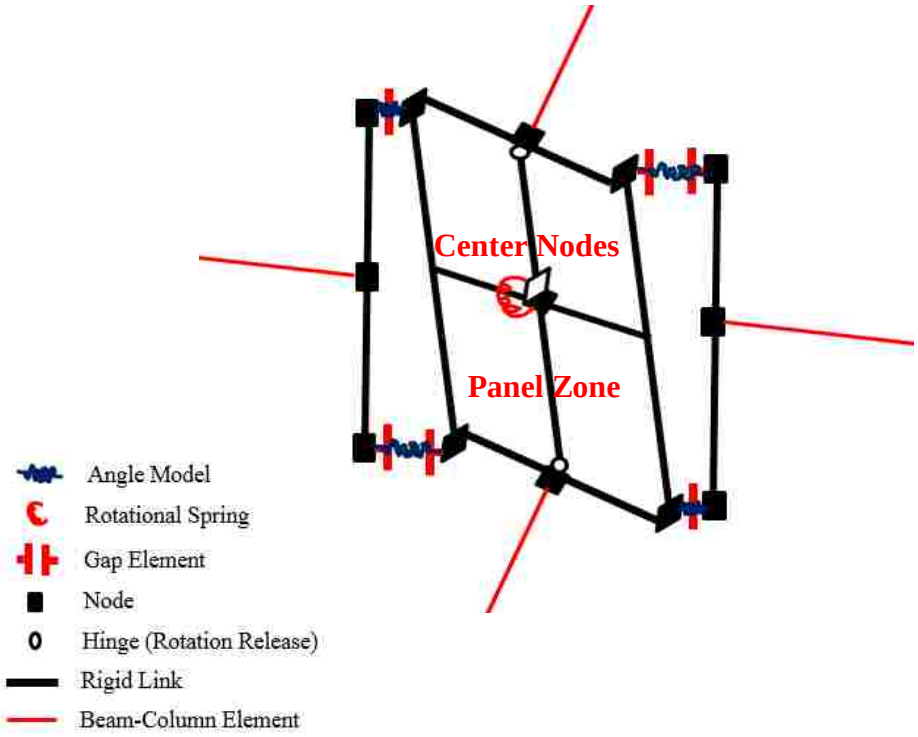

Figure 5. 6. Schematic of SC beam-to-column moment connection details of simplified models.

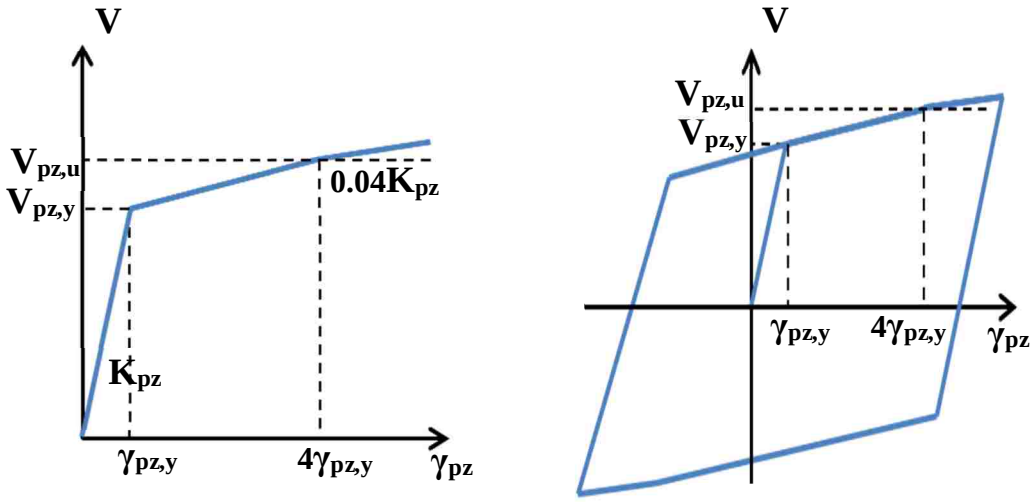

(a) Monotonic loading (b) Cyclic loading

Figure 5. 7. Panel zone shear force-distortion relation, Krawinkler's modified model.

(a)

(b)

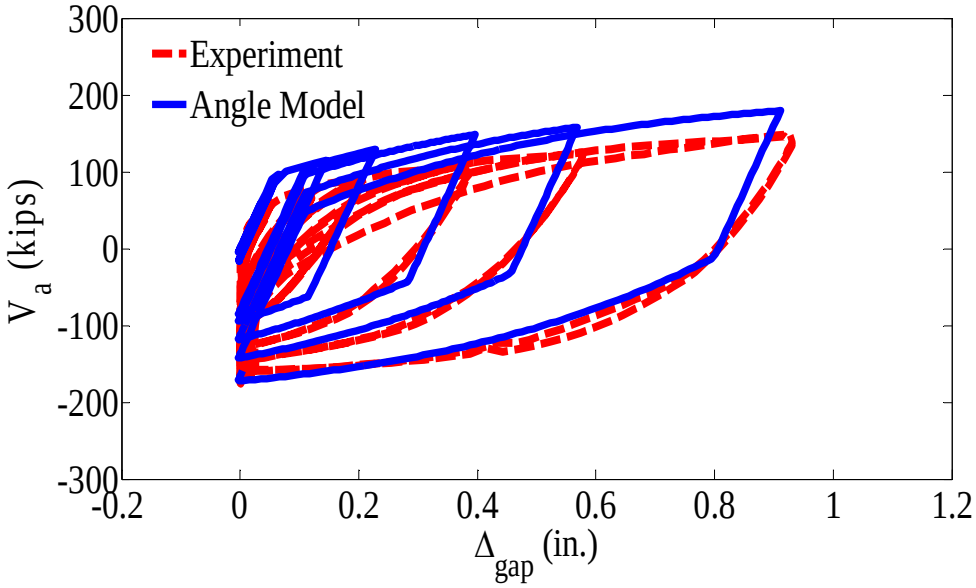

Figure 5. 8. (a) Photograph of an angle of Test specimen 20s-18 of Garlock (2002), (b) Comparison of test data with angle model prediction of Test specimen 20s-18.

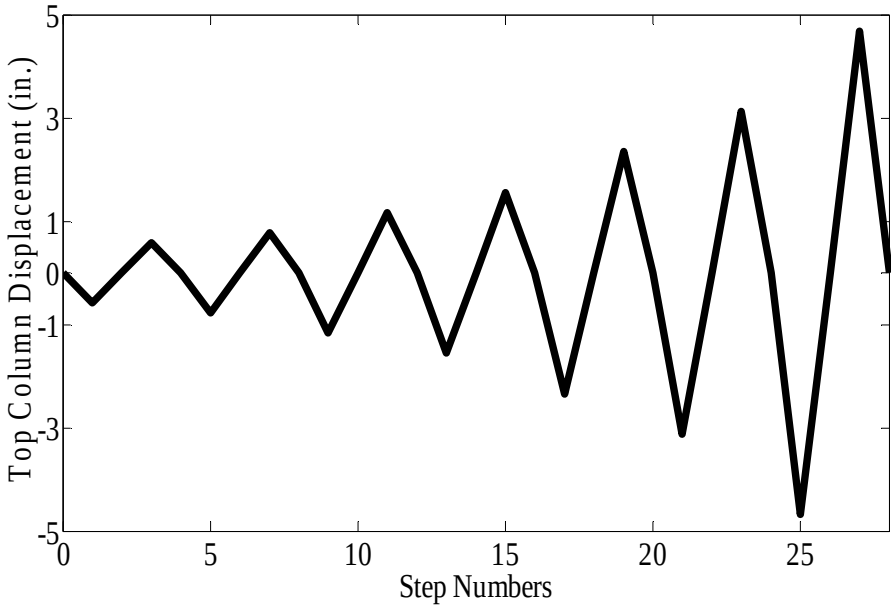

Figure 5. 9. Quasi static lateral displacement history applied at top of the column.

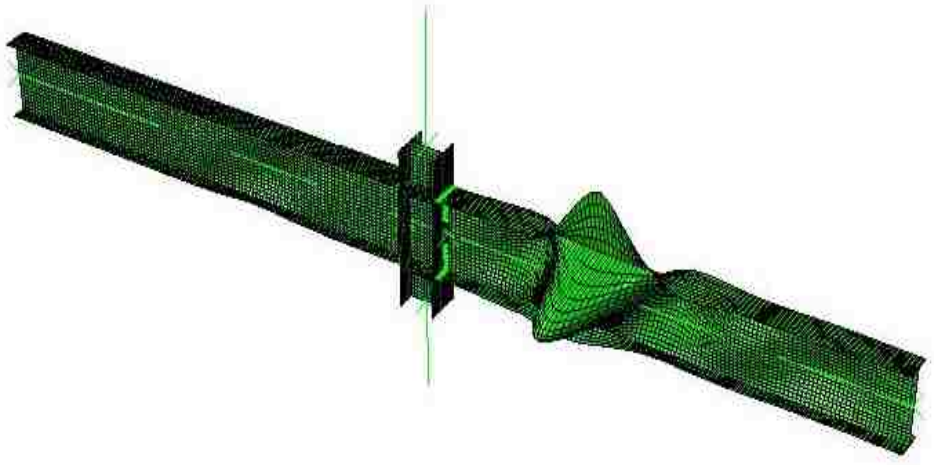

Figure 5. 10. First buckling mode for Model-A.

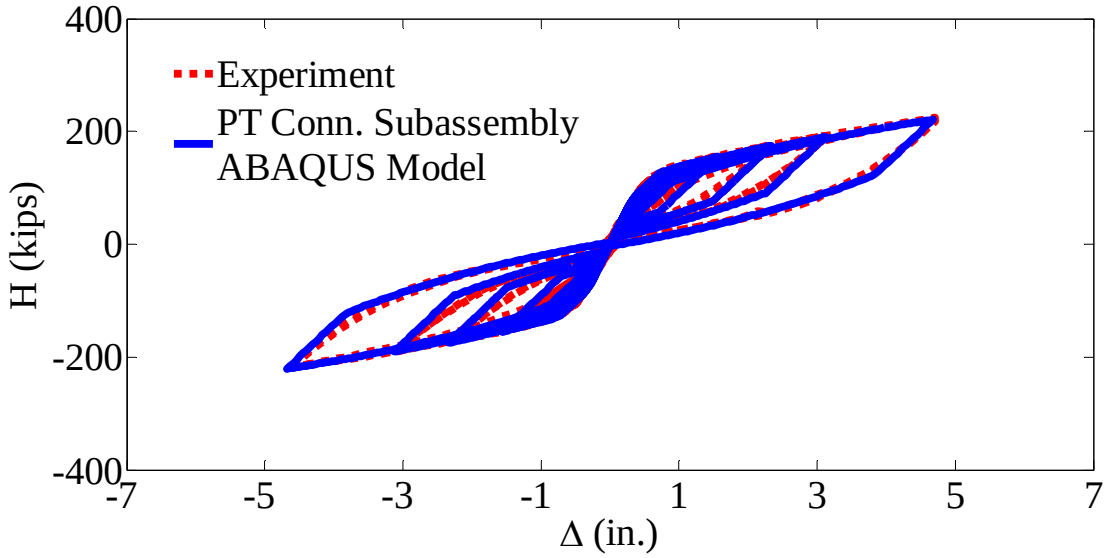

Figure 5. 11. Comparison of test results with analytical results for applied force-top column displacement (H-Δ), Test Specimen 20s-18, Model-A.

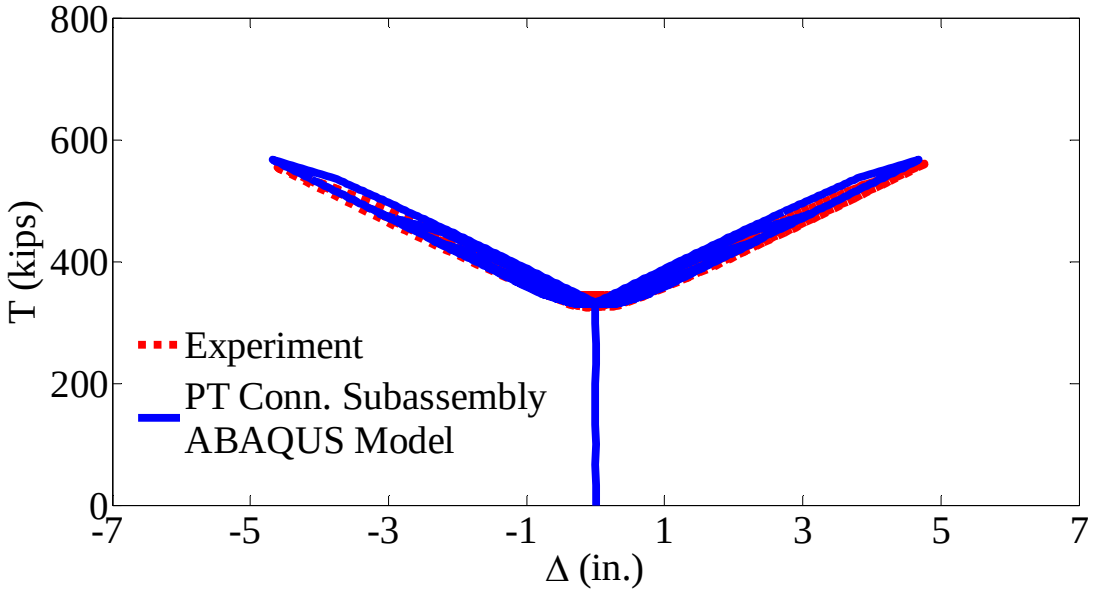

Figure 5. 12. Comparison of test results with analytical results for total PT strand force-top column displacement (T-Δ), Test Specimen 20s-18, Model-A.

(a)

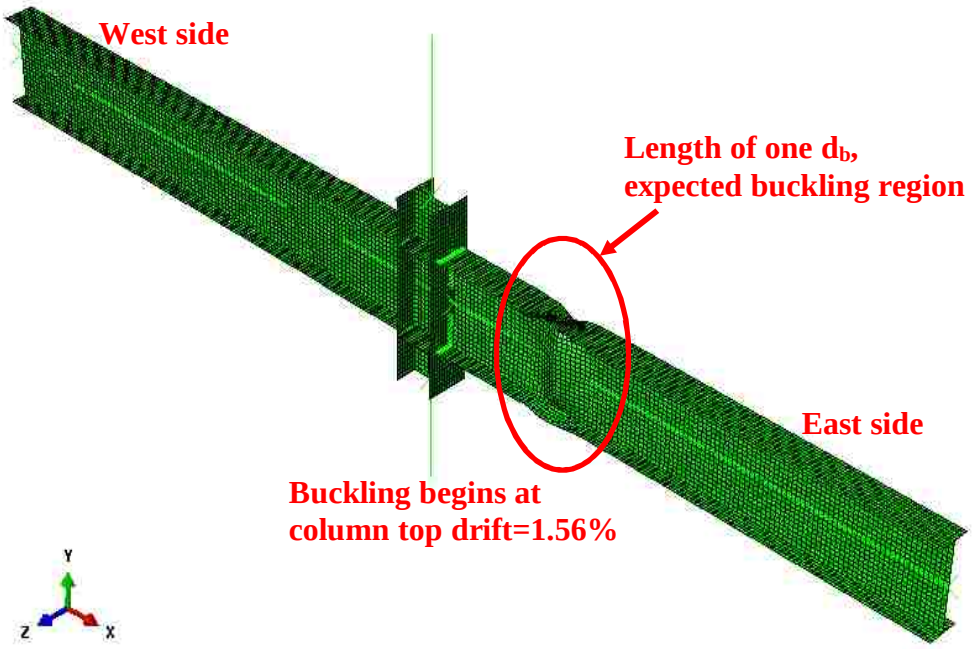

(b)

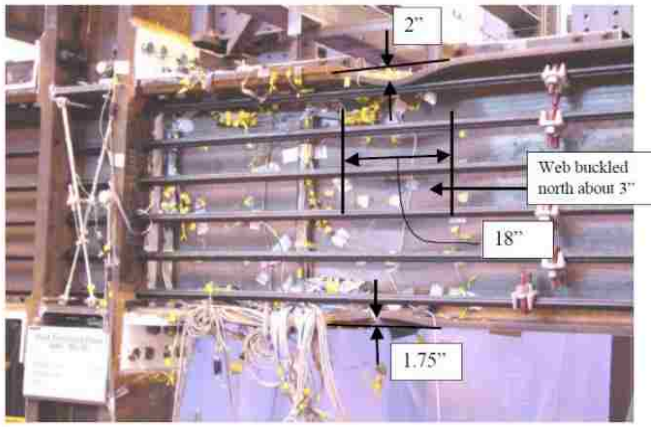

Figure 5. 13. Schematic of model deformation of: (a) finite element local buckling model (Model-B) in comparison with (b) experimental response (Garlock (2002)), Test Specimen 36s-30.

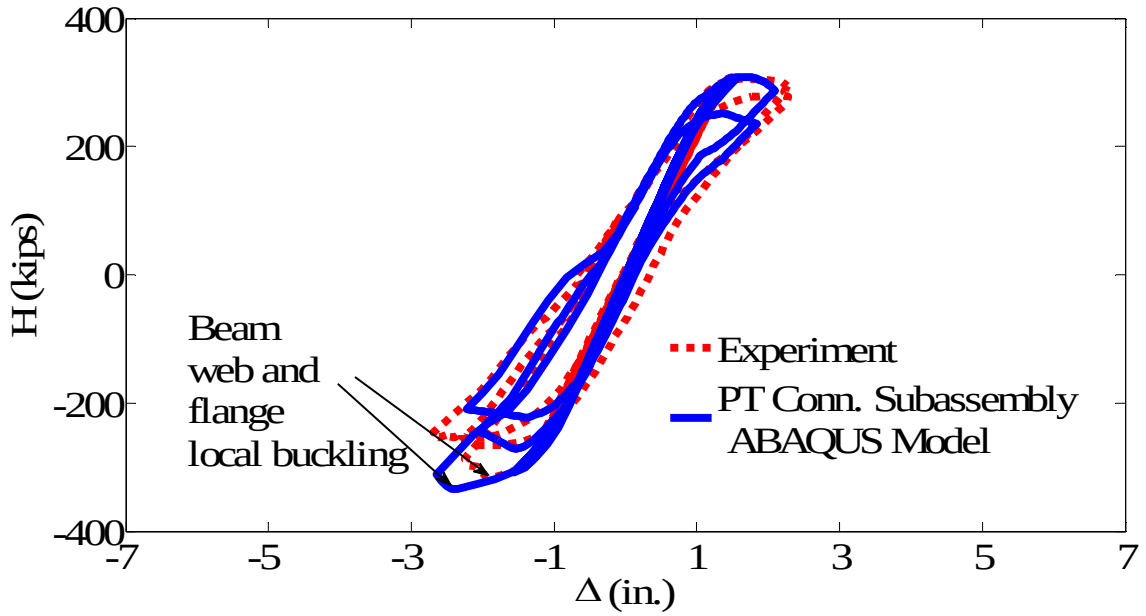

Figure 5. 14. Comparison of test results with analytical results for applied force-top column displacement (H-Δ), Test Specimen 36s-30, Model-B.

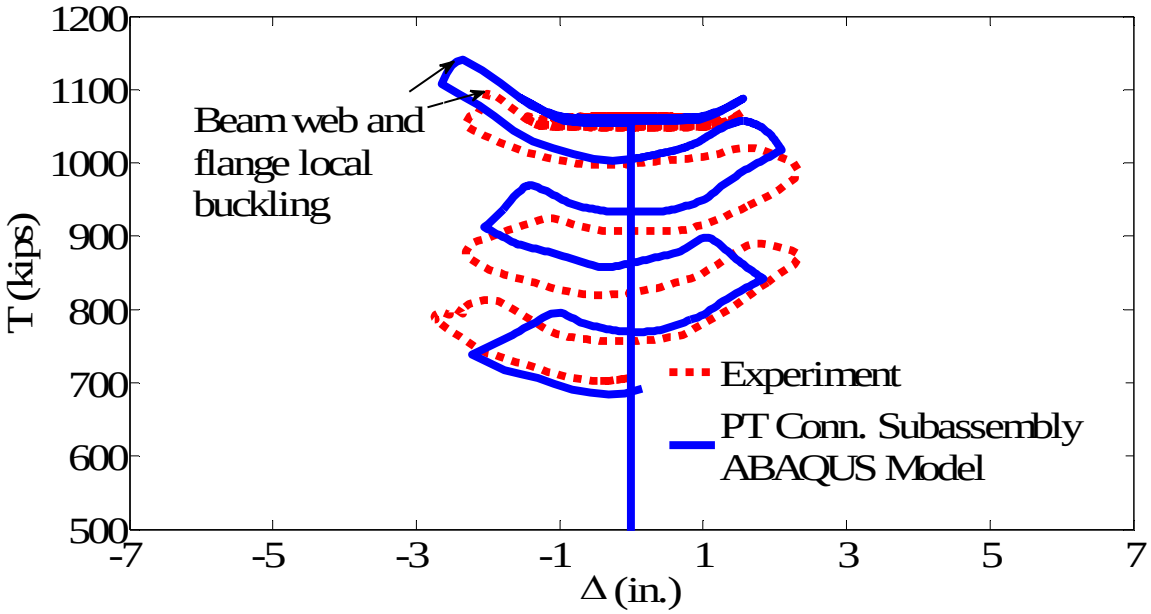

Figure 5. 15. Comparison of test results with analytical results for total PT strand force-top column displacement (T-Δ), for Test Specimen 36s-30, Model-B.

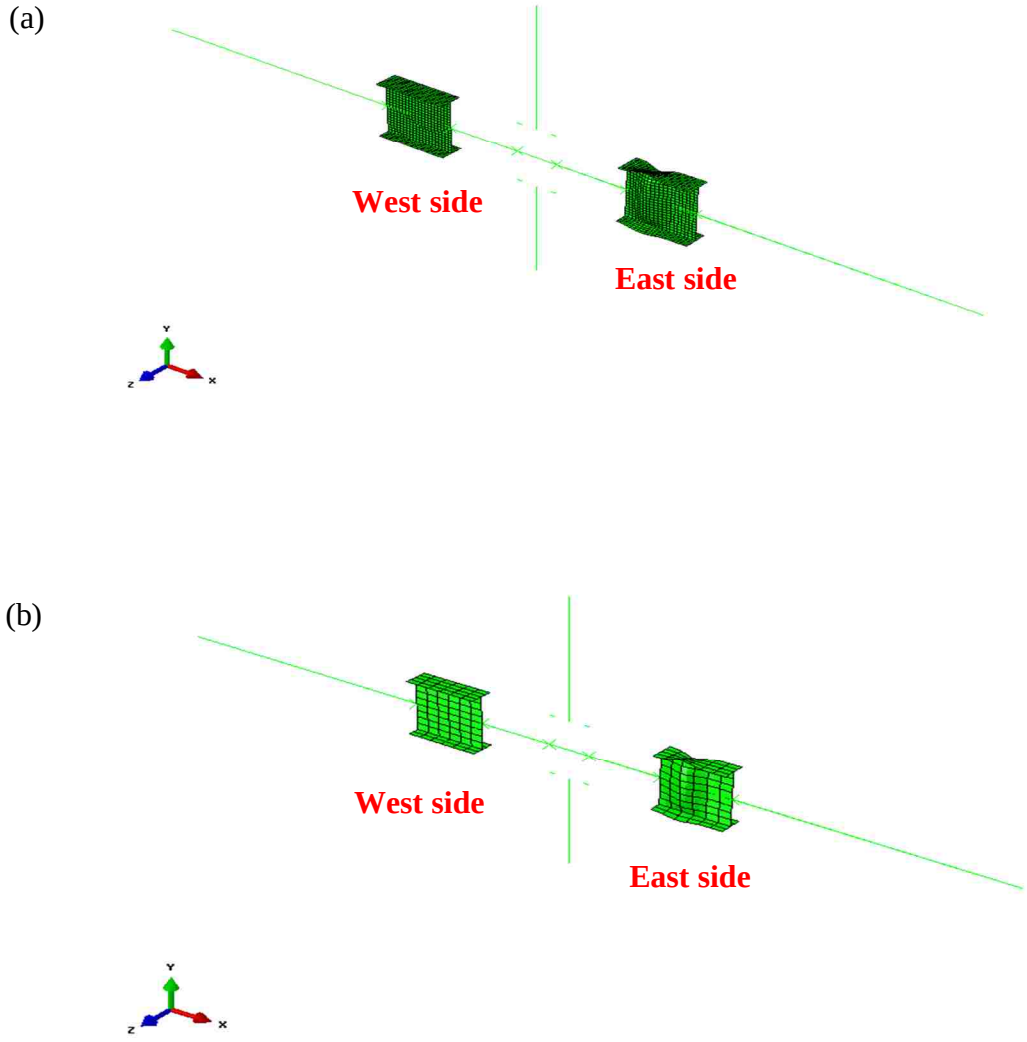

Figure 5. 16. Schematic of model deformation: (a) simplified model with fine mesh (Model-C), (b) simplified model with coarse mesh (Model-D), Test Specimen 36s-30.

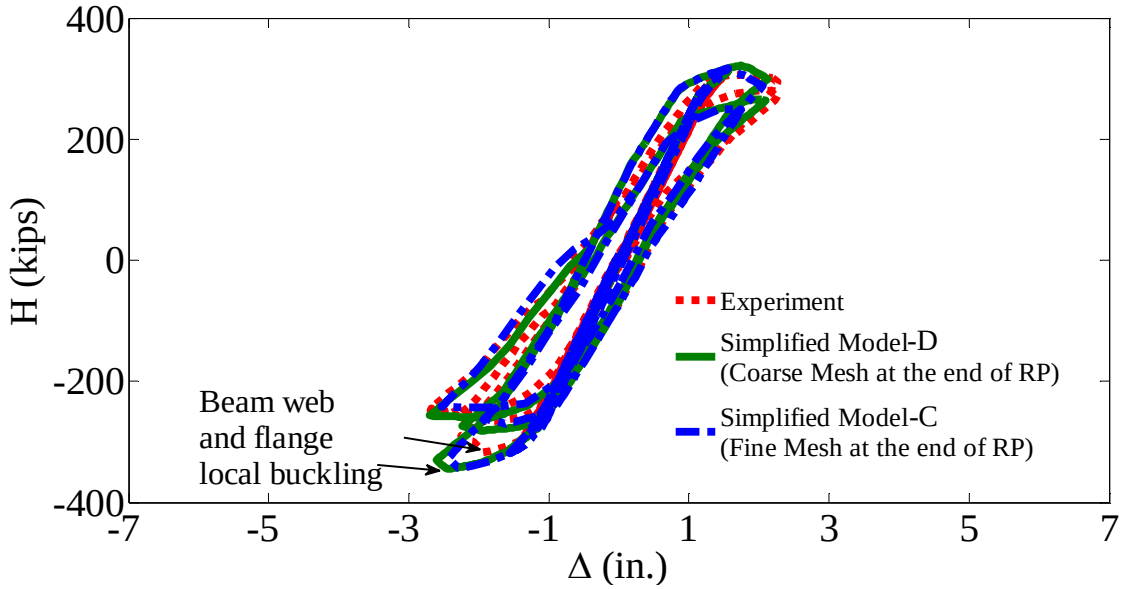

Figure 5. 17. Comparison of test results with analytical results for applied force-top column displacement (H-Δ), for Test Specimen 36s-30, Model-C and Model-D.

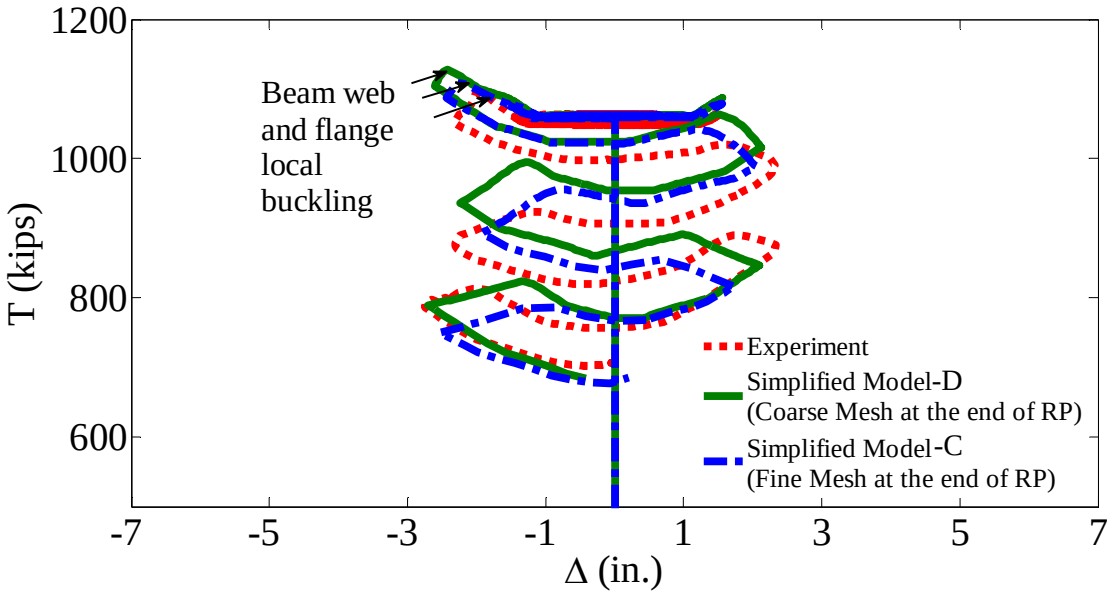

Figure 5. 18. Comparison of test results with analytical results for total PT strand force-top column displacement (T-Δ), Test Specimen 36s-30, Model-C and Model-D.

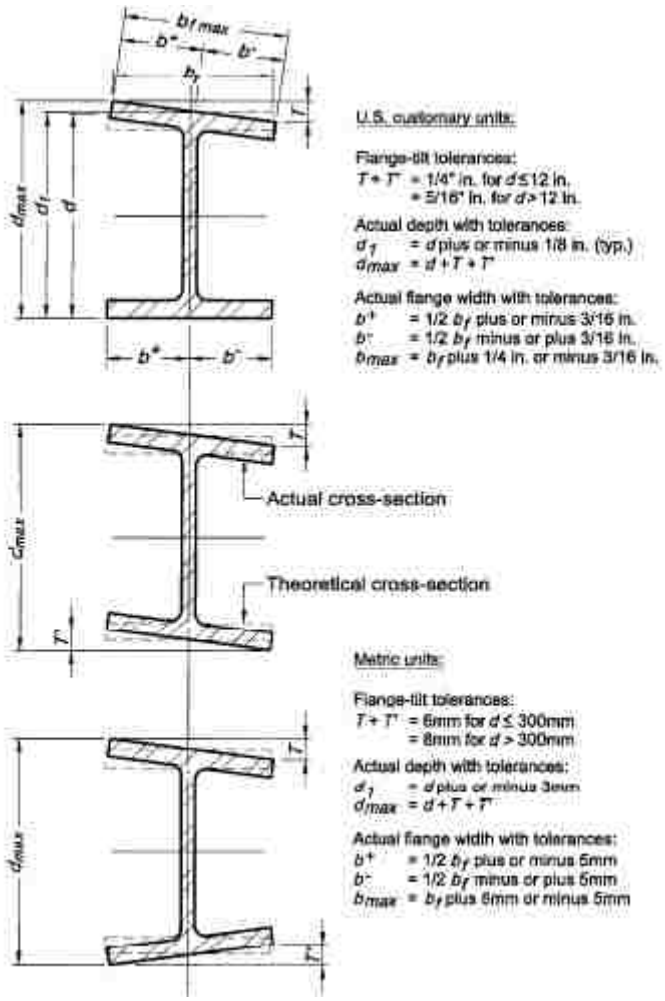

Figure 5. 19. Mill tolerances for beam flanges.

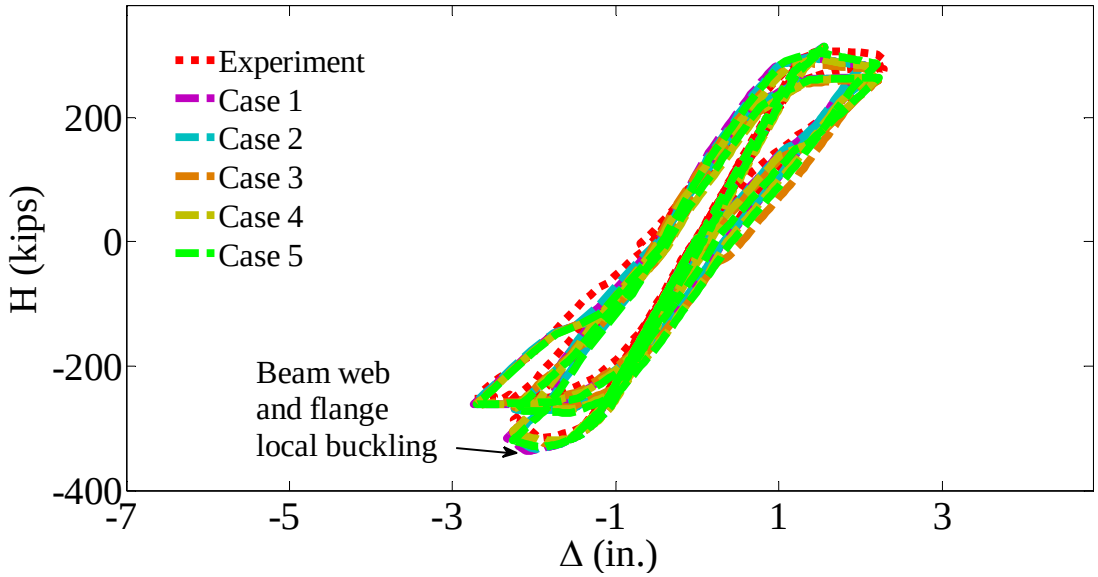

Figure 5. 20. Initial imperfection sensitivity analyses, comparison of test results with analytical results for applied force-top column displacement (H-Δ), Test Specimen 36s-30, Model-D.

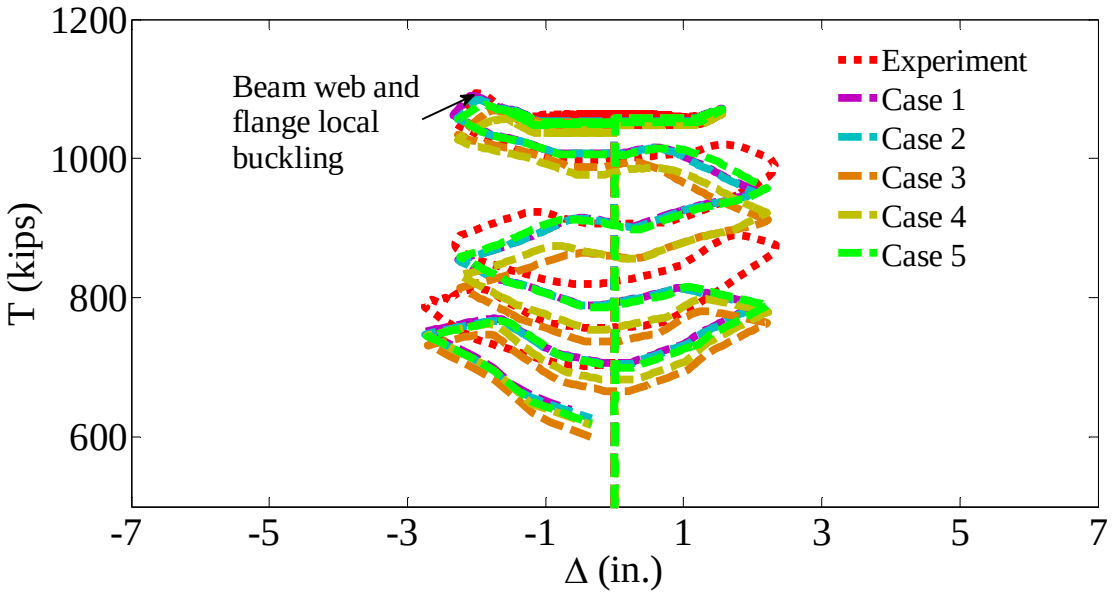

Figure 5. 21. Initial imperfection sensitivity analyses, comparison of test results with analytical results for total PT strand force-top column displacement (T-Δ), Test Specimen 36s-30, Model-D.

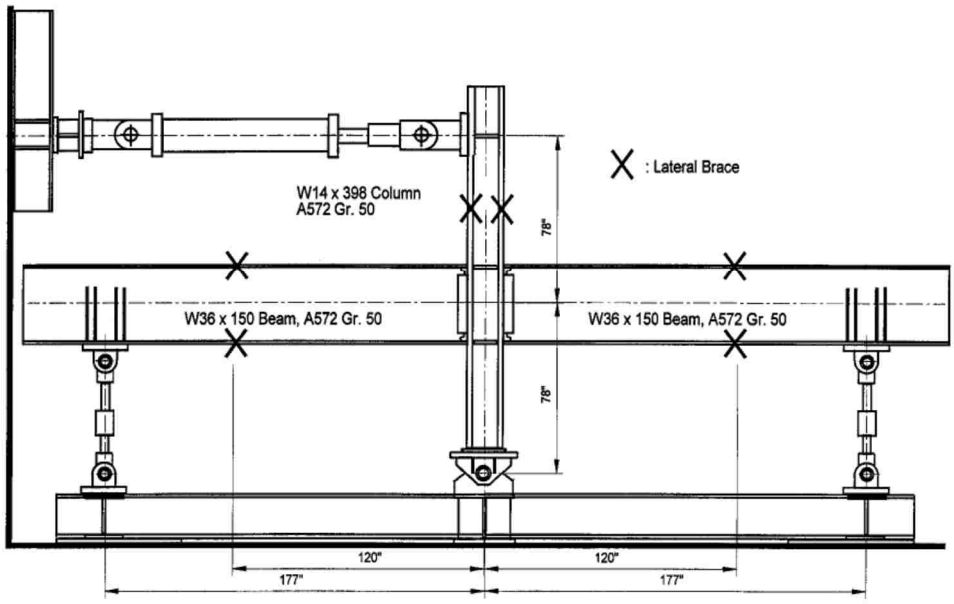

Figure 5. 22. Schematic of test-setup of rigid beam-to-column moment connection subassembly (Ricles et al (2000)).

(a)

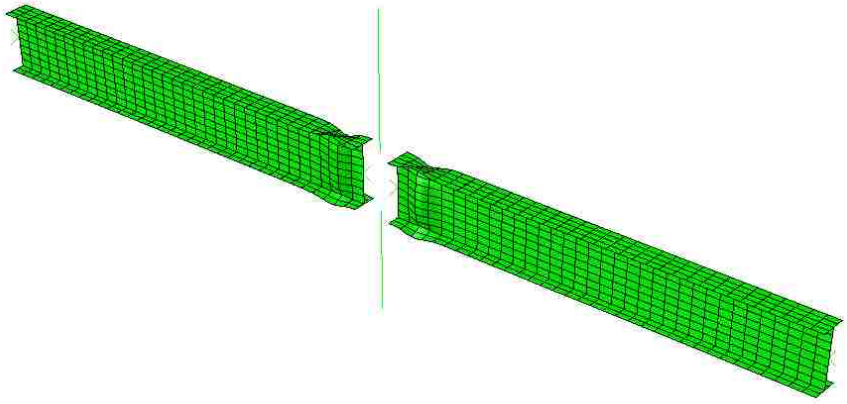

(b)

Figure 5. 23. Schematic of model deformation of: (a) finite element local buckling model in comparison with (b) experimental response (Ricles et al (2000)) for rigid beam-to-column moment connection subassembly, Detailed-model.

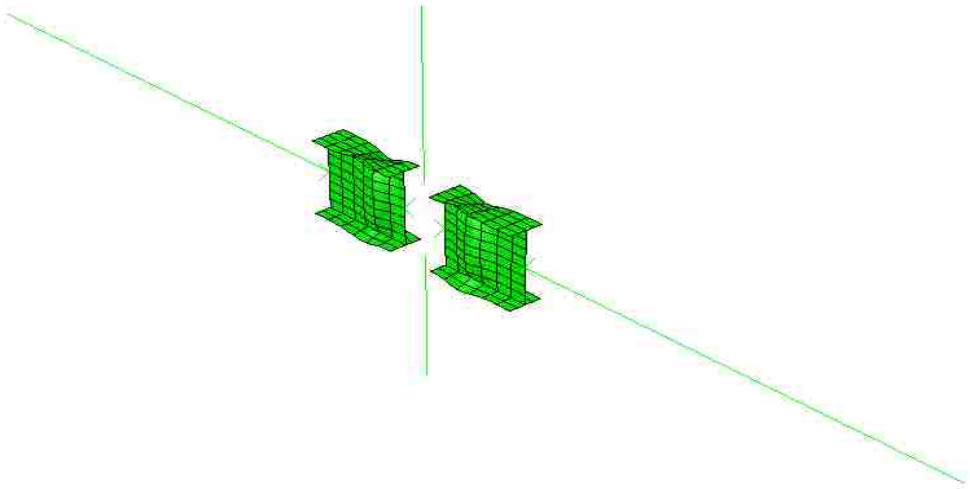

Figure 5. 24. Schematic of model deformation for rigid beam-to-column moment connection subassembly, Simplified-model.

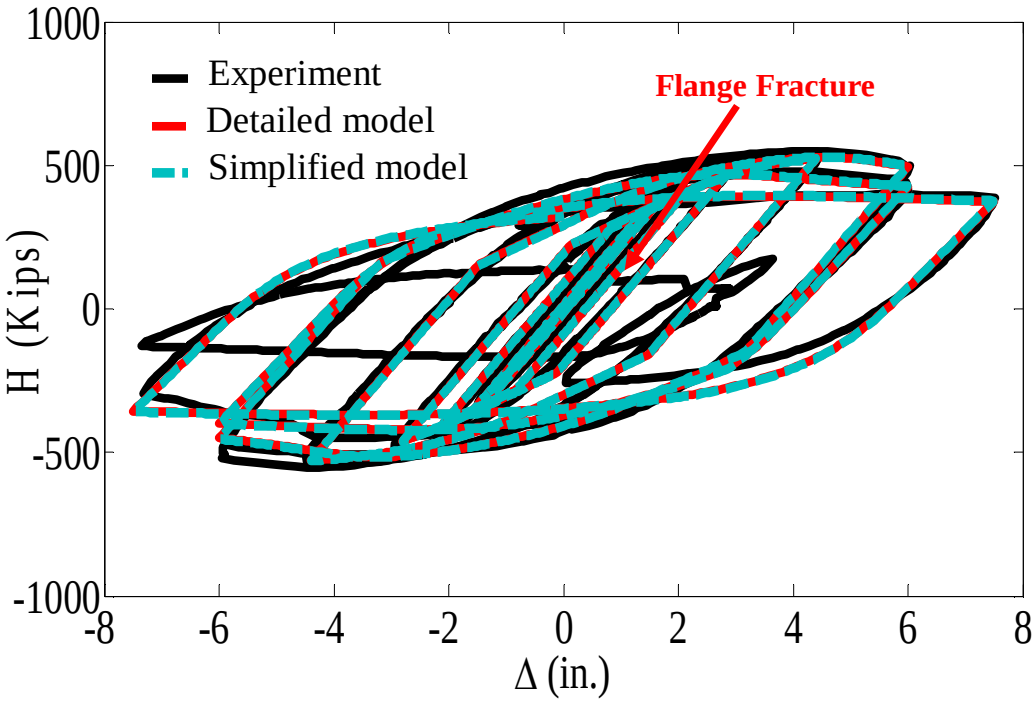

Figure 5. 25. Comparison of Top column applied force-top column displacement (H-Δ) for rigid beam-to-column connection subassembly, Detailed and Simplified models.

Chapter 6

Frame Model

6.1. General

The prototype buildings were described in Chapter 4. The connection finite element modeling and calibration were presented in Chapter 5. The development of the frame models used to investigate the seismic collapse resistance of an SC steel frame system and a conventional steel frame are presented in this chapter. The frame model and the elements used in this frame model are described. The experimental results of a test frame studied by Lin (2012) are compared with the predictions of the model developed in ABAQUS.

6.2. SC-MRF Model

A finite element model is developed for the study of two SC-MRF designs (Designs 1 and 2). It consists of stress-resultant and continuum shell elements in order to model the complete structural system while capturing the important limit states that can occur during an extreme earthquake. Theses limit states were discussed in Chapter 5 and include: gap opening at the beam column interface; yielding of PT strands; yielding and inelastic deformations in the members (beams, columns, panel zones); second order (P-delta) effects due to gravity loads imposed on the gravity load frames; and beam flanges and web local buckling at the end of the reinforcing plates.

As stated in Chapter 4, the prototype building was designed using the PBD procedure by Lin (2012) and denoted as Design 1. The building is a 7x7-bay office building with

four stories above ground and a one-story basement below ground (see Figure 4.1). Each side of the building perimeter contains two 2-bay SC-MRFs as shown in Figure 4.1. The floor diaphragm at each level is attached to only one bay in order to develop gap opening at the beam-to-column SC connections (see Figure 4.2(a) and (b)). The building has a symmetric floor plan (see Figure 4.1(a)) in both directions. Therefore, one of the perimeter SC-MRFs is studied under unidirectional ground motions. A lean-on column is included in the model to account for the P-Δ effects from the vertical loads on the interior gravity columns of the gravity frames of the building that are within the tributary seismic mass of the one perimeter SC-MRF. The seismic mass is determined based on one-quarter of the total floor plan area (i.e., tributary area). The cross-section area and flexural stiffness of the lean-on column is based on the summation of the areas and flexural stiffness of the gravity columns in the tributary area (i.e., one quarter of the total floor plan area). Table 6.1 summarizes the seismic mass at each floor level. The lean-on column nodes at each floor level, where the lumped seismic masses from the tributary area are located, are connected with the beam of only one bay at each floor level of the SC-MRF by multi-point constraints (i.e., equal degrees of freedom) in the horizontal direction (Figure 6.1) in order to develop gap opening and closing at the beam-to-column SC connections under dynamic loading. The beam and column member sizes and other characteristics of the SC-MRFs (Design 1 and 2) were summarized in Tables 4.7 and 4.8. The results and conclusions of the verification studies performed for a SC connection subassembly (see Chapter 5) are used to develop the SC-MRFs herein.

6.2.1. Continuum Elements

As discussed in Chapter 5, in order to develop a computational efficient model, the

continuum shell elements are used only at the end of the reinforcing plates. The Shell elements are utilized for a length of one beam depth, d_b, where the beam local buckling is expected to occur in the SC-MRFs (see Figure 6.2 (a) and (b)). In Figure 6.2, L_{rp} indicates the reinforcing plate length as presented in Table 4.8 for the SC-MRF Designs 1 and 2. Similar to the elements used for the connection subassembly model in Chapter 5, the 8-node shell element, S8R, available in the ABAQUS element library with five section integration points through the thickness (Simpson's rule) is utilized. Each node has 6 degrees of freedom. As studied in Chapter 5, the simplified model with the coarse mesh was capable of predicting the experimental results for the SC connection subassembly while providing a computational efficient model with using 96 shell elements at the end of reinforcing plates. Thus, the shell elements with a coarse mesh are used for modeling the SC-MRFs to capture the beam local buckling at the end of reinforcing plates (see Figure 6.3). Initial imperfection is imposed on the shell elements to initiate any local buckling in the beams. In order to impose the initial imperfection, the buckling mode shapes are scaled where the continuum elements are assumed to be under pure compression in order to find the buckling mode shapes. The values of 50% of the web thickness for the beam web out-of-flatness and 50% of the mill tolerances for the beam flanges out-of-flatness are selected as the maximum imposed imperfection on the shell elements per sensitivity analyses performed in Chapter 5. The steel material is modeled by considering nonlinear combined kinematic-isotropic hardening to account for cyclic behavior of steel material, calibrated with the test data from Kaufmann (2001), as presented in Chapter 5. The material properties are used in the model's stress-strain relationship of a yield stress of 52.5 ksi and 60.1 ksi for the beam flanges and the beam

web, respectively. The corresponding thickness and the material properties are assigned to the shell elements where they are used to model the beam flanges and the beam webs in the SC-MRFs.

6.2.2. Stress-Resultant Elements

The procedure discussed in Chapter 5 was used to develop the frame models using stress-resultant elements for other portions of the beams and the columns (see Figure 6.2(b)). The stress-resultant Timoshenko beam-column element (B32OS element) available in the ABAQUS element library is used. The Timoshenko beam-column elements account for the transverse shear deformation. A multi-point constraint boundary condition is used to model the plane sections remaining plane at the interface between the shell elements and a stress-resultant element where used for the modeling in the beams. The material properties cannot be defined separately for the flanges and the web of the beams and columns in a stress-resultant element. Hence, the flange material properties are used for the stress-resultant elements to obtain a more reasonable flexural capacity, which is dominated by the stresses developed in the flanges in actual wide flange sections.

6.2.3. Truss and Gap Elements

Similar to the procedure presented in Chapter 5, the PT strands are modeled using inelastic truss elements (T3D2 element) available in the ABAQUS element library. In the model the strands are lumped together to form one strand at the location of the force resultant of the group of strands which passes through the mid-depth of the beam cross section. The cross-sectional area assigned to the truss element is based on all of the PT

strands at each floor level. The number of PT strands were summarized in Table 4.8 for the SC-MRFs (Design 1 and 2). The strand material is modeled by using bi-linear stress-strain relation with kinematic hardening to account for cyclic behavior, where the tensile yield stress of 243 ksi was used. A strain hardening slope of 0.03E was used, where E=27600 ksi is the Young's Modulus of the strand. The material is assigned to the truss elements. The amount of strain in the PT strands is calculated to produce the target initial PT force, T_0, at each floor summarized in Table 4.7. A larger than the calculated strain is imposed to the PT strand elements as an initial condition to accommodate the PT force loss due to frame bay shortening. Static analysis is performed and the initial strain is transformed to the internal force in the elements to satisfy an internal equilibrium.

As presented in Chapter 5, there is a need for elements which are able to transfer only compressive forces at the beam column interface. Compression-only gap element (GAPUNI element) available in the ABAQUS element library is used to transfer the compressive force between the nodes at the beam column interface as shown in Figure 6.2(c). Figure 6.2(c) shows the SC-WFD connection model detail used in the SC-MRFs. These gap elements consider the contact flexibility at the beam column interface as illustrated by Lin (2012). In order to allow the compressive deformation at the contact regions in the analytical model, the calibrated compressive stiffness of the contact elements in the analytical model is assigned. The axial compressive stiffness of the gap elements in the analytical model is found by trial and errors in order to predict the experimental responses from the test frame by Lin (2012).The test frame and the results are presented later. The axial stiffness of 8000 kips/in was used for the compression-only gap elements at 1st and 2nd floors. The axial stiffness of 4000 kips/in was used for the

compression-only gap elements at the 3rd and 4th floors. A schematic of the frame model in ABAQUS is presented later.

6.2.4. Panel Zones and Friction Devices

A kinematic based panel zone model is used in the SC-MRFs as described in Chapter 5. The rotational spring is modeled with element type CONN3D2 in the ABAQUS element library located between two center nodes shown in the panel zone model (see Figure 6.2(c)). Equations (5.1) through (5.5) are used to determine the panel zone rotational spring moment-flexibility relation at each floor level of the SC-MRF.

The friction device provides the friction force components after gap opening occurs. The Friction force F_f is computed from Equations (2.7) and (2.2) for a known β_E and T_0 presented in Table 4.7 at each floor level for the SC-MRF. The friction device (FD) is modeled with two perpendicular rigid plastic spring elements (see Figure 6.2(c)), located between the two nodes close to each other where the FDs are attached to the beam web, modeling the friction force components after gap opening occurs. As shown in Figure 6.2(c) and where the FD is located between the two nodes, one of these nodes is slaved to the node located on the column face and the other node is one of the beam nodes. By connecting these two nodes with the friction device element composed of two perpendicular rigid plastic spring elements as shown in Figure 6.2(c), the friction force F_f is produced where a moment develops at the beam column interface and gap opening occurs under cyclic loading (see Figure 2.10(c)). Table 6.2 summarizes the spring forces developed in the rigid plastic springs used to model the friction devices when gap opening occurs.

6.2.5. Dynamic Analysis

The implicit dynamic method with the Hilber-Hughes-Taylor direct integration algorithm is utilized to perform dynamic analyses in ABAQUS with parameter $\alpha = -1/3$ which provides the maximum numerical damping and improves the solution convergence under extreme seismic loading. The modified Newton method with a line search algorithm is used to solve the nonlinear equations. The line search algorithm improves the robustness of the Newton method and the efficiency of the solution. The time increments should not be larger than ground motion time steps. The automatic time incrimination is used in ABAQUS in order to control adjustments to the time increment size for the implicit dynamic procedure based on convergence behavior of the Newton iterations and the accuracy of the time integration. The time step is allowed to be reduced up to 10^{-15} sec. since severe nonlinearities and local buckling develop in the model.

The model uses mass combined with stiffness non-proportional damping to introduce the inherent damping into the analytical model. The damping model is used where the initially damping ratios of 2% in the first mode and 5% in the third mode are used in the analytical model in order to determine the proportional mass and stiffness damping coefficients. The first and the third mode shape periods are 1.64 sec. and 0.3 sec., respectively, from an eigenvalue analysis of the analytical model. However, due to the fact that the system will soften due to nonlinear behavior under extreme loading, the damping model may introduce unreasonably large damping forces in elements with inelastic deformation by using the initial stiffness. In order to avoid developing unreasonable damping force during nonlinear response, zero damping is used for the gap elements and the elements which undergo significant yielding under extreme earthquake

loading. Thus, in regions where nonlinear response is expected in the model only mass proportional damping is used. Geometric nonlinearity is taken into account by formulating equilibrium in the current configuration using the Lagrangian formulation and current nodal positions.

Figure 6.3 shows a schematic of the computational efficient ABAQUS frame model as described above for the seismic collapse resistance evaluation of the SC-MRF. As shown in Figure 6.3 and stated previously, the lean-on column nodes, where the lumped seismic masses are located, are connected with the beams of only one bay at each floor level of the frame by multi-point constraints in the horizontal direction. The subsequent chapters present the results of extensive dynamic analyses performed using this model.

6.3. SMRF Model

The conventional steel frame presented in Chapter 4 does not include reinforcing plates. Thus, the beams are modeled with continuum elements from the face of the column for a length of one beam depth where local buckling is expected to happen. Similar to the SC-MRF, the initial imperfection is imposed to initiate any beam local buckling in the beams under severe dynamic loading. The buckling mode shapes are scaled for imperfections where the continuum elements are assumed to be under pure compression in order to find the buckling mode shapes. The values of 50% of the web thickness for the beam web out-of-flatness and 50% of the mill tolerances for the beam flanges out-of-flatness are selected as the maximum imposed imperfection on the shell elements, similar to the SC-MRF. Figure 6.4 shows a schematic of the SMRF ABAQUS model. The modeling details and elements are similar to the SC-MRF except the gap elements, truss elements and WFD elements are used for an SMRF modeling. The rigid

floor diaphragm at each floor level is attached to both bays of the perimeter SMRFs in the prototype building. Thus, the lean-on column nodes, where the lumped seismic masses are located, are connected with the beams of both bays at each floor level of the frame by multi-point constraints (i.e., equal degrees of freedom) in the horizontal direction as shown in Figure 6.4.

6.4. Validation of SC-MRF Modeling Procedure

Lin (2012) performed an experimental study using a 0.6-scale SC-MRF. Figure 6.5 shows the test frame dimensions and member sizes. The test frame was designed by the PBD procedure presented in Chapter 3. As a result, beam local buckling was not observed under the MCE dynamic loading.

For validation of the SC-MRF modeling procedure the model predictions are compared with the test results. The test structure is modeled using the procedure described. The results are presented for the DBE and MCE intensity levels. The results are compared for the south bay, the south and north beam-to-column connections, denoted as SS and SN, respectively. The north-bay and the north direction are identified in Figure 6.5. Floor displacement time histories, total PT force time histories, total PT force vs. connection rotation and connection moment vs. connection rotation are shown in Figures 6.6 to 6.13 for the DBE and MCE levels. The ABAQUS model results are compared with the experimental data by Lin (2012). As seen, the ABAQUS model results match the experimental data well under the DBE and MCE level. The beam local buckling did not occur in the test frame, however this limit sate and its effects on the building were validated using connection subassembly test results compared to the

analytical model response predictions in Chapter 5. The ABAQUS model is utilized in subsequent chapters to investigate the seismic collapse resistance of the frames.

Table 6. 1. Seismic mass at each floor level for SC-MRF and SMRF prototype frames.

Floor	Seismic Mass (kip. sec^2/in)
Roof	1.92
3rd	3.13
2nd	3.13
1st	3.19

Table 6. 2. Spring forces developed in rigid plastic spring elements to model friction force components in web friction devices.

Floor	Spring Force (kips)	
	Horizontal Component	Vertical Component
Roof	48	73
3rd	80	150
2nd	80	150
1st	80	150

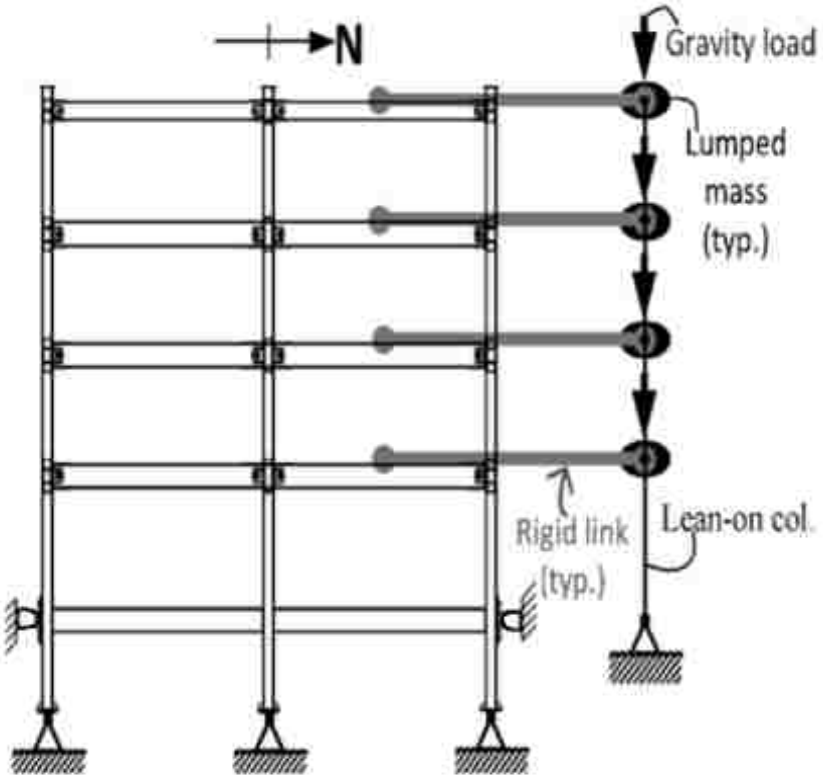

Figure 6. 1. Schematic of SC-MRF and gravity frame model.

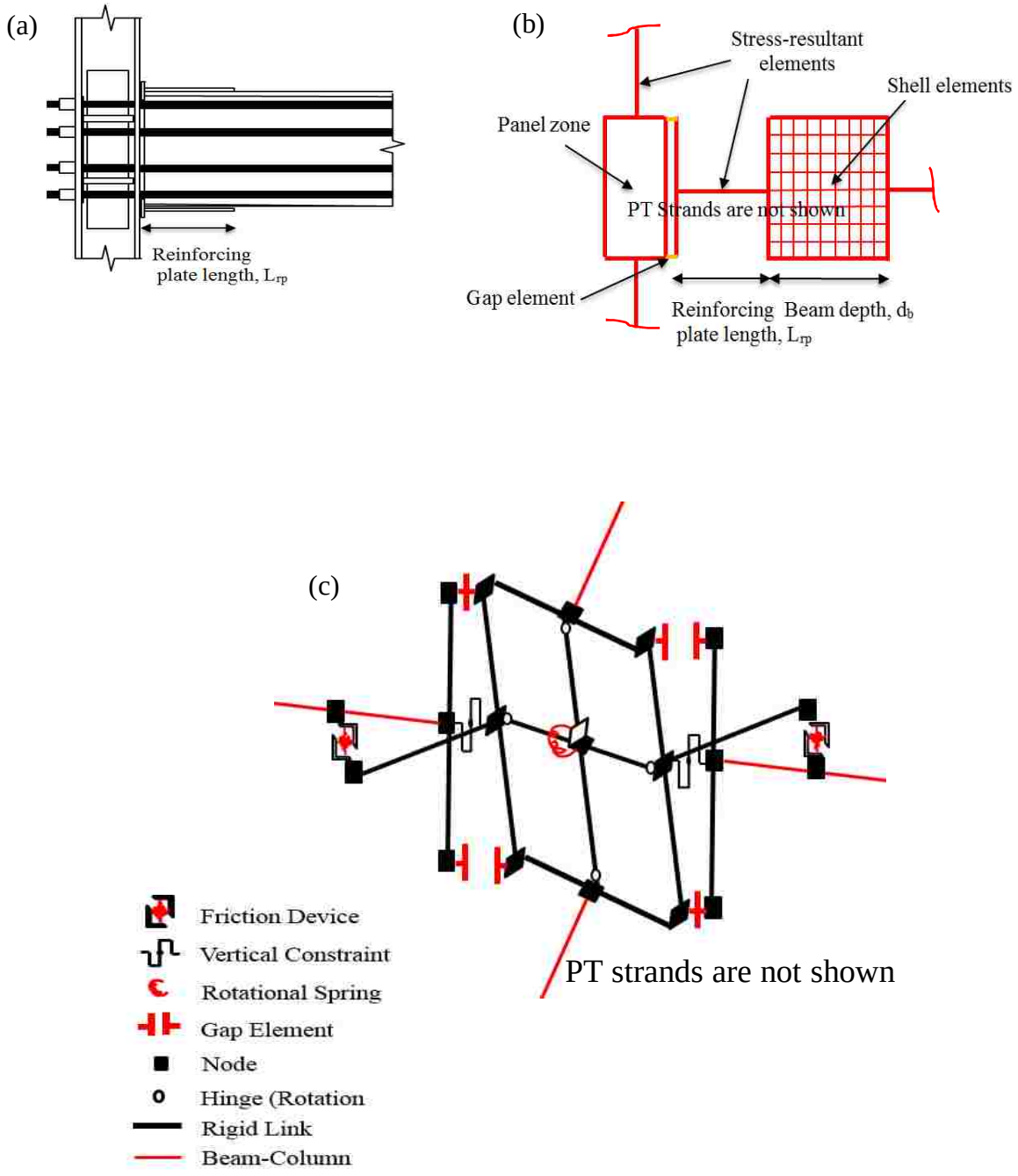

Figure 6. 2. (a) Schematic of SC-WFD connection; (b) model of SC connection using shell elements at the end of reinforcing plate length; (c) model details of SC-WFD connection.

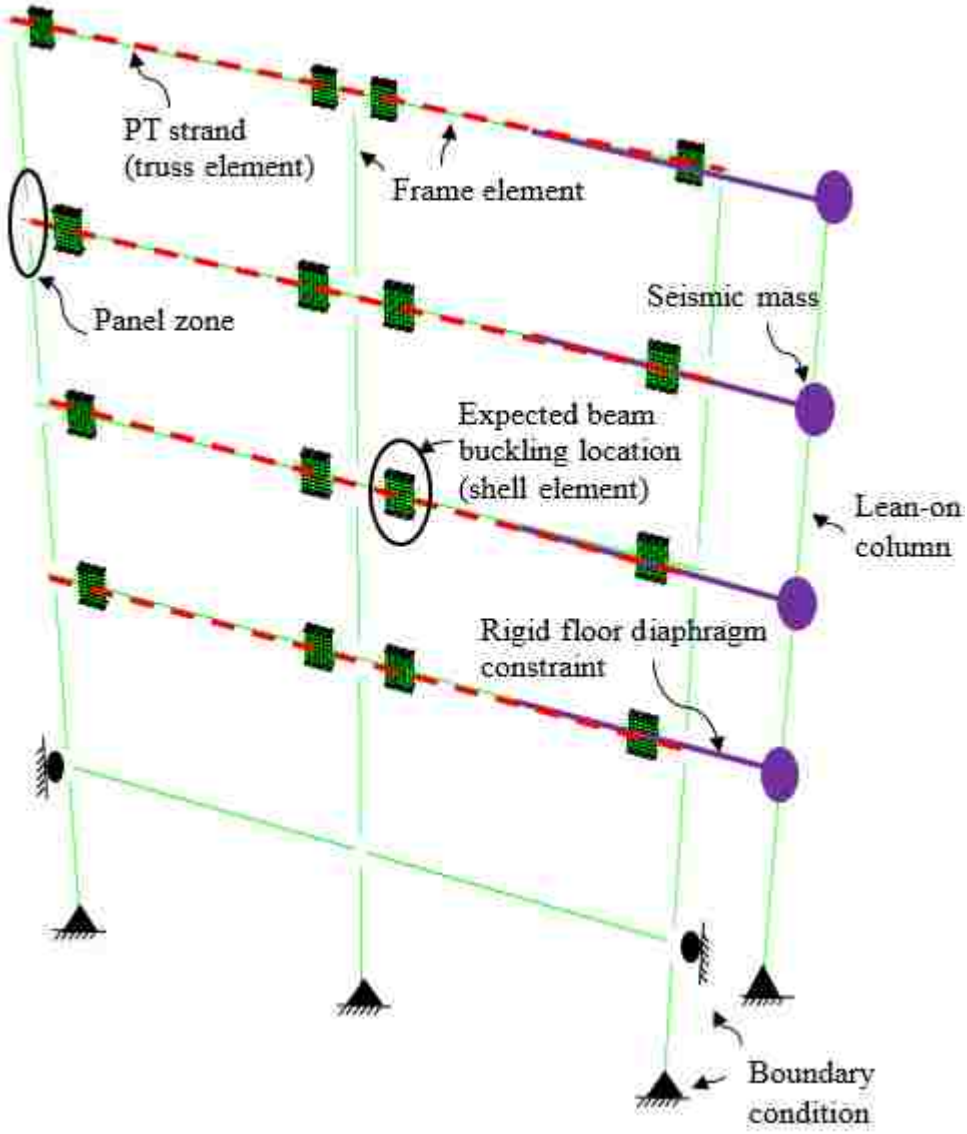

Figure 6. 3. Schematic of SC-MRF ABAQUS model.

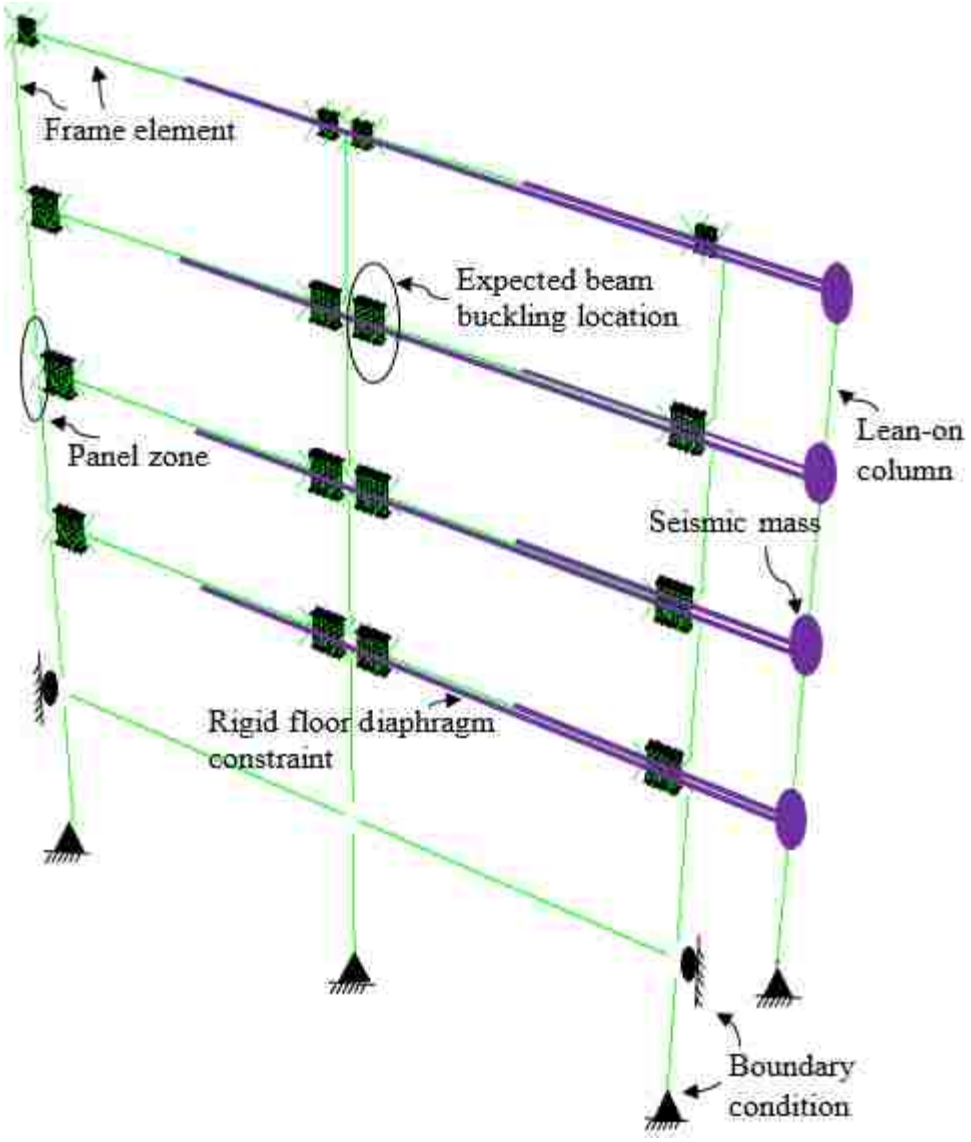

Figure 6. 4. Schematic of SMRF ABAQUS model.

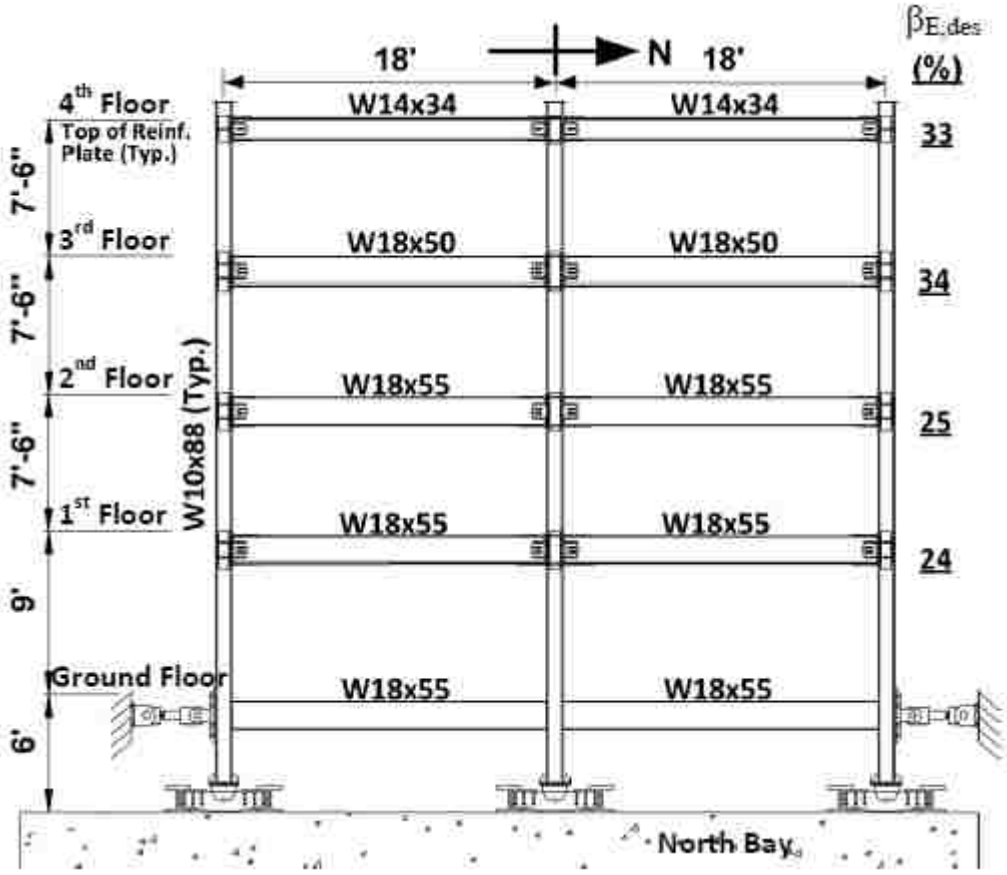

Figure 6. 5. Schematic of tested SC-MRF, Lin (2012).

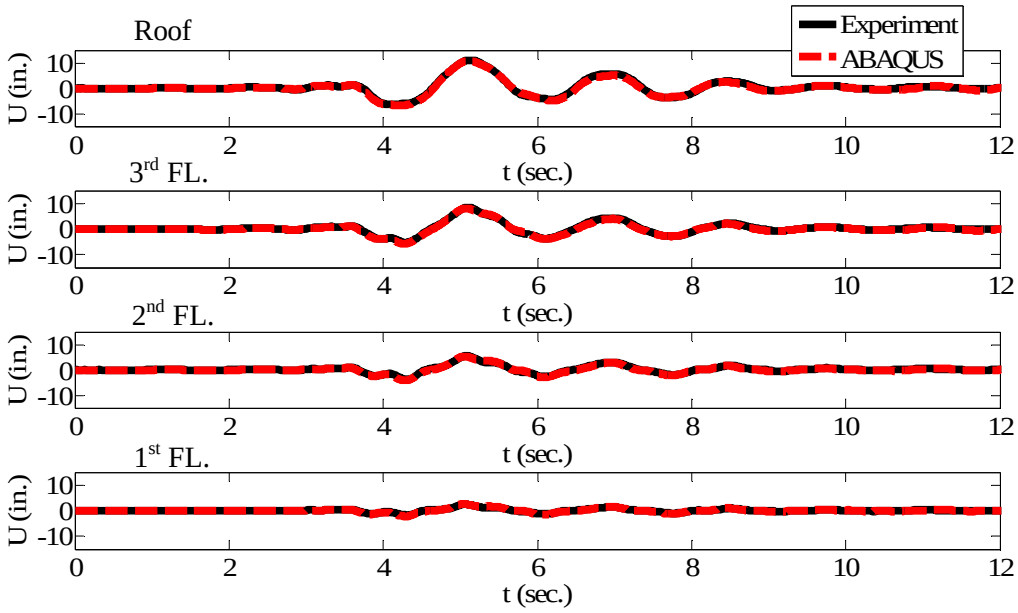

Figure 6. 6. Comparison of floor displacement time history of experimental data with ABAQUS model results under DBE for LOS000 ground motion.

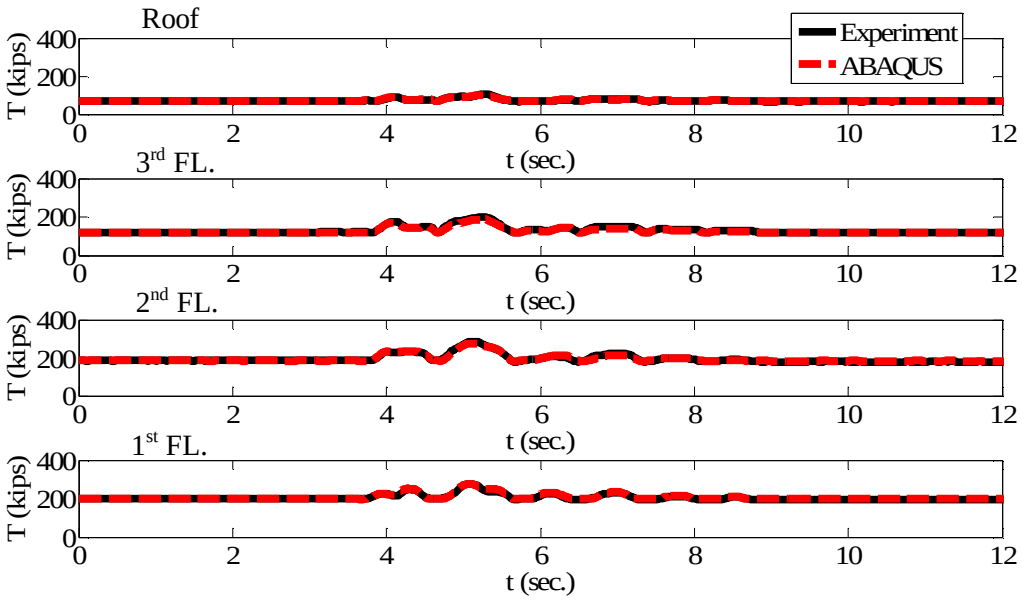

Figure 6. 7. Comparison of total PT force time history of experimental data with ABAQUS model results under DBE for LOS000 ground motion.

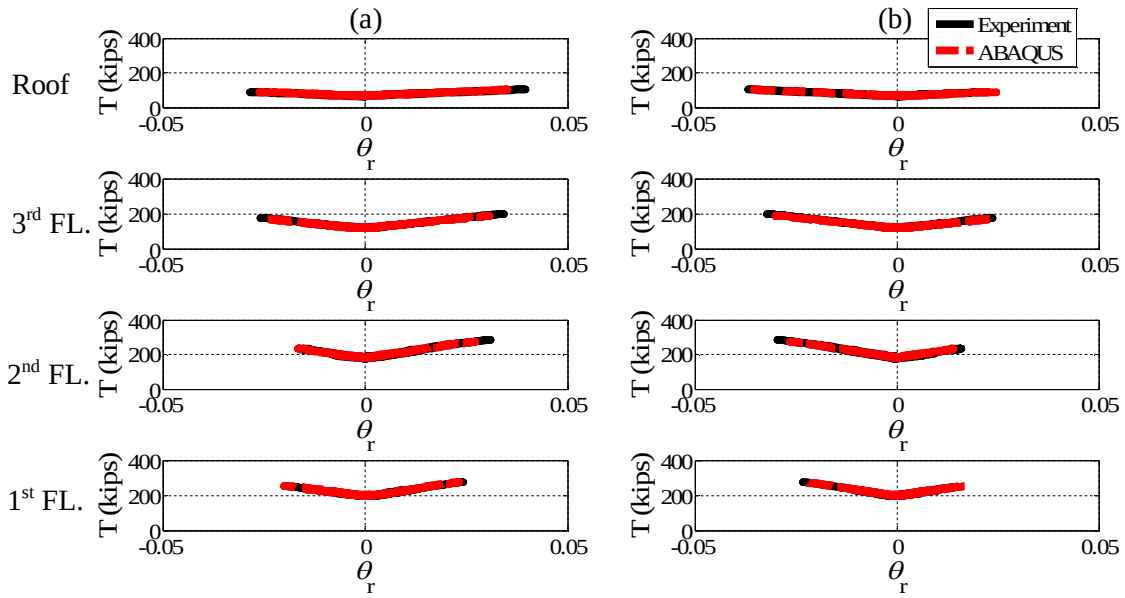

Figure 6. 8. Comparison of total PT force-connection rotation (T-Θ_r) for (a) SS and (b) SN connections of experimental data with ABAQUS model results under DBE for LOS000 ground motion.

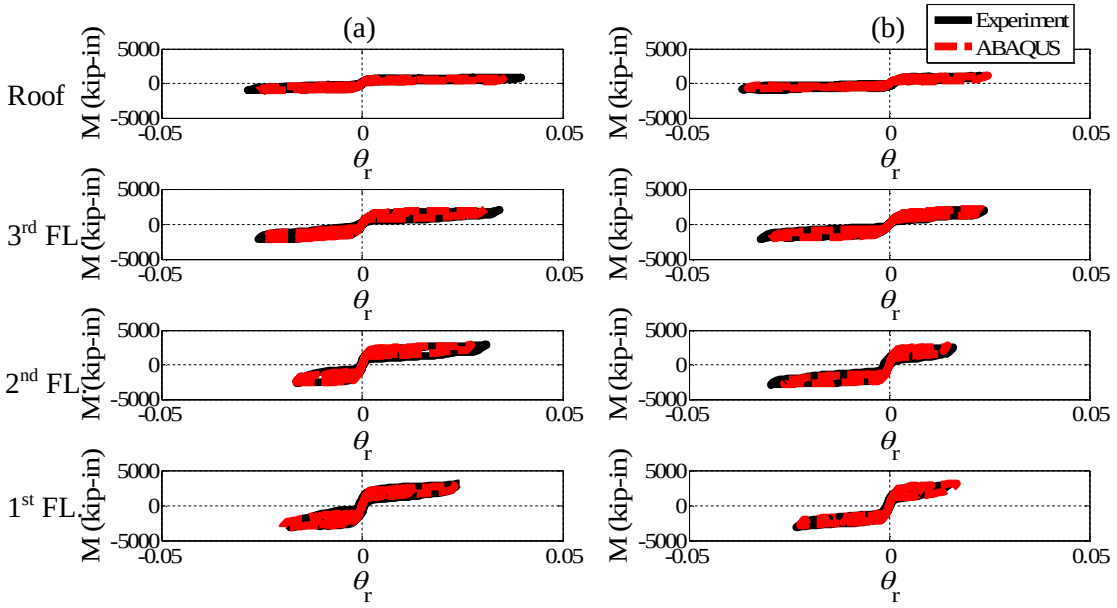

Figure 6. 9. Comparison of connection moment-connection rotation (M-Θ_r) for (a) SS and (b) SN connections of experimental data with ABAQUS model results under DBE for LOS000 ground motion.

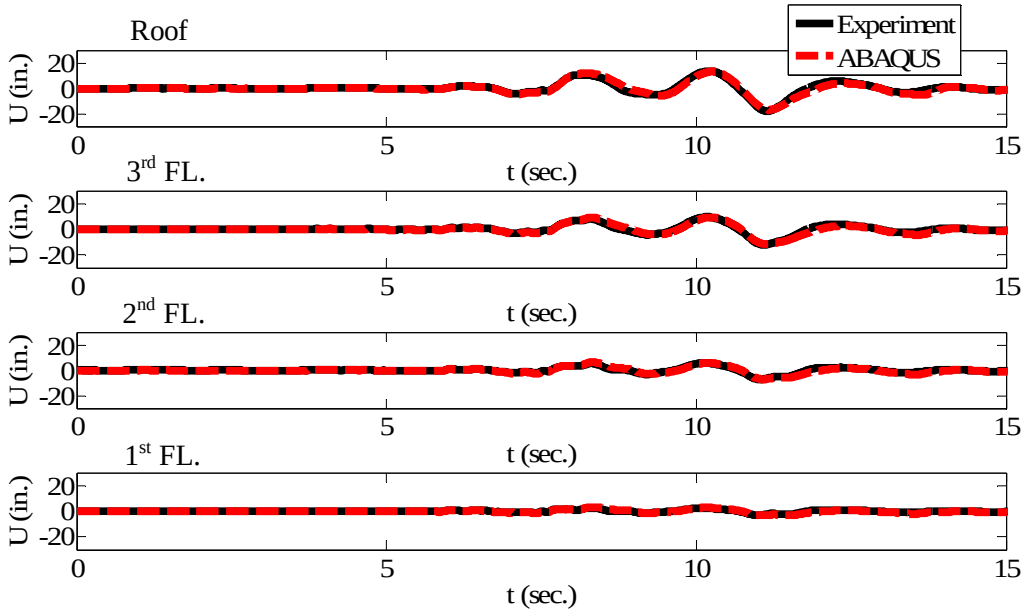

Figure 6. 10. Comparison of floor displacement time history of experimental data with ABAQUS model results under MCE for STM090 ground motion.

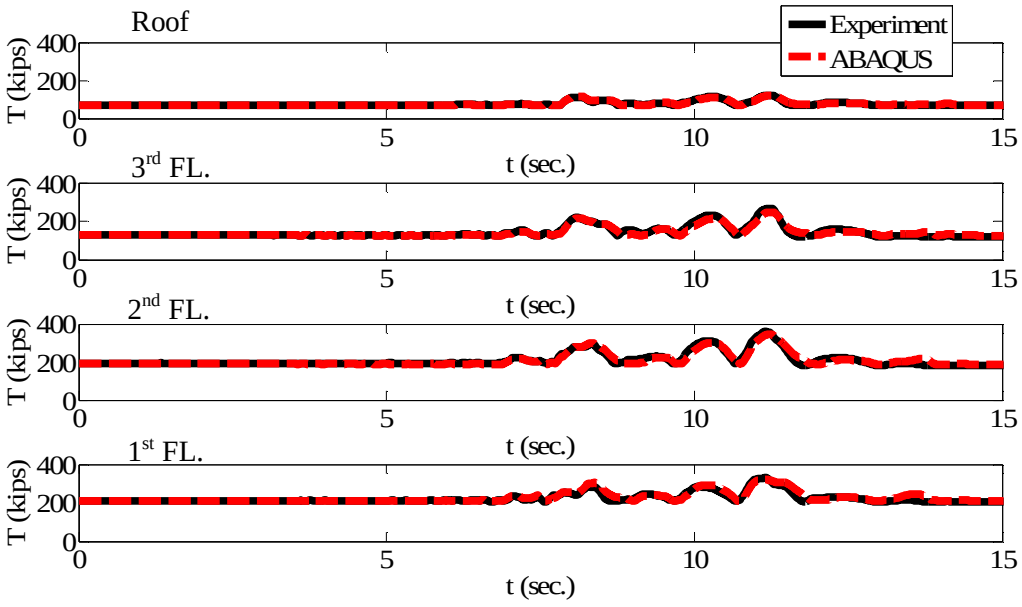

Figure 6. 11. Comparison of total PT force time history of experimental data with ABAQUS model results under MCE for STM090 ground motion.

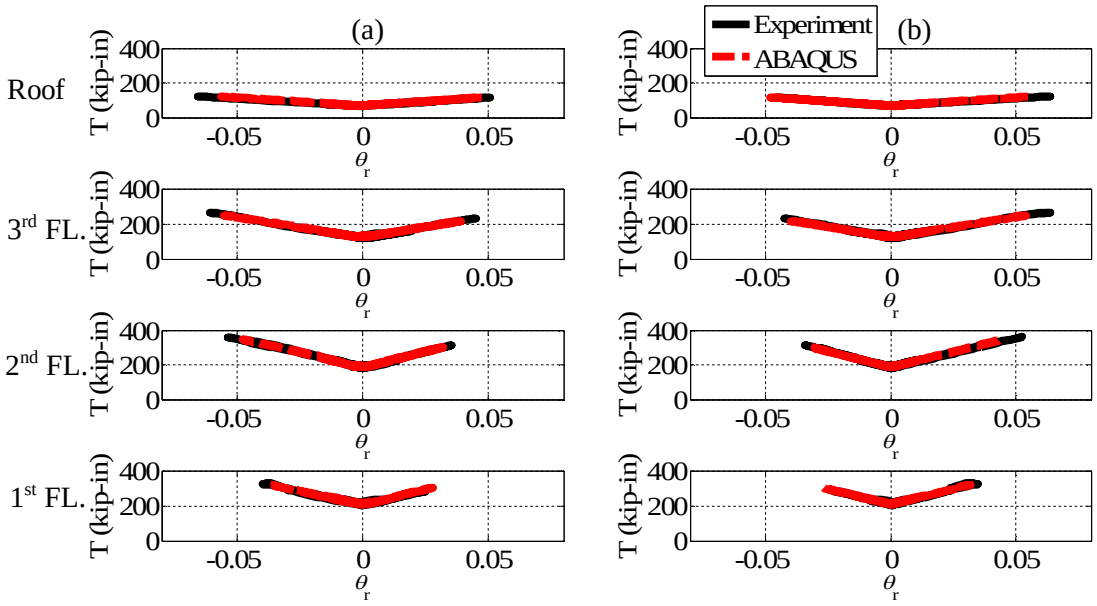

Figure 6. 12. Comparison of total PT force-connection rotation (T-Θ_r) for (a) SS and (b) SN connections of experimental data with ABAQUS model results under MCE for STM090 ground motion.

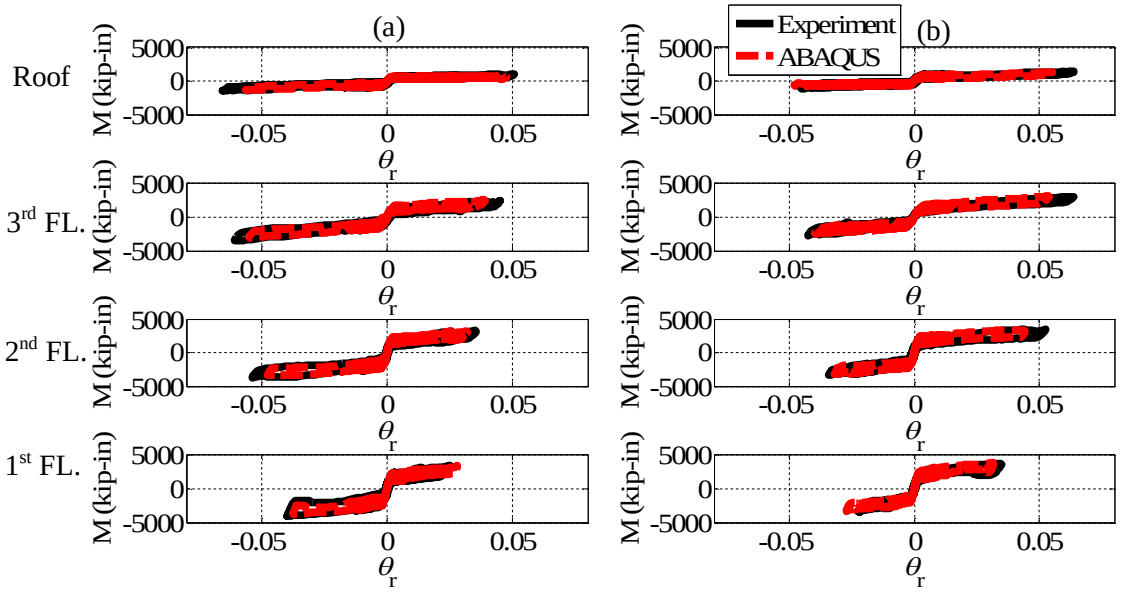

Figure 6. 13. Comparison of connection moment-connection rotation (M-Θ_r) for (a) SS and (b) SN connections of experimental data with ABAQUS model results under MCE for STM090 ground motion.

Chapter 7

Collapse Assessment Background

7.1. General

This chapter describes the collapse assessment methodology presented in FEMA P695 (2009) to provide the basic knowledge for obtaining the results presented in subsequent chapters. The collapse evaluation of a seismic resisting system is mainly presented by a dimensionless ratio named the Collapse Margin Ratio (CMR). In order to obtain the CMR a series of nonlinear dynamic analyses are required, denoted as Incremental Dynamic Analyses (IDA). Ground motions and the scaling method which is a key part of IDA procedure are presented in this chapter. The CMR is related to incipient collapse (referred to herein as the point of collapse) of the system. Different criteria for determining the point of collapse are presented. Finally, the effect of sources of uncertainty are described in order to obtain the probability of collapse for a specific hazard level.

7.2. Collapse Assessment Methodology

The IDA procedure is used to assess the seismic collapse capacity under a set of 22 far-field records, which includes 44 ground motion components from FEMA P695 (see Table 7.1). The far-field ground motion record pairs shown in Table 7.1 are from sites located greater than or equal to 10 km from the fault rupture. The IDA is a parametric analysis method in which individual ground motions are scaled to increasing intensities until the structure reaches incipient collapse. The median collapse is the ground motion intensity in which half of the records in the set cause collapse of an archetype model. The

concept of IDA was proposed by Vamvatsikos and Cornell (2006). As an example, Figure 7.1 shows IDA results for a single structure subjected to a suite of ground motions scaled to increasing intensities. In this figure the collapse prediction is based on lateral dynamic instability, or excessive lateral displacements which is explained later. The collapse data point for each ground motion is the intensity level at which the structure reaches instability. The collapse fragility curves can be defined through a cumulative distribution function (CDF) using the collapse data points obtained from the IDA results. The fragility curve relates the ground motion intensity to the probability of collapse (Ibarra et al. (2002)). The probability of collapse at a given spectral acceleration, $S_T(T_1)$, associated with the fundamental period of structure, T_1, is related to the number of ground motions which cause collapse at that spectral acceleration. The results for $S_T(T_1)$, related to the collapse data points for each ground motion from the IDA, are ranked in ascending order, each being treated as an equally likely outcome. The collapse fragility curve is obtained by fitting a cumulative distribution function (CDF) to the collapse data points, often assuming a lognormal distribution. As an example, Figure 7.2 shows a cumulative distribution plot obtained by fitting a lognormal distribution to the collapse data from Figure 7.1. From the fragility curve the median collapse capacity $\hat{S}_{CT}$ can be determined and is associated with the $S_T(T_1)$ value where half of the ground motions cause the structure to collapse as stated previously. The ratio between $\hat{S}_{CT}$ and the MCE-code specified spectral acceleration intensity, S_{MT}, at the fundamental period of the structure is defined as the collapse margin ratio, CMR:

$$\text{CMR} = \frac{\hat{S}_{CT}}{S_{MT}} \tag{7.1}$$

Note that the fundamental period in FEMA P695 used to obtain the CMR is defined to be the same as the design period, T_1, defined in ASCE 7-10 ($T_1 = C_u T_a$, where C_u and T_a were given in Chapter 3). The seismic design parameters were presented in Chapter 3 in order to obtain S_{MT} in accordance with FEMA P695.

As an example, the CMR is 2.5 in Figure 7.1 where $\hat{S}_{CT}$=2.8g and S_{MT}=1.1g. FEMA P695 also introduces the Adjusted Collapse Margin Ratio (ACMR) to account for the frequency content (spectral shape) of the ground motion record set. The CMR value is modified to obtain an ACMR, where:

$$\text{ACMR} = \text{SSF} \times \text{CMR} \tag{7.2}$$

In Equation (7.2) SSF is the value for the spectral shape factor. One of the parameters needed to calculate SSF is the period-based ductility, μ_T, which is defined as follows:

$$\mu_T = \frac{\delta_u}{\delta_{y,eff}} \tag{7.3}$$

where μ_T is the ratio of ultimate roof displacement δ_u (taken as the roof displacement when a loss of 20% of the base shear capacity is achieved) which is established from the pushover analysis results and $\delta_{y,eff}$ is the effective yield roof displacement. $\delta_{y,eff}$ represents the effective roof displacement for an elastic system loaded to the maximum base shear capacity of the system. The value of $\delta_{y,eff}$ can be found using the following equation per FEMA P695:

$$\delta_{y,eff} = C_0 \frac{V_{max}}{W} \frac{g}{4\pi^2} \left(\max(T_1, T_{1,eigen})\right)^2 \tag{7.4}$$

where C_0 is a modification factor to relate the displacement of an equivalent single degree of freedom system to the roof displacement of the building, determined from the following equation (FEMA P695):

$$C_0 = \phi_{1,r} \frac{\sum_1^N m_x \phi_{1,x}}{\sum_1^N m_x \phi_{1,x}^2} \tag{7.5}$$

where m_x is the mass at level x, and $\phi_{1,x}$ and $\phi_{1,r}$ are the ordinate of the fundamental mode at levels x and roof, respectively; and N is the number of levels. V_{max} is the maximum base shear in Equation (7.4) which is established from the pushover analysis results; W is seismic weight of the building, T_1 is the fundamental design period of the building and $T_{1,eigen}$ is first mode period of the structural model computed using an eigenvalue analysis. Using μ_T, the SSF values can be found from Table 7.2. Acceptable performance per FEMA P695 is defined by the probability of collapse under MCE ground motions to be 10% or less across a performance group. Performance groups reflect major differences in configuration, design gravity and seismic load intensity, structural period and other factors that may significantly affect seismic behavior. In addition, the average value of an adjusted collapse margin ratio (ACMR) needs to exceed $ACMR_{10\%}$ (per FEMA P695) for the performance group, where $ACMR_{10\%}$ is the adjusted collapse margin ratio based on β_{TOT} (described later) and a 10% probability of collapse. Furthermore, for each archetype within a performance group the probability of collapse needs to be 20% or less and the ACMR exceed $ACMR_{20\%}$ (adjusted collapse margin ratio based on β_{TOT} and a 20% probability of collapse. Table 7.3 presents the acceptable ACMR values (i.e., $ACMR_{10\%}$ and $ACMR_{20\%}$) for a system per FEMA P695.

Since only one prototype building is evaluated in this research to investigate the

seismic collapse resistance of an SC-MRF, the main scope is to obtain the margin against collapse for an SC-MRF in contrast to a conventional SMRF. Since one prototype building is studied in this study, the results of this study only show the potential of this system to be accepted in accordance with FEMA P695 considering only one archetype and one performance group.

7.3. Ground Motion Scaling Method

Ground motion records are scaled to represent specific spectral acceleration intensity at the fundamental period T_1 of the structure. In FEMA P695 record scaling involves two steps. First, each individual ground motion component in each record set (i.e., each record set involves two horizontal components) is normalized by a peak ground velocity (PGV) in order to remove unwarranted variability between records due to inherent differences in event magnitude, distance to source, source type and site conditions, without eliminating record to record variability. Normalization is done with respect to the value of the PGV computed in the PEER NGA data base PGV_{PEER} (FEMA P695), which is the geometric mean of PGV of the two horizontal components for each record set. The normalization factor for each record set is defined as the ratio of the median of PGV_{PEER} values of records with respect to the PGV_{PEER} of that record. Then, both horizontal components of the record set are factored by the computed normalization factor. Equations (7.6) and (7.7) define the normalization factor, NM_i, and calculation of the normalized horizontal components for the i^{th} record, respectively:

$$NM_i = \text{Median}(PGV_{PEER,i}) / PGV_{PEER} \tag{7.6}$$

$$NTH_{1,i} = NM_i \, TH_{1,i} \tag{7.7,a}$$

$$NTH_{2,i} = NM_i\, TH_{2,i} \quad (7.7,b)$$

In Equation (7.7) $TH_{1,i}$ and $TH_{2,i}$ represent the record components (components 1 and 2, respectively) of the i^{th} record, and $NTH_{1,i}$ and $NTH_{2,i}$ represent the associated normalized components, respectively. Normalization factors are given in FEMA P695 (Table A-4D in FEMA P695) for all 22 records in the far-field record set (see Table 7.4). The second step in the ground motion scaling involve scaling the normalized ground motions to a specific ground motion spectral acceleration intensity (called the target spectrum) such that the median spectral acceleration of the ground motion components matches the spectral acceleration of the target spectrum at the fundamental period of the structure that is being analyzed. For instance, Figure 7.3 shows the spectral acceleration, SA, for far-field unscaled normalized ground motions along with the median spectral acceleration of ground motions and the design spectrum which is the target spectrum for this example. The goal is to scale the ground motions to the design spectrum at the fundamental period, T_1, such that the median spectral acceleration of the ground motions matches the design spectrum at the fundamental period, T_1. Figure 7.4 shows the result for the scaled ground motions.

7.4. Collapse Point Definition

Dynamic instability of a structure is defined as the ground motion intensity, measured by the 5% damped median spectral acceleration intensity $S_T(T_1)$ of the far-field record set at the fundamental period of the structure systematically scaled up until the maximum story drift becomes large with a small increase in ground motion intensity, leading to the occurrence of incipient collapse where the frame model becomes globally unstable under the lateral seismic forces. This defines the dynamic instability of the frame. However,

since the structure undergoes excessive story drift at collapse it is more practical to define the collapse of a structure by defining a maximum story drift where structure is collapsed. To indicate the point of incipient collapse of the structure, the following definitions are utilized to indicate the collapse spectral acceleration $S_{CT}(T_1)$ for each ground motion:

1) $S_{CT}(T_1)$ of the frame model is the smaller of the $S_T(T_1)$ value at the end of the corresponding IDA curve where convergence failed in the analysis due to incipient collapse and the $S_T(T_1)$ value at the transient story drift of 10%;

2) $S_{CT}(T_1)$ of the frame model is the smaller of the $S_T(T_1)$ value at the end of the corresponding IDA curve where convergence failed in the analysis due to incipient collapse and the $S_T(T_1)$ value at the transient story drift of 15%;

3) $S_{CT}(T_1)$ of the frame model is the smaller of the $S_T(T_1)$ value at the end of the corresponding IDA curve where convergence failed in the analysis due to incipient collapse and the $S_T(T_1)$ value at which an 80% slope reduction in the initial slope of the IDA curve takes place for a ground motion.

The CMR obtained from these different collapse definitions are compared to assess the sensitivity of the CMR to the definition of incipient collapse in a subsequent chapter.

7.5. Effect of Sources of Uncertainty on Collapse Assessment

Various sources of uncertainty contribute to variability in collapse capacity. A larger variability in the uncertainty causes a larger probability of collapse. Four main sources of uncertainty are considered in FEMA P695 in order to assess the probability of collapse:

1) Record to record uncertainty (RTR)

RTR accounts for the variability in the response of the structure to different ground motions. Record to record variability is evident in IDA curves and is due to the variation in characteristics of various records.

2) Design requirement uncertainty (DR)

DR is related to completeness of the design requirements. DR-related uncertainty is quantified in terms of quality of design requirements.

3) Test data uncertainty (TD)

TD is related to the completeness of the test data used to define the system. TD-related uncertainty is quantified in terms of quality of test data.

4) Modeling uncertainty (MDL)

MDL is related to how well the model represents the response characteristics of the system and how well it captures the structural collapse behavior. MDL-related uncertainty is quantified in terms of quality of model.

FEMA P695 defines a quality rating for the above mentioned uncertainties and translates them into quantitative values of uncertainty. The amount of uncertainty is defined as 0.1, 0.2, 0.35 and 0.5 for superior, good, fair and poor quality rates, respectively. The lognormal standard deviation for record to record variability, β_{RTR}, ranges from 0.2 to 0.4 depending on system ductility and potential period elongation due to stiffness reduction up to collapse under extreme ground motions. FEMA P695 suggests the use of β_{RTR}=0.4 (for systems with $\mu_T \geq 3$) in the performance evaluation of systems. β_{RTR} can also be computed by fitting a lognormal CDF on the collapse data used to develop the fragility curve. Both computed β_{RTR} and fixed β_{RTR}=0.4 values are used to compute the total system uncertainty, β_{TOT}, in order to obtain the probability of collapse

at MCE level and compare the sensitivity of results to β_{TOT}. A good or fair quality rates are assumed for the other sources of uncertainties in subsequent chapters. Values for the lognormal standard deviation of RTR, DR, TD and MDL are assumed to be statistically independent and presented by lognormally distributed random variables λ_{RTR}, λ_{DR}, λ_{TD}, and λ_{MDL}, respectively. These random variables have a median of unity and lognormal standard deviation of β_{RTR}, β_{DR}, β_{TD}, and β_{MDL}. The combined uncertainty is represented by the random variable λ_{TOT}, where:

$$\lambda_{TOT} = \lambda_{RTR}\lambda_{DR}\lambda_{TD}\lambda_{MDL} \tag{7.8}$$

where λ_{TOT} is lognormally distributed with a median of unity and lognormal standard deviation of β_{TOT} (total amount of system uncertainty), where:

$$\beta_{TOT} = \sqrt{\beta_{RTR}^2 + \beta_{DR}^2 + \beta_{TD}^2 + \beta_{MDL}^2} \tag{7.9}$$

β_{TOT} is needed in order to calculate the probability of collapse at a selected level of intensity other than the median collapse capacity (e.g., MCE level intensity). For instance, the two fragility curves shown in Figure 7.5 have the same collapse median spectral acceleration while fragility curve (b) has a larger uncertainty than the fragility curve (a). It is seen that the probability of collapse under the MCE level intensity is larger for curve (b) than (a) due to larger amount of uncertainty in collapse data. In Figure 7.5, curve (a) just considers RTR variability as the source of uncertainty while curve (b) takes into account the uncertainty associated with RTR, DR, TD, and MDL.

Table 7. 1. Summary of earthquake event and recording station data for the far-field record set (Table A-4A in FEMA P695).

ID No.	Earthquake			Recording Station	
	M	Year	Name	Name	Owner
1	6.7	1994	Northridge	Beverly Hills - Mulhol	USC
2	6.7	1994	Northridge	Canyon Country-WLC	USC
3	7.1	1999	Duzce, Turkey	Bolu	ERD
4	7.1	1999	Hector Mine	Hector	SCSN
5	6.5	1979	Imperial Valley	Delta	UNAMUCSD
6	6.5	1979	Imperial Valley	El Centro Array #11	USGS
7	6.9	1995	Kobe, Japan	Nishi-Akashi	CUE
8	6.9	1995	Kobe, Japan	Shin-Osaka	CUE
9	7.5	1999	Kocaeli, Turkey	Duzce	ERD
10	7.5	1999	Kocaeli, Turkey	Arcelik	KOERI
11	7.3	1992	Landers	Yermo Fire Station	CDMG
12	7.3	1992	Landers	Coolwater	SCE
13	6.9	1989	Loma Prieta	Capitola	CDMG
14	6.9	1989	Loma Prieta	Gilroy Array #3	CDMG
15	7.4	1990	Manjil, Iran	Abbar	BHRC
16	6.5	1987	Superstition Hills	El Centro Imp. Co.	CDMG
17	6.5	1987	Superstition Hills	Poe Road (temp)	USGS
18	7.0	1992	Cape Mendocino	Rio Dell Overpass	CDMG
19	7.6	1999	Chi-Chi, Taiwan	CHY101	CWB
20	7.6	1999	Chi-Chi, Taiwan	TCU045	CWB
21	6.6	1971	San Fernando	LA - Hollywood Stor	CDMG
22	6.5	1976	Friuli, Italy	Tolmezzo	--

Table 7. 2. Spectral Shape Factor (*SSF*) for archetypes designed for seismic design category D (Table 7-1b in FEMA P695).

T (sec.)	Period-Based Ductility, μ_T							
	1.0	1.1	1.5	2	3	4	6	≥ 8
≤ 0.5	1.00	1.05	1.1	1.13	1.18	1.22	1.28	1.33
0.6	1.00	1.05	1.11	1.14	1.2	1.24	1.3	1.36
0.7	1.00	1.06	1.11	1.15	1.21	1.25	1.32	1.38
0.8	1.00	1.06	1.12	1.16	1.22	1.27	1.35	1.41
0.9	1.00	1.06	1.13	1.17	1.24	1.29	1.37	1.44
1.0	1.00	1.07	1.13	1.18	1.25	1.31	1.39	1.46
1.1	1.00	1.07	1.14	1.19	1.27	1.32	1.41	1.49
1.2	1.00	1.07	1.15	1.2	1.28	1.34	1.44	1.52
1.3	1.00	1.08	1.16	1.21	1.29	1.36	1.46	1.55
1.4	1.00	1.08	1.16	1.22	1.31	1.38	1.49	1.58
≥ 1.5	1.00	1.08	1.17	1.23	1.32	1.4	1.51	1.61

Table 7. 3. Acceptable values of ACMR ratio ($ACMR_{10\%}$ and $ACMR_{20\%}$) (Table 7-3 in FEMA P695).

Total System Collapse Uncertainty	Collapse Probability				
	5%	10% ($ACMR_{10\%}$)	15%	20% ($ACMR_{20\%}$)	25%
0.275	1.57	1.42	1.33	1.26	1.20
0.300	1.64	1.47	1.36	1.29	1.22
0.325	1.71	1.52	1.40	1.31	1.25
0.350	1.78	1.57	1.44	1.34	1.27
0.375	1.85	1.62	1.48	1.37	1.29
0.400	1.93	1.67	1.51	1.40	1.31
0.425	2.01	1.72	1.55	1.43	1.33
0.450	2.10	1.78	1.59	1.46	1.35
0.475	2.18	1.84	1.64	1.49	1.38
0.500	2.28	1.90	1.68	1.52	1.40
0.525	2.37	1.96	1.72	1.56	1.42
0.550	2.47	2.02	1.77	1.59	1.45
0.575	2.57	2.09	1.81	1.62	1.47
0.600	2.68	2.16	1.86	1.66	1.50
0.625	2.80	2.23	1.91	1.69	1.52
0.650	2.91	2.30	1.96	1.73	1.55
0.675	3.04	2.38	2.01	1.76	1.58
0.700	3.16	2.45	2.07	1.80	1.60

Table 7. 4. Summary of factors used to normalize recorded ground motions, and parameters of normalized ground motions for the far-field record set (Table A-4D in FEMA P695).

ID No.	As-Recorded Parameters			Normaliz-ation Factor	Normalized Motions	
	1-Sec. Spec. Acc. (g)		PGVPEER (cm/s.)		PGA_{max} (g)	PGV_{max} (cm/s.)
	Comp. 1	Comp. 2				
1	1.02	0.94	57.2	0.65	0.34	41
2	0.38	0.63	44.8	0.83	0.40	38
3	0.72	1.16	59.2	0.63	0.52	39
4	0.35	0.37	34.1	1.09	0.37	46
5	0.26	0.48	28.4	1.31	0.46	43
6	0.24	0.23	36.7	1.01	0.39	43
7	0.31	0.29	36.0	1.03	0.53	39
8	0.33	0.23	33.9	1.10	0.26	42
9	0.43	0.61	54.1	0.69	0.25	41
10	0.11	0.11	27.4	1.36	0.30	54
11	0.50	0.33	37.7	0.99	0.24	51
12	0.20	0.36	32.4	1.15	0.48	49
13	0.46	0.28	34.2	1.09	0.58	38
14	0.27	0.38	42.3	0.88	0.49	39
15	0.35	0.54	47.3	0.79	0.40	43
16	0.31	0.25	42.8	0.87	0.31	40
17	0.33	0.34	31.7	1.17	0.53	42
18	0.54	0.39	45.4	0.82	0.45	36
19	0.49	0.95	90.7	0.41	0.18	47
20	0.30	0.43	38.8	0.96	0.49	38
21	0.25	0.15	17.8	2.10	0.44	40
22	0.25	0.30	25.9	1.44	0.50	44

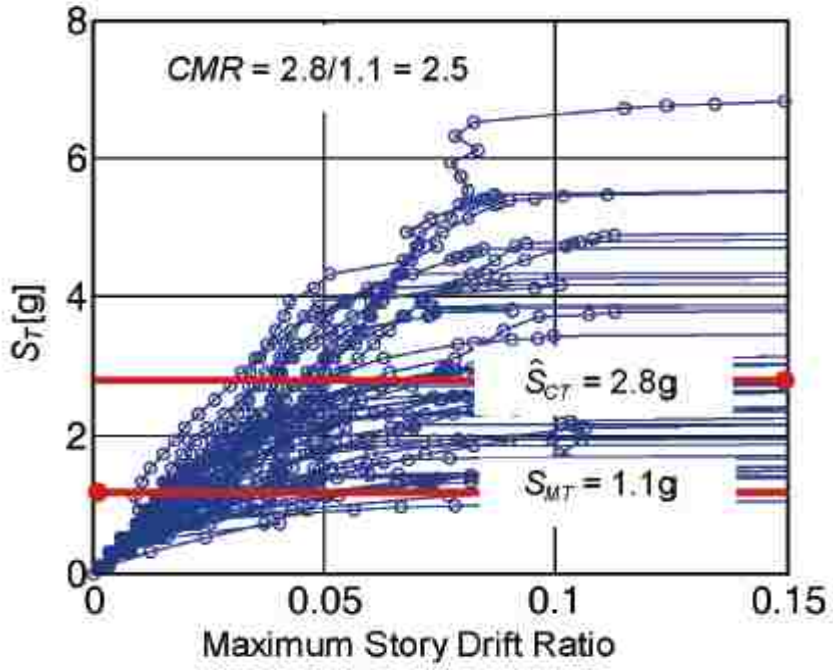

Figure 7. 1. Incremental dynamic analysis response plot of spectral acceleration versus maximum story drift ratio (FEMA P695).

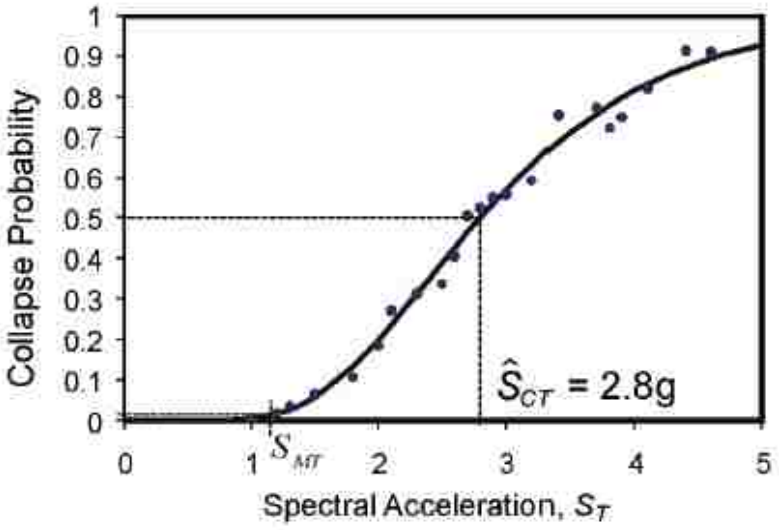

Figure 7. 2. Collapse fragility curve (FEMA P695).

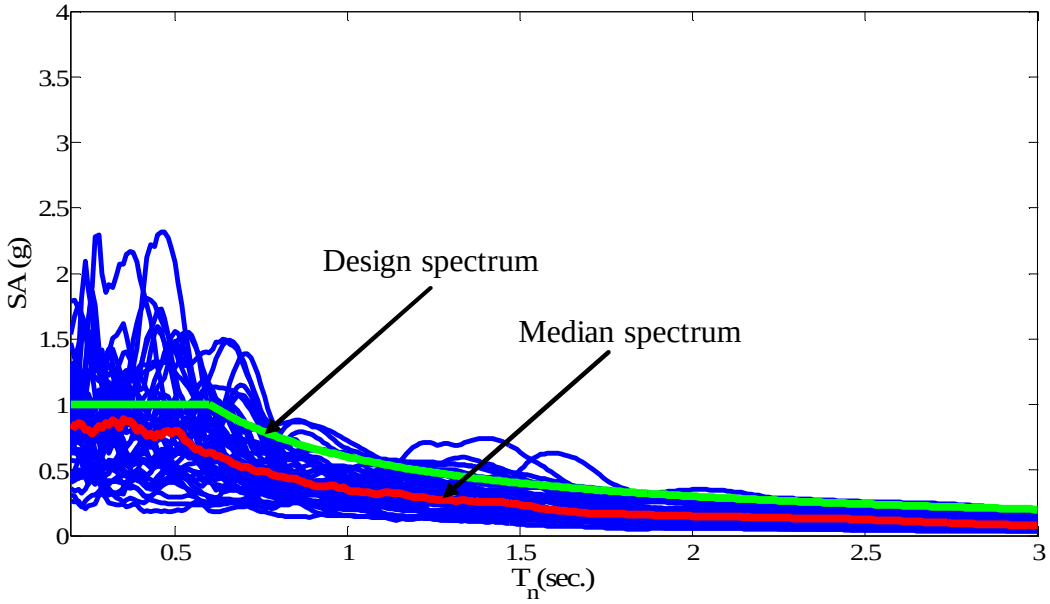

Figure 7. 3. Far-field normalized, unscaled response spectra along with the median spectrum and design spectrum of ASCE7-10.

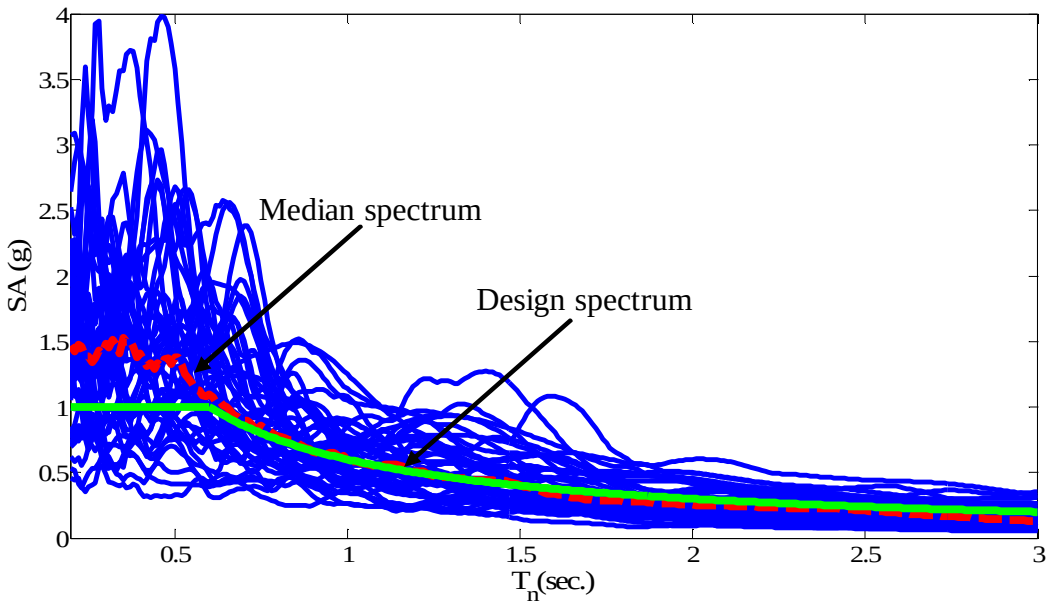

Figure 7. 4. Far-field normalized, scaled response spectra at T_1=0.932 sec along with the median spectrum and design spectrum of ASCE7-10.

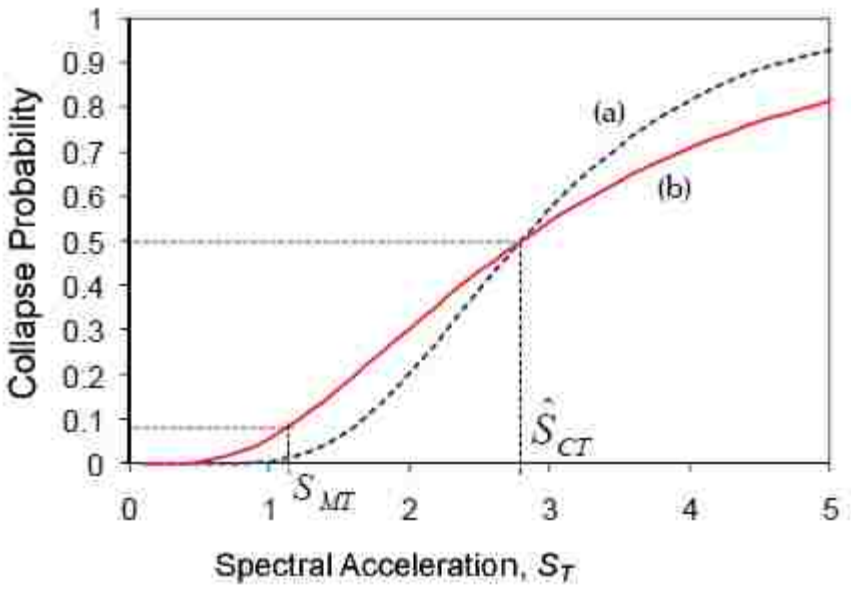

Figure 7. 5. Collapse fragility curves; (a) β_{TOT}=0.4; (b) β_{TOT}=0.65 (FEMA P695).

Chapter 8

Seismic Collapse Assessment of SC-MRF Designs 1 and 2: Far-Field Ground Motions

8.1. General

This chapter presents the results for the seismic collapse assessment of the two SC-MRFs designs. The SC-MRF behavior leading to collapse is discussed. The FEMA P695 collapse assessment methodology presented in Chapter 7 is used to determine the seismic collapse resistance of SC-MRF Designs 1 and 2 under the ensemble of far-field ground motions. The IDA curves, fragility curves and probabilistic studies on PT strand maximum strains are presented and discussed in this chapter.

8.2. Behavior of SC-MRF Leading to Collapse

As stated previously, the beams in an SC-MRF are subject to large moments, M, combined with appreciable axial force, P, caused by the PT and diaphragm forces, making the beams susceptible to local buckling under extreme loading scenarios leading to collapse. The beam local bucking at the end of the reinforcing plates and PT strand yielding are the main limit states that occur at incipient collapse under the ground motions that exceed the MCE hazard level. The occurrence of local buckling in the beam leads to shortening of the member, which in turn results in a loss of PT force and, since the moment capacity is affected by axial force P, subsequent loss of moment capacity, M, of a post-tensioned SC connection leading to collapse and excessive story drift. Similarly, PT strand yielding results in a loss of PT force which leads to a loss of moment capacity

of the SC connection causing collapse. The gap opening at the beam column interface, inelastic deformations in the members, mainly yielding and hinge formation in the columns are the other limit states that may occur at incipient collapse and cause excessive story drifts.

The SC-MRF Design 1 behavior at collapse is discussed herein. The discussion is applicable to SC-MRF Design 2 which had similar behavior. Figure 8.1 shows an schematic of the SC-MRF at collapse for SHI090 far-field ground motion scaled up to exceed the MCE hazard level and cause collapse. The beam local buckling, PT strand yielding, gap opening and hinge formation at the columns are indicated in Figure 8.1. South and north bays are shown in Figure 8.1. The SC connections located at the south side of the south-bay are named the SS connections at each floor level. Similarly, the other SC connections are indicated with SN, NS, and NN symbols at each floor level (see Figure 8.1). Figure 8.2 presents the PT stand force, T, versus the average connection relative rotation (i.e., the average for all connections at one floor level), θ_r^{ave}, for each floor level. As seen in Figure 8.2 the occurrence of beam local buckling and PT strand yielding are identified, resulting in the loss of PT strand force due to PT strand yielding and beam shortening due to beam local buckling. Figure 8.3 shows the PT strand force T time history at each floor level. Figure 8.4 presents the connection moment M versus connection relative rotation θ_r, for the south-bay for the SS and SN connections at each floor level. Figure 8.5 shows the M-θ_r for the north-bay for the NS and NN connections. The loss of connection moment capacity seen in Figures 8.4 and 8.5 is due to beam local buckling and PT strand yielding. Figure 8.6 shows the M-θ_r relation for the connection located at the first floor at south-bay south-side (SS). The occurrence of beam local

buckling is identified in Figure 8.6. Figure 8.7 presents the IDA curve for this ground motion, where the occurrence of incipient collapse is identified. The behavior of the frame presented above occurs at the maximum story drift of 16% corresponding to the last data point of IDA curve. Figure 8.8 shows the story drift time history for each floor level where the maximum story drifts are 7.4%, 16.1%, 11.3%, and 9.6% for the 1st, 2nd, 3rd floor levels, and at the roof, respectively.

8.3. Results for SC-MRF Design 1

8.3.1. IDA Results

Figure 8.9 shows the IDA curves for the SC-MRF Design 1 under 44 far-field ground motions. As discussed in Chapter 7, the horizontal axis shows the maximum inter-story drift, $\Theta_{max,s}$, and the vertical axis presents the spectral acceleration, $S_T(T_1)$, measured by 5% damped median spectral acceleration intensity of the far-field record set at the fundamental period of the structure, T_1. Each data point determines the maximum story drift at a given $S_T(T_1)$. The record to record variability can be seen in the results, where for each ground motion a different path and maximum spectral acceleration is achieved for each IDA curve.

8.3.2. Fragility Curves

Three different collapse point assumptions were defined in Chapter 7 to indicate the collapse spectral acceleration $S_{CT}(T_1)$ associated with incipient collapse for each ground motion obtained from an IDA curve. The results of different collapse scenarios are presented below.

Figure 8.10 shows the fragility curve when $S_{CT}(T_1)$ is based on the smaller of the $S_T(T_1)$ value at the end of the corresponding IDA curve where convergence failed in the

analysis due to incipient collapse and the $S_T(T_1)$ value at the transient story drift of 10%. The median collapse capacity is formed to be $\hat{S}_{CT}$=2.04g. The collapse fragility curve obtained by fitting a CDF, assuming a lognormal distribution, to the ranked $S_{CT}(T_1)$ data points, is shown in Figure 8.10 where the $\hat{S}_{CT}$ and the associated standard deviation β_{RTR}=0.31 of the natural logarithm of the data are indicated in Figure 8.10. The MCE code specified spectral acceleration intensity (S_{MT}) at the fundamental period (i.e., the design period defined in ASCE7-10) of the structure, T_1=0.932 sec. is 0.966g, and consequently CMR=2.11.

Similarly, Figure 8.11 shows the fragility curve when $S_{CT}(T_1)$ is based on the smaller of the $S_T(T_1)$ value at the end of the corresponding IDA curve where convergence failed in the analysis due to incipient collapse and the $S_T(T_1)$ value at the transient story drift of 15%. The results have a $\hat{S}_{CT}$=2.43g and β_{RTR}=0.26. The CMR is 2.52.

Figure 8.12 shows the fragility curve when $S_{CT}(T_1)$ is based on the smaller of the $S_T(T_1)$ value at the end of the corresponding IDA curve where convergence failed in the analysis due to incipient collapse and the $S_T(T_1)$ value at which an 80% slope reduction in the initial slope of the IDA curve takes place for a ground motion. The results have a $\hat{S}_{CT}$=2.12g and β_{RTR}=0.42. The CMR is 2.19.

The sensitivity of $S_{CT}(T_1)$ data to the incipient collapse definition is seen in Figures 8.10 through 8.12 led to different values for the $\hat{S}_{CT}$, and consequently different CMRs. The variability of $S_{CT}(T_1)$ associated with the incipient collapse affects $\hat{S}_{CT}$ and the amount of uncertainty corresponding to record to record (RTR) variability, β_{RTR}, resulting in a variability in the probability of collapse at a given hazard level. The probability of collapse at the MCE level considering other sources of uncertainty in addition to RTR

variability is discussed and presented later. The results of different cases presented above are compared in Chapter 11.

8.3.3. Fragility Curves for Different Amounts of Uncertainty

As stated in Chapter 7, the different sources of uncertainty considered in FEMA P695 are record to record variability (RTR), design requirement (DR), test data (TD) and modeling uncertainty (MDL). In this section fragility curves are developed considering these sources of uncertainty. To compute the β_{TOT} per Equation (7.6), β_{RTR} is based on the data. In addition, the value of β_{RTR}=0.4 is also considered in accordance with FEMA P695. The other sources of uncertainty are given numerical values by selecting qualitative ratings defined in FEMA P695. Good quality was assumed for modeling and test data, where β_{MDL}=0.2 and β_{TD}=0.2. For the design requirement, two different qualities were assumed, good (where β_{DR}=0.2) and fair (where β_{DR}=0.35). The two cases were assumed since the design procedure per Lin (2012) has not undergone a peer review. Table 8.1 summarizes the values for the different combinations of uncertainty to calculate the total amount of uncertainty. The collapse point assumptions are named as 10% story drift, 15% story drift and 80% slope reduction in the Table 8.1.

Figure 8.13(a) shows the fragility curves corresponding to $\hat{S}_{CT}$ and β_{TOT} considering β_{RTR}=0.31 where $S_{CT}(T_1)$ is the smaller of the $S_T(T_1)$ value at the end of the corresponding IDA curve where convergence failed in the analysis due to incipient collapse and the $S_T(T_1)$ value at the transient story drift of 10%. The curves are based on an assumed lognormal distribution. Note that two different uncertainty qualities are considered for β_{DR} in Figure 8.13(a) as stated previously (β_{DR}=0.2 and β_{DR}=0.35). Figure 8.13(b) shows the fragility curves when the value of β_{RTR}=0.4 is used. The probability of

collapse at the MCE level are indicated on the fragility curves while the values are tabulated in Table 8.1. As seen in Table 8.1, the probability of collapse at the MCE level increases for a larger amount of uncertainty β_{TOT}. This can be seen in Figure 8.13 where S_{MT} shows the spectral acceleration at the MCE level. For instance, the probability of collapse at MCE level is 10.6% and 7.9% for β_{TOT}=0.6 and β_{TOT}=0.53, respectively, in Figure 8.5(b).

Figures 8.14(a) and (b) show the corresponding fragility curves where $S_{CT}(T_1)$ is the smaller of the $S_T(T_1)$ value at the end of the corresponding IDA curve where convergence failed in the analysis due to incipient collapse and the $S_T(T_1)$ value at the transient story drift of 15%. β_{RTR}=0.26 and β_{RTR}=0.4 are used for Figures 8.14(a) and (b). The probability of collapse is smaller for this collapse scenario in contrast to the two other incipient collapse definitions. The probability of collapse is larger for a higher amount of uncertainty β_{TOT}. For example, the probability of collapse at the MCE level is 6.2% and 4.1% for β_{TOT}=0.6 and β_{TOT}=0.53 (see Table 8.1), respectively, in Figure 8.14(b) where S_{MT} shows the spectral acceleration at the MCE level.

Figures 8.15(a) and (b) show the fragility curves where $S_{CT}(T_1)$ is the smaller of the $S_T(T_1)$ value at the end of the corresponding IDA curve where convergence failed in the analysis due to incipient collapse and the $S_T(T_1)$ value at which an 80% slope reduction in the initial slope of the IDA curve takes place for a ground motion. β_{RTR}=0.42 and β_{RTR}=0.4 are used for Figures 8.15(a) and (b). As seen in Table 8.1, the β_{RTR}=0.42 found from the data leads to higher amount of uncertainty in the system, β_{TOT}. The probability of collapse at MCE level increases for a system with a higher amount of uncertainty β_{TOT}. For instance, the probability of collapse at the MCE level is 10.2% and 7.3% for

β_{TOT}=0.62 and β_{TOT}=0.54 (see Table 8.1), respectively, in Figure 8.15(a) where S_{MT} shows the spectral acceleration at the MCE level.

The fragility curves and the probability of collapse at MCE level are discussed further and compared in Chapter 11.

8.3.4. PT Strand Strain Demand and Fracture

As stated in Chapter 3, in Design 1 the total PT strand force at MCE is limited to 90% of total strand yield force to avoid PT strand yielding at the MCE level. PT strand yielding or fracture may occur beyond the MCE level due to a substantial PT strand force increase from gap opening. However, when beam local buckling occurs, a loss in PT strand force occurs and yielding of the PT strands does not happen. The maximum PT strand strain, ε_{max}, for each floor level are selected for each ground motion from the IDA data, where the maximum transient story drift associated with structure collapse is limited to 15% for each ground motion. The data for ε_{max} are used to find the median PT strand strain, ε_{median}, and the lognormal standard deviation, ζ. Figure 8.8 shows the frequency distribution for ε_{max} of the PT strands for each floor level where the area underneath the frequency distribution is unity. The PT strand yielding (deterministic value, ε_y=0.88%) and the ε_{median} are indicated in Figure 8.16. Table 8.2 summarizes the ε_{median} and the ζ for ε_{max} for each story level along with the $\varepsilon_{median}/\varepsilon_y$ ratio. Included in Figure 8.16 is a plot for probability density functions (PDFs) assuming a lognormal distribution for ε_{max}. The probability of ε_{max} exceeding ε_y for each floor level is obtained from the PDFs and summarized in Table 8.2. The probability is interpreted as the area underneath a PDF where the strain is greater than ε_y. As seen in Figure 8.16 and from the results presented in Table 8.2, the probability of ε_{max} exceeding ε_y is larger at the 3rd floor and roof,

67.96% and 38.58%, respectively, in contrast to 11.55% and 0.96% for the 2nd and 1st floors, respectively. The minimum fracture strain of 2% is required by the International Code Council Evaluation Service (ICC-ES) as acceptance criteria for post-tensioning anchorages and couplers used for pre-stressed concrete. Walsh and Kurama (2010) showed from PT strand tests that there is a significant scatter in the strain at fracture, with fractures occurring at strains ranging from 1% to 4%. Table 8.3 presents the probability of ε_{max} exceeding 1% and 2% strain. Note that the PT strand fracture strain resistance in Table 8.3 is assumed to be a deterministic variable. The probability of ε_{max} exceeding 2% is negligible. The probability of ε_{max} exceeding 1% has the values of 37.82% and 11.19% at the roof and 3rd floor, respectively, in comparison to the lower floors having negligible values. The fracture strand strain can be treated as a random variable. The test data from Walsh and Kurama (2010) is used to find the strand median fracture strain of ε_{median}=0.0242 and the lognormal standard deviation of ζ=0.003374 for 0.6 in. diameter strands used in the prototype frame for cast-anchor and barrel-anchor types (see Figure 8.17). ε_{max} is considered as a lognormal random variable (denoted as $S(\lambda_S,\zeta_S)$). The PT strand fracture strain resistance is also considered as a lognormal random variable with the parameters from test results for 0.6 in. diameter strands presented above (denoted as $R(\lambda_R,\zeta_R)$). λ is the lognormal mean for a lognormal distributed random variable, and equal to the natural log of the median value.

The probability of fracture, P_f, can be found by Equation (8.1) when S and R are two statistically independent random variables:

$$P_f = P(R \leq S) = \int_0^\infty \int_0^S f_R(r) f_S(s) dr\, ds = \int_0^\infty F_R(s) f_S(s) ds \quad (8.1)$$

where $f_R(r)$ and $f_S(s)$ are the lognormal PDFs. In Equation (8.1) $F_R(s)$ is the lognormal cumulative density function (CDF). Figure 8.18 shows the PDFs for the strain fracture (R) and maximum strain demand ε_{max} (S). For the strain fracture (R) the PDFs are shown in Figure 8.18 based on a mean of λ_R, λ_R-$2\zeta_R$, and λ_R-$3\zeta_R$ for each floor level. Table 8.4 summarizes the probability of fracture assuming three different mean values for the fracture strain in order to assess the sensitivity of the probability of fracture to the median fracture strain. As seen in Table 8.4, the probability of fracture has the maximum values at each floor level utilizing the PDF for the strain fracture (R) based on a mean of λ_R-$3\zeta_R$. The probability of strain fracture at the roof is 58.20% for the case with a mean of λ_R-$3\zeta_R$. Note that the mean value of λ_R-$3\zeta_R$ results in a ε_{median} of 0.88% which is in the range of ε_y. Using the PDF for the R with a mean of λ_R leads to the probability of strain fracture of 0.64% at the roof. The probability of strain fracture of 24.48% was obtained at the roof using the PDF for the R with a mean of λ_R-$2\zeta_R$. The results are discussed further and compared in Chapter 11.

8.3.5. Adjusted CMR

FEMA P695 introduces the Adjusted Collapse Margin Ratio (ACMR) to account for the frequency content (spectral shape) of the ground motion record set. In order to find the ACMR, Spectral Shape Factor (SSF) is needed per FEMA P695 where the period-based ductility μ_T and the design period of the structure T_1 are used in Table 7.2. To find μ_T per Equation (7.3), a pushover analysis is performed. The results are shown in Figure 8.19 where a plot of base shear-roof displacement (V-δ_r) appears. Note that the ultimate roof displacement δ_u in Figure 8.19 is corresponding to the point where the convergence failed in the pushover analysis and not related to the point associated with 80% of V_{max}

per FEMA P695. Table 8.5 summarizes the parameters needed to find the SSF. C_0 was obtained from Equation (7.5). μ_T is larger in reality since δ_u is associated with the point where 80% of V_{max} is reached which occurs beyond the point where the convergence failed. However SSF is a constant value for the systems with $\mu_T \geq 8$ (see Table 7.2). The ACMR value can be found by multiplying the CMR values by the SSF value. The ACMR values for SC-MRF Design 1 for the different incipient collapse definitions are presented in Chapter 11 in order to compare with the values for the other systems and with the acceptable values per FEMA P695. The probability of collapse at the MCE level is also discussed for SC-MRF Design 1 in Chapter 11 using the ACMR and compared with the acceptable values per FEMA P695.

8.4. Results for SC-MRF Design 2

8.4.1. IDA Results

Similar to what presented for SC-MRF Design 1, Figure 8.20 shows the IDA curves for SC-MRF Design 2 under the far-field ground motions.

8.4.2. Fragility Curves

Assuming $S_{CT}(T_1)$ is the smaller of the $S_T(T_1)$ value at the end of the corresponding IDA curve where convergence failed in the analysis due to incipient collapse and the $S_T(T_1)$ value at the transient story drift of 10% results in $\hat{S}_{CT}$=1.93g and β_{RTR}=0.32. Figure 8.21 shows the associated fragility curve. As stated before, the MCE code specified spectral acceleration intensity (S_{MT}) at the fundamental period of the structure, T_1=0.932 is 0.966g. Thus, the CMR equals 2.00.

Assuming $S_{CT}(T_1)$ is the smaller of the $S_T(T_1)$ value at the end of the corresponding IDA curve where convergence failed in the analysis due to incipient collapse and the

$S_T(T_1)$ value at the transient story drift of 15% results in $\hat{S}_{CT}$=2.25g and β_{RTR}=0.26. Figure 8.22 shows the associated fragility curve. Therefore, CMR is 2.33.

Assuming $S_{CT}(T_1)$ is the smaller of the $S_T(T_1)$ value at the end of the corresponding IDA curve where convergence failed in the analysis due to incipient collapse and the $S_T(T_1)$ value at which an 80% slope reduction in the initial slope of the IDA curve takes place for a ground motion results in $\hat{S}_{CT}$=2.03g and β_{RTR}=0.29. Figure 8.23 shows the associated fragility curve. In this case, CMR is obtained as 2.10.

The sensitivity of $S_{CT}(T_1)$ data to the incipient collapse definition is seen in Figures 8.21 through 8.23 led to different values for the $\hat{S}_{CT}$, and consequently different values for CMRs. Variability in the probability of collapse at a given hazard level is associated with the variability of $S_{CT}(T_1)$ at the incipient collapse points influencing $\hat{S}_{CT}$ and the amount of uncertainty corresponding to RTR variability, β_{RTR}. The probability of collapse at the MCE level considering other sources of uncertainty in addition to RTR variability is discussed and presented below for different collapse scenarios. The results of different cases presented above are compared in Chapter 11.

8.4.3. Fragility Curves for Different Amount of Uncertainty

Table 8.6 summarizes different combinations of uncertainty values to calculate the total amount of uncertainty β_{TOT} for each collapse point assumption indicated in Chapter 7 for SC-MRF Design 2. Similar to what was presented for the SC-MRF Design 1, Figures 8.24(a) and (b) show the corresponding fragility curves assuming $S_{CT}(T_1)$ is the smaller of the $S_T(T_1)$ value at the end of the corresponding IDA curve where convergence failed in the analysis due to incipient collapse and the $S_T(T_1)$ value at the transient story drift of 10%. β_{RTR}=0.32 and β_{RTR}=0.4 are used in Figures 8.24(a) and (b). As seen in

Table 8.6, the probability of collapse at the MCE level increases for a larger amount of uncertainty β_{TOT}. For instance, the probability of collapse at the MCE level is 12.4% and 9.6% for β_{TOT}=0.6 and β_{TOT}=0.53, respectively, in Table 8.6 and Figure 8.24(b) where S_{MT} shows the spectral acceleration at the MCE level.

Figures 8.25(a) and (b) show the corresponding fragility curves assuming $S_{CT}(T_1)$ is the smaller of the $S_T(T_1)$ value at the end of the corresponding IDA curve where convergence failed in the analysis due to incipient collapse and the $S_T(T_1)$ value at the transient story drift of 15%. β_{RTR}=0.26 and β_{RTR}=0.4 are used in Figures 8.25(a) and (b). The probability of collapse is smaller for this collapse scenario in contrast to the two other incipient collapse definitions. However, the probability of collapse is larger for higher amount of uncertainty β_{TOT}. As an example, the probability of collapse at MCE level is 7.9% and 5.5% for β_{TOT}=0.6 and β_{TOT}=0.53 (see Table 8.6), respectively, in Figure 8.25(b) where S_{MT} shows the spectral acceleration at the MCE level.

Figures 8.26(a) and (b) show the fragility curves for $S_{CT}(T_1)$ based on the smaller of the $S_T(T_1)$ value at the end of the corresponding IDA curve where convergence failed in the analysis due to incipient collapse and the $S_T(T_1)$ value at which an 80% slope reduction in the initial slope of the IDA curve takes place for a ground motion. β_{RTR}=0.29 and β_{RTR}=0.4 are used for Figures 8.26(a) and (b). The probability of collapse at MCE level are indicated on the fragility curves in Figures 8.24 through 8.26. The probability values are tabulated in Table 8.6. As seen in Table 8.6 and Figures 8.24 through 8.26, the probability of collapse at the MCE level increases for a system with a higher amount of uncertainty β_{TOT}. For instance, the probability of collapse at the MCE level is 10.8% and 8% for β_{TOT}=0.6 and β_{TOT}=0.53, respectively, in Table 8.6 and Figure 8.26(b) where S_{MT}

shows the spectral acceleration at the MCE level.

The fragility curves and the probability of collapse for SC-MRF Design 2 at the MCE level are further discussed and compared in Chapter 11.

8.4.4. PT Strand Strain Demand and Fracture

As stated in Chapter 4, in SC-MRF Design 2 the total PT strand force at MCE is limited to 75% of total strand yield force at the MCE level. Figure 8.27 shows the frequency distribution for ε_{max} of the PT strands for each floor level where the area underneath the frequency distribution is unity. The PT strand yielding (deterministic value, ε_y=0.88%) and the ε_{median} are indicated in Figure 8.27. Table 8.2 summarizes the ε_{median} and the ζ for ε_{max} for each story level along with the $\varepsilon_{median}/\varepsilon_y$ ratio. Figure 8.27 includes a plot for the PDFs assuming a lognormal distribution for ε_{max}. The probability of PT strand strain exceeding ε_y for each floor level is obtained from the PDFs and summarized in Table 8.2 for SC-MRF Design 2. As seen in Figure 8.27 and from the results presented in Table 8.2, the probability of ε_{max} exceeding ε_y has the maximum value of 8.8% at the roof and other values of probability of ε_{max} exceeding ε_y at the other floor levels are negligible. Table 8.3 presents the probability of ε_{max} exceeding 1% and 2% strain, assuming PT strand fracture strain resistance as a deterministic variable. The probability of ε_{max} exceeding 2% is negligible. The probability of ε_{max} exceeding 1% has the maximum value of 0.94% at the roof. The probability of ε_{max} exceeding 1% is small and negligible at the other floor levels. The probability of fracture, P_f, is summarized in Table 8.4 for SC-MRF Design 2 for three different mean values for the fracture strain in order to assess the sensitivity of probability of fracture to the median fracture strain. Figure 8.28 shows the lognormal PDFs for S and R random variables for each floor level.

As seen in Table 8.4, using the PDF for the R with a mean of λ_R leads to the negligible probability of strain fracture at all floor levels. For R with a mean of λ_R-$2\zeta_R$, the maximum probability of strain fracture of 7.87% exists at the roof level. The probability of fracture has the maximum values at each floor level utilizing the PDF for the strain fracture (R) with a mean of λ_R-$3\zeta_R$ where at the roof it is equal to 31.60%. Note that the value of λ_R-$3\zeta_R$ results in a value for ε_{median} of 0.88% which is in the range of ε_y. The results are discussed further and comparisons between SC-MRF Designs 1 and 2 are made in Chapter 11.

8.4.5. Adjusted CMR

Similarly, to find μ_T per Equation (7.3) a pushover analysis is performed shown in Figure 8.29. Table 8.5 summarizes the parameters needed to find the SSF. ACMR is obtained by multiplying the CMR values by the SSF. The ACMR values for SC-MRF Design 2 for different incipient collapse definitions are presented in Chapter 11 in order to compare with the values for the other systems and with the acceptable values per FEMA P695. The probability of collapse at the MCE level is also discussed in Chapter 11 for SC-MRF Design 2 using the ACMR and compared with the acceptable values per FEMA P695.

Table 8. 1. Variability in probability of collapse at MCE level for different amounts of uncertainty; SC-MRF Design 1, far-field ground motions.

Collapse Point Definition	$\hat{S}_{CT}$ (g)	β_{RTR}	β_{MDL}	β_{TD}	β_{DR}	β_{TOT}	Probability of Collapse at MCE (%)
10% story drift	2.04	0.31	0.20	0.20	0.20	0.46	5.2
	2.04	0.31	0.20	0.20	0.35	0.55	8.7
	2.04	0.40	0.20	0.20	0.20	0.53	7.9
	2.04	0.40	0.20	0.20	0.35	0.60	10.6
15% story drift	2.43	0.26	0.20	0.20	0.20	0.43	1.6
	2.43	0.26	0.20	0.20	0.35	0.52	3.8
	2.43	0.40	0.20	0.20	0.20	0.53	4.1
	2.43	0.40	0.20	0.20	0.35	0.60	6.2
80% slope reduction in IDA curve	2.12	0.42	0.20	0.20	0.20	0.54	7.3
	2.12	0.42	0.20	0.20	0.35	0.62	10.2
	2.12	0.40	0.20	0.20	0.20	0.53	6.7
	2.12	0.40	0.20	0.20	0.35	0.60	9.5

Table 8. 2. Median PT strand strain, ε_{median}, and lognormal standard deviation, ζ, for each floor level along with $\varepsilon_{median}/\varepsilon_y$ ratio and probability of PT strand strain exceeding ε_y; SC-MRF Designs 1and 2 for far-field ground motions.

Floor	ε_{median}		ζ		$\varepsilon_{median}/\varepsilon_y$		$P(\varepsilon_{max} > \varepsilon_y)$ (%)	
	SC-MRF Design 1	SC-MRF Design 2	SC-MRF Design 1	SC-MRF Design 2	SC-MRF Design 1	SC-MRF Design 2	SC-MRF Design 1	SC-MRF Design 2
Roof	0.0095	0.0074	0.001654	0.001281	1.08	0.84	67.96	8.80
3rd	0.0084	0.0065	0.001433	0.001136	0.96	0.74	38.58	0.39
2nd	0.0076	0.0061	0.001181	0.001114	0.87	0.69	11.55	0.05
1st	0.0073	0.0054	0.000805	0.000995	0.83	0.62	0.96	6E-5

Table 8. 3. Probability of PT strain exceeding 1% and 2% fracture strain; SC-MRF Designs 1 and 2, far-field ground motions.

Floor	$P(\varepsilon_{max} > 0.01)$ (%)		$P(\varepsilon_{max} > 0.02)$ (%)	
	SC-MRF Design 1	SC-MRF Design 2	SC-MRF Design 1	SC-MRF Design 2
Roof	37.82	0.94	3E-4	4E-13
3rd	11.19	0.01	7E-8	0
2nd	1.01	5E-4	1E-14	0
1st	0.005	4E-8	0	0

Table 8. 4. Probability of PT strand fracture assuming strand fracture resistance R as a random variable; SC-MRF Designs 1 and 2, far-field ground motions.

Floor	$R(\lambda_R, \zeta_R)$		$R(\lambda_R - 2\zeta_R, \zeta_R)$		$R(\lambda_R - 3\zeta_R, \zeta_R)$	
	$P_f = P(R \leq S)$ (%)		$P_f = P(R \leq S)$ (%)		$P_f = P(R \leq S)$ (%)	
	ε_{median} =2.42%		ε_{median} =1.23%		ε_{median} =0.88%	
	SC-MRF Design 1	SC-MRF Design 2	SC-MRF Design 1	SC-MRF Design 2	SC-MRF Design 1	SC-MRF Design 2
Roof	0.64	0.05	24.48	7.87	58.20	31.60
3rd	0.20	0.01	15.09	3.63	45.54	19.83
2nd	0.06	5E-3	9.05	2.41	34.67	15.23
1st	0.03	1E-3	6.50	0.99	29.40	8.55

Table 8. 5. Parameters for calculation of SSF

System	C_0	V_{max} (kips)	W (kips)	$\max(T_1, T_{eigen})$	δ_u (in.)	μ_T >	SSF
SC-MRF Design 1	1.33	774	4398	1.64	83.4	13.5	1.446
SC-MRF Design 2	1.33	793	4398	1.63	73.3	11.7	1.446

Table 8. 6. Variability in probability of collapse at MCE level for different amounts of uncertainty; SC-MRF Design 2, far-field ground motions.

Collapse Point Definition	$\hat{S}_{CT}$ (g)	β_{RTR}	β_{MDL}	β_{TD}	β_{DR}	β_{TOT}	Probability of Collapse at MCE (%)
10% story drift	1.93	0.32	0.20	0.20	0.20	0.47	7.0
	1.93	0.32	0.20	0.20	0.35	0.55	10.4
	1.93	0.40	0.20	0.20	0.20	0.53	9.6
	1.93	0.40	0.20	0.20	0.35	0.60	12.4
15% story drift	2.25	0.26	0.20	0.20	0.20	0.43	2.5
	2.25	0.26	0.20	0.20	0.35	0.52	5.2
	2.25	0.40	0.20	0.20	0.20	0.53	5.5
	2.25	0.40	0.20	0.20	0.35	0.60	7.9
80% slope reduction in IDA curve	2.03	0.29	0.20	0.20	0.20	0.45	4.9
	2.03	0.29	0.20	0.20	0.35	0.54	8.4
	2.03	0.40	0.20	0.20	0.20	0.53	8.0
	2.03	0.40	0.20	0.20	0.35	0.60	10.8

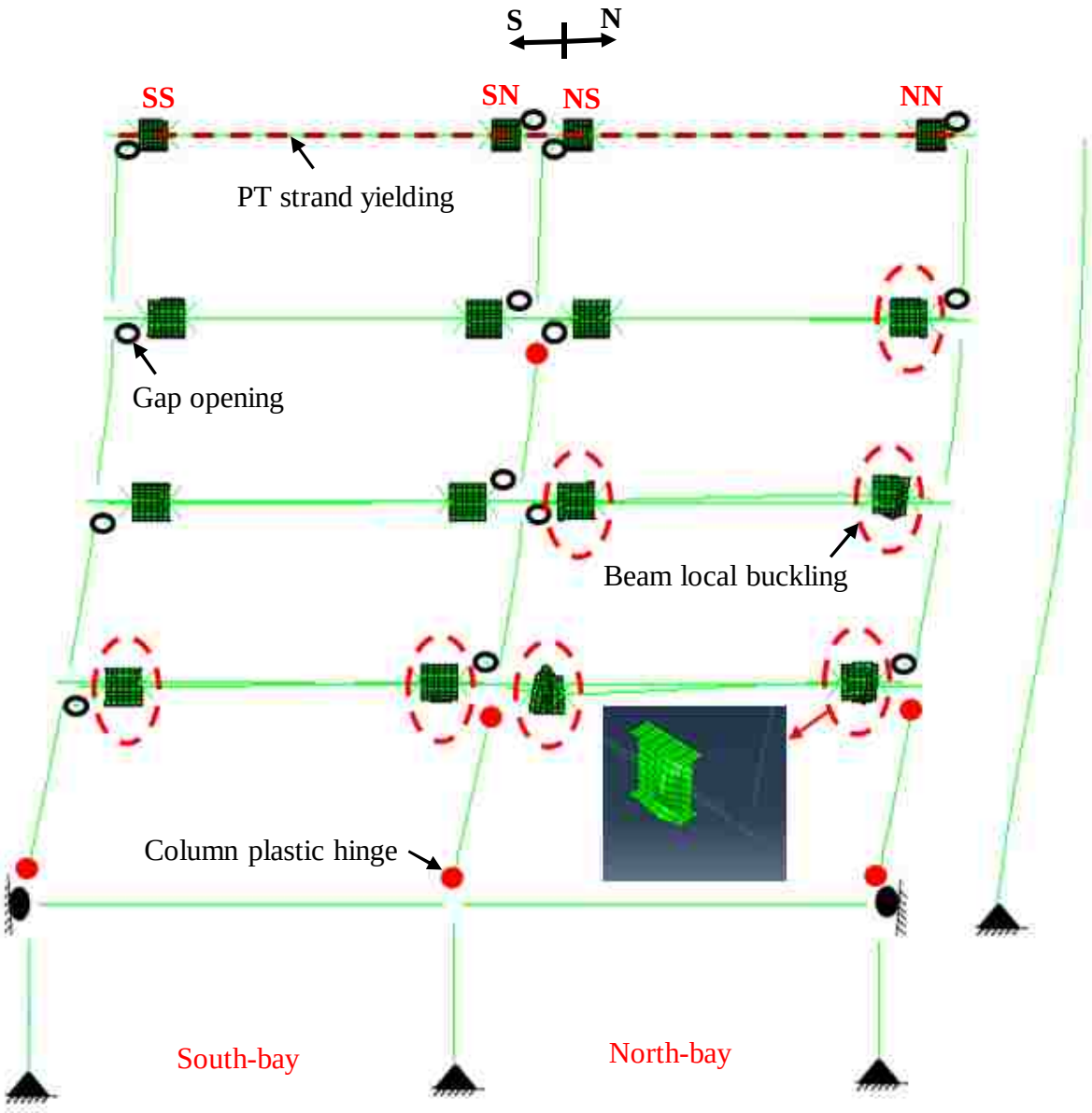

Figure 8. 1. Schematic of SC-MRF Design 1 collapse mode under SHI090 far-field ground motion at collapse.

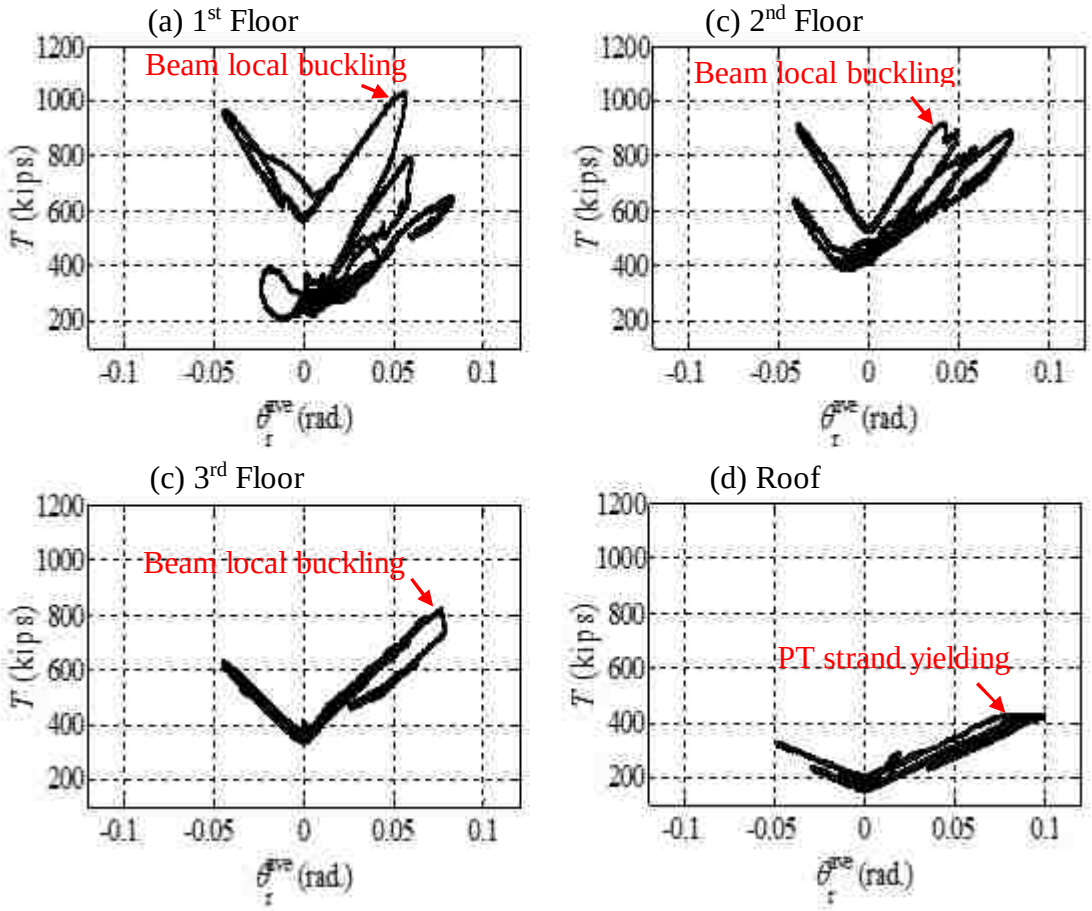

Figure 8. 2. PT stand force versus average connection relative rotation (T-θ_r^{ave}) for SC-MRF Design 1 at (a) 1st floor, (b) 2nd floor, (c) 3rd floor, and (d) roof under SHI090 far-field ground motion at collapse.

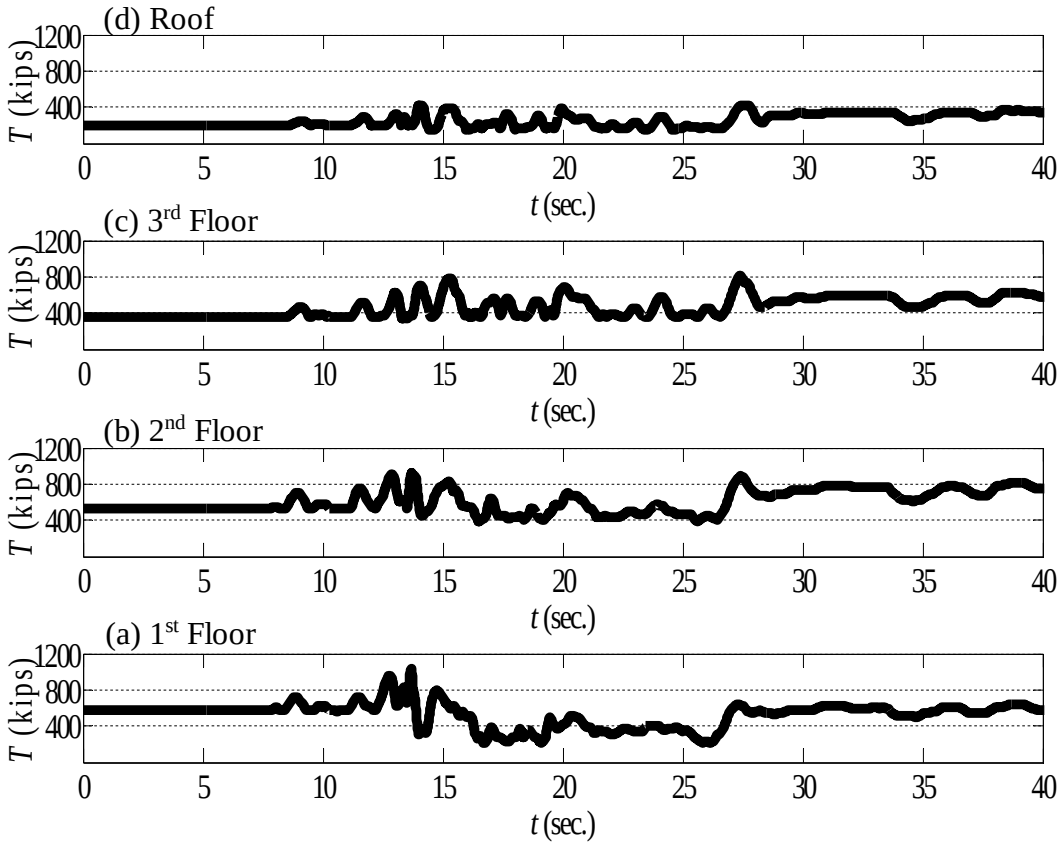

Figure 8. 3. PT stand force time history for SC-MRF Design 1 at (a) 1st floor, (b) 2nd floor, (c) 3rd floor, and (d) roof under SHI090 far-field ground motion at collapse.

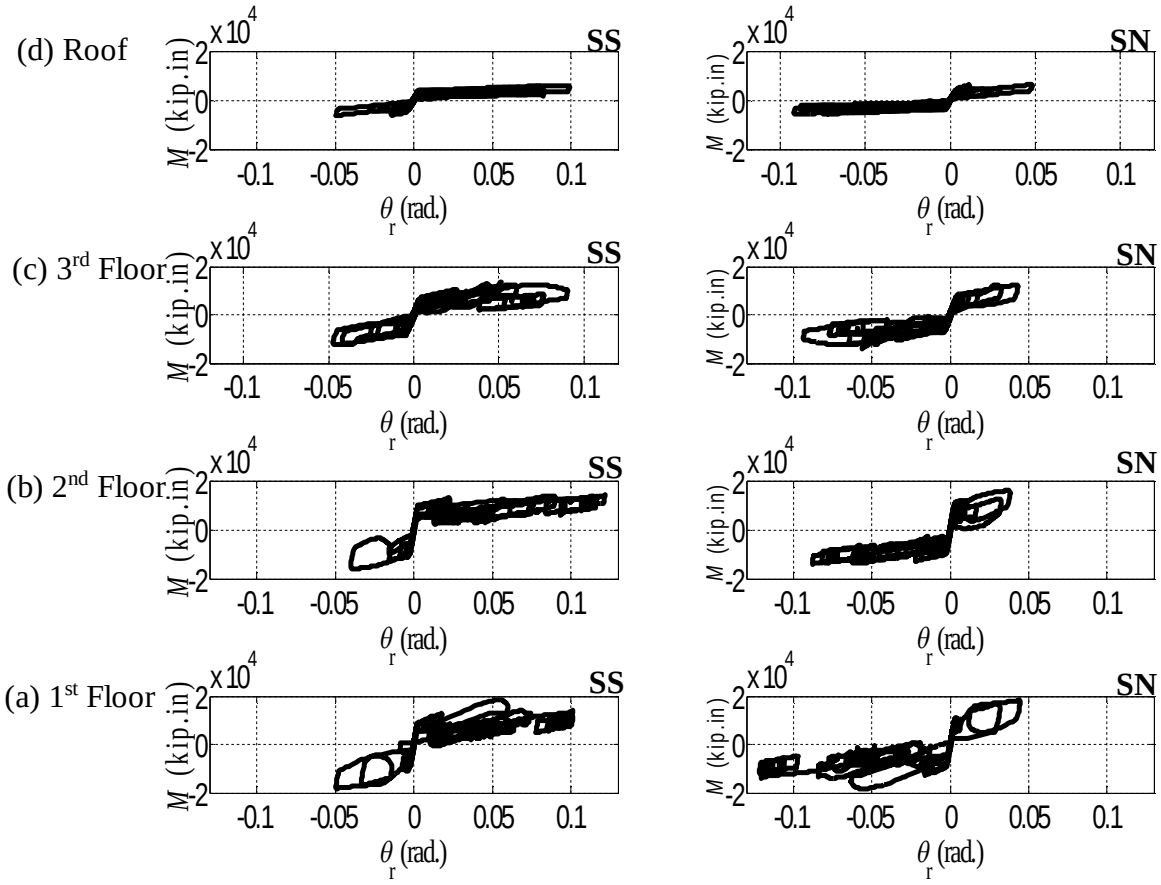

Figure 8. 4. Connection moment versus connection relative rotation (M-θ_r) for SC-MRF Design 1 at south-bay, south and north sides (SS and SN) for (a) 1st floor, (b) 2nd floor, (c) 3rd floor, and (d) roof under SHI090 far-field ground motion at collapse.

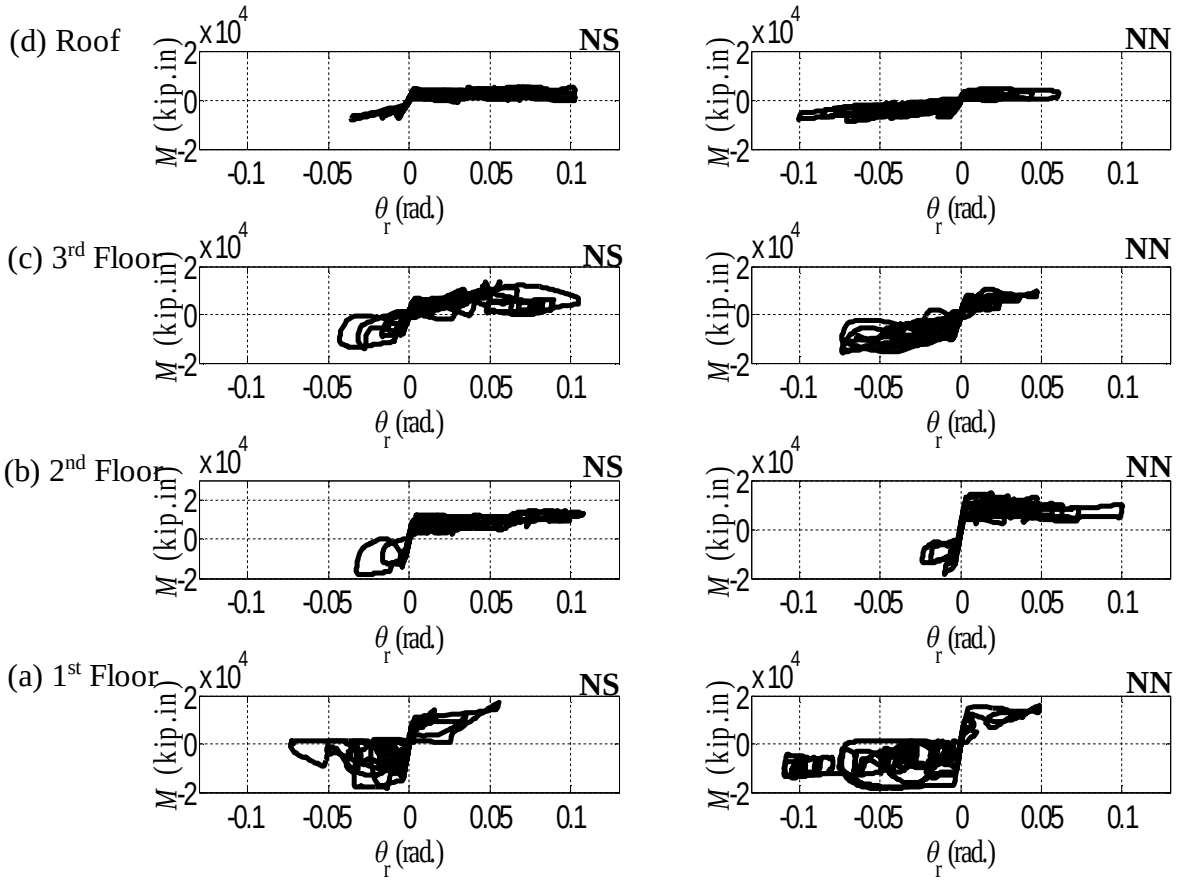

Figure 8. 5. Connection moment versus relative connection rotation (M-θ_r) for SC-MRF Design 1 at north-bay, south and north sides (NS and NN) for (a) 1st floor, (b) 2nd floor, (c) 3rd floor, and (d) roof under SHI090 far-field ground motion at collapse.

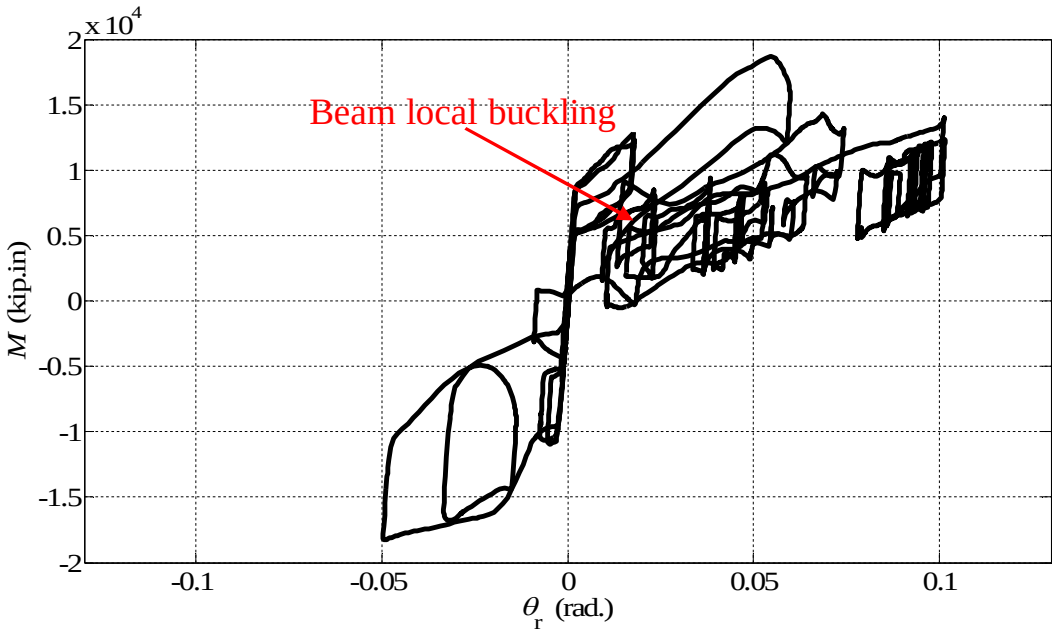

Figure 8. 6. Connection moment vs. relative connection rotation (M-θ_r) for SC-MRF Design 1 at 1st floor south-bay, south side (SS) under SHI090 far-field ground motion at collapse.

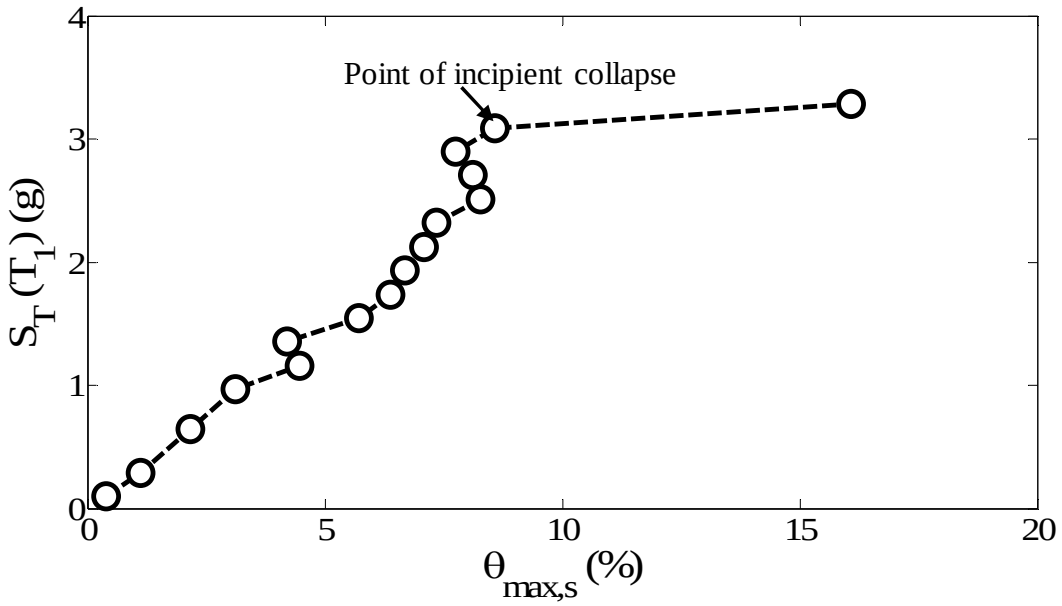

Figure 8. 7. Incremental dynamic analysis response plot of spectral acceleration versus maximum story drift ratio ($S_T(T_1)$-$\Theta_{max,S}$) for SC-MRF Design 1 under SHI090 far-field ground motion.

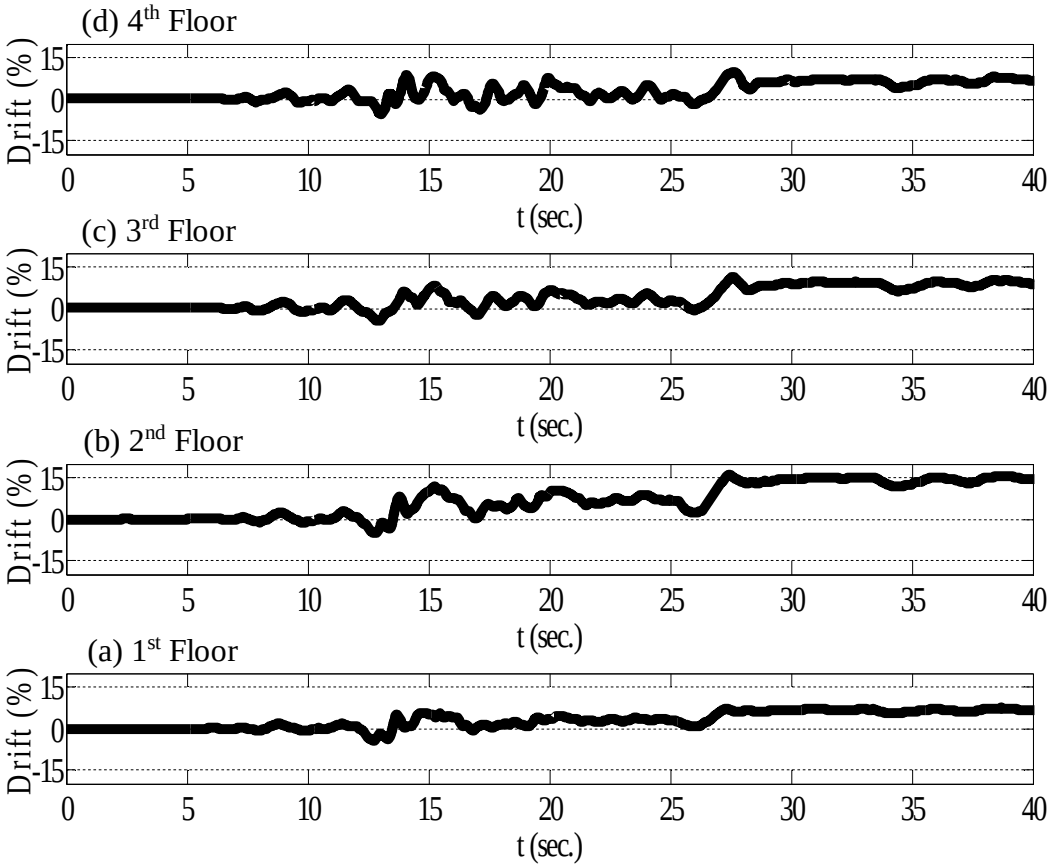

Figure 8. 8. Story drift time history for SC-MRF Design 1 at (a) 1st floor, (b) 2nd floor, (c) 3rd floor, and (d) roof under SHI090 far-field ground motion at collapse.

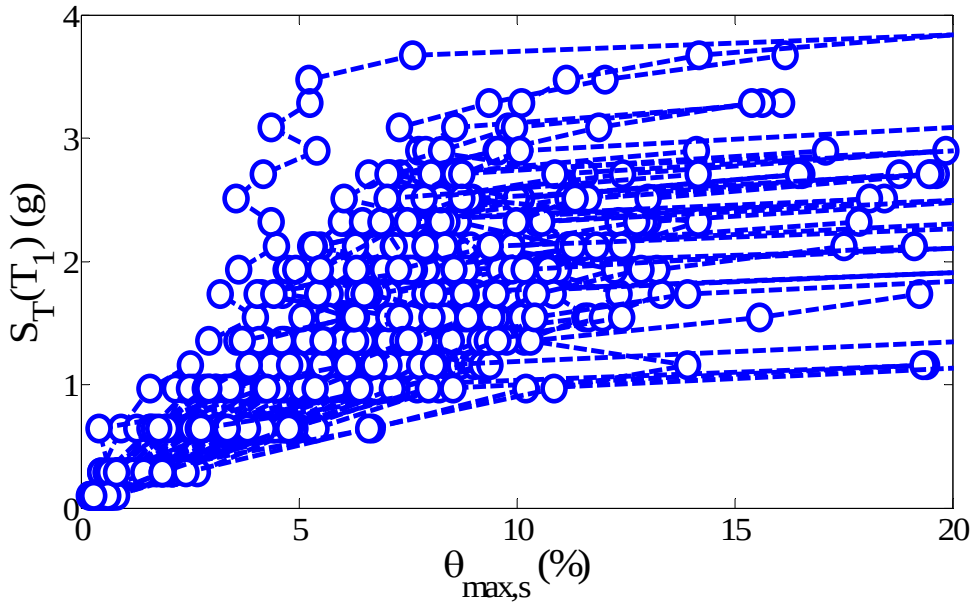

Figure 8. 9. Incremental dynamic analysis response plot of spectral acceleration versus maximum story drift ratio ($S_T(T_1)$-$\Theta_{max,S}$) for SC-MRF Design 1, far-field ground motions.

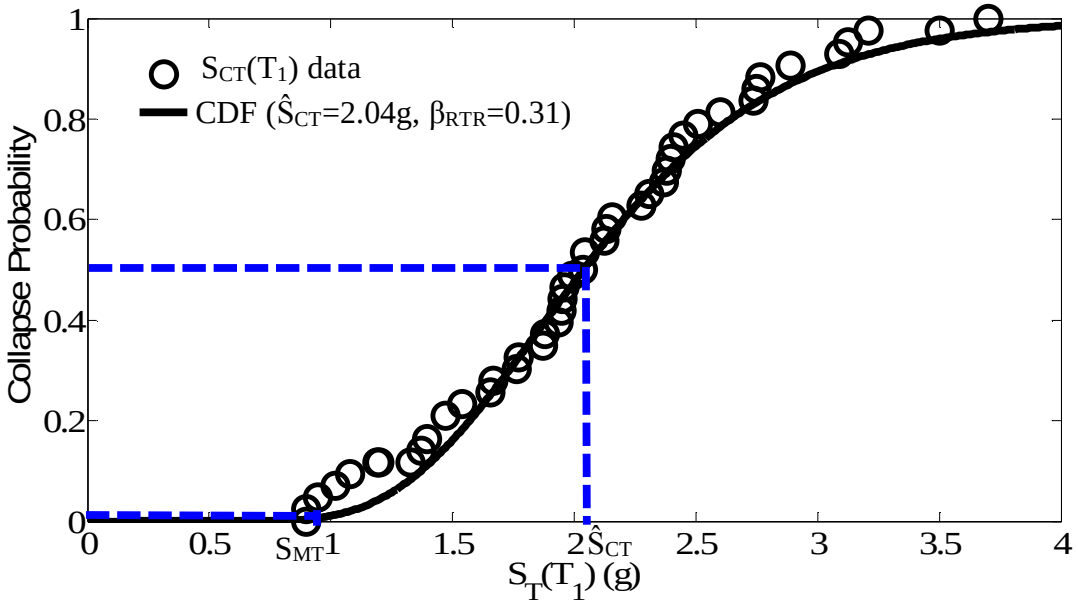

Figure 8. 10. Collapse fragility curve for SC-MRF Design 1, $S_{CT}(T_1)$ based on minimum of $S_T(T_1)$ at incipient collapse and 10% maximum story drift, far-field ground motions.

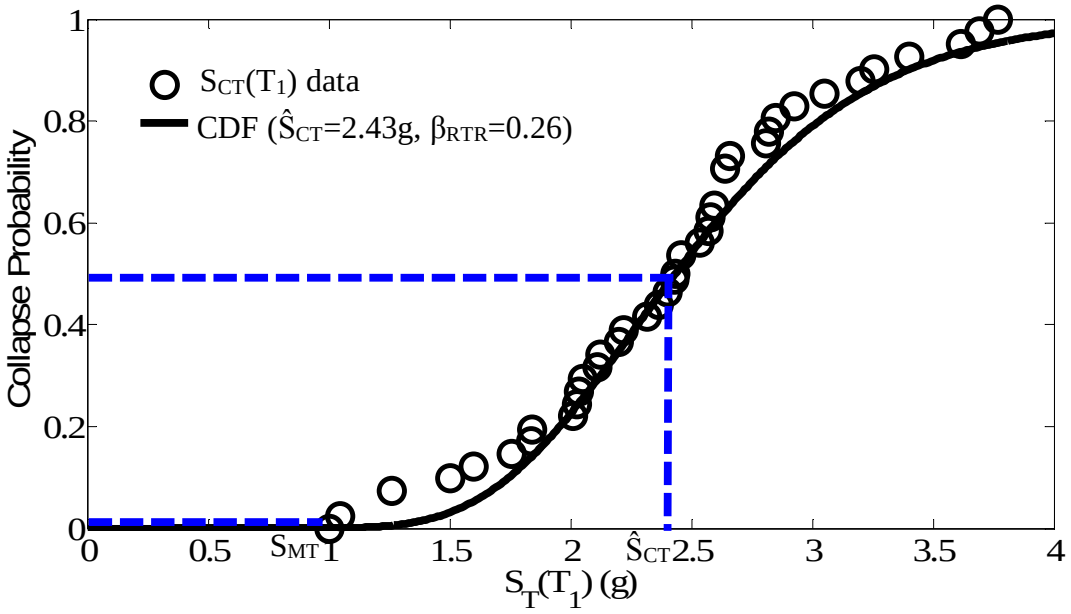

Figure 8. 11. Collapse fragility curve for SC-MRF Design 1, $S_{CT}(T_1)$ based on minimum of $S_T(T_1)$ at incipient collapse and 15% maximum story drift, far-field ground motions.

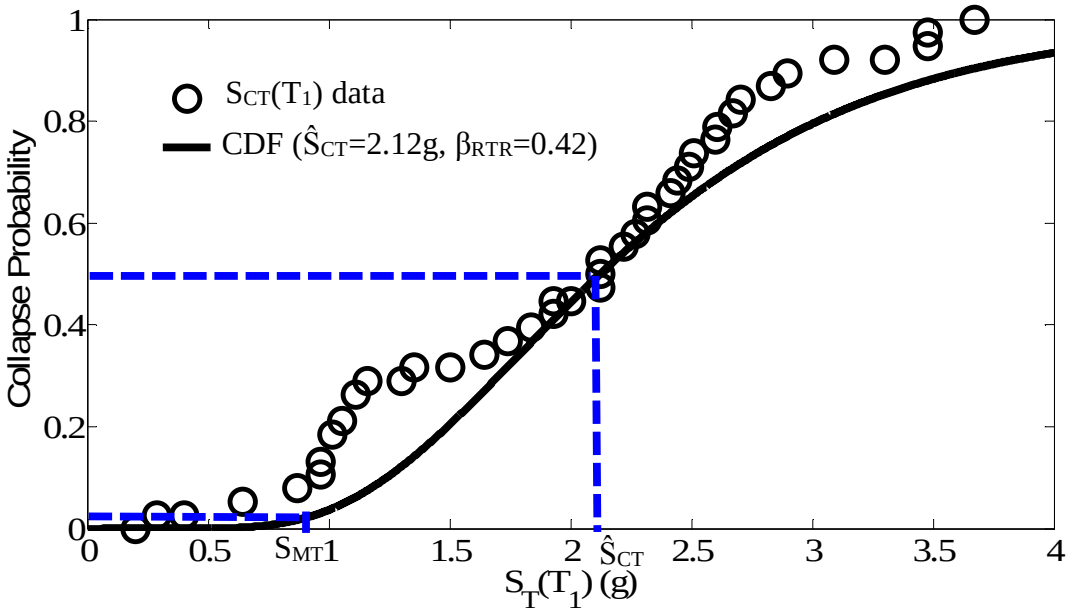

Figure 8. 12. Collapse fragility curve for SC-MRF Design 1, $S_{CT}(T_1)$ based on minimum of $S_T(T_1)$ at incipient collapse and at which an 80% slope reduction in the initial slope of the IDA curve takes place, far-field ground motions.

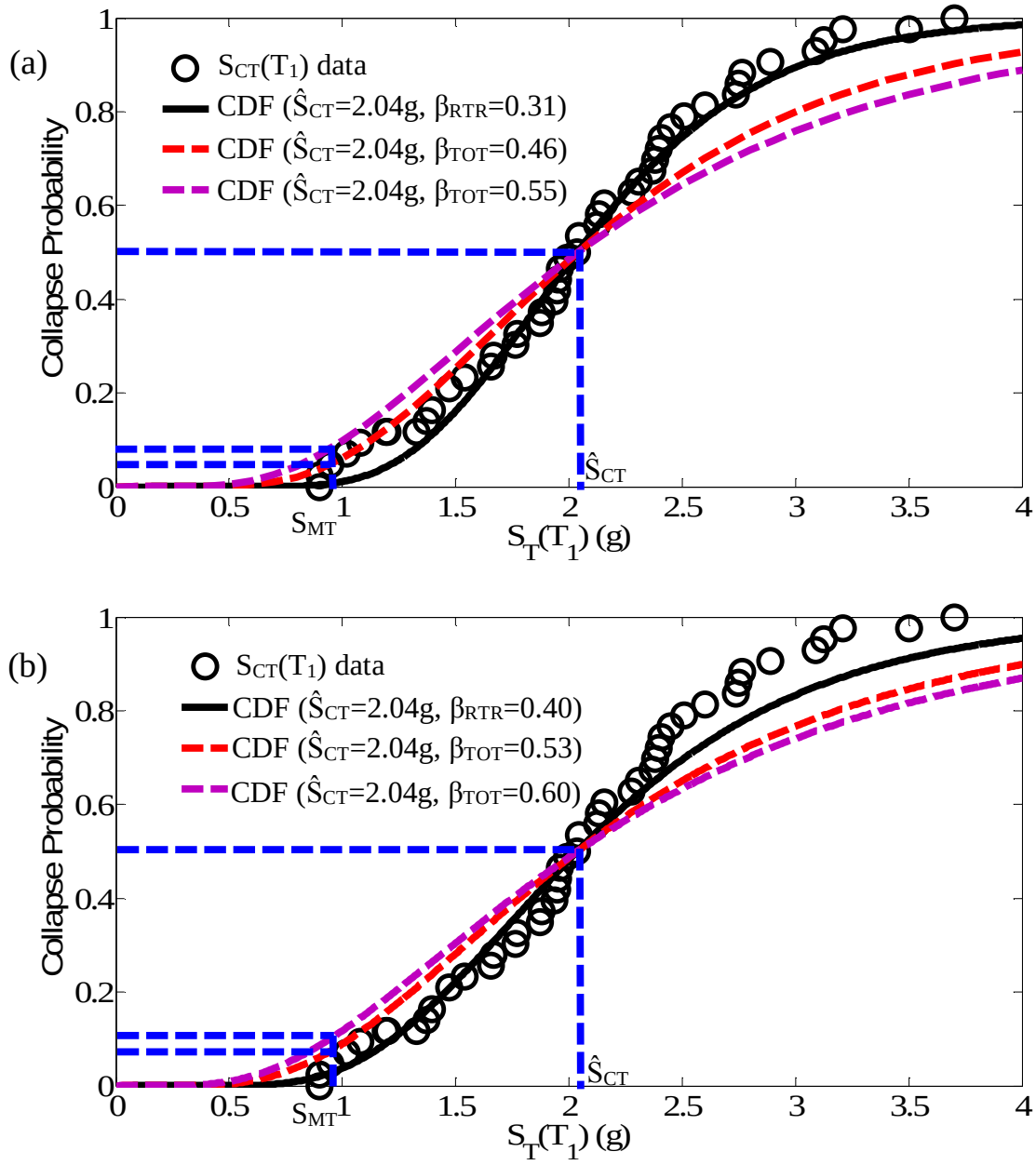

Figure 8. 13. SC-MRF Design 1: (a) collapse fragility curves using β_{RTR}=0.31; (b) collapse fragility curves using β_{RTR}=0.4; $S_{CT}(T_1)$ based on minimum of $S_T(T_1)$ at incipient collapse and 10% maximum story drift, far-field ground motions.

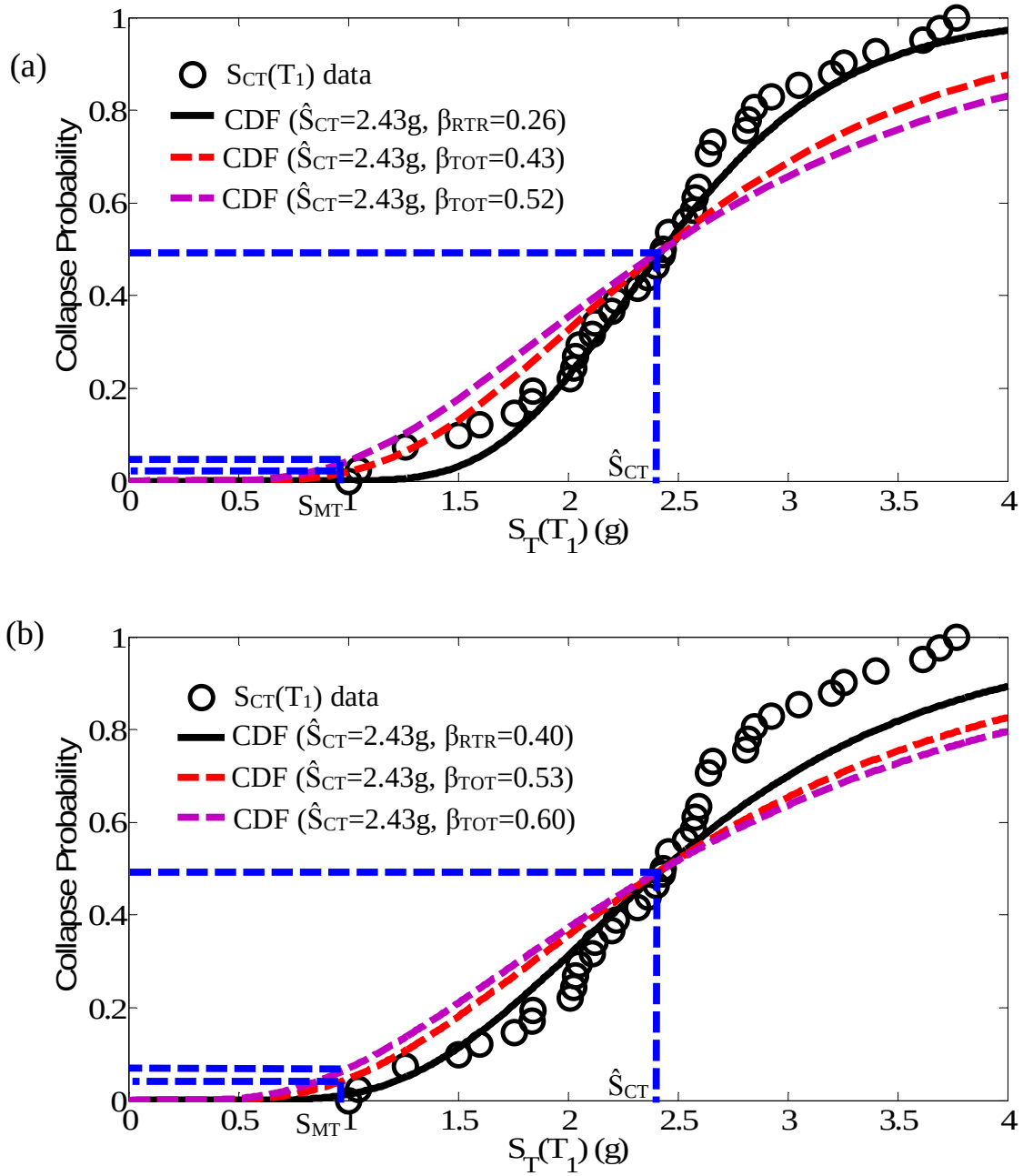

Figure 8. 14. SC-MRF Design 1: (a) collapse fragility curves using β_{RTR}=0.26; (b) collapse fragility curves using β_{RTR}=0.4; $S_{CT}(T_1)$ based on minimum of $S_T(T_1)$ at incipient collapse and 15% maximum story drift, far-field ground motions.

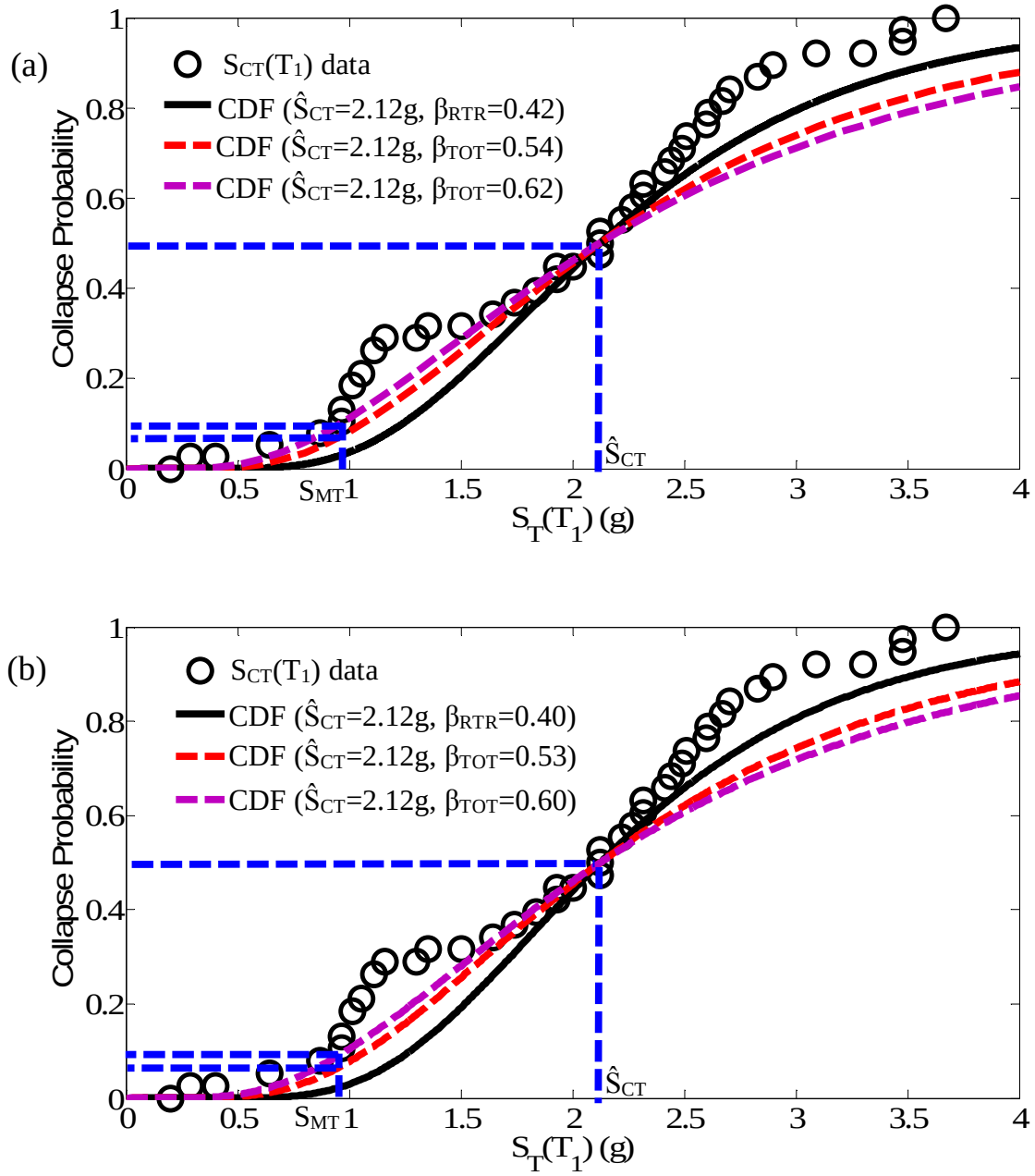

Figure 8. 15. SC-MRF Design 1: (a) collapse fragility curves using β_{RTR}=0.42; (b) collapse fragility curves using β_{RTR}=0.4; $S_{CT}(T_1)$ based on minimum of $S_T(T_1)$ at incipient collapse and at which an 80% slope reduction in the initial slope of the IDA curve takes place, far-field ground motions.

(a)

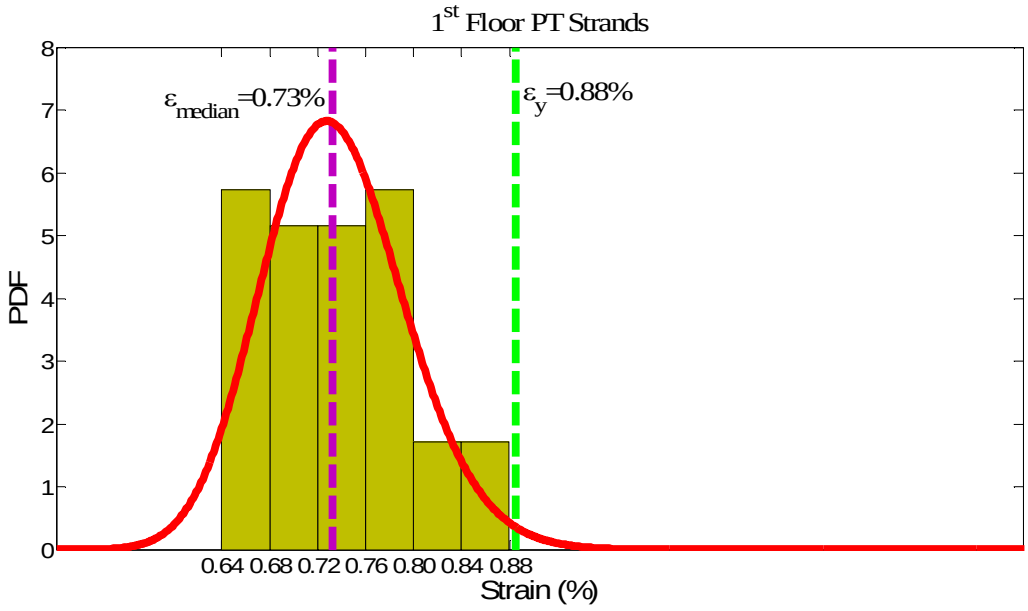
1st Floor PT Strands
εmedian=0.73%
εy=0.88%
PDF
0
1
2
3
4
5
6
7
8
0.64 0.68 0.72 0.76 0.80 0.84 0.88
Strain (%)

(b)

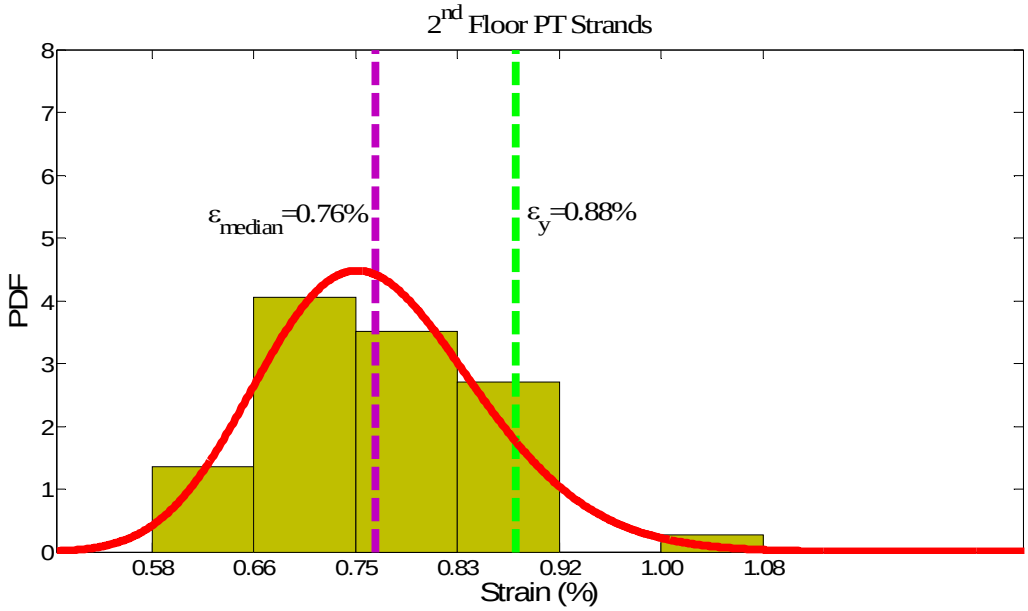
2nd Floor PT Strands
εmedian=0.76%
εy=0.88%
PDF
0
1
2
3
4
5
6
7
8
0.58
0.66
0.75
0.83
0.92
1.00
1.08
Strain (%)

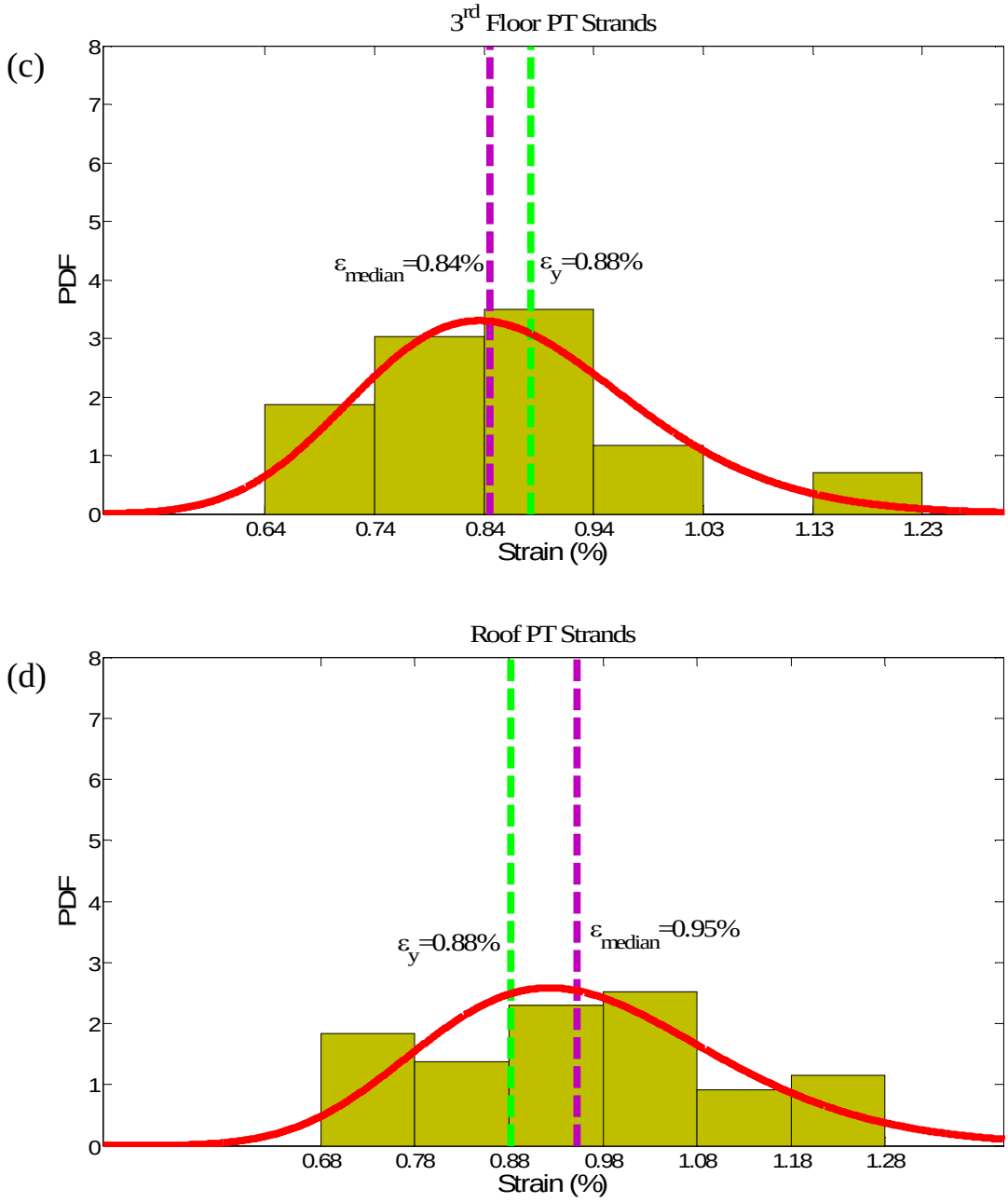

Figure 8. 16. Frequency distribution plots and PDFs of PT strand maximum strain ε_{max}: (a) 1st floor, (b) 2nd floor, (c) 3rd floor, and (d) Roof for SC-MRF Design 1, far-field ground motions.

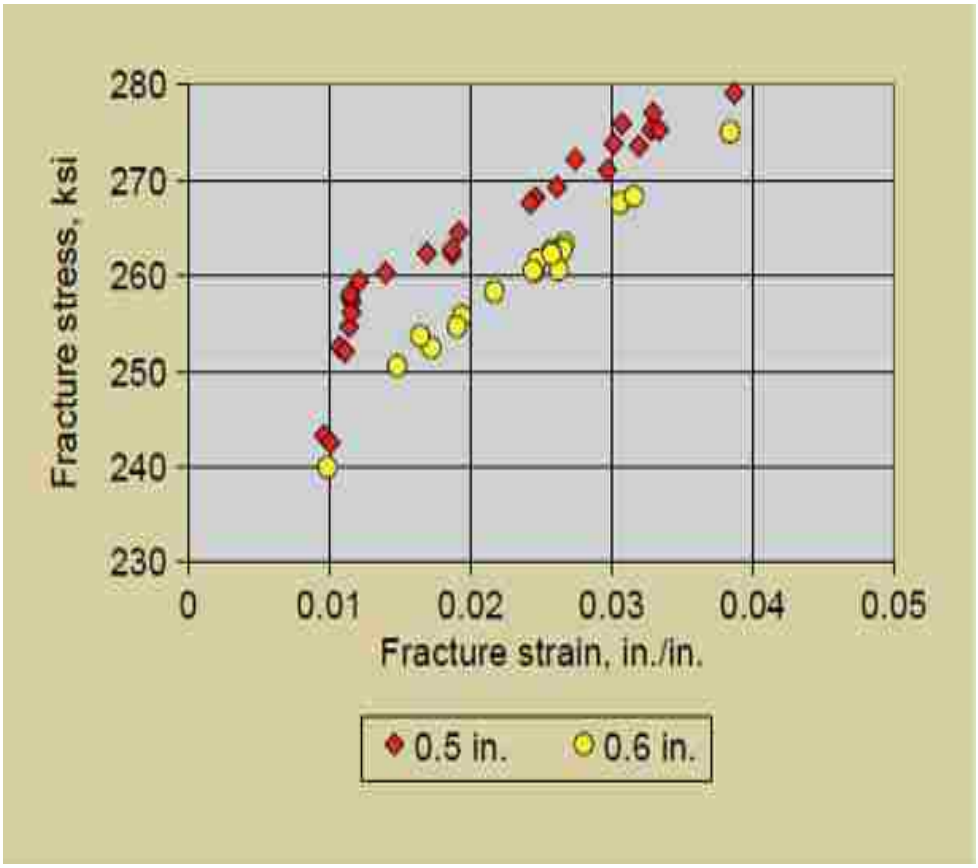

Figure 8. 17. Strand fracture stress vs. fracture strain, Walsh and Kurama (2010).

(a)

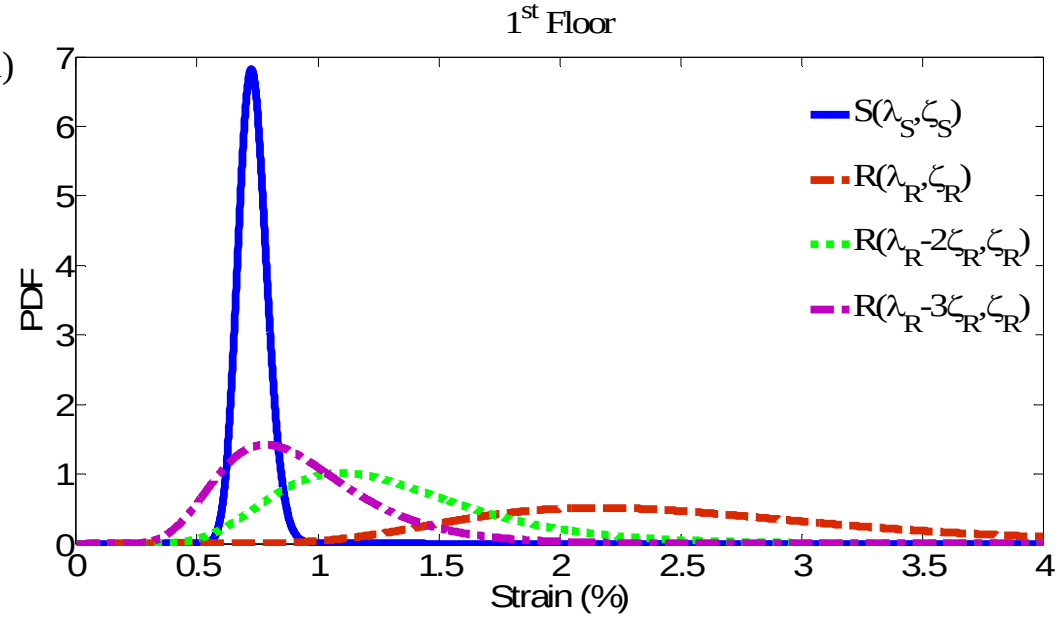
1st Floor
PDF
Strain (%)
S(λS,ζS)
R(λR,ζR)
R(λR-2ζR,ζR)
R(λR-3ζR,ζR)

(b)

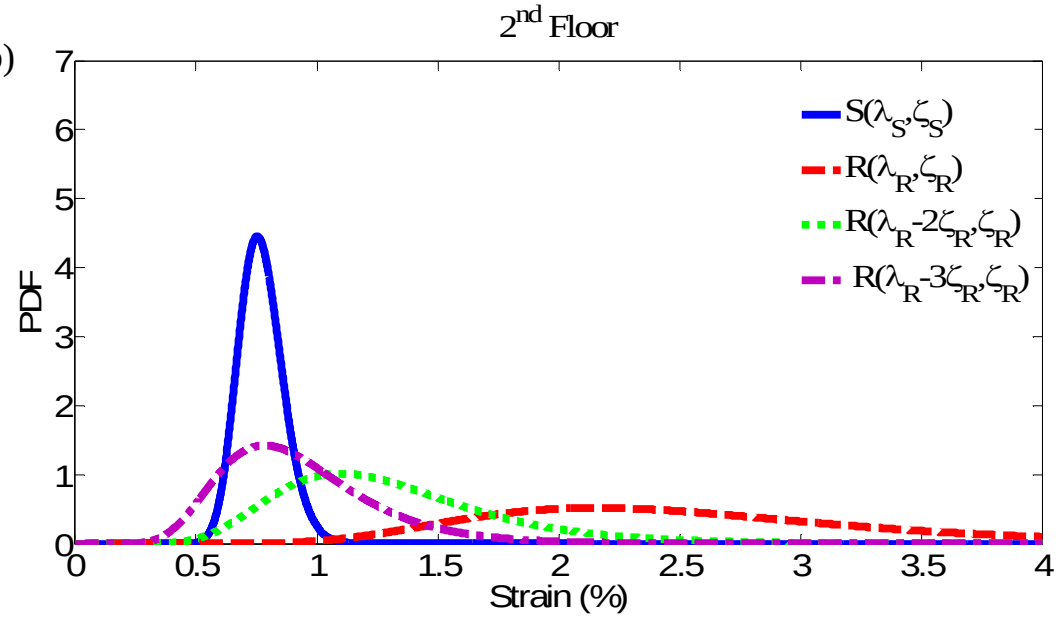
2nd Floor
PDF
Strain (%)
S(λS,ζS)
R(λR,ζR)
R(λR-2ζR,ζR)
R(λR-3ζR,ζR)

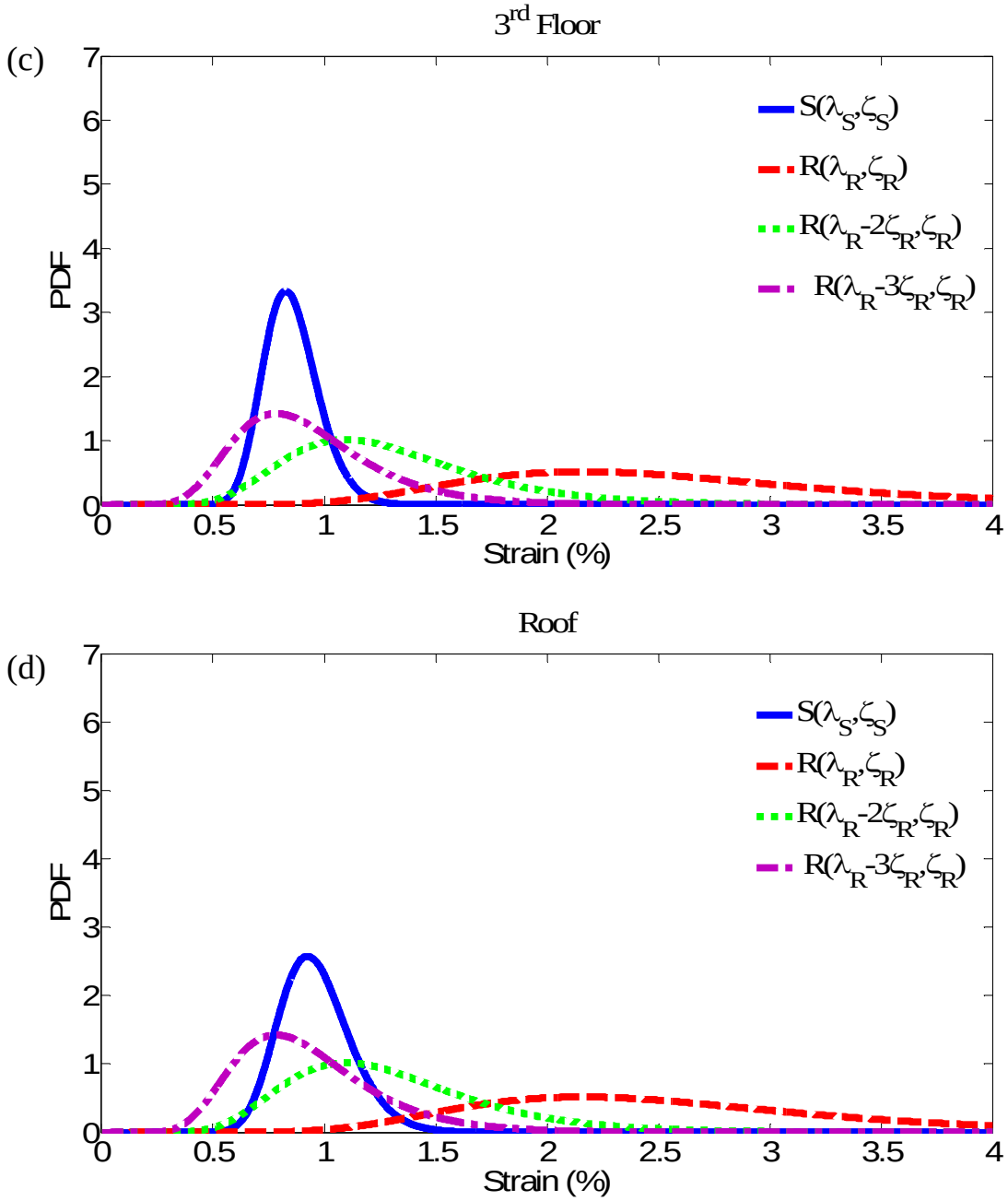

Figure 8. 18. PDFs for PT maximum strand strain (S) and strand fracture strain (R): (a) 1st floor, (b) 2nd floor, (c) 3rd floor, and (d) Roof for SC-MRF Design 1, far-field ground motions.

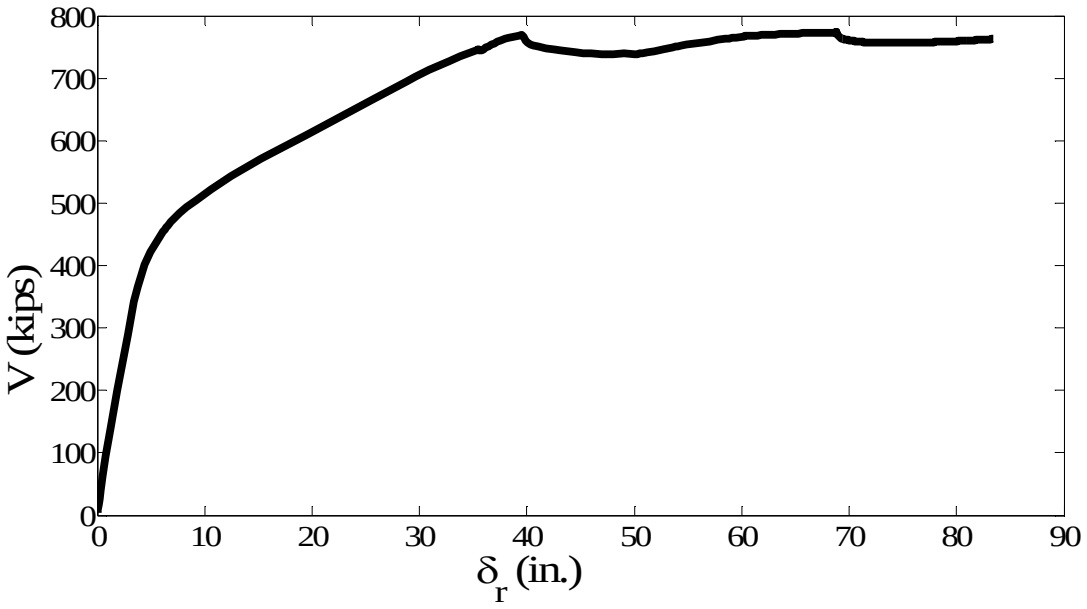

Figure 8. 19. Pushover curve for SC-MRF Design 1.

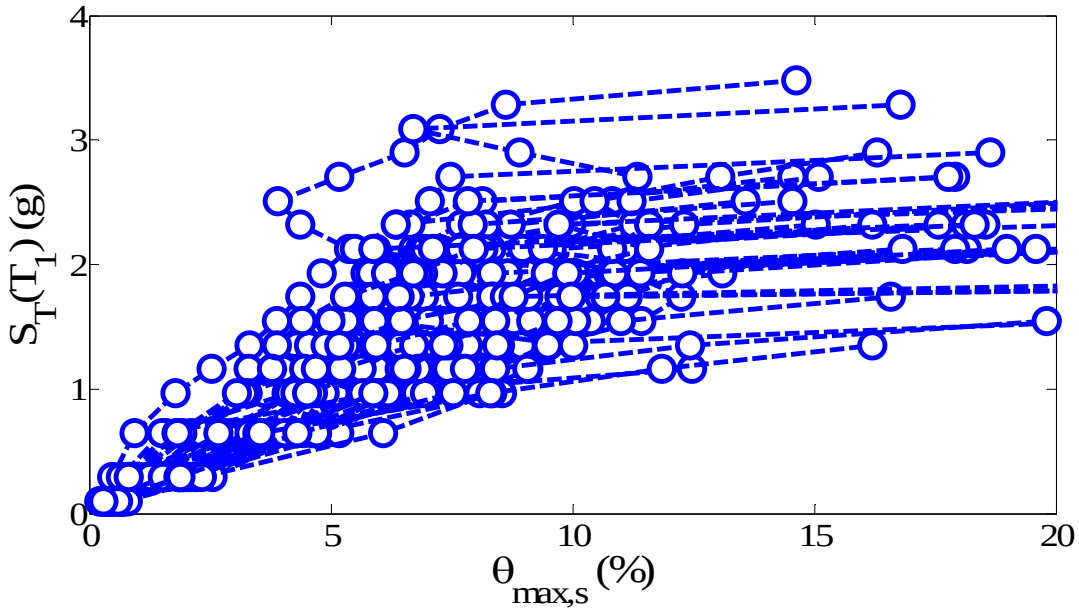

Figure 8. 20. Incremental dynamic analysis response plot of spectral acceleration versus maximum story drift ratio ($S_T(T_1)$-$\Theta_{max,S}$) for SC-MRF Design 2, far-field ground motions.

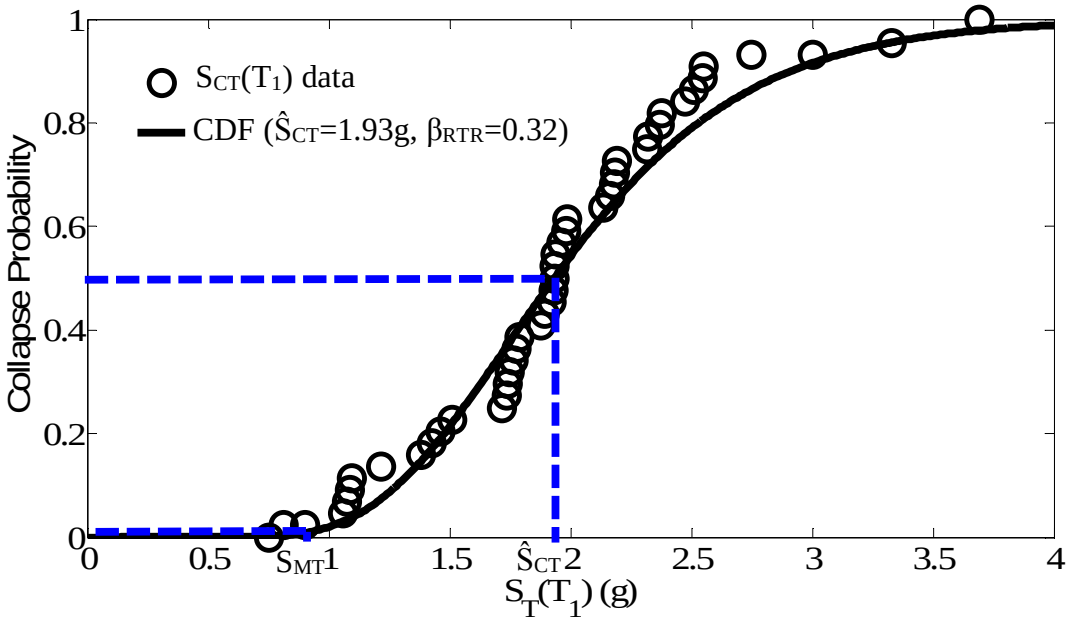

Figure 8. 21. Collapse fragility curve for SC-MRF Design 2, $S_{CT}(T_1)$ based on minimum of $S_T(T_1)$ at incipient collapse and 10% maximum story drift, far-field ground motions.

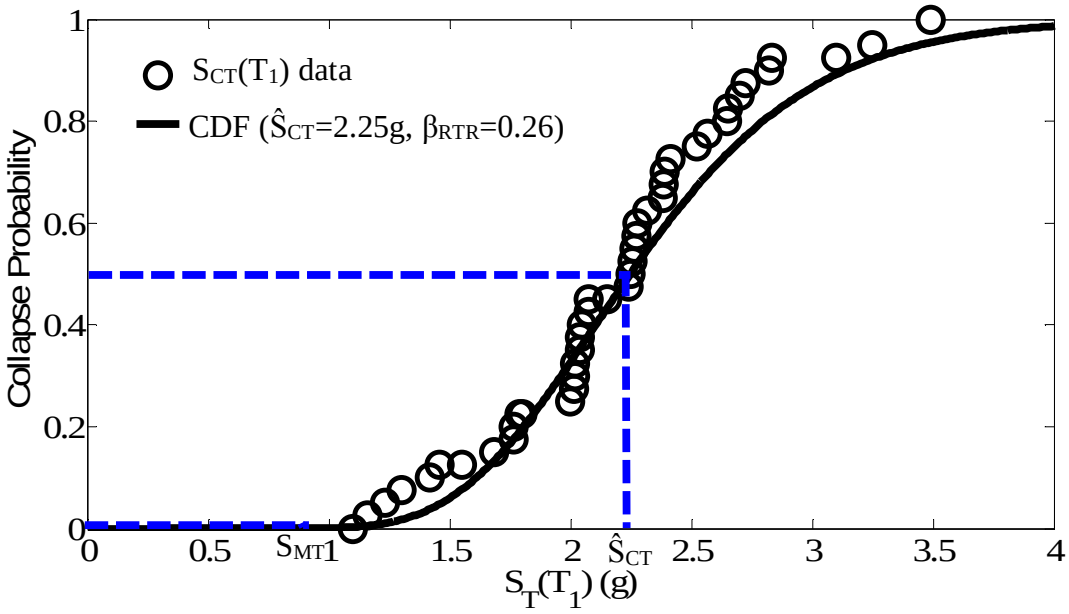

Figure 8. 22. Collapse fragility curve for SC-MRF Design 2, $S_{CT}(T_1)$ based on minimum of $S_T(T_1)$ at incipient collapse and 15% maximum story drift, far-field ground motions.

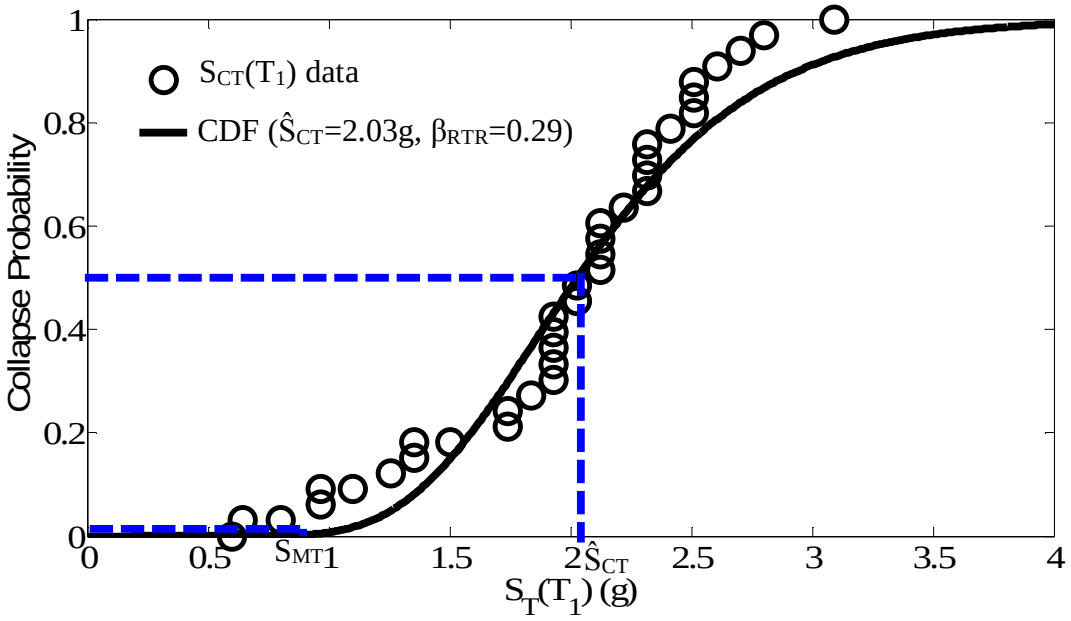

Figure 8. 23. Collapse fragility curve for SC-MRF Design 2, $S_{CT}(T_1)$ based on minimum of $S_T(T_1)$ at incipient collapse and at which an 80% slope reduction in the initial slope of the IDA curve takes place, far-field ground motions.

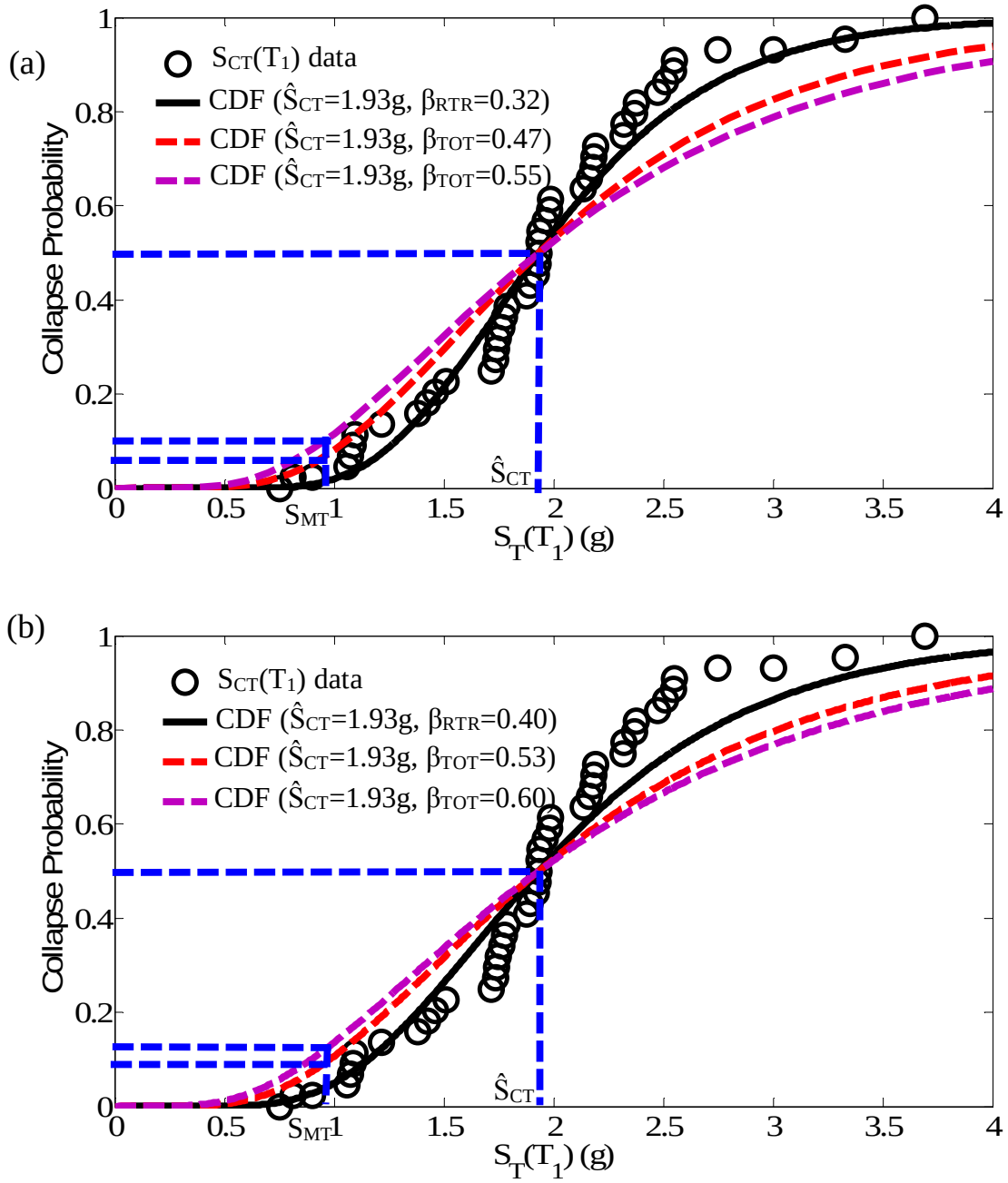

Figure 8. 24. SC-MRF Design 2: (a) collapse fragility curves using β_{RTR}=0.32; (b) collapse fragility curves using β_{RTR}=0.4; $S_{CT}(T_1)$ based on minimum of $S_T(T_1)$ at incipient collapse and 10% maximum story drift, far-field ground motions.

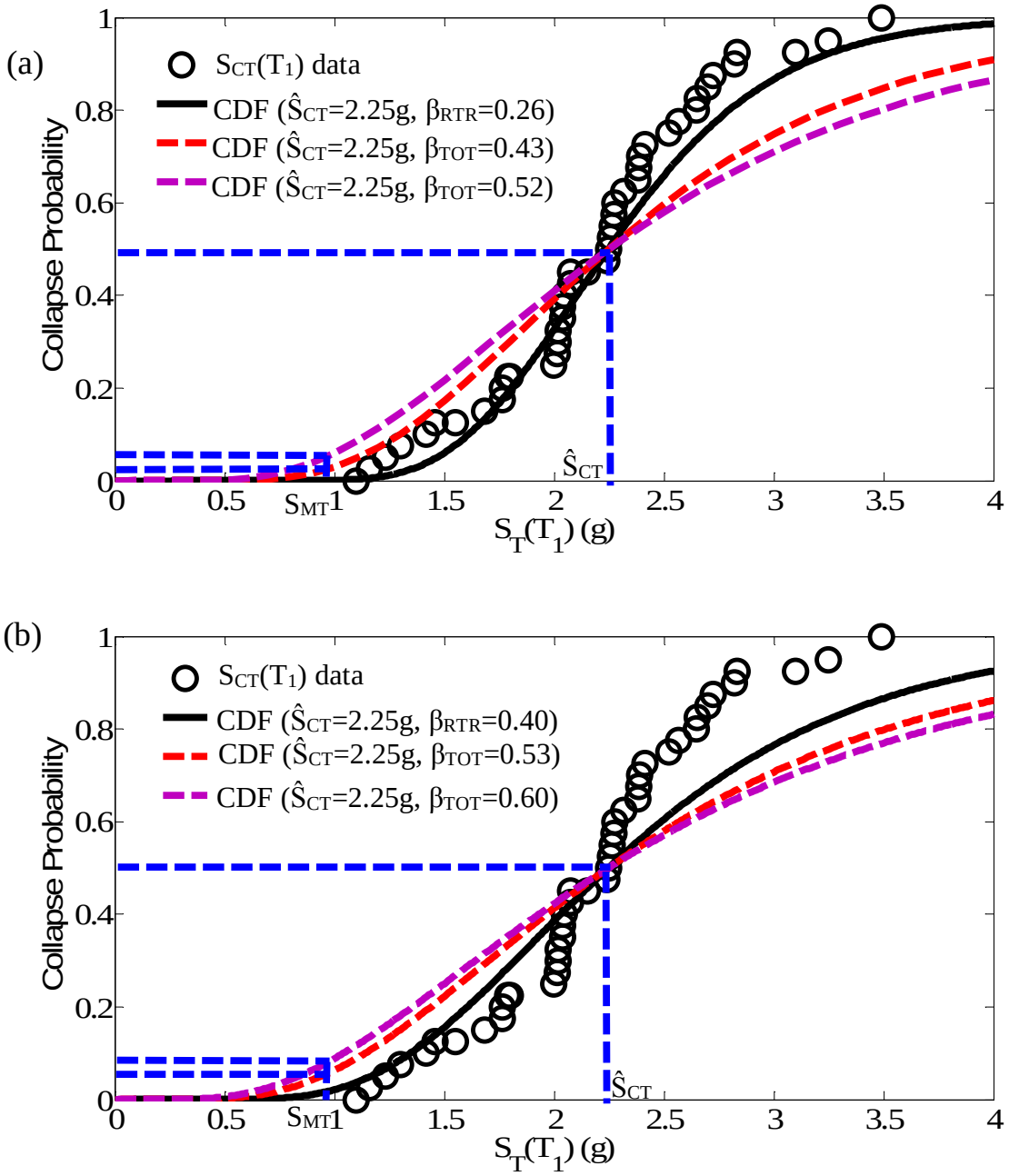

Figure 8. 25. SC-MRF Design 2: (a) collapse fragility curves using β_{RTR}=0.26; (b) collapse fragility curves using β_{RTR}=0.4; $S_{CT}(T_1)$ based on minimum of $S_T(T_1)$ at incipient collapse and 15% maximum story drift, far-field ground motions.

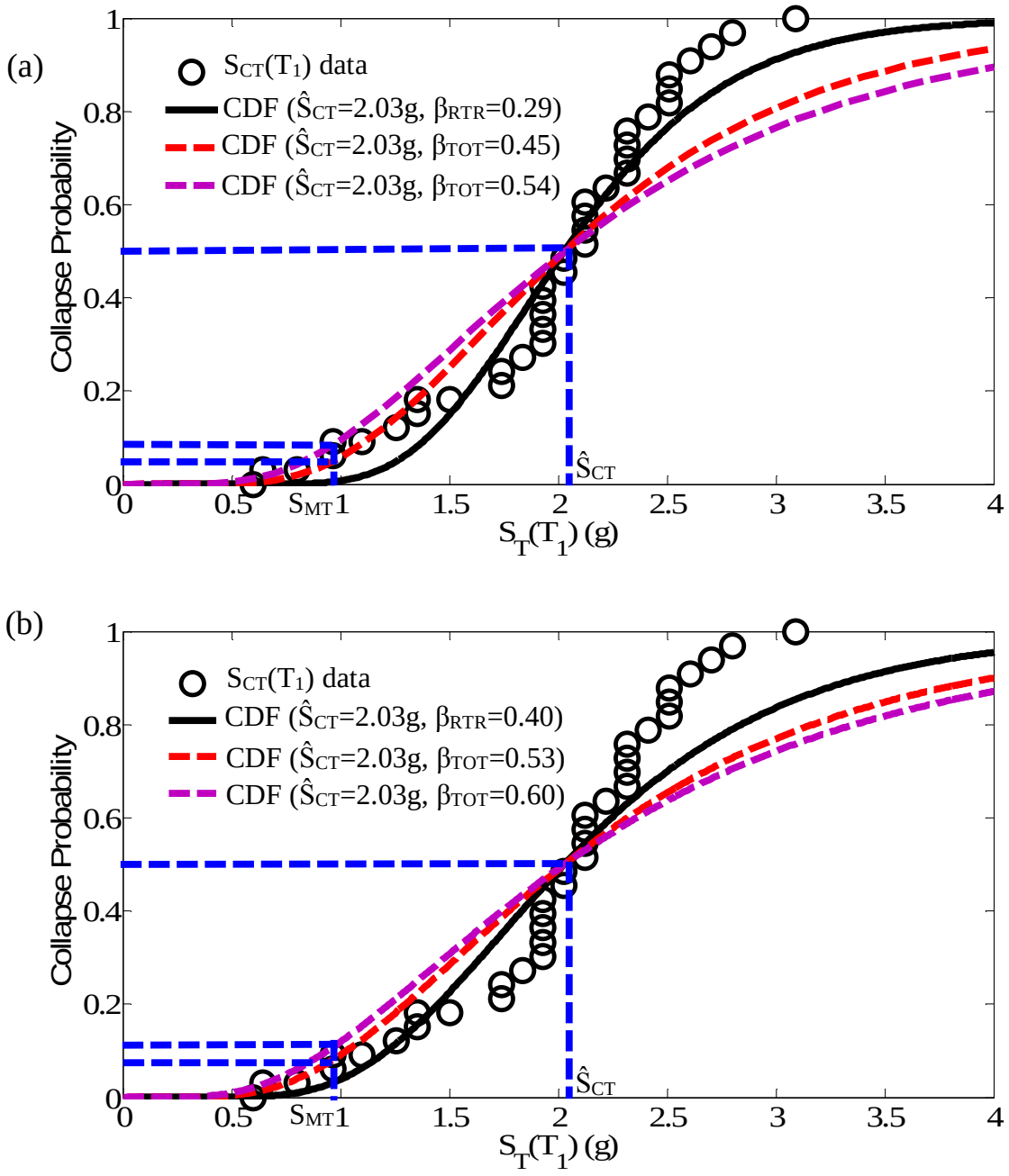

Figure 8. 26. SC-MRF Design 2: (a) collapse fragility curves using β_{RTR}=0.26; (b) collapse fragility curves using β_{RTR}=0.4; $S_{CT}(T_1)$ based on minimum of $S_T(T_1)$ at incipient collapse and at which an 80% slope reduction in the initial slope of the IDA curve takes place, far-field ground motions.

(a)

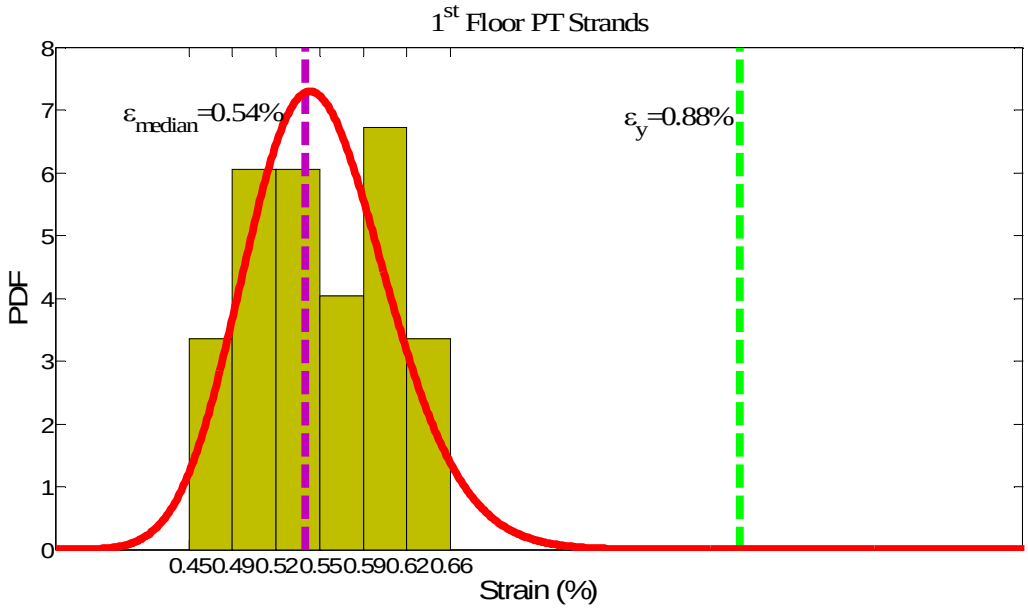
1st Floor PT Strands
εmedian=0.54%
εy=0.88%
PDF
0
1
2
3
4
5
6
7
8
0.45 0.49 0.52 0.55 0.59 0.62 0.66
Strain (%)

(b)

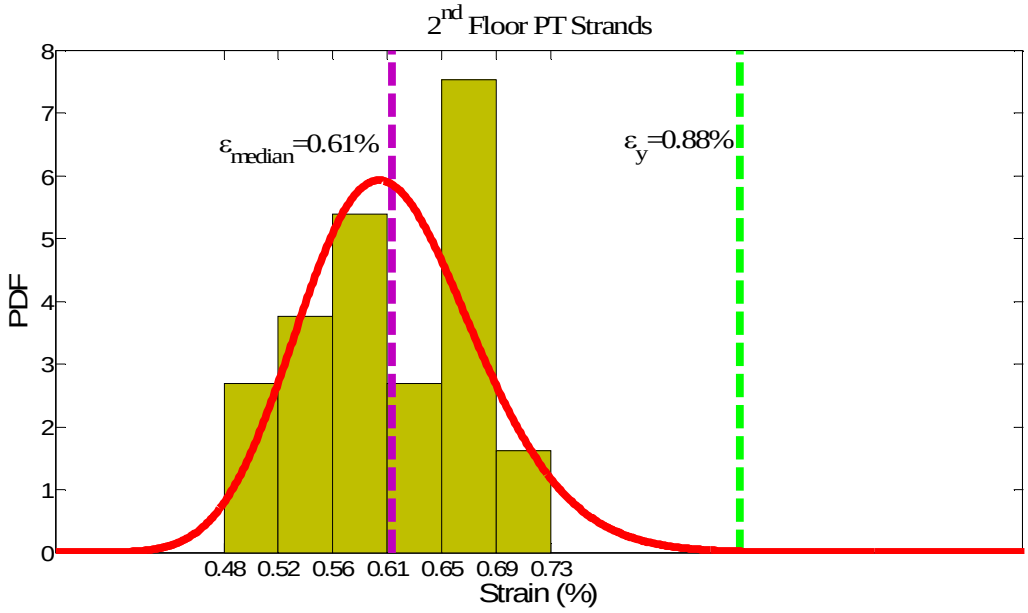
2nd Floor PT Strands
εmedian=0.61%
εy=0.88%
PDF
0
1
2
3
4
5
6
7
8
0.48 0.52 0.56 0.61 0.65 0.69 0.73
Strain (%)

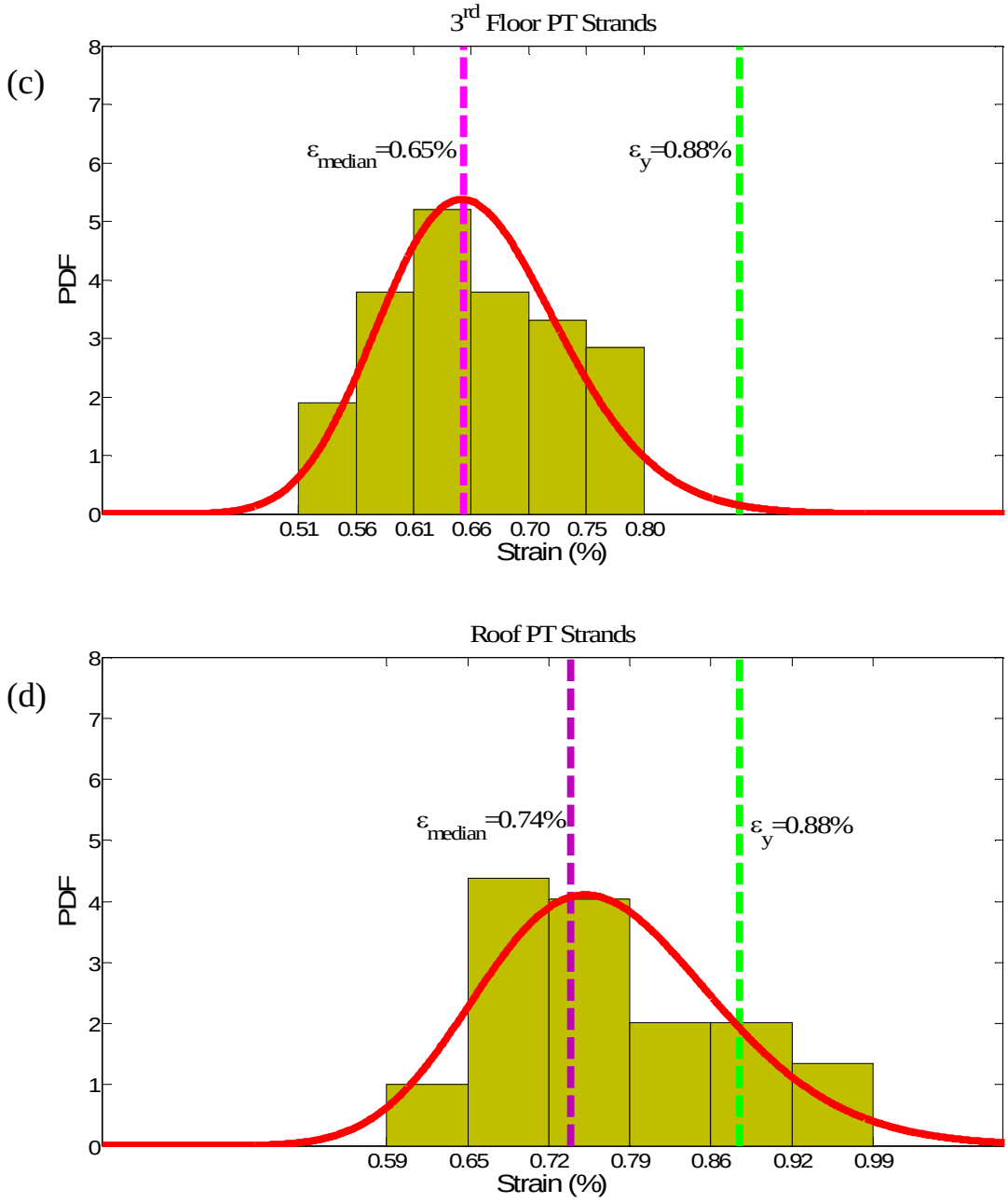

Figure 8. 27. Frequency distribution plots and PDFs of PT strand maximum strain ε_{max}: (a) 1st floor, (b) 2nd floor, (c) 3rd floor, and (d) Roof for SC-MRF Design 2, far-field ground motions.

(a)

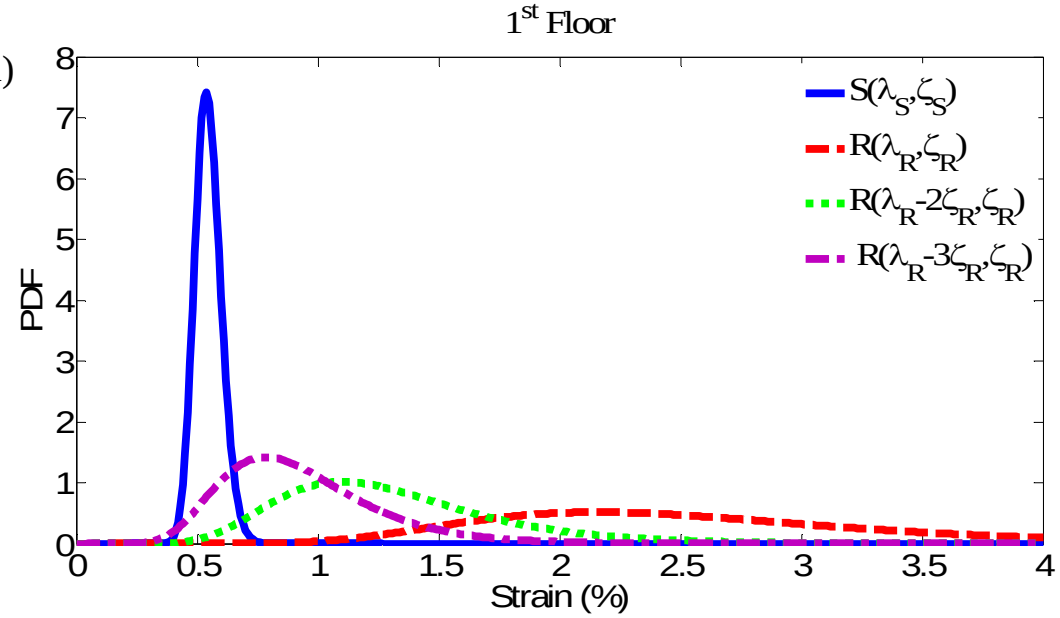
1st Floor
PDF
Strain (%)
S(λS,ζS)
R(λR,ζR)
R(λR-2ζR,ζR)
R(λR-3ζR,ζR)

(b)

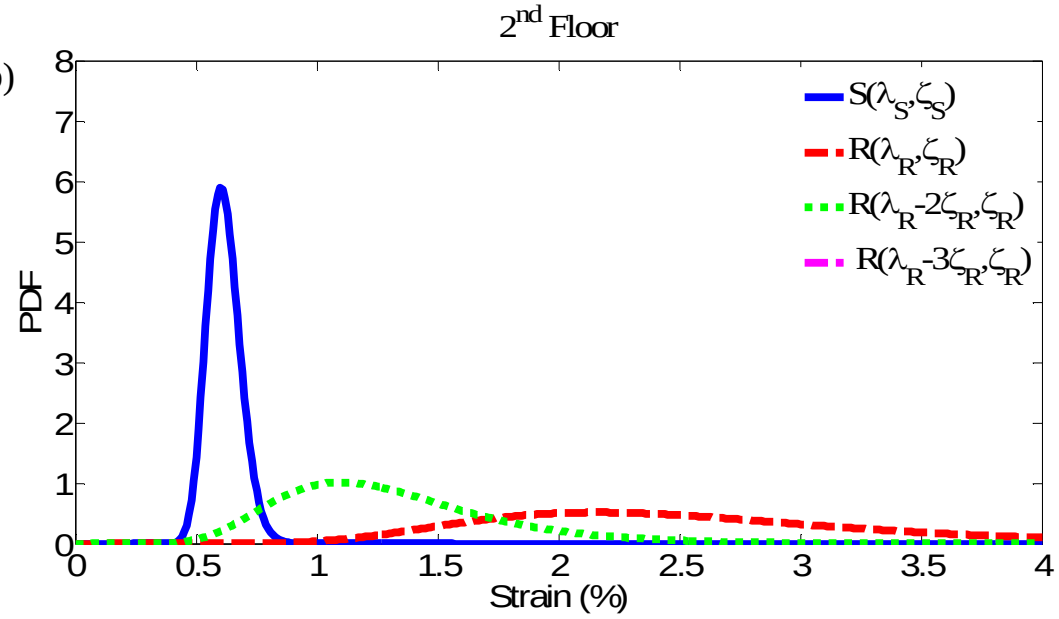
2nd Floor
PDF
Strain (%)
S(λS,ζS)
R(λR,ζR)
R(λR-2ζR,ζR)
R(λR-3ζR,ζR)

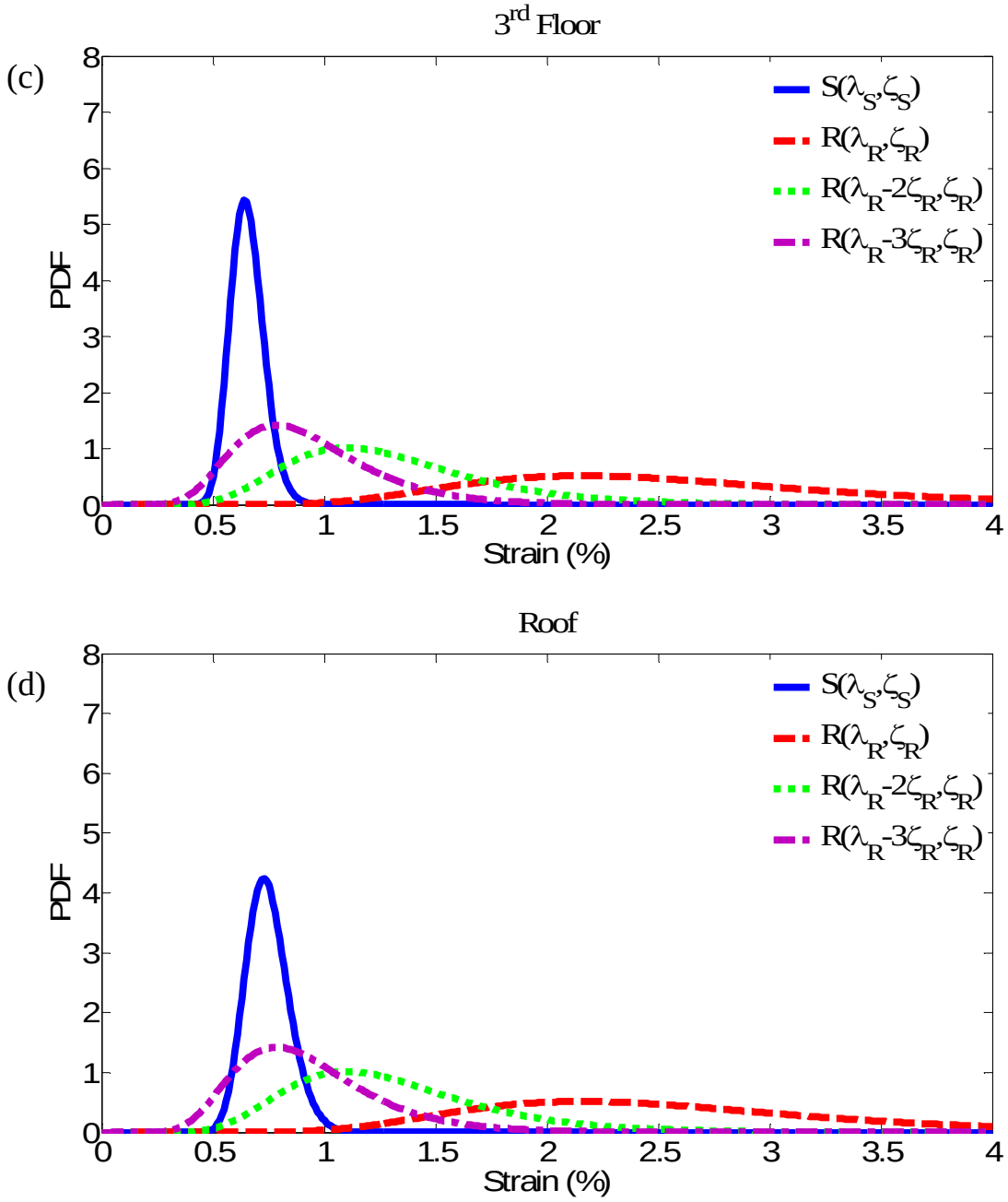

Figure 8. 28. PDFs for PT maximum strand strain (S) and strand fracture strain (R): (a) 1st floor, (b) 2nd floor, (c) 3rd floor, and (d) Roof for SC-MRF Design 2, far-field ground motions.

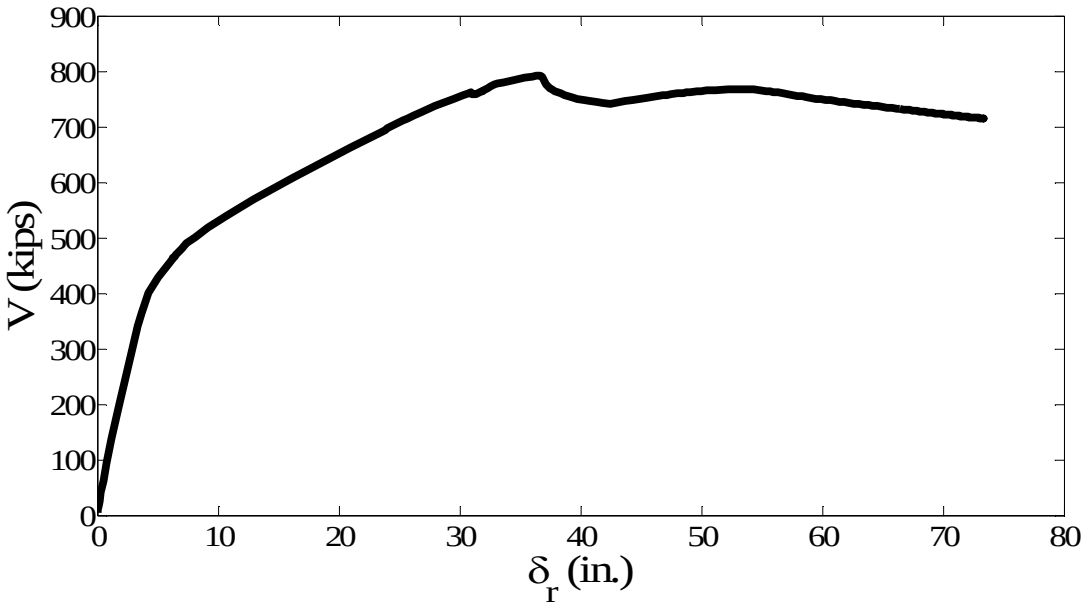

Figure 8. 29. Pushover curve for SC-MRF Design 2.

Chapter 9

Seismic Collapse Assessment of SMRF: Far-Field Ground Motions

9.1. General

This chapter presents the results for the seismic collapse assessment of the SMRF. The FEMA P695 collapse assessment methodology presented in Chapter 7 is used to determine the seismic collapse resistance of SMRF under the ensemble of far-field ground motions. The IDA curves and fragility curves are presented and discussed in this chapter.

9.2. Results for SMRF

9.2.1. IDA Results

Figure 9.1 shows the IDA curves for the SC-MRF Design 1 under 44 far-field ground motions. As discussed in Chapter 7, the horizontal axis shows the maximum inter-story drift, $\Theta_{max,s}$, and the vertical axis presents the spectral acceleration, $S_T(T_1)$, measured by 5% damped median spectral acceleration intensity of the far-field record set at the fundamental period of the structure, T_1=0.932 sec. Each data point determines the maximum story drift at a given $S_T(T_1)$.

9.2.2. Fragility Curves

The fragility curves obtained from the set of IDA curves for different collapse scenarios are presented below. Figure 9.2 shows the fragility curve when $SCT(T_1)$ is based on the smaller of the $S_T(T_1)$ value at the end of the corresponding IDA curve where

convergence failed in the analysis due to incipient collapse and the $S_T(T_1)$ value at the transient story drift of 10%. The median collapse capacity is formed to be $\hat{S}_{CT}$=1.96g. The collapse fragility curve obtained by fitting a CDF, assuming a lognormal distribution, to the ranked S_{CT} data points is shown in Figure 9.2 where the $\hat{S}_{CT}$ and the associated standard deviation β_{RTR}=0.30 of the natural logarithm of the data are indicated in Figure 9.2. The MCE code specified spectral acceleration intensity (S_{MT}) at the fundamental period (i.e., the design period defined in ASCE7-10) of the structure, T_1=0.932 sec. is 0.966g, and consequently CMR=2.03.

Similarly, Figure 9.3 shows the fragility curve when $S_{CT}(T_1)$ is based on the smaller of the $S_T(T_1)$ value at the end of the corresponding IDA curve where convergence failed in the analysis due to incipient collapse and the $S_T(T_1)$ value at the transient story drift of 15%. The results have a $\hat{S}_{CT}$=2.33g and β_{RTR}=0.29. The CMR is 2.41.

Figure 9.4 shows the fragility curve when $S_{CT}(T_1)$ is based on the smaller of the $S_T(T_1)$ value at the end of the corresponding IDA curve where convergence failed in the analysis due to incipient collapse and the $S_T(T_1)$ value at which an 80% slope reduction in the initial slope of the IDA curve takes place for a ground motion. The results have a $\hat{S}_{CT}$=2.08g and β_{RTR}=0.30. The CMR is 2.15.

The sensitivity of $S_{CT}(T_1)$ data to the incipient collapse definition is seen in Figures 9.2 through 9.4 led to different values for the $\hat{S}_{CT}$, and consequently different CMR values. The variability of $S_{CT}(T_1)$ associated with the incipient collapse affects $\hat{S}_{CT}$ and the amount of uncertainty corresponding to record to record (RTR) variability, β_{RTR}, results in a variability in the probability of collapse at a given hazard level. The probability of collapse at the MCE level considering other sources of uncertainty in

addition to RTR variability is discussed and presented later for different collapse scenarios. The results of different cases presented above are compared in Chapter 11.

9.2.3. Fragility Curves for Different Amounts of Uncertainty

In this section fragility curves are developed considering the sources of uncertainty. To compute the β_{TOT} per Equation (7.6), β_{RTR} is based on the data. In addition, the value of β_{RTR}=0.4 is also considered in accordance with FEMA P695. The other sources of uncertainty are given numerical values by selecting qualitative ratings defined in FEMA P695. Good quality was assumed for modeling and test data, where β_{MDL}=0.2 and β_{TD}=0.2. For the design requirement, two different qualities were assumed, good (where β_{DR}=0.2) and fair (where β_{DR}=0.35). The two cases were assumed similar to Chapter 8 to compare with the corresponding cases presented for SC-MRF Designs 1 and 2. Table 9.1 summarizes the values for the different combinations of uncertainty to calculate the total amount of uncertainty. The collapse point assumptions are named similar to Chapter 8 as 10% story drift, 15% story drift and 80% slope reduction in Table 9.1.

Figure 9.5(a) shows the fragility curves corresponding to $\hat{S}_{CT}$ and β_{TOT} considering β_{RTR}=0.30 where SCT(T_1) is the smaller of the $S_T(T_1)$ value at the end of the corresponding IDA curve where convergence failed in the analysis due to incipient collapse and the $S_T(T_1)$ value at the transient story drift of 10%. The curves are based on assumed lognormal distribution. Note that two different uncertainty qualities are considered for β_{DR} in Figure 9.5(a) as stated previously (β_{DR}=0.2 and β_{DR}=0.35). Figure 9.5(b) shows the fragility curves when the value of β_{RTR}=0.4 is used. The probability of collapse at the MCE level are indicated on the fragility curves while the values are tabulated in Table 9.1. As seen in Table 9.1, the probability of collapse at MCE level

increases for a larger amount of uncertainty β_{TOT}. This can be seen in Figure 9.5 where S_{MT} shows the spectral acceleration at the MCE level. For instance, the probability of collapse at the MCE level is 11.9% and 9.1% for β_{TOT}=0.6 and β_{TOT}=0.53, respectively, in Figure 9.5(b) and Table 9.1.

Figures 9.6(a) and (b) show the corresponding fragility curves where $S_{CT}(T_1)$ is the smaller of the $S_T(T_1)$ value at the end of the corresponding IDA curve where convergence failed in the analysis due to incipient collapse and the $S_T(T_1)$ value at the transient story drift of 15%. β_{RTR}=0.29 and β_{RTR}=0.4 are used for Figures 9.6(a) and (b). The probability of collapse is smaller for this collapse scenario in contrast to the two other incipient collapse definitions. The probability of collapse is larger for higher amount of uncertainty β_{TOT}. For example, the probability of collapse at the MCE level is 7.1% and 4.8% for β_{TOT}=0.6 and β_{TOT}=0.53 (see Table 9.1), respectively, in Figure 9.6(b) where S_{MT} shows the spectral acceleration at the MCE level.

Figures 9.7(a) and (b) show the fragility curves where $S_{CT}(T_1)$ is the smaller of the $S_T(T_1)$ value at the end of the corresponding IDA curve where convergence failed in the analysis due to incipient collapse and the $S_T(T_1)$ value at which an 80% slope reduction in the initial slope of the IDA curve takes place for a ground motion. β_{RTR}=0.30 and β_{RTR}=0.4 are used for Figures 9.7(a) and (b). As seen in Table 9.1, the probability of collapse at MCE level increases for a system with a higher amount of uncertainty β_{TOT}. For instance, the probability of collapse at MCE level is 10.0% and 7.4% for β_{TOT}=0.60 and β_{TOT}=0.53, respectively, in Figure 9.7(b) where S_{MT} shows the spectral acceleration at the MCE level.

The fragility curves and the probability of collapse at MCE level are discussed further

and compared in Chapter 11.

9.2.4. Adjusted CMR

Similar to the SC-MRFs presented in Chapter 8, to find μ_T for the SMRF per Equation (7.3) a pushover analysis is performed. The results are shown in Figure 9.8. Table 9.2 summarizes the parameters needed to find the SSF. The ACMR values can be found by multiplying the CMR values for the SMRF by SSF. The ACMR values for the SMRF for different incipient collapse definitions are presented in Chapter 11, when they are compared with the values for the SC-MRFs and acceptable values per FEMA P695. The probability of collapse at the MCE level is also discussed for SMRF using the ACMR values in Chapter 11 and compared with the acceptable values per FEMA P695.

Table 9. 1. Variability in probability of collapse at MCE level for different amounts of uncertainty; SMRF, far-field ground motions.

Collapse Point Definition	$\hat{S}_{CT}$ (g)	β_{RTR}	β_{MDL}	β_{TD}	β_{DR}	β_{TOT}	Probability of Collapse at MCE (%)
10% story drift	1.96	0.30	0.20	0.20	0.20	0.46	6.2
	1.96	0.30	0.20	0.20	0.35	0.54	9.5
	1.96	0.40	0.20	0.20	0.20	0.53	9.1
	1.96	0.40	0.20	0.20	0.35	0.60	11.9
15% story drift	2.33	0.29	0.20	0.20	0.20	0.45	2.5
	2.33	0.29	0.20	0.20	0.35	0.54	5.1
	2.33	0.40	0.20	0.20	0.20	0.53	4.8
	2.33	0.40	0.20	0.20	0.35	0.60	7.1
80% slope reduction in IDA curve	2.08	0.30	0.20	0.20	0.20	0.46	4.8
	2.08	0.30	0.20	0.20	0.35	0.54	7.8
	2.08	0.40	0.20	0.20	0.20	0.53	7.4
	2.08	0.40	0.20	0.20	0.35	0.60	10.0

Table 9. 2. Parameters for calculation of SSF

System	C_0	V_{max} (kips)	W (kips)	$\max(T_1, T_{eigen})$	δ_u (in.)	$\mu_T >$	SSF
SMRF	1.39	1037	4398	1.48	83.4	11.9	1.446

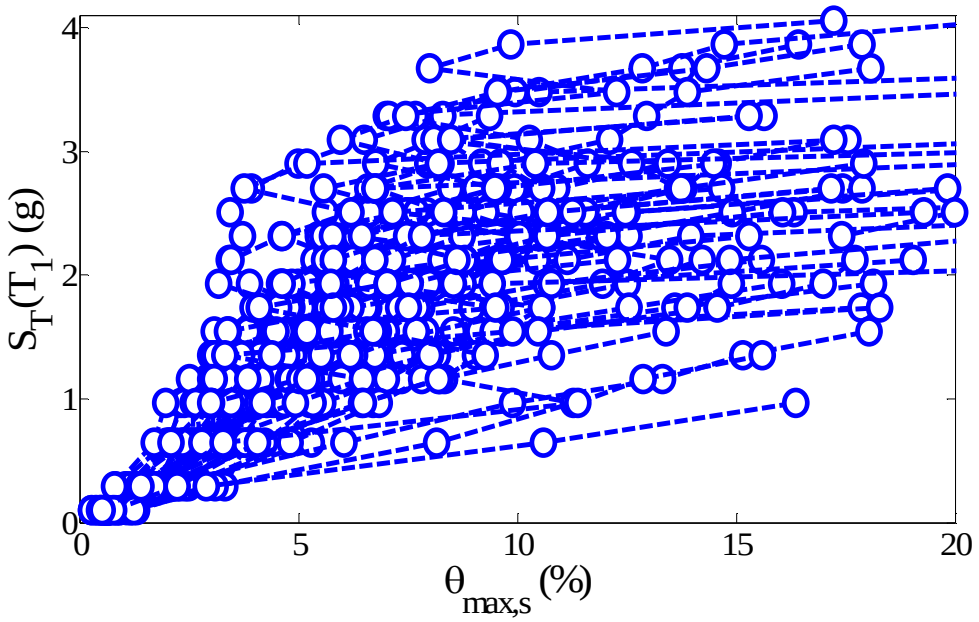

Figure 9. 1. Incremental dynamic analysis response plot of spectral acceleration versus maximum story drift ratio ($S_T(T_1)$-$\Theta_{max,S}$) for SMRF, far-field ground motions.

.

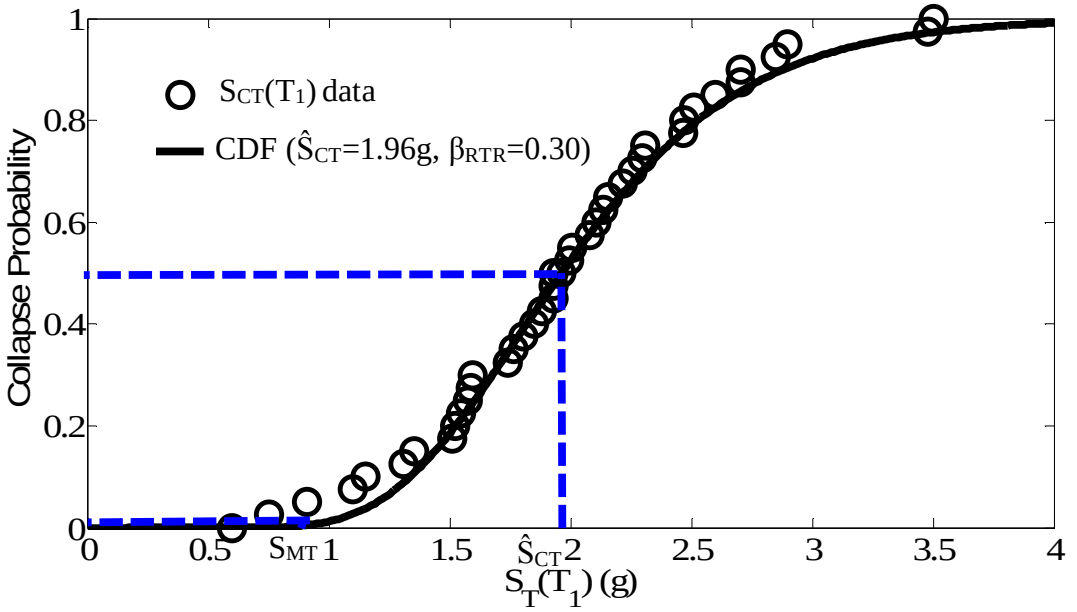

Figure 9. 2. Collapse fragility curve for SMRF, $S_{CT}(T_1)$ based on minimum of $S_T(T_1)$ at incipient collapse and 10% maximum story drift, far-field ground motions.

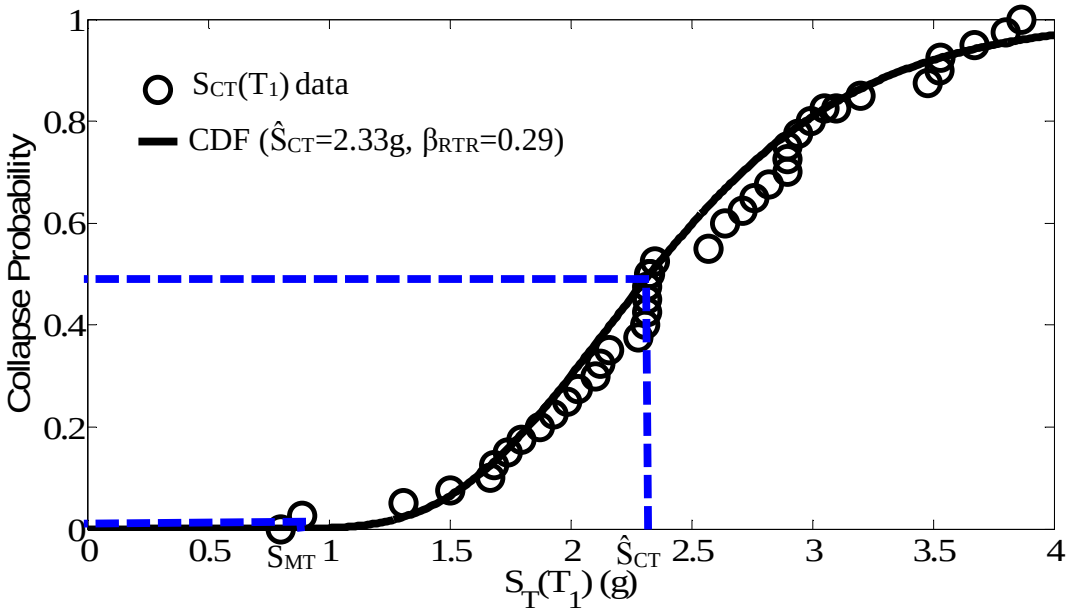

Figure 9. 3. Collapse fragility curve for SMRF, $S_{CT}(T_1)$ based on minimum of $S_T(T_1)$ at incipient collapse and 15% maximum story drift, far-field ground motions.

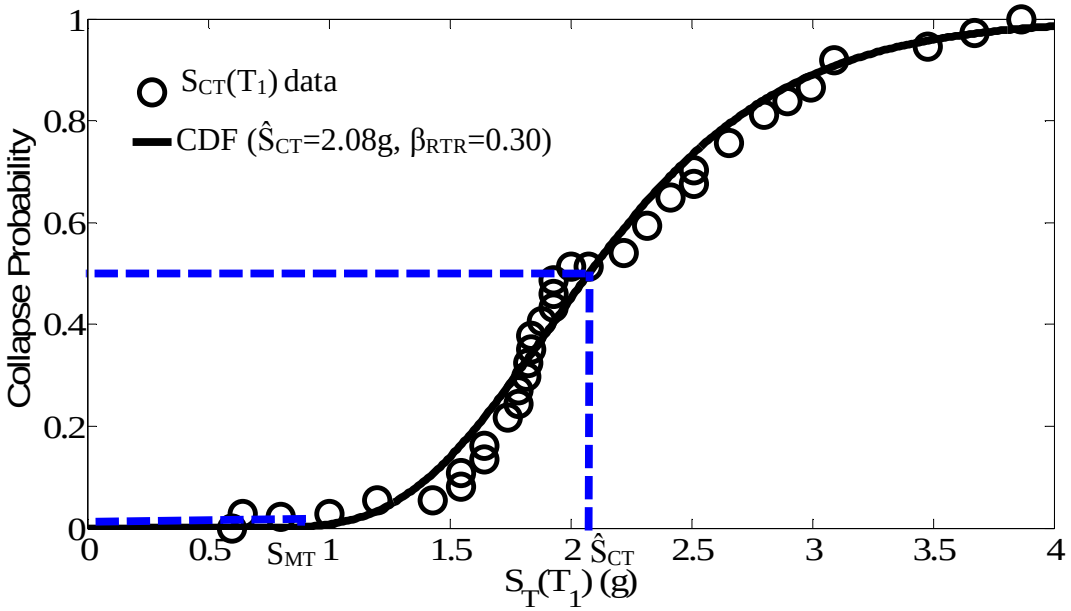

Figure 9. 4. Collapse fragility curve for SMRF, $S_{CT}(T_1)$ based on minimum of $S_T(T_1)$ at incipient collapse and at which an 80% slope reduction in the initial slope of the IDA curve takes place, far-field ground motions.

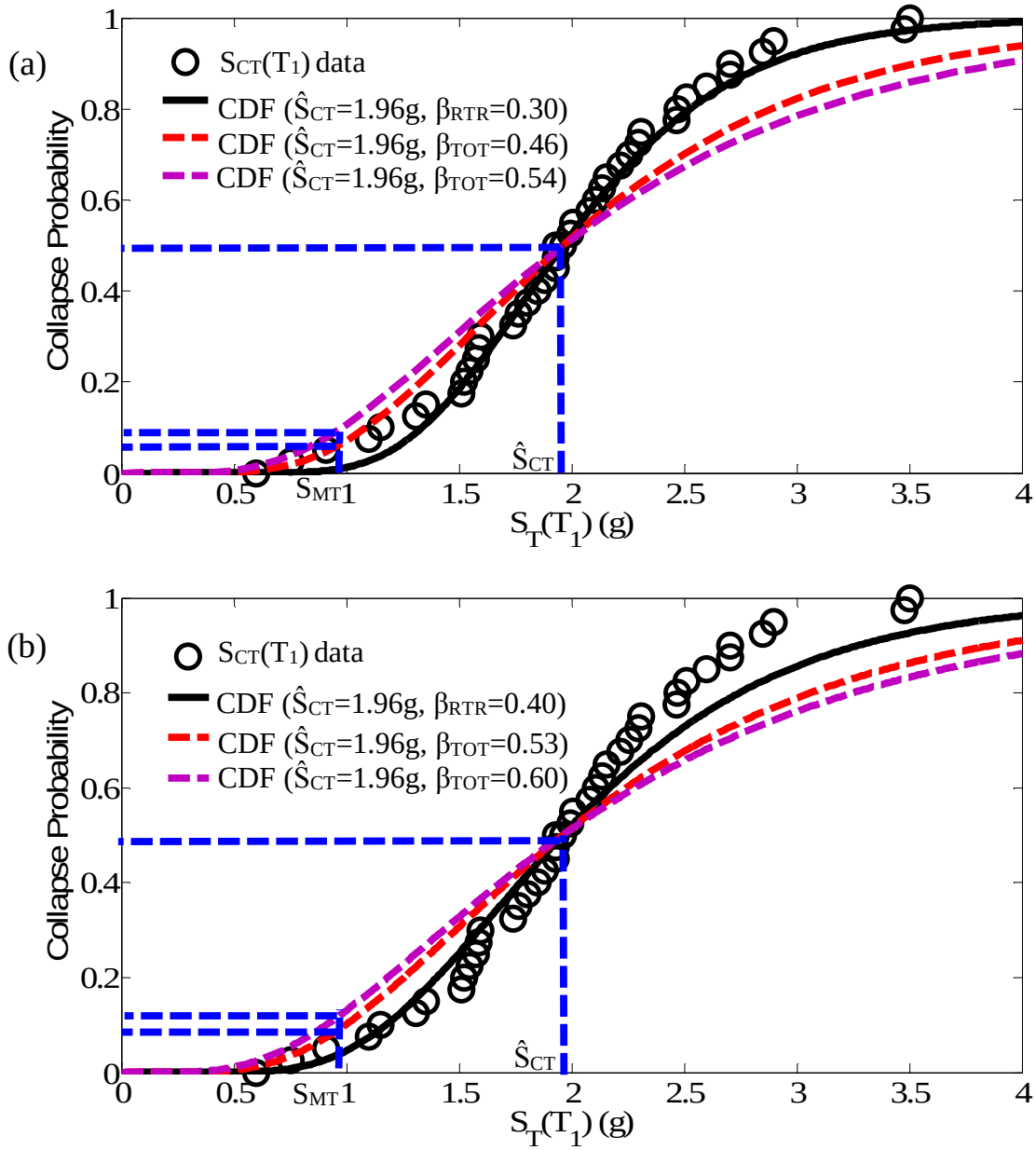

Figure 9. 5. SMRF: (a) collapse fragility curves using β_{RTR}=0.3; (b) collapse fragility curves using β_{RTR}=0.4; $S_{CT}(T_1)$ based on minimum of $S_T(T_1)$ at incipient collapse and 10% maximum story drift, far-field ground motions.

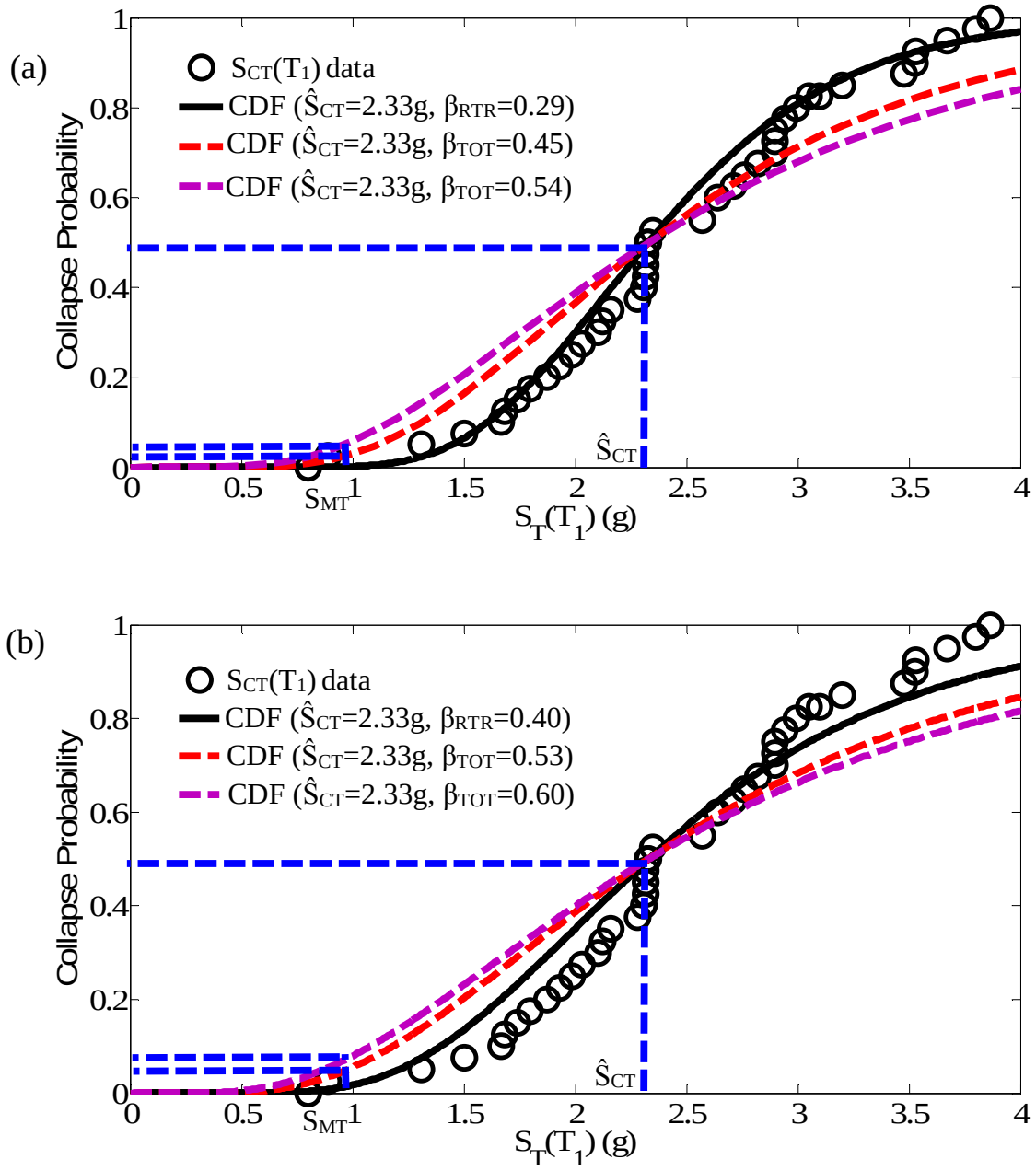

Figure 9. 6. SMRF: (a) collapse fragility curves using β_{RTR}=0.29; (b) collapse fragility curves using β_{RTR}=0.4; $S_{CT}(T_1)$ based on minimum of $S_T(T_1)$ at incipient collapse and 15% maximum story drift, far-field ground motions.

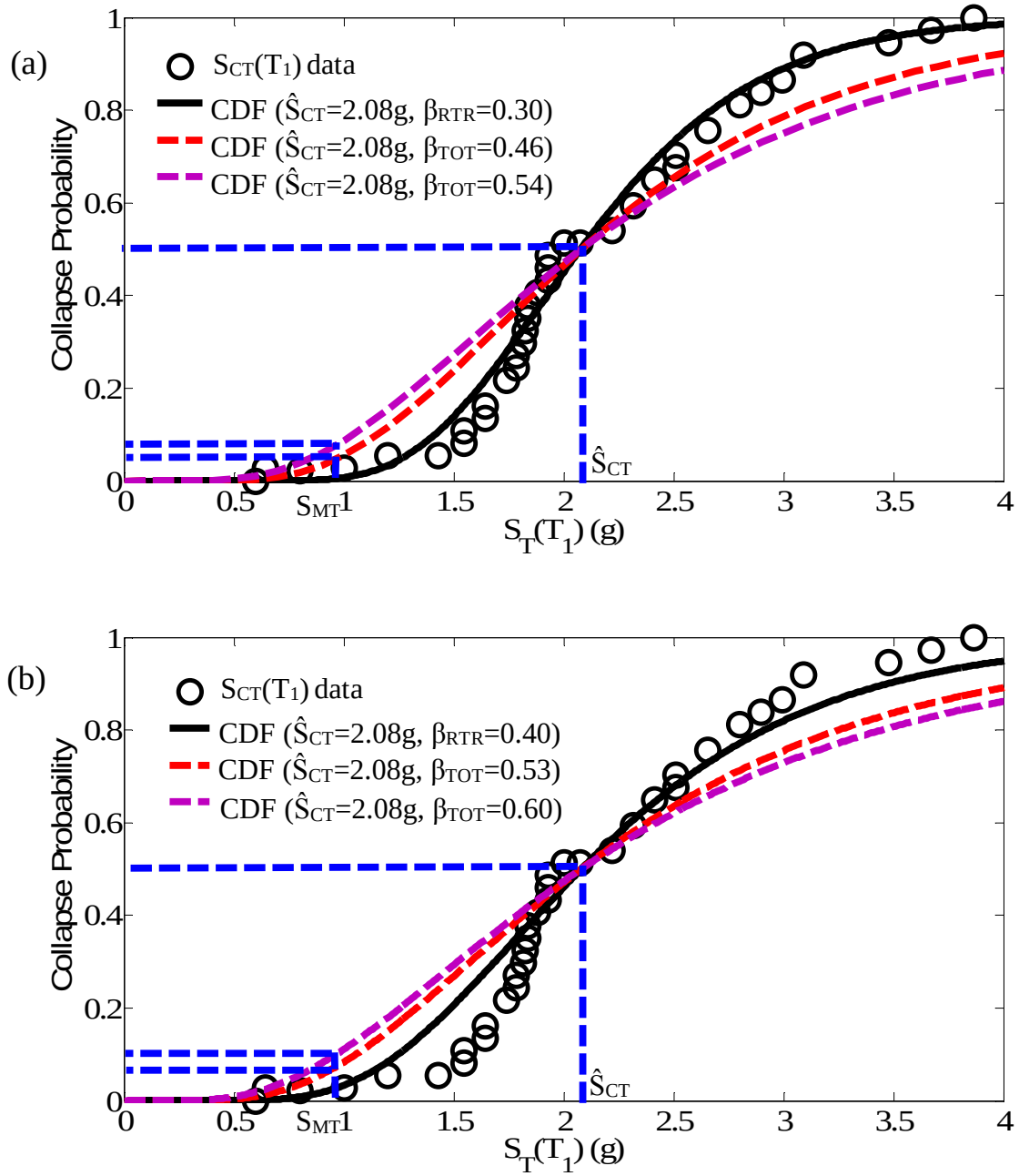

Figure 9. 7. SMRF: (a) collapse fragility curves using β_{RTR}=0.3; (b) collapse fragility curves using β_{RTR}=0.4; $S_{CT}(T_1)$ based on minimum of $S_T(T_1)$ at incipient collapse and at which an 80% slope reduction in the initial slope of the IDA curve takes place, far-field ground motions.

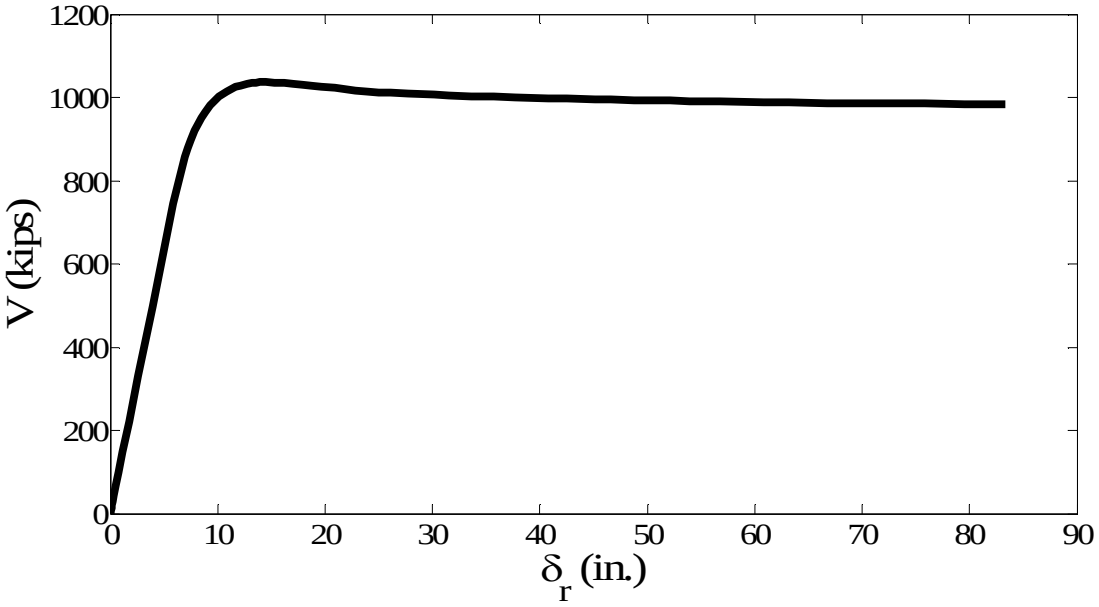

Figure 9. 8. Pushover curve for SMRF.

Chapter 10

Seismic Collapse Assessment of SC-MRF Design 1: Near-Field Ground Motions

10.1. General

This chapter presents the seismic collapse assessment of SC-MRF Design 1 under near-field ground motions. As stated in Chapter 7, the collapse capacity is evaluated basically under a set of 22 far-field records which includes 44 ground motion components from FEMA P695. However, structures are built where active faults may be in close proximity. The seismic collapse resistance of the SC-MRF Design 1 is studied under near-field ground motions to compare with the results for far-field ground motions. The IDA curves and fragility curves are presented and discussed in this chapter.

10.2. Motivation

The performance objectives for an SC-MRF designed by PBD procedure have been typically to design the system to enable gap opening to occur at the beam-to-column connections to avoid damage under the DBE, with collapse prevention under the MCE. The SC-MRF has been studied for response under the DBE and MCE, where typically far-field ground motions were used in these studies. However, structures are built where active faults may be in close proximity. The seismic collapse resistance of the SC-MRF Design 1 is studied under near-field ground motions in this chapter. Table 10.1 (Table A-6A in FEMA P695) summarizes the earthquake event and recording station data for the near-field record set utilized herein. There is a set of 28 near-field records which include

56 ground motion components divided into pulse record subset and no pulse record subset. The scaling method was described in Chapter 7 where the near-field ground motions are used instead of far-field record set. Normalization factors are given in Table A-6D in FEMA P695 for the near-field record set.

10.2.1. IDA Curves

Figure 10.1 shows the IDA curve for the SC-MRF Design 1 under near-field ground motions. The horizontal axis shows the maximum inter-story drift, $\Theta_{max,S}$, and the vertical axis presents the spectral acceleration, $S_T(T_1)$, measured by 5% damped median spectral acceleration intensity of the near-field record set at the fundamental period of the structure, T_1=0.932 sec. As stated in Chapter 7, the median collapse capacity $\hat{S}_{CT}$ can be determined and is associated with the $S_T(T_1)$ value where half of the ground motions reach the point of incipient collapse and cause the structure to collapse. The CMR value is the main parameter to assess the seismic collapse resistance of a system which is independent from sources of uncertainties. For the sake of computing the fragility curves for the near-field ground motions the set of analysis are stopped when half of ground motions cause collapse.

10.2.2. Fragility Curves

Table 10.2 summarizes different combinations of uncertainty values to calculate the total amount of uncertainty β_{TOT} for the incipient collapse scenarios introduced previously in Chapter 7. The value of RTR variability, β_{RTR}=0.4, is used in Table 10.2. Similar quantitative values for the sources of uncertainty are used in Table 10.2 in order to compare with the corresponding results from the SC-MRF Design 1 under far-field ground motions.

Figure 10.2 shows the fragility curves for $\hat{S}_{CT}$=1.78g and two values of β_{TOT} for the sources of uncertainty summarized in Table 10.2, when $S_{CT}(T_1)$ is the smaller of the $S_T(T_1)$ value at the end of the corresponding IDA curve where convergence failed in the analysis due to incipient collapse and the $S_T(T_1)$ value at the transient story drift of 10% for a ground motion. The MCE code specified spectral acceleration intensity at the fundamental period of the structure is S_{MT}=0.966g. Thus, CMR=1.84. The probability of collapse at the MCE level is 15.4% and 12.4% for β_{TOT}=0.6 and β_{TOT}=0.53 (see Table 10.2), respectively.

Figure 10.3 shows the fragility curve for $\hat{S}_{CT}$=2.04g and two values of β_{TOT} when $S_{CT}(T_1)$ is the smaller of the $S_T(T_1)$ value at the end of the corresponding IDA curve where convergence failed in the analysis due to incipient collapse and the $S_T(T_1)$ value at the transient story drift of 15% for a ground motion. Therefore, CMR is 2.11. The probability of collapse at the MCE level is 10.6% and 7.9% for β_{TOT}=0.6 and β_{TOT}=0.53 (see Table 10.2), respectively.

Figure 10.4 shows the fragility curve for $\hat{S}_{CT}$=1.93g and two values of β_{TOT} when $S_{CT}(T_1)$ is based on the smaller of the $S_T(T_1)$ value at the end of the corresponding IDA curve where convergence failed in the analysis due to incipient collapse and the $S_T(T_1)$ value at which an 80% slope reduction in the initial slope of the IDA curve takes place for a ground motion. Therefore, CMR is 2.00. The probability of collapse at the MCE level is 12.4% and 9.6% for β_{TOT}=0.6 and β_{TOT}=0.53 (see Table 10.2), respectively.

The probability of collapse at the MCE level is smaller for the point of incipient collapse based on 15% story drift in contrast to the corresponding values for the other incipient collapse definitions, whereas it is largest for 10% story drift (see Table 10.2).

The S_{MT} are shown in Figures 10.2 through 10.4. A comparison of results for the SC-MRF Design 1 under far-field and near-field ground motions is given in Chapter 11.

10.2.3. Adjusted CMR

Similar to the SC-MRFs and SMRF presented in Chapters 8 and 9, respectively, the ACMR is determined for SC-MRF Design 1 under near-field ground motions. Table 7.2 should not be used to determine the SSF since it is only for far-field ground motions. To compute the SSF for near-field ground motion, the procedure presented in Appendix-B of FEMA P695 is used. In FEMA P695, εp is defined as the number of logarithmic standard deviations between the observed spectral value and the median prediction from an attenuation function to account for the spectral shape for adjusting the collapse capacity. The SSF is computed by using Equation (10.1):

$$SSF = \exp[\beta_1 (\varepsilon p_0^{ave}(T_1) - \varepsilon p_{,record}^{ave}(T_1))] \quad (10.1)$$

where β_1 is 0.32 for μ_T>8 per FEMA P695. β_1 depends on the building inelastic deformation capacity. εp_0^{ave} is the mean expected epsilon depending on both site and hazard level of interest. εp_0^{ave} is equal to 1.5 for seismic design category D per FEMA P695. $\varepsilon p_{,record}^{ave}(T_1)$ is for the record set and equal to zero for periods less than 1.5 sec. for a near-field record set per FEMA P695. Note that T_1 is equal to 0.932 sec. for SC-MRF Design 1. Therefore, SSF is found to be equal to 1.62 for near-field ground motions. The ACMR values are found by multiplying the CMR values by SSF. The ACMR values for the SC-MRF Design 1 under near-field ground motions for different incipient collapse definitions are presented in Chapter 11, where they are compared with the values for the SC-MRF Design 1 under far-field ground motions and acceptable values per FEMA P695.

Table 10. 1. Summary of earthquake event and recording station data for the near-field record set (Table A-6A in FEMA P695).

ID No.	Earthquake			Recording Station	
	M	Year	Name	Name	Owner
Pulse Records Subset					
1	6.5	1979	Imperial Valley-06	El Centro Array #6	CDMG
2	6.5	1979	Imperial Valley-06	El Centro Array #7	USGS
3	6.9	1980	Irpinia, Italy-01	Sturno	ENEL
4	6.5	1987	Superstition Hills-02	Parachute Test Site	USGS
5	6.9	1989	Loma Prieta	Saratoga - Aloha	CDMG
6	6.7	1992	Erzican, Turkey	Erzincan	--
7	7.0	1992	Cape Mendocino	Petrolia	CDMG
8	7.3	1992	Landers	Lucerne	SCE
9	6.7	1994	Northridge-01	Rinaldi Receiving Sta	DWP
10	6.7	1994	Northridge-01	Sylmar - Olive View	CDMG
11	7.5	1999	Kocaeli, Turkey	Izmit	ERD
12	7.6	1999	Chi-Chi, Taiwan	TCU065	CWB
13	7.6	1999	Chi-Chi, Taiwan	TCU102	CWB
14	7.1	1999	Duzce, Turkey	Duzce	ERD
No Pulse Records Subset					
15	6.8	6.8	Gazli, USSR	Karakyr	--
16	6.5	1979	Imperial Valley-06	Bonds Corner	USGS
17	6.5	1979	Imperial Valley-06	Chihuahua	UNAMUCSD
18	6.8	1985	Nahanni, Canada	Site 1	--
19	6.8	1985	Nahanni, Canada	Site 2	--
20	6.9	1989	Loma Prieta	BRAN	UCSC
21	6.9	1989	Loma Prieta	Corralitos	CDMG
22	7.0	1992	Cape Mendocino	Cape Mendocino	CDMG
23	6.7	1994	Northridge-01	LA - Sepulveda VA	USGS/VA
24	6.7	1994	Northridge-01	Northridge - Saticoy	USC
25	7.5	1999	Kocaeli, Turkey	Yarimca	KOERI
26	7.6	1999	Chi-Chi, Taiwan	TCU067	CWB
27	7.6	1999	Chi-Chi, Taiwan	TCU084	CWB
28	7.9	2002	Denali, Alaska	TAPS Pump Sta. #10	CWB

Table 10. 2. Variability in probability of collapse at MCE level for different amounts of uncertainty; SC-MRF Design 1, near-field ground motions.

Collapse Point Definition	$\hat{S}_{CT}$ (g)	β_{RTR}	β_{MDL}	β_{TD}	β_{DR}	β_{TOT}	Probability of Collapse at MCE (%)
10% story drift	1.78	0.40	0.20	0.20	0.20	0.53	12.4
	1.78	0.40	0.20	0.20	0.35	0.60	15.4
15% story drift	2.04	0.40	0.20	0.20	0.20	0.53	7.9
	2.04	0.40	0.20	0.20	0.35	0.60	10.6
80% slope reduction in IDA curve	1.93	0.40	0.20	0.20	0.20	0.53	9.6
	1.93	0.40	0.20	0.20	0.35	0.60	12.4

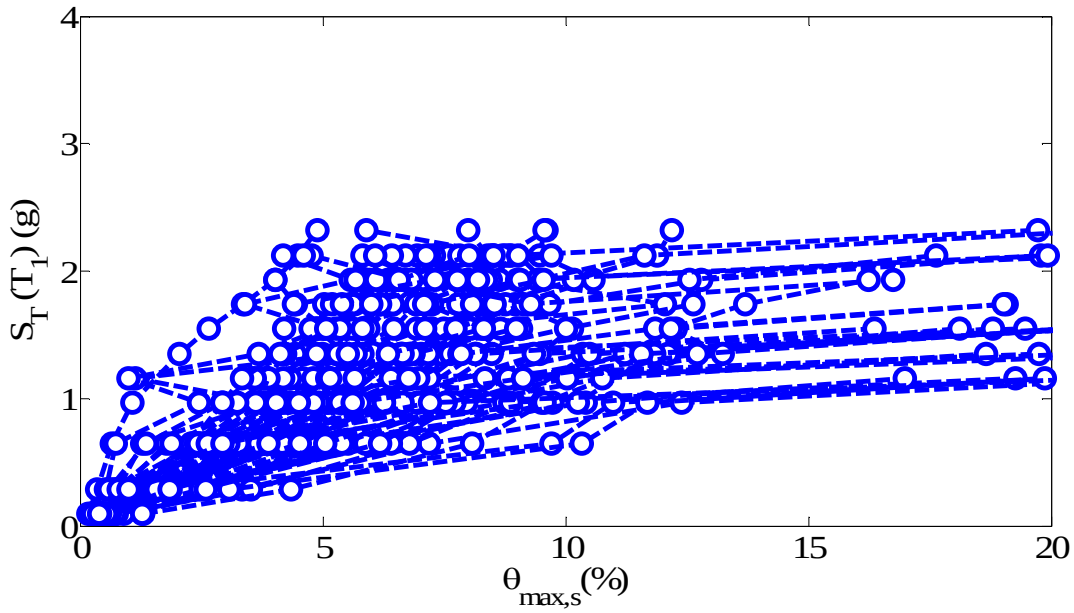

Figure 10. 1. Incremental dynamic analysis response plot of spectral acceleration versus maximum story drift ratio ($S_T(T_1)$-$\Theta_{max,S}$) for SC-MRF Design 1, near-field ground motions.

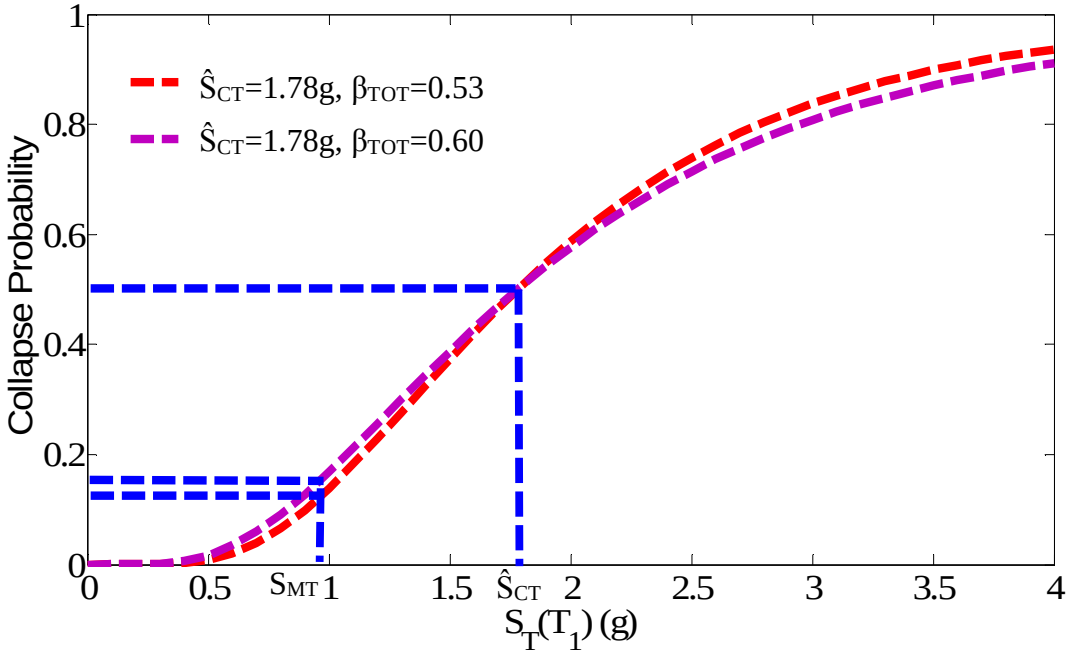

Figure 10. 2. SC_MRF Design 1 collapse fragility curves using β_{TOT}=0.53 and β_{TOT}=0.6, $S_{CT}(T_1)$ based on minimum of $S_T(T_1)$ at incipient collapse and 10% maximum story drift, near-field ground motions.

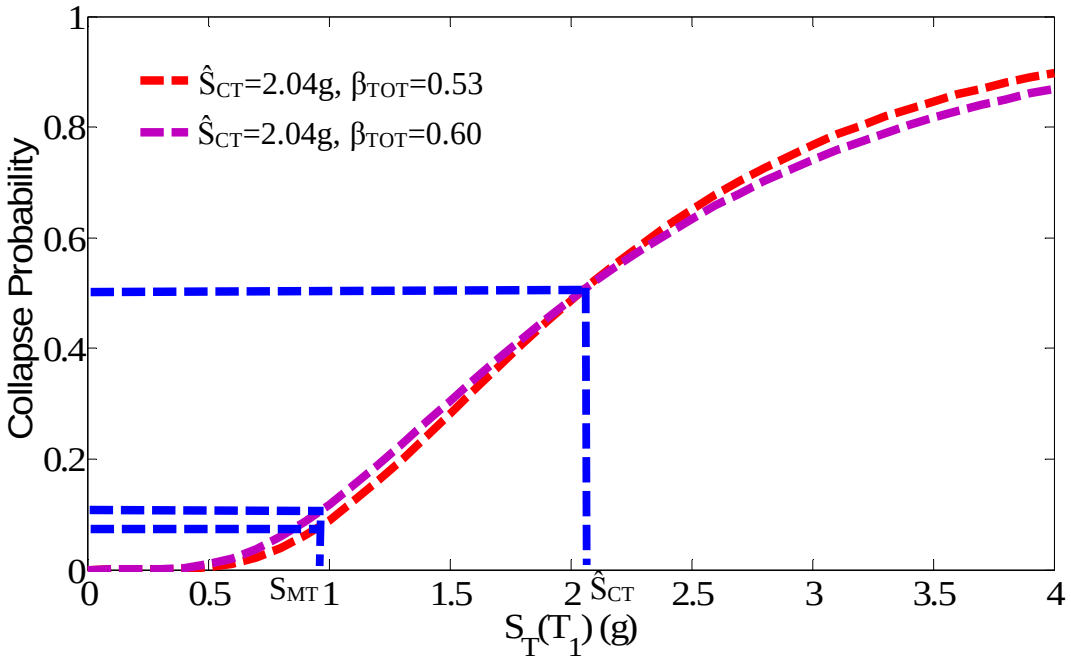

Figure 10. 3. SC_MRF Design 1 collapse fragility curves using β_{TOT}=0.53 and β_{TOT}=0.6, $S_{CT}(T_1)$ based on minimum of $S_T(T_1)$ at incipient collapse and 15% maximum story drift, near-field ground motions.

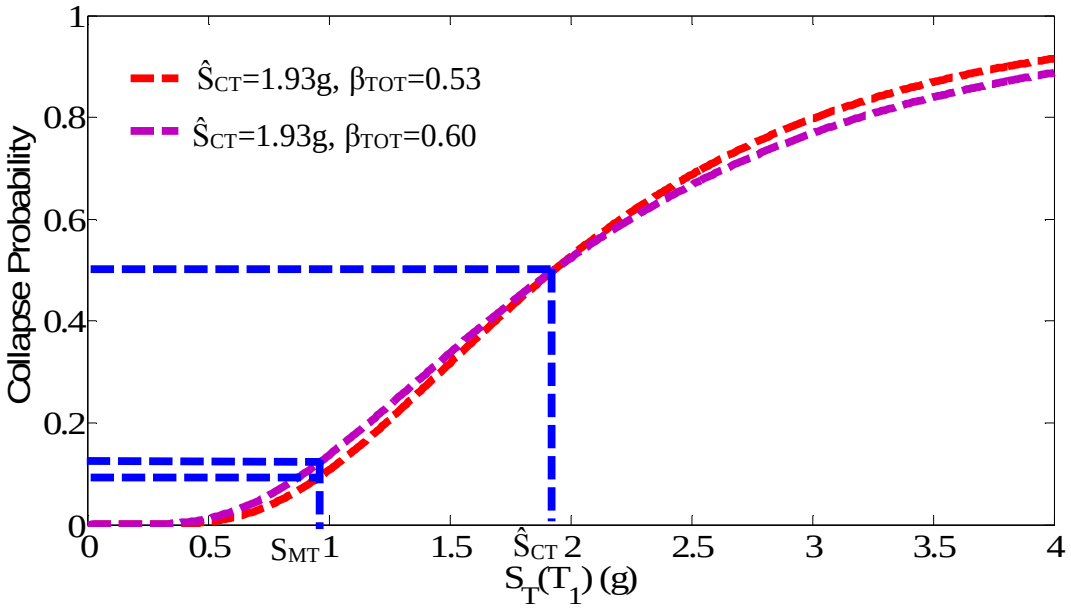

Figure 10. 4. SC_MRF Design 1 collapse fragility curves using β_{TOT}=0.53 and β_{TOT}=0.6, $S_{CT}(T_1)$ based on minimum of $S_T(T_1)$ at incipient collapse and at which an 80% slope reduction in the initial slope of the IDA curve takes place, near-field ground motions.

Chapter 11

Comparison of Collapse Resistance of Case Studies

11.1. General

This chapter compares the results presented in the previous chapters for the different case studies. As stated previously, different case studies are conducted in order to assess the seismic collapse resistance of steel frame systems, namely SC-MRF Design 1, SC-MRF Design 2 and an SMRF. All are evaluated under far-field ground motions per FEMA P695, in addition to Design 1 being evaluated under both near-field and far-field ground motions. The CMR and the probability of collapse at the MCE level are compared.

11.2. SC-MRF Design 1 vs. SC-MRF Design 2

As shown in Table 11.1, the CMR is smaller for SC-MRF Design 2 than Design 1 for the different collapse definitions. Design 2 limited the PT design force at the MCE level to 75 percent of the PT yield force while keeping the initial PT force T_0 the same as what used in Design 1. In Design 1 the PT design force was limited to 90 percent of the PT yield force. As a result the force per PT strand in the Design 2 is reduced compared to that of the Design 1. To maintain the same initial total PT force, the number of PT strands was increased in Design 2 which can lead to larger PT strand forces and therefore larger beam axial forces and bending moments after gap opening occurs. Equations (2.4) and (2.5) give the beam bending moment M and the beam axial force, respectively, for a SC connection. The PT strand force T affects the beam axial force P and subsequently the beam bending moment M. Equation (2.6) determines the PT strand force T. The

parameters in Equations (2.4) through (2.6) were defined in Chapter 2. As an example, Figure 11.1 shows the T-θ_r^{ave} relation from Equation (2.6) for a range of θ_r^{ave} at the first floor for Designs 1 and 2. The $\theta_{r,DBE}^{ave}$ and $\theta_{r,MCE}^{ave}$ (see Chapter 4) are shown in Figure 11.1. As seen Design 2 develops a larger PT strand force than Design 1 after gap opening occurs due to a larger post gap-opening PT stiffness. This leads to a larger beam axial force P and subsequently M when the SC connection experiences extreme dynamic loading for SC-MRF Design 2 than that of Design 1. Therefore, the reinforcing plate lengths were modified to limit the strain at the end of the plates to be less than twice the yield strain under the DBE level for SC-MRF Design 2. Larger beam axial force and bending moments after gap opening increases the possibility of occurrence of earlier beam local buckling at the end of the reinforcing plates and reduces the CMR accordingly while the possibility of PT strand yielding and fracture has reduced due to less PT force per strand. Moreover, the collapse resistance (CMR) depends on the definition of incipient collapse.

For 10% story drift considered as the collapse point, the CMR equals 2 for SC-MRF Design 2 while it is 2.11 for SC-MRF Design 1. Similarly, for SC-MRF Design 2 the CMR equals 2.33 and 2.10 for 15% story drift and 80% slope reduction in IDA curves considered as the incipient collapse point, respectively, while for SC-MRF Design 1 the CMR equals 2.52 and 2.19 for 15% story drift and 80% slope reduction in IDA curves, respectively. As seen in Table 8.1 and Table 8.5 by increasing the amount of uncertainty which is taken into account by parameter β_{TOT} (introduced in Chapter 7) the probability of collapse at the MCE level has increased for both SC-MRF Designs 1 and 2 for all three different collapse definitions. The fragility curves are defined by assuming a lognormal

CDF for collapse data points for a β_{RTR}=0.4 per FEMA P695; the probability of collapse at the MCE level is larger for SC-MRF Design 2 for every collapse definition than that of SC-MRF Design 1 (see Table 11.2). However, if β_{RTR} is computed by fitting a lognormal curve to the collapse data points, the β_{TOT} varies for each design and which collapse definition is used as presented in Tables 8.1 and 8.5.

The ACMR values and minimum acceptable ACMR values per FEMA P695 are summarized in Table 11.3. $ACMR_{10\%}$ and $ACMR_{20\%}$ were defined in Chapter 7. The $ACMR_{10\%}$ and $ACMR_{20\%}$ are related to β_{TOT} of the system as presented in Table 11.3. β_{RTR}=0.4 is used to calculate β_{TOT} and determine $ACMR_{10\%}$ and $ACMR_{20\%}$ per FEMA P695 for systems with $\mu_T \geq 3$. As seen, the ACMR values for Designs 1 and 2 are within the acceptable values per FEMA P695. This means that the probability of collapse at the MCE level is acceptable for each archetype within the performance group per FEMA P695. Note that only one archetype was studied for Designs 1 and 2.

As stated the PT design force per strand is reduced in SC-MRF Design 2 (see Table 4.8), consequently, the probability of the PT strand maximum strain exceeding the PT strand yielding strain ($P(\varepsilon_{max} > \varepsilon_y)$) is reduced compared to Design 1 as presented in Table 8.2 at all floor levels. $P(\varepsilon_{max} > \varepsilon_y)$ is 68%, 38.6%, 11.6% and 1% at 4th, 3rd, 2nd and 1st floors, respectively, for SC-MRF Design 1 while it is 8.8%, 0.4%, 0.05% and 6E-5% at 4th, 3rd, 2nd and 1st floors, respectively, for SC-MRF Design 2. As seen in Figure 8.2 the average connection relative rotation (i.e., the average for all connections at one floor level), θ_r^{ave} is larger at the roof for Design 1 under one typical ground motion at incipient collapse. This value of θ_r^{ave} can be treated as an indicator for larger PT strand elongation at the roof in comparison to the other floor levels. Equation (2.6) gives the flexibility of

PT strands at each floor level which is related to the axial stiffness of the beams and PT strands within one bay and the distance d defined in Chapter 2. As a result, larger PT strand elongation leads to the larger probability of PT strand yielding at the roof.

In addition, by considering 1% or 2% as fracture strain assuming the fracture strain as a deterministic variable, the probability of the PT strand maximum strain exceeding the strand fracture strain $P(\varepsilon_{max} > \varepsilon_r)$ was presented in Table 8.3. As seen, $P(\varepsilon_{max} > \varepsilon_r)$ is small and negligible when ε_r =2% for both designs. The probability that ε_{max} exceeding 1% is 38.8%, 11.2%, 1%, and 0.01% at 4th, 3rd, 2nd ,and 1st floors, respectively, for SC-MRF Design 1 while it is 0.9%, 0.01%, 5E-4%, and 4E-8% at 4th, 3rd, 2nd ,and 1st floors, respectively, for SC-MRF Design 2. By comparing the above results assuming the fracture strain as a deterministic variable, it is observed that the probability of PT strand yielding and fracture is considerably less in SC-MRF Design 2 than in SC-MRF Design 1.

The probability of strand fracture assuming the fracture strain as a random variable was presented in Table 8.4. If the strand fracture strain is assumed as a random variable with a mean of λ_R-2ζ_R as described in Chapter 8, the probability of strand fracture is 24.5%, 15.1%, 9.1%, and 6.5% at 4th, 3rd, 2nd, and 1st floors, respectively, for SC-MRF Design 1 while it is 7.8%, 3.6%, 2.4% and 1% at 4th, 3rd, 2nd, and 1st floors, respectively, for SC-MRF Design 2. Therefore, it is observed that the probability of strand fracture is generally less in SC-MRF Design 2 due to a smaller PT force per strand. A similar conclusion is derived when different mean values for the fracture strain resistance random variables is assumed. A seen in Table 8.4, by decreasing the mean fracture strain, the probability of strand fracture increases and it is more likely to occur in SC-MRF

Design 1. It is seen that, in general, the probability of PT strand yielding and fracture is larger at the upper floor levels while beam local buckling is more likely at the lower floor levels due to larger beam axial force and bending moments, which as presented in Chapter 8 reduces the strand PT force and subsequently lowers the probability of PT strand yielding and fracture. While the probability of PT strand yielding and fracture is less in SC-MRF Design 2, the higher beam axial forces and bending moments that develop after gap opening occurs cause an earlier beam local buckling that lead to a reduction in the CMR values in SC-MRF Design 2 compared to SC-MRF Design 1.

11.3. SC-MRF vs. SMRF

In Table 11.1 the CMR values are shown to be equal to 2.03, 2.41, and 2.15 for 10% story drift, 15% story drift, and 80% slope reduction in IDA curves, at which the SMRF considered to collapse, respectively. As shown in Table 11.1, while the CMR values in SC-MRF Design 1 are larger than the corresponding values for the SMRF, the CMR values for SC-MRF Design 2 are smaller than those of the SMRF. This shows that the collapse resistance of SC-MRF systems under extreme ground motions depends on the design procedure compared to the SMRF. Moreover, the collapse resistance (CMR) depends on the definition of incipient collapse. For instance, for a 10% story drift at which the system is assumed to collapse, the CMR values are 2.11, 2.00, and 2.03 for SC-MRF Designs 1, and 2, and the SMRF, respectively, while the CMR values are 2.52, 2.33, and 2.41 for SC-MRF Designs 1, and 2, and the SMRF, respectively, for a 15% story drift at which the structure is considered to collapse. As seen in Table 11.1 the SC-MRF Design 2 has CMR values closer to the values that of the SMRF for different collapse definitions.

As stated previously, by increasing the amount of uncertainty (see Table 9.1) the probability of collapse at the MCE level will be increased for all three different collapse definitions. Table 11.2 shows a comparison among the probability of collapse at the MCE level for SC-MRF Designs 1, and 2, and SMRF systems for when a value of β_{RTR}=0.4 is used (i.e., not by fitting a lognormal curve on collapse data points). Two different β_{DR} are assumed to obtain β_{TOT} in Table 11.2 (β_{DR}=0.2 and β_{DR}=0.35).

As seen in Table 11.2, the probability of collapse is larger for SC-MRF Design 2 for every collapse definition and the CMR is smaller for this design in contrast to Design 1 and the SMRF. For instance, the probability of collapse at the MCE level is 10.6%, 12.4% and 11.9% for SC-MRF Design 1, SC-MRF Design 2 and SMRF, respectively, if a 10% story drift is considered as the collapse point and β_{TOT}=0.6. The probability of collapse at the MCE level is less when β_{TOT}=0.53 (see Table 11.2). Table 11.3 summarizes the ACMR and acceptable values for the SC-MRFs and the SMRF. The ACMR values are within the acceptable values per FEMA P695. Note that one archetype was studied for each system.

11.4. SC-MRF Design 1: Far-Field vs. Near-Field Ground Motions

As seen in Table 11.1, the CMR for SC-MRF Design 1 under near-field ground motions is less than that for Design 1 under the far-field ground motions. For instance, the CMR is 1.84 under near-field ground motions while it is 2.11 under far-field ground motions if a 10% story drift defines incipient collapse. The probability of collapse under the MCE level is subsequently larger under the near-field ground motions for a given β_{TOT} (see Table 10.2 and Table 11.2).

Figure 11.2 shows the unscaled far-field and near-field response spectra along with the median spectrums for a range of natural periods T_n. As seen, the median spectrum for near-field ground motions has larger spectral acceleration than that for far-field ground motions. When the system softens due to the nonlinear behavior of the members under scaled ground motions, the period of the structure increases while the median spectral acceleration is still larger for near-field ground motions than that for far-field ground motions. This leads to an earlier collapse for the near-field ground motions, causing a smaller CMR and larger probability of collapse under the MCE level. Table 11.3 shows the ACMR values for different collapse definitions. As seen the ACMR values are acceptable per FEMA P695. Since one archetype was studied for near-filed ground motions, the obtained results show that an SC-MRF has the potential to be used in areas close to active faults providing acceptable margin against collapse.

Table 11. 1. CMR summary of case studies for different definitions of collapse.

Case	CMR		
	Collapse Definition		
	10% Story Drift	15% Story Drift	80% Slope Reduction
SC-MRF Design 1 far-field	2.11	2.52	2.19
SC-MRF Design 2 far-field	2.00	2.33	2.10
SMRF far-field	2.03	2.41	2.15
SC-MRF Design 1 near-field	1.84	2.11	2.00

Table 11. 2. Probability of collapse at MCE level for SC-MRF Designs 1 and 2 far-field, SMRF far-field, and SC-MRF Design 1 near-field ground motions.

Collapse Point Definition	β_{TOT}	System			
		SC-MRF Design 1 far-field	SC-MRF Design 2 far-field	SMRF far-field	SC-MRF Design 1 near-field
		Probability of Collapse at MCE (%)			
10% story drift	0.53	7.9	9.6	9.1	12.4
	0.60	10.6	12.4	11.9	15.4
15% story drift	0.53	4.1	5.5	4.8	7.9
	0.60	6.2	7.9	7.1	10.6
80% slope reduction in IDA curve	0.53	6.7	8.0	7.4	9.6
	0.60	9.5	10.8	10	12.4

Table 11. 3. ACMR summary of case studies for different definitions of collapse and minimum ACMR values per FEMA P695.

Case	ACMR			β_{TOT}	Minimum ACMR per FEMA P695	
	Collapse Definition					
	10% Story Drift	15% Story Drift	80% Slope Reduction		$ACMR_{10\%}$*	$ACMR_{20\%}$**
SC-MRF Design 1 far-field	3.05	3.64	3.17	0.53	1.96	1.56
				0.60	2.16	1.66
SC-MRF Design 2 far-field	2.89	3.37	3.04	0.53	1.96	1.56
				0.60	2.16	1.66
SMRF far-field	2.93	3.48	3.11	0.53	1.96	1.56
				0.60	2.16	1.66
SC-MRF Design 1 near-field	2.98	3.42	3.24	0.53	1.96	1.56
				0.60	2.16	1.66

*Allowable value on average across a performance group (FEMA P695) leading to 10% probability of collapse at the MCE level.

**Allowable value for each archetype within a performance group (FEMA P695) leading to 20% probability of collapse at the MCE level.

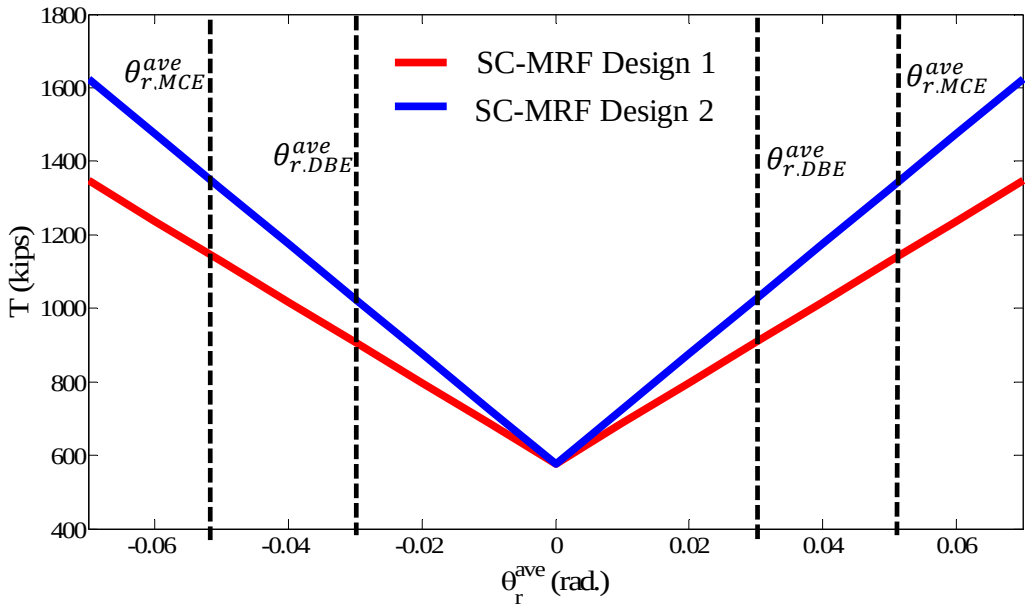

Figure 11. 1. T-θ_r^{ave} relation for a range of θ_r^{ave} values, SC-MRF Designs 1 and 2 at the 1st floor.

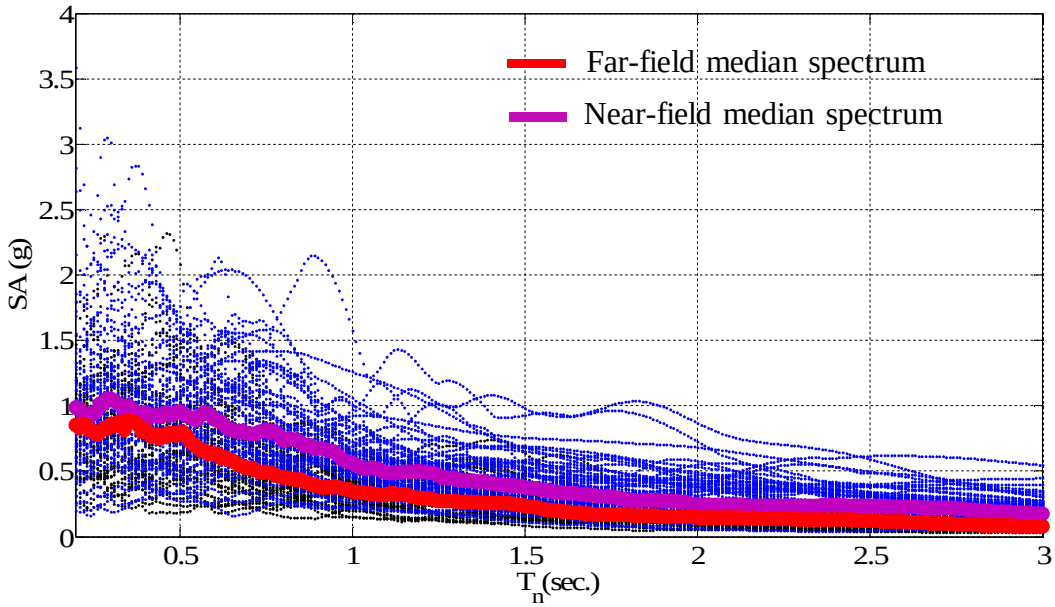

Figure 11. 2. Far-field and near-field, unscaled response spectra along with the median spectrums.

Chapter 12

Summary, Conclusions and Recommended Future Research

12.1. Summary

12.1.1. Motivation for Present Research

Conventional steel welded special moment resisting frames (SMRFs) use fully restrained welded connections between the beams and columns. The design method used for these connections leads to significant inelastic deformations in the beams and formation of plastic hinges under the design basis earthquake (DBE). Plastic hinges may cause significant damage which may result in residual drift. Miranda (2009) found that the amplitude of residual story drift is the most important contributor to economic losses for ductile structures and leads to a significant increased probability for demolishing the structure after an earthquake despite the fact that the ductile structures are highly resistant to collapse when subjected to intense ground motions. Repair or replacement of damaged members and removing residual drift is usually prohibitively expensive and difficult. Thus, it is often more economical to demolish rather than to repair a building possessing residual drift.

To minimize structural damage during the DBE and avoid permanent residual drift, post-tensioned beam-to-column connections for self-centering moment resisting frames (SC-MRF) were developed by Ricles et al. (2001). The behavior of an SC-MRF is characterized by connection gap opening and closing at the beam-column interfaces. The gap opening allows the beam to rotate relative to the column, enabling an SC-MRF to drift laterally without damaging the beams or columns. An SC-MRF uses horizontally-

oriented high strength post-tensioning (PT) strands to pre-compress the beams to the columns. The PT force closes the gaps that develop under earthquake loading, which returns (i.e., self-centering) the frame to its initial pre-earthquake position. Energy is dissipated by special energy dissipation devices to reduce the seismic response of an SC-MRF, rather than by forming inelastic regions in the structural members. Several research studies (Garlock et al. 1998; Ricles et al. 2001; Rojas et al. 2005; Tsai et al. 2008; Kim and Christopoulos 2008; Wolski et al. 2009; Iyama et al. 2009; Lin et al. 2012) have experimentally demonstrated that a properly designed connection in an SC-MRF is capable of a softening behavior without causing structural damage and has self-centering characteristics with negligible residual drift under the design earthquake. Prior research focused on experimental studies of connection subassemblies and numerical studies of SC-MRF systems. The behavior, performance, and design concepts of an SC-MRF system at various earthquake input levels were investigated.

A comprehensive knowledge of the collapse resistance of an SC-MRF system under strong ground motions is still lacking. This knowledge gap and need for additional research forms the basis for this research.

12.1.2. Research Objectives and Scope

The overall research objectives of this research are: (1) to investigate the seismic collapse performance of a low-rise SC-MRF system; and (2) to compare the seismic collapse performance of an SC-MRF with a comparable conventional SMRF system.

To achieve the research objectives, the following tasks were performed:

1. Design of a low-rise prototype building with SC-MRFs as the lateral force resisting system:

   A low-rise 4-story prototype building designed by Lin et al. (2012) was selected as the basis for the analytical studies in this research. This building is located in a high seismic zone and designed in compliance with ASCE7 (2010). The SC-MRFs were designed using a performance-based design (PBD) procedure and criteria developed by Lin. The PBD procedure developed by Lin was adapted and modified from the work by Garlock et al. (2007).

2. Numerical modeling of an SC-MRF for response prediction to extreme earthquakes:

   The beams are expected to yield and develop potential local buckling under appreciable axial force and bending moment under extreme ground motions, an important collapse limit state that needs to be taken into account. A computational efficient model is needed for the collapse assessment of an SC-MRF, where many simulations are required for the incremental dynamic analyses. To evaluate the seismic collapse performance of an SC-MRF, there is a need for a model which includes stress-resultant and continuum shell elements in order to efficiently model the complete structural system and capture the important limit states that can occur under extreme ground motions, including gap opening at the beam-column interface, yielding of the PT strands, yielding and inelastic deformations in the members (beams, columns, panel zones), second order (P-delta) effects due to gravity loads imposed on the gravity load frames, and beam local flange and web buckling at the end of the reinforcing plates. In the model, the continuum

elements were started from the end of the reinforcing plates and continued for one beam depth along the span of the beam where local buckling is expected to develop.

3. Calibration of SC-MRF model:

   In order to develop a computational efficient model capable of capturing beam local buckling limit state to investigate the collapse resistance of an SC-MRF, the connection behavior is studied by comparing the analytical model results with the experimental test data (Garlock (2002)) for an interior subassembly connection. Initial imperfections are imposed on the shell elements to initiate local buckling in the beam. The first buckling mode shape is scaled to impose web and flange out-of-flatness imperfections in the beams. A sensitivity analysis was performed using representative values of web and flange out-of-flatness.

4. Seismic collapse assessment of an SC-MRF:

   The incremental dynamic analysis (IDA) method was used to assess the collapse capacity under a pair of 22 far-field records which included 44 ground motion components from FEMA P695 (2009). IDA is a parametric analysis method (Vamvatsikos and Cornell (2006)) in which individual ground motions are scaled to increasing intensities until the structure reaches a collapse point. The collapse point is defined when the structure reaches a large maximum story drift (for instance, 10 percent maximum story drift) under dynamic loading or when the structure undergoes dynamic instability which means the structure experiences a large maximum story drift for a small incremental increase in ground motion intensity. In this study, the collapse point for when incipient collapse occurs was

based on three assumptions: 10% transient story drift; 15% transient story drift; and 80% slope reduction in the initial slope of the IDA curve takes place for a ground motion. The collapse fragility curve is obtained by fitting a cumulative distribution function, assuming a lognormal distribution, to the collapse data points (Ibarra et al. (2002)). The seismic resistance of the selected low-rise SC-MRF is then determined from the fragility curves. Different sources of uncertainty are considered in order to adjust the fragility curves based on FEMA P695 to determine the probability of collapse under the Maximum Considered Earthquake (MCE) level. The Collapse Margin Ratio (CMR) is obtained as the ratio between the spectral acceleration intensity, at which half of the ground motions causes the structure to collapse, and the MCE code-specified spectral acceleration intensity at the fundamental period of the structure.

5. Parametric study on design limit for the maximum PT strand force:

   Designers have the option to lower the design limit for the maximum PT strand force in order to avoid PT strand yielding and fracture scenarios. In order to investigate the implication of this design parameter on the seismic collapse resistance of an SC-MRF, the SC-MRF design was modified to limit the total PT force under the MCE to 75 percent of the total PT yield force instead of 90 percent of the total PT yield force in the original design while keeping the initial total PT force the same. To maintain the same initial total PT force, the number of PT strands is increased. In the design with more PT strands the total axial stiffness of the PT strands increases, which can lead to larger PT strand forces and therefore larger beam axial forces after gap opening occurs. The beam axial forces

and bending moments that develop requires a design change of the reinforcing plate length in accordance with the current PBD procedure. The IDA method is used to assess the seismic collapse resistance of the SC-MRF with the changed design criterion for PT strands. The two designed SC-MRFs are referred to as SC-MRF Design 1, where the total PT force under the MCE is limited to 90 percent of the total PT yield force, and SC-MRF Design 2, where the total PT force under MCE is limited to 75 percent of the total PT yield force.

6. Seismic collapse resistance of an SC-MRF for near-field ground motion:

   The SC-MRF has been studied for response under the DBE and MCE, where typically far-field ground motions were used in these studies. However, structures are built where active faults may be in close proximity. The seismic collapse resistance of an SC-MRF (SC-MRF, Design 1) is studied under near-field ground motions.

7. Comparison of the seismic collapse resistance of SC-MRFs with an SMRF:

   A 4-story prototype office building with SMRFs was designed with the same floor plan and elevation as the prototype building with SC-MRFs. The building is assumed to be located at the same site as the prototype building with SC-MRFs. The SMRF is modeled in a similar manner as the SC-MRF using continuum and stress-resultant elements. In the model the continuum elements were started from the face of the column and continued for one beam depth over the length of the beam where local buckling is expected to develop since the SMRF has been designed without reinforcing plates. The first buckling mode shape is scaled to impose web and flange out-of-flatness imperfections in the beams. In order to

validate the modeling procedure for an SMRF, the connection behavior is studied by comparing the analytical model results with the experimental test data of Ricles et al. (2000) for an interior subassembly connection. IDA are performed to obtain the CMR and fragility curve for collapse.

12.1.3. Findings

This section summarizes the findings from this research.

- It was found that the CMR values depended on the definition of collapse. The CMR was lowest for the systems for the collapse definition of 10% story drift and highest for the collapse definition of 15% story drift.
- It was observed that larger variability in sources of uncertainty causes a larger probability of collapse at the MCE level.
- It was observed that the CMR is larger for SC-MRF Design 1 for different collapse definitions and provides more seismic collapse resistance than a comparable SMRF.
- It was found that the design procedure affects the seismic collapse resistance of an SC-MRF. The SC-MRF Design 2 has smaller CMR values than the SC-MRF Design 1 for different collapse definitions. The stiffness of the post-gap opening response of the connection moment-relative rotation relationship in an SC-MRF appears to have a significant effect on the collapse resistance. The larger the post-gap opening stiffness in this relationship, the larger amount of axial force that develops in the PT strands and the beams, making the beams more susceptible to local web and flange buckling following gap opening in

the connection, and consequently a reduction in the collapse resistance of the SC-MRF.

- It was seen that the design of an SC-MRF affects the seismic collapse resistance compared to a comparable SMRF. The SC-MRF design 2 has smaller CMR values than the SMRF for different collapse definitions while the SC-MRF Design 1 has larger CMR values than the SMRF.
- It was observed that the ACMR values for systems are acceptable per FEMA P695 for different collapse definitions.
- It was found that the PT strand yielding is more likely to occur in SC-MRF Design 1. The probability of PT strand maximum strain exceeding the yield strand strain varies at different floor levels and is the highest at the roof for an SC-MRF.
- It was seen that the probability of the PT strand maximum strain exceeding a strand fracture strain of 2%, assuming the fracture strain as a deterministic variable, is small and negligible for SC-MRF Designs 1 and 2.
- It was found that the probability of the PT strand maximum strain exceeding a strand fracture strain of 1%, assuming the fracture strain as a deterministic variable, is higher for SC-MRF Design 1 while it is smaller and negligible for SC-MRF Design 2. The maximum probability of the PT strand maximum strain exceeding the strand fracture strain of 1% occurs at the roof for SC-MRF Design 1.

- Treating the fracture strain as a random variable, it was found that PT strand fracture is more likely to occur in SC-MRF Design 1 than Design 2. The possibility of PT strand fracture is the highest at the roof.
- It was found that the seismic collapse resistance of an SC-MRF (i.e., CMR) is less for near-field found motions than far-field ground motions.

12.2. Conclusions

This research has led to the following conclusions:

- Design criteria of SC-MRF studied in this research provides an adequate margin against collapse under extreme ground motions while it enables immediate occupancy (IO) performance with minimal yielding in the main structural members under the DBE and achieves collapse prevention (CP) performance with minor damage under the MCE.
- Collapse performance of an SC-MRF is controlled by beam local buckling and PT strand yielding and fracture under extreme loading. Beam local buckling occurs at the lower floors while the beams develop the larger beam axial forces and bending moments. The PT strand yielding occurs in the upper floors where the connections experience larger PT strand elongation, leading to larger PT strand forces.
- The probability of PT strand yielding and fracture of an SC-MRF considerably decreases by varying the number of PT strands and level of PT force per strand. However, the increased number of strands leads to a higher post-gap opening stiffness resulting in larger axial forces that results in local buckling developing in the beams. This leads to a higher probability of collapse. A design limit

needs to be placed on the connection post-gap opening moment-relative rotation stiffness, which is directly related to the number of PT strands, in order to ensure that an adequate collapse margin ratio and probability of collapse value of the SC-MRF are achieved. Establishing this limit will require further studies.

- An SC-MRF has a reduced collapse resistance (i.e., CMR) when subjected to near-field ground motions compared to the same SC-MRF subjected to far-field ground motions.
- The collapse resistance of an SC-MRF with the PT design force based on 90% of the yield force under the MCE is found to exceed that of a comparable SMRF assuming the same amount of dispersion. Therefore, in addition to the already established fact that an SC-MRF system can perform in a resilient manner under the DBE, it appears that the SC-MRF in this study has a satisfactory margin against collapse that is comparable, or better than a conventional steel SMRF.
- The collapse resistance is sensitive to a change in design parameters, particularly the PT design force and post gap-opening PT stiffness.
- The collapse margin ratio and probability of collapse at the MCE level is dependent on the point in which the structure assumed to collapse. Subsequently, three different collapse definitions were considered in this study and the results provided for each case. The probability of collapse at the MCE level for an SC-MRF is less than 20% for all three collapse definitions

(Allowable value for each archetype within a performance group per FEMA P695).

- The ACMR values for an SC-MRF is within the acceptable values per FEMA P695 for different collapse definition for near-field and far-field ground motions.
- Sources of uncertainty contribute to variability in collapse capacity. Uncertainty affects the collapse probability at the MCE level intensity. Larger variability in sources of uncertainty cause larger probability of collapse at the MCE level.

12.3. Original Research Contributions

This research project makes the following original contributions in the field of earthquake engineering:

- Evaluates the seismic collapse resistance of an SC-MRF system.
- Evaluates the sensitivity of collapse resistance of an SC-MRF to the PT strand detailing, by varying the number of PT strands and level of PT force in strand yield design criterion, and expands the knowledge base of the effect of this parameter on seismic collapse resistance and the probability of PT strand yielding and fracture in SC-MRFs.
- Evaluates the seismic collapse resistance of an SC-MRF built where an active fault may be in close proximity.
- Although an evaluation of the response modification factor R is not the goal of this research, this research can show whether using R=8 is an appropriate value

to design SC-MRFs by establishing whether an acceptable ACMR value is obtained from the IDA results as stipulated in FEMA P695.

- Seismic collapse of SC-MRFs in comparison with conventional steel SMRFs, showing which system has higher probability of collapse under MCE level and is less reliable for designing buildings.

12.4. Recommended Future Research

The research presented in this dissertation can be expanded to address the additional areas of study, and broaden the knowledge of behavior and performance of SC-MRFs under extreme ground motions. The following are recommended for further investigation:

- This research showed that SC-MRFs have the potential to perform better than SMRFs, however various archetypes and performance groups must be considered and studied to qualify the system whereby it has appropriate design factors in order that it has acceptable resistance to collapse per FEMA P695.
- Design detailing may affect the collapse resistance of SC-MRFs in contrast to conventional steel SMRFs. For instance, reinforcing plate lengths and variability in friction force in web friction devices may affect the collapse resistance of an SC-MRF.
- Experimental studies up to collapse point under extreme dynamic loading.
- A comprehensive parameter study is to develop an optimum design procedure to enable efficient designs that provide an acceptable collapse resistance per FEMA P695. This study should include investigating the

collapse resistance sensitivity of SC-MRFs to post-gap opening moment-relative rotation connection stiffness, establishing a design limit for this stiffness to ensure acceptable margins against collapse under severe earthquake ground motions.

References

ABAQUS, Inc. (2013). ABAQUS Analysis User's Manual, v. 6.13.

AISC (2010), Seismic Provisions for Structural Steel Buildings, American Institute of Steel Construction, Chicago, IL.

AISC (2010), Steel Construction Manual, American Institute of Steel Construction, Chicago, IL.

ASCE 7 (2010), Minimum Design Loads for Buildings and Other Structures, ASCE Standard 7-10, American Society of Civil Engineers (ASCE), Reston, VA.

ASTM A416 (2006), Standard Specification for Steel Strand, Uncoated Seven-Wire for Pre-stressed Concrete, American Society for Testing and Materials, Conshohocken, PA.

BSSC (2003), NEHRP Recommended Provisions for Seismic Regulations for New Buildings and Other Structures. FEMA 450. Building Seismic Safety Council, National Institute of Building Sciences, Washington, D.C.

Chen, S.J., Yeh, C.H., and Chu, J.M., (1996), "Ductile Steel Beam-to-Column Connections for Seismic Resistance," Journal of Structural Engineering, ASCE; 122:11, 1292-1299.

Engelhardt, M.D., and Sobol, T.A., (1998). "Reinforcing of Steel Moment Connections with Cover Plates: Benefits and Limitations," Engineering Structures, 20:4-6, 510-520.

FEMA (2009), Quantification of Building Seismic Performance Factors. *Report FEMA P695*, Federal Emergency Management Agency (FEMA), Washington, D.C.

Garlock, M., Ricles, J.M., Sause, R., Peng, S.-W., Zhao, C., and Lu, L.-W., (1998), "Post Tensioned Seismic Resistant Connections for Steel Frames," Workshop Proceedings, Frames with Partially Restrained Connections, Atlanta.

Garlock, M., (2002), "Full-Scale Testing, Seismic Analysis, and Design of Post-Tensioned Seismic Resistant Connections for Steel Frames," Ph.D. Dissertation, Dept. of Civil and Environmental Eng., Lehigh University, Bethlehem, PA.

Garlock, M., Ricles, J., Sause, R., (2005), "Experimental studies on full-scale post-tensioned steel connections," Journal of Structural Engineering, ASCE; 131(3): 438–448.

Garlock, M., Sause, R., and M., Ricles, J., (2007), "Behavior and Design of Post-tensioned Steel Frame Systems," Journal of Structural Engineering, ASCE; 133:3, 389–399.

Herrera, R., (2005), "Seismic Behavior of Concrete-Filled Tube Column-Wide Flange Beam Frames," Ph.D. Dissertation, Civil and Environmental Engineering Department, Lehigh University, Bethlehem, PA.

Ibarra L., Medina R., Krawinkler H., (2002), "Collapse assessment of deteriorating SDOF systems", Proceedings, 12th European Conference on Earthquake Engineering, London; Elsevier Science Ltd, paper #665.

Iyama, J, Seo, C.-Y., Ricles, J.M., Sause, R., (2009), "Self-centering MRFs with bottom flange friction devices under earthquake loading" Journal of Constructional Steel Research; 65:2, 314-325.

Kasai, K., (1998), "Seismic Performance of Steel Buildings with Semi-Rigid Connections," Proceedings of SAC Progress Meeting, SAC, Los Angeles, CA. 354.

Kaufmann E.J., Metrovich B., Pense A.W., (2001). "Characterization of cyclic inelastic strain behavior on properties of A572 Gr 50 and A913 Gr. 50 rolled sections", Lehigh University, Bethlehem, PA: ATLSS report No. 01-13.

King, A., (2007), "Design of Collector Elements for Steel Self-Centering Moment Resisting Frames," M.S. Thesis, Dept. of Civil Eng., Purdue University, West Lafayette, IN.

Krawinkler H., (1978). "Shear in Beam-Column Joints in Seismic Design of Steel Frames," Engineering Journal, AISC, 15(3), pp. 82-91.

Kim, H.-J., Christopoulos, C., (2008), "Friction Damped Posttensioned Self-Centering Steel Moment-Resisting Frames," Journal of Structural Engineering, ASCE; 134:11, 1768-1779.

Kim, H.-J., Christopoulos, C., (2009), "Seismic design procedure and seismic response of post-tensioned self-centering steel frames," Earthquake Engineering and Structural Dynamics; 38:3, 355-376.

Lemaitre J., Chaboche J-L., (1990), "Mechanics of Solid Materials". :Cambridge University Press.

Lin Y-C., (2012), "Seismic Performance of a Steel Self-Centering Moment Resisting Frame System with Beam Web Friction Device", Lehigh University, Bethlehem, PA: Ph.D. Dissertation, Dept. of Civil and Environmental Engineering.

Miranda, E., (2009), "Enhanced Building-Specific Seismic Performance Assessment," Proceedings, ACES Workshop: Advances in Performance-Based Earthquake Engineering, Corfu, Greece, July 4-7.

Petty, G.D., (1999), "Evaluation of a Friction Component for a Post-Tensioned Steel Connection," MS Thesis, Department of Civil and Environmental Engineering, Lehigh University, Bethlehem, PA.

Ricles, J.M., Sause, R., Garlock, M., Zhao, C., (2001), "Post-Tensioned Seismic-Resistant Connections for Steel Frames", Journal of Structural Engineering, ASCE; 127:2, 113-121.

Ricles J., Sause R., Peng S.W., Lu L.W., (2002), "Experimental Evaluation of Earthquake Resistant Posttensioned Steel Connections", Journal of Structural Engineering, ASCE, 128(7), 850-859.

Ricles J. M., Mao C.,Lu L-W., Fisher, J. W., (2000), "Development and Evaluation of Improved Details for Ductile Welded Unreinforced Flange Connections," Bethlehem, PA: ATLSS Report No: 00-04.

Ricles J. M., Sause R., Garlock M., Zhao C., (2001), "Post-Tensioned Seismic-Resistant Connections for Steel Frames," Journal of Structural Engineering, ASCE; 127:2, 113-121.

Rojas P. (2003), "Seismic Analysis, Design, and Evaluation of Post-Tensioned Friction Damped Connections for Steel Moment Resisting Frames," Ph.D. Dissertation, Dept. of Civil and Environmental Eng., Lehigh University, Bethlehem, PA.

Rojas, P., Ricles J.M., and Sause R., (2005), "Seismic Performance of Post-Tensioned Steel Moment Resisting Frames with Friction Devices," Journal of Structural Engineering, ASCE; 131:4, 529-540.

Seo C-Y., Sause R., (2005). "Ductility Demands on Self-Centering Systems under Earthquake Loading," ACI Structural Journal; 102:2, 275-285.

Tsai, K.-C., Chou, C.-C., Lin, C.-L., Chen, P.-C., and Jhang, S.-J., (2008), "Seismic Self-Centering Steel Beam-to-Column Moment Connections Using Bolted Friction Devices," Earthquake Engineering and Structural Dynamics; 37:4, 627–645.

Vamvatsikos D., Cornell C. A., (2006). "Direct estimation of seismic demand and capacity of multi-degree of freedom systems through incremental dynamic analysis of single degree of freedom approximation," 131(No. 4, April 1), pp. 589-599.

Walsh, K.Q. and Kurama, Y.C., (2010), "Behavior of Unbonded Post-Tensioning Monostrand Anchorage Systems under Monotonic Tensile Loading," PCI Journal, Winter; 97-117.

Wolski, M., (2006), "Experimental Evaluation of a Bottom Flange Friction Device for a Self-Centering Seismic Moment Resistant Frame with Post-Tensioned Steel Moment Connections," M.S. Thesis, Dept. of Civil and Environmental Eng., Lehigh University, Bethlehem, PA.

Wolski, M., Ricles, J., and Sause, R., (2009), "Experimental Study of a Self-Centering Beam-Column Connection with Bottom Flange Friction Device," Journal of Structural Engineering, ASCE; 135:5, 479-488.

Youssef, N., Bonowitz, D., and Gross, J., (1995). “A Survey of Steel Moment Resisting Frame Buildings Affected by the 1994 Northridge Earthquake,” Report NISTIR 5625, National Institute of Standards and Technology, Gaithersburg, MD.

VITA

Omid Ahmadi was born on January 13, 1985, to Majid Ahmadi and his wife Mehri Atarod.

In July 2007, Omid graduated from Isfahan University of Technology, Isfahan, Iran, with the degree of Bachelor of Science in Civil Engineering. In February 2010, he graduated from Isfahan University of Technology with the degree of Master of Science in Structural Engineering under the guidance of Dr. Amir Mahdi Halabian. His thesis title was "Performance-Based Analysis of Asymmetric R/C Dual Structural Systems Subjected to Bi-Directional Excitations".

Omid entered Lehigh University in the fall of 2010. He was appointed as research assistant and teaching assistant for research projects and courses during his doctoral studies. He will receive his Doctor of Philosophy degree in Structural Engineering in September 2016.